# MECHANICAL DEFORMATION AND STRENGTHENING MECHANISMS IN CALCITE SINGLE CRYSTALS

A Dissertation

Presented to the Faculty of the Graduate School

of Cornell University

In Partial Fulfillment of the Requirements for the Degree of

Doctor of Philosophy

by

Joseph David Carloni

December 2017

# MECHANICAL DEFORMATION AND STRENGTHENING MECHANISMS OF CALCITE SINGLE CRYSTALS

Joseph David Carloni, Ph.D.

Cornell University 2017

Calcite (the most stable form of $CaCO_3$) is a common mineral that naturally exists in geology and biology, and can also be grown synthetically. In its pure and defect-free form, calcite is relatively soft and brittle. Amazingly though, despite its intrinsic shortcomings as a structural material, calcite often serves a structural purpose in biology. For example, the teeth, shells, and spines of many marine organisms contain, or are entirely composed of, calcite. These biogenic calcite-containing structures are much stronger and tougher than a pure control calcite crystal, and small-scale indentation testing suggests that even the single-crystals of calcite that make up these structures may be significantly harder than a pure control. The exact mechanisms of the increased hardness are not known, thus there is much interest in creating model synthetic calcite crystals to replicate and help explain such hardening effects.

However, it is difficult to interpret the differences in hardness between different biogenic and synthetic calcites because the reference hardness of pure single-crystal calcite is not well known (there are large variations in previously-reported data). In this work, strides are made towards achieving a better understanding of the strengthening of biogenic and synthetic calcites in three ways: (1) Previous reports of the indentation hardness of calcite are compiled and compared, and new experiments are performed to quantify the effect of the indentation size effect and crystal anisotropy on hardness measurements of calcite. (2) A new indentation method is developed that allows for accurate measurements to be made on small, embedded

particles (like biogenic and synthetic calcite crystals), by accounting for the effect of a dissimilar matrix material. And (3) it is demonstrated that the hardness of pure synthetic calcite crystals can be increased by simply varying the kinetics of their growth. Additionally, previously published collaborative work (included in the Appendix) explains an important impurity-based strengthening mechanism in calcite.

## BIOGRAPHICAL SKETCH

Joe Carloni was born in 1990 to parents Elizabeth and David Carloni, and grew up in Clifton Park, NY. In Fall 2008, Joe started his undergraduate studies in engineering at Binghamton University in Binghamton, NY. In the summer of 2011, Joe was introduced to materials research through an internship at Colorado School of Mines in Golden, CO where he worked in the group of Prof. Corinne Packard. Back at Binghamton that fall, Joe continued to be involved in materials research working in the group of Prof. Junghyun Cho. Joe completed his B.S. in Mechanical Engineering at Binghamton in Spring 2012, and then started his Ph.D. in Materials Science at Cornell University that summer, working in the groups of Professors Shefford Baker and Lara Estroff. After successfully defending his dissertation in 2017, Joe started work as an engineer at Intel in Portland, OR.

Dedicated to my special lady, Alexandra

# ACKNOWLEDGMENTS

I'm grateful for the help of many people during my time at Cornell. First of all I'd like to thank my research advisors, Professors Shefford Baker and Lara Estroff, for providing me an interesting project to work on, the opportunity to pursue a Ph.D., and guidance along the way.

I'd also like to thank all of my collaborators. Thanks to fellow lab members both past and present, especially Dr. Miki Kunitake for helping me in the early stages of my project (and throughout). Thanks to Dr. John Mason and Prof. Terry Jordan for helping me learn to study rocks, and Dr. Yi-Yeoun Kim and Prof. Fiona Meldrum of Leeds Univeristy for providing me with interesting synthetic samples to study and papers to co-author. Thanks to Hysitron, Inc. for providing the Baker group with the nanoindenter, and thanks to the scientists at Hysitron with whom I collaborated. And thanks to everyone that enabled me to use my research skills to do consulting work on the side, including Professors Dieter Ast and Bruce van Dover, and Dr. Mats Larsson of Applied Materials.

Finally, I'd like to thank friends and family. Thanks to my close friends and study group for the learning and the laughs: David Lynch, Ben Revard, and Ben Richards (a.k.a., the "A-Team"). Thanks to my close friend and undergrad roommate Jason Guss for also choosing to do his Ph.D. at Cornell. Thanks to my intramural teammates (shout-out to Ryo Wakabayashi) for helping me to stay physically active. And thanks to my parents, my brother David, and my girlfriend Alexandra Tharp, for always being there for me and patiently waiting for me to finish writing.

This work was supported by the National Science Foundation (NSF) via the Materials World Network grant (DMR-1210304). Additional chapter-specific acknowledgements are included in Chapters 4-6.

TABLE OF CONTENTS

LIST OF FIGURES

**Appendix Figures**

LIST OF TABLES

# CHAPTER 1: INTRODUCTION

Calcite (the most thermodynamically stable form of $CaCO_3$) is a common mineral that exists in geology, contained in sedimentary rocks like limestone and shale, and also in biology, for example in the shells, teeth, and spines of marine organisms. The mechanical properties of calcite are important for a number of practical reasons. For example, calcite is an important ingredient in man-made structural materials like concrete and cement [1, 2]; crushed calcite powders are used as low-hardness abrasives or pressed together into pharmaceutical antacid tablets [3]; and the mechanical strength of calcite-containing limestone and shale is important in $CO_2$ sequestration processes used to store greenhouse gas pollutants [4], as well as the hydraulic fracturing processes used to release trapped oil and gas [5]. Another reason the mechanical properties of calcite are interesting is that many biological organisms use it for structural purposes.

In a pure and defect-free form, calcite is relatively soft and brittle. For example, pure crystals of calcite can be compacted together to form a soft and crumbly piece of chalk suitable for writing on a blackboard (*e.g.*, Figure 1.1a). Examples of such pure and defect free crystals are usually either of geologic origin, or grown synthetically under certain growth conditions. The mechanical strength of such crystals has been measured by bulk compressive testing [6] and, in many cases, indentation [7-37]. These crystals are prone to fracture, and their hardness is low. In fact, of the common biominerals (*e.g.*, silica, apatite, and calcite), pure calcite has the lowest hardness [31]. However, despite the inherent mechanical weakness of calcite in its pure and perfect form, biological organisms somehow manage to effectively use calcite for structural purposes (*e.g.*, Figure 1.1b). For example, the teeth, shells, and spines of many marine organisms contain, or are entirely composed of, calcite. Mechanical testing of these

biogenic calcite-containing structures on the scale of multiple crystals shows that they are much stronger and tougher than a pure and perfect control calcite crystal [38-40]. Some of this difference in mechanical properties can be attributed to the polycrystalline and composite nature of the biogenic structures, in which calcite crystals are often cemented together by organic material and/or mixed with other mineral phases (*e.g.*, aragonite, a less stable, and inherently harder [31], polymorph of $CaCO_3$). Interestingly though, small-scale mechanical testing (*i.e.*, indentation hardness testing) on individual single crystals of calcite from biogenic structures suggests that even the single crystal constituents can be more than 60% harder than a pure and perfect control crystal: These reports include measurements on calcite from within the shells of brachiopods [17, 18, 41] and mollusks [23, 26, 27, 42-46], the teeth [25, 32] and spines [20, 47, 48] of sea urchins, as well as the spicule of a sponge [49]. Such crystals have been shown to include solutes [16, 23, 41, 47, 50] that provide solid solution strengthening [51] as well as occluded molecules and second phase particles [23, 41, 52] that impede both dislocation [53] and crack [54] motion. There is much interest in better understanding and synthetically replicating the mechanisms that could lead to such single-crystal strengthening using model synthetic calcite. For example, synthetic crystals have been produced that include biomimetic impurities like solutes [51], small molecules [53], and second phase particles [19, 33, 37], as well as crystals with exotic impurities like carbon nano-tubes [34] and 2D sheets of graphene [36]

Studying the difference in hardness between different calcite crystals is complicated by a number of experimental factors. The small size of many biogenic and bio-inspired synthetic crystals (often <100 $\mu$m) requires small-scale mechanical testing techniques, such as micro- or nano-indentation. In general, indentation measurements can be affected by many factors, including the indentation size [55, 56].

Indentation measurements on single crystals can also be affected by additional factors related to crystal orientation [57, 58]. Furthermore, indentation measurements on small particles can be affected by any dissimilar material surrounding the particle of interest [59-63]. Existing literature values for the hardness of various calcites are clouded by these complications. Indeed, the reported values of indentation hardness of even pure defect-free single crystal "control" calcite crystals cover a large range of 1.5-3.5 GPa [7-37], nearly comparable to the 1-4.5 GPa range reported for biogenic calcite crystals [17, 18, 20, 23, 25-27, 32, 41-49]. In order to understand the hardness of biogenic calcites, a fundamental understanding of any variations in the indentation hardness of control calcite crystals must first be achieved.

In this thesis, I use careful indentation experiments on calcite crystals to help quantify and explain the difference in hardness between biogenic, synthetic, and control calcite crystals. Towards this end, first I determine how experimental factors such as indentation load and crystal orientation can affect indentation measurements on calcite crystals, and what role those factors play in the large variations in hardness data reported in the literature. Then, I determine the effect that dissimilar material surrounding a small particle (like a biogenic or synthetic crystal) has on indentation measurements of small particles. Together, these achievements help develop a good baseline for comparing calcite crystals with real, intrinsic differences. Once the effect of experimental factors like crystal orientation and surrounding material are understood, I then apply this understanding to measure the hardness of pure synthetic calcite crystals grown at different rates, and apparently with different defect structures (possibly due to a different growth mechanism, similar to that observed in biology).

Additionally, previously published collaborative work (included in the Appendix) explains an important impurity-based strengthening mechanism, which is controlled by the force to break apart the covalent bond holding a molecular impurity together.

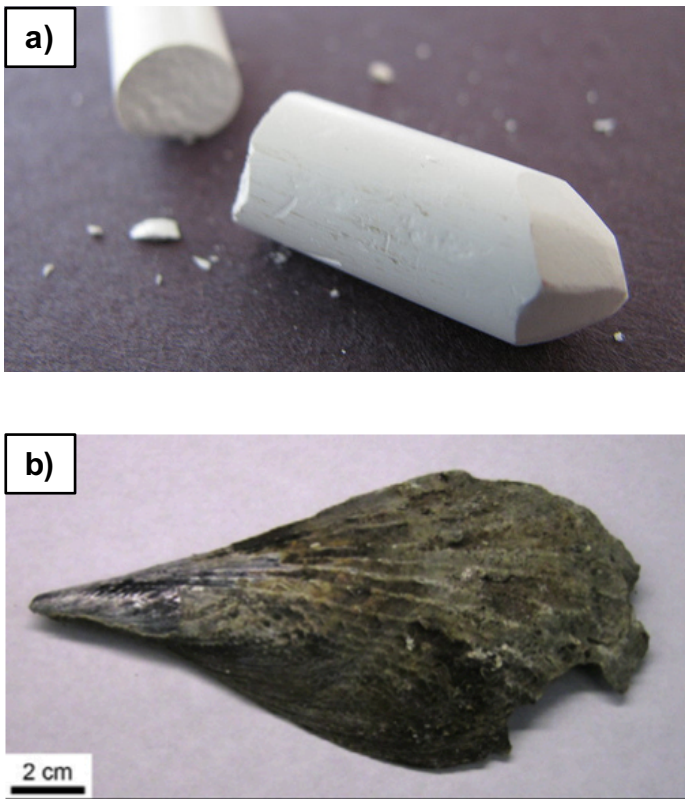


**Figure 1.1:** Examples of $CaCO_3$ structures. a) A crumbly piece of chalk made of pure calcite, compared to b) the shell of the mollusk *Atrina rigida*, which is a composite containing calcite in the outer protective layer.

*Part a from https://www.flickr.com/photos/thisisher/3259010655

*Part b reproduced with permission from Kunitake, M.E., et al., *Evaluation of strengthening mechanisms in calcite single crystals from mollusk shells*. Acta Biomaterialia, 2013. **9**(2): p. 5353-5359.

## REFERENCES


1. De Muynck, W., N. De Belie, and W. Verstraete, *Microbial carbonate precipitation in construction materials: A review*. Ecological Engineering, 2010. **36**(2): p. 118-136.

2. Matschei, T., B. Lothenbach, and F.P. Glasser, *The role of calcium carbonate in cement hydration*. Cement and Concrete Research, 2007. **37**(4): p. 551-558.

3. Carretero, M.I. and M. Pozo, *Clay and non-clay minerals in the pharmaceutical and cosmetic industries Part II. Active ingredients*. Applied Clay Science, 2010. **47**(3-4): p. 171-181.

4. Bachu, S., *Sequestration of CO2 in geological media: criteria and approach for site selection in response to climate change*. Energy Conversion and Management, 2000. **41**(9): p. 953-970.

5. Gale, J.F.W., R.M. Reed, and J. Holder, *Natural fractures in the Barnett Shale and their importance for hydraulic fracture treatments*. AAPG Bulletin, 2007. **91**(4): p. 603-622.

6. DeBresser, J.H.P. and C.J. Spiers, *Strength characteristics of the r, f, and c slip systems in calcite*. Tectonophysics, 1997. **272**(1): p. 1-23.

7. Taylor, E.W., *Correlation of the Mohs's scale of hardness with the Vickers's hardness numbers*. Mineralogical Magazine, 1949. **28**: p. 718-721.

8. Barber, D.J. and H.R. Wenk, *Deformation twinning in calcite, dolomite, and other rhombohedral carbonates*. Physics and Chemistry of Minerals, 1979. **5**(2): p. 141-165.

9. Pandya, J.R. and L.J. Bhagia, *Comparison of knoop and vickers hardness numbers on calcite cleavages*. Indian Journal of Pure & Applied Physics, 1984. **22**(7): p. 439-440.

10. Carter, G.M., J.L. Henshall, and R.J. Wakeman, *Influence of surfactants on the mechanical-properties and comminution of wet-milled calcite*. Powder Technology, 1991. **65**(1-3): p. 403-410.

11. Wong, T.Y. and R.C. Bradt, *Microhardness anisotropy of single-crystals of calcite, dolomite and magnesite on their cleavage planes*. Materials Chemistry and Physics, 1992. **30**(4): p. 261-266.

12. Carter, G.M., J.L. Henshall, and R.J. Wakeman, *Knoop-hardness and fracture anisotropy of calcite*. Journal of Materials Science Letters, 1993. **12**(6): p. 407-410.

13. Wakeman, R.J., J.L. Henshall, and G.M. Carter, *Solution environment effects on the hardness and toughness of calcite during grinding*. Chemical Engineering Research & Design, 1993. **71**(A4): p. 361-370.

14. Hangen, U.D., *A comparision of nano-hardness and scratch-resistance on Mohs minerals*. Zeitschrift Fur Metallkunde, 2001. **92**(9): p. 1074-1077.

15. Zugner, S., K. Marquardt, and I. Zimmermann, *Influence of nanomechanical crystal properties on the comminution process of particulate solids in spiral jet mills*. European Journal of Pharmaceutics and Biopharmaceutics, 2006. **62**(2): p. 194-201.

16. Griesshaber, E., et al., *Crystallographic texture and microstructure of terebratulide brachiopod shell calcite: An optimized materials design with hierarchical architecture*. American Mineralogist, 2007. **92**(5-6): p. 722-734.

17. Schmahl, W.W., et al., *Hierarchical fibre composite structure and micromechanical properties of phosphatic and calcitic brachiopod shell biomaterials - an overview*. Mineralogical Magazine, 2008. **72**(2): p. 541-562.

18. Merkel, C., et al., *Mechanical properties of modern calcite- (Mergerlia truncata) and phosphate-shelled brachiopods (Discradisca stella and Lingula anatina) determined by nanoindentation*. Journal of Structural Biology, 2009. **168**(3): p. 396-408.

19. Kim, Y.Y., et al., *Bio-Inspired Synthesis and Mechanical Properties of Calcite-Polymer Particle Composites*. Advanced Materials, 2010. **22**(18): p. 2082-+.

20. Presser, V., et al., *Determination of the elastic modulus of highly porous samples by nanoindentation: a case study on sea urchin spines*. Journal of Materials Science, 2010. **45**(9): p. 2408-2418.

21. Raman, S. and R. Kumar, *Construction and nanomechanical properties of the exoskeleton of the barnacle, Amphibalanus reticulatus*. Journal of Structural Biology, 2011. **176**(3): p. 360-369.

22. Bandini, A., et al., *Effects of intra-crystalline microcracks on the mechanical behavior of a marble under indentation*. International Journal of Rock Mechanics and Mining Sciences, 2012. **54**: p. 47-55.

23. Kunitake, M.E., et al., *Evaluation of strengthening mechanisms in calcite single crystals from mollusk shells*. Acta Biomaterialia, 2013. **9**(2): p. 5353-5359.

24. Olson, I.C., et al., *Crystal lattice tilting in prismatic calcite*. Journal of Structural Biology, 2013. **183**(2): p. 180-190.

25. Goetz, A.J., et al., *Tailored order: The mesocrystalline nature of sea urchin teeth*. Acta Biomaterialia, 2014. **10**(9): p. 3885-3898.

26. Li, L. and C. Ortiz, *Pervasive nanoscale deformation twinning as a catalyst for efficient energy dissipation in a bioceramic armour*. Nature Materials, 2014. **13**(5): p. 501-507.

27. Lv, J.L., Y.G. Jiang, and D.Y. Zhang, *Structural and Mechanical Characterization of Atrina Pectinata and Freshwater Mussel Shells*. Journal of Bionic Engineering, 2015. **12**(2): p. 276-284.

28. Metzler, R.A., et al., *Composition and Structure of Oyster Adhesive Reveals Heterogeneous Materials Properties in a Biological Composite*. Advanced Functional Materials, 2016. **26**(37): p. 6814-6821.

29. Winchell, H., *The knoop microhardness tester as a mineralogical tool*. American Mineralogist, 1945. **30**(9-10): p. 583-595.

30. Beste, U. and S. Jacobson, *Micro scale hardness distribution of rock types related to rock drill wear*. Wear, 2003. **254**(11): p. 1147-1154.

31. Broz, M.E., R.F. Cook, and D.L. Whitney, *Microhardness, toughness, and modulus of Mohs scale minerals*. American Mineralogist, 2006. **91**(1): p. 135-142.

32. Ma, Y., et al., *Sea urchin tooth design: An "All-Calcite" polycrystalline reinforced fiber composite for grinding rocks*. Advanced Materials, 2008. **20**(8): p. 1555-+.

33. Kim, Y.Y., et al., *An artificial biomineral formed by incorporation of copolymer micelles in calcite crystals*. Nature Materials, 2011. **10**(11): p. 890-896.

34. Calvaresi, M., et al., *Morphological and mechanical characterization of composite calcite/SWCNT-COOH single crystals*. Nanoscale, 2013. **5**(15): p. 6944-6949.

35. Muller, W.E.G., et al., *The sponge silicatein-interacting protein silintaphin-2 blocks calcite formation of calcareous sponge spicules at the vaterite stage*. RSC Advances, 2014. **4**(6): p. 2577-2585.

36. Giosia, M.D., et al., *Bioinspired Nanocomposites: Ordered 2D Materials Within a 3D Lattice*. Advanced Functional Materials, 2016.

37. Kim, Y.Y., et al., *Structure and Properties of Nanocomposites Formed by the Occlusion of Block Copolymer Worms and Vesicles Within Calcite Crystals*. Advanced Functional Materials, 2016. **26**(9): p. 1382-1392.

38. Dunlop, J.W.C. and P. Fratzl, *Biological Composites*. Annual Review of Materials Research, 2010. **40**(1): p. 1-24.

39. Ji, B. and H. Gao, *Mechanical Principles of Biological Nanocomposites*. Annual Review of Materials Research, 2010. **40**(1): p. 77-100.

40. Meyers, M.A., et al., *Biological materials: Structure and mechanical properties*. Progress in Materials Science, 2008. **53**(1): p. 1-206.

41. Perez-Huerta, A., et al., *Material properties of brachiopod shell ultrastructure by nanoindentation*. Journal of the Royal Society Interface, 2007. **4**(12): p. 33-39.

42. Lee, S.W., G.H. Kim, and C.S. Choi, *Characteristic crystal orientation of folia in oyster shell, Crassostrea gigas*. Materials Science & Engineering C-Biomimetic and Supramolecular Systems, 2008. **28**(2): p. 258-263.

43. Schneider, A.S., et al., *Hierarchical super-structure identified by polarized light microscopy, electron microscopy and nanoindentation: Implications for the limits of biological control over the growth mode of abalone sea shells*. Bmc Biophysics, 2012. **5**.

44. Metzger, T.H., et al., *Nanostructure of Biogenic Calcite and Its Modification under Annealing: Study by High-Resolution X-ray Diffraction and Nanoindentation*. Crystal Growth & Design, 2014. **14**(10): p. 5275-5282.

45. Fitzer, S.C., et al., *Ocean acidification alters the material properties of Mytilus edulis shells*. Journal of the Royal Society Interface, 2015. **12**(103).

46. Chen, G.W., et al., *Vertically oriented structure and its fracture behavior of the Indonesia white-pearl oyster*. Journal of the Mechanical Behavior of Biomedical Materials, 2017. **66**: p. 211-223.

47. Moureaux, C., et al., *Structure, composition and mechanical relations to function in sea urchin spine*. Journal of Structural Biology, 2010. **170**(1): p. 41-49.

48. Lemloh, M.L., et al., *Low Mg/Ca ratio alters material properties in sea urchin larvae skeleton*. Bioinspired Biomimetic and Nanobiomaterials, 2013. **2**(1): p. 28-34.

49. Muller, W.E.G., et al., *The enzyme carbonic anhydrase as an integral component of biogenic Ca-carbonate formation in sponge spicules*. Febs Open Bio, 2013. **3**: p. 357-362.

50. Wang, R.Z., L. Addadi, and S. Weiner, *Design strategies of sea urchin teeth: Structure, composition and micromechanical relations to function*.

Philosophical Transactions of the Royal Society of London Series B-Biological Sciences, 1997. **352**(1352): p. 469-480.

51. Kunitake, M.E., S.P. Baker, and L.A. Estroff, *The effect of magnesium substitution on the hardness of synthetic and biogenic calcite*. MRS Communications, 2012. **2**(3): p. 113-116.

52. Li, H.Y., et al., *Calcite Prisms from Mollusk Shells (Atrina Rigida): Swiss-cheese-like Organic-Inorganic Single-crystal Composites*. Advanced Functional Materials, 2011. **21**(11): p. 2028-2034.

53. Kim, Y.-Y., et al., *Tuning hardness in calcite by incorporation of amino acids*. Nature materials, 2016.

54. Aizenberg, J. and G. Hendler, *Designing efficient microlens arrays: lessons from Nature*. Journal of Materials Chemistry, 2004. **14**(14): p. 2066-2072.

55. Sangwal, K., *Review: Indentation size effect, indentation cracks and microhardness measurement of brittle crystalline solids - some basic concepts and trends*. Crystal Research and Technology, 2009. **44**(10): p. 1019-1037.

56. Bull, S.J., *On the origins and mechanisms of the indentation size effect*. Zeitschrift Fur Metallkunde, 2003. **94**(7): p. 787-792.

57. Brookes, C.A., J.B. Oneill, and B.A.W. Redfern, *Anisotropy in hardness of single crystals*. Proceedings of the Royal Society of London Series a-Mathematical and Physical Sciences, 1971. **322**(1548): p. 73-&.

58. Vlassak, J.J. and W.D. Nix, *Measuring the elastic properties of anisotropic materials by means of indentation experiments*. Journal of the Mechanics and Physics of Solids, 1994. **42**(8): p. 1223-1245.

59. Jakes, J.E., et al., *Experimental method to account for structural compliance in nanoindentation measurements*. Journal of Materials Research, 2008. **23**(4): p. 1113-1127.

60. Jakes, J.E. and D.S. Stone, *The edge effect in nanoindentation*. Philosophical Magazine, 2011. **91**(7-9): p. 1387-1399.

61. Vivanco, J., et al., *Accounting for structural compliance in nanoindentation measurements of bioceramic bone scaffolds*. Ceramics International, 2014. **40**(8): p. 12485-12492.

62. Yan, W.Y., et al., *Some issues on nanoindentation method to measure the elastic modulus of particles in composites*. Composites Part B-Engineering, 2011. **42**(8): p. 2093-2097.

63. Zhao, Y. and T.C. Ovaert, *Error estimation of nanoindentation mechanical properties near a dissimilar interface via finite element analysis and analytical solution methods*. Journal of Materials Research, 2010. **25**(12): p. 2308-2316.

# CHAPTER 2: BACKGROUND

## 2.1. Structure and Mechanical Properties of Calcite

### 2.1.1. Solid phases of $CaCO_3$

At room temperature and pressure, calcite is the most stable polymorph of $CaCO_3$. It has a trigonal-rhombohedral crystal structure that belongs to the $R\bar{3}c$ space group (International Union of Crystallography No. 167). Calcite has a density of 2.71 g/cm$^3$, and under high enough hydrostatic pressure, calcite is known to convert to at least two other spontaneously-reversible phases, calcite II (at 1.7 GPa) and calcite III (at ~2 GPa) [1]. The other crystalline polymorphs of $CaCO_3$ are aragonite (orthorhombic structure) and vaterite (hexagonal structure), and they have densities of 2.95 and 2.56 g/cm$^3$, respectively. Additionally, $CaCO_3$ can exist in the form of hydrates (such as hexahydrate and monohydrate), and as a solid amorphous phase, called "amorphous calcium carbonate" (ACC) [2]. Each of these phases is metastable and in a pure form will readily convert to calcite over time at room temperature and pressure. In this work, I focus on the properties of the stable crystalline phase of $CaCO_3$, calcite.

### 2.1.2. Morphology and structure of calcite

The macroscopic morphology of a pure and defect-free calcite crystal is exemplified by the relatively large and optically transparent, geologic single crystals known as Iceland spar, named after a famous outcrop of such crystals in Iceland [3]. An example of an Iceland spar crystal is shown in Figure 2.1a. The optical transparency of Iceland spar crystals is related to the high degree of purity and crystallographic perfection of such crystals. Furthermore, these crystals are faceted, with a rhombohedral morphology that reflects the low-surface-energy planes of the underlying crystal structure.

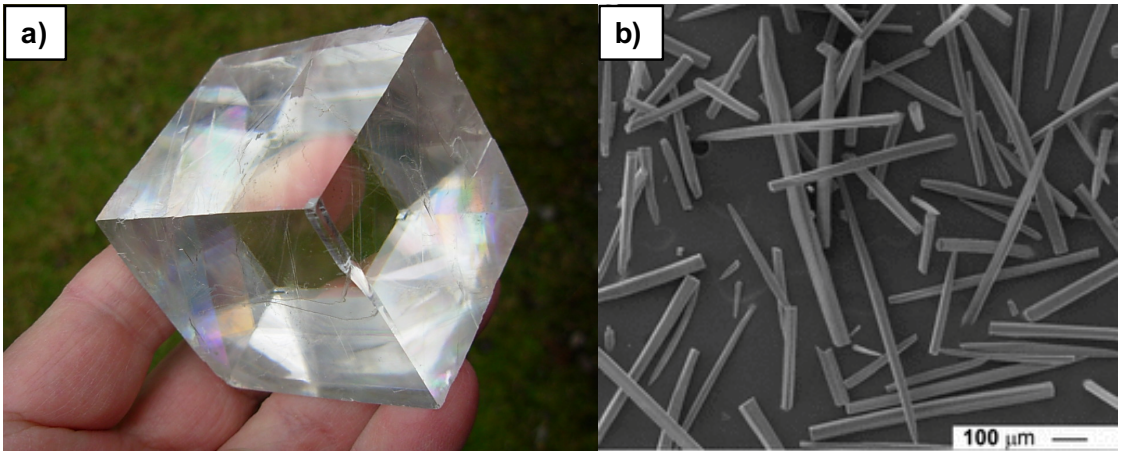


**Figure 2.1:** Examples of calcite single crystals. a) A large, faceted single crystal of pure, geologic Iceland spar calcite. b) Elongated and impure single crystal prisms of calcite extracted from the outer layer of the shell of the mollusk *Atrina rigida*.

*Part a from http://www.spiritrockshop.com/images/DSCN4947.JPG,

*Part b reproduced with permission from: Li, H.Y., et al., *Calcite Prisms from Mollusk Shells (Atrina Rigida): Swiss-cheese-like Organic-Inorganic Single-crystal Composites*. Advanced Functional Materials, 2011. **21**(11): p. 2028-2034.

In general, I will refer any such crystal with a high degree of purity and perfection as a "control" crystal. In contrast, biological organisms often grow small (micrometer-scale) calcite crystals with defects and irregular morphologies. For example, an SEM micrograph of elongated single-crystal prisms extracted from the outer layer of the shell of a mollusk [4] is shown in Figure 2.1b**.** In general, I will refer to any such crystal with biological origins as a "biogenic" crystal.

The calcite crystal structure is schematically illustrated in Figure 2.2. The crystal structure has trigonal-rhombohedral symmetry, but the unit cell is commonly referenced using hexagonal notation [5]. The dimensions of the hexagonal unit cell are $a = 4.99$ and $c = 17.06$ Å. A 3D view of this hexagonal unit cell in Figure 2.2a shows that the crystal is composed of alternating layers of $Ca^{2+}$ and $CO_3^{2-}$ ions that are vertically stacked in the direction of the *c*-axis, with 3-fold symmetry about the *c*-axis. Each alternating $Ca^{2+}$ or $CO_3^{2-}$ layer is slightly shifted horizontally with respect to adjacent layers. Furthermore, in every other layer of $CO_3^{2-}$, the C-O bond of each $CO_3^{2-}$ group is rotated about the crystal *c*-axis by 60 degrees, with respect to adjacent layers of $CO_3^{2-}$. The arrangement of these layers is more easily interpreted in the cross-sectional view in Figure 2.2b, looking down the $+a_2$-axis ($-a_2$-axis pointing out of the page). Note that in this cross-sectional view any atoms not in the plane of the page are simply projected forward, as are the boundaries of the unit cell. In this view, each layer of $CO_3^{2-}$ is oriented such that the direction of the C-O bonds alternates pointing in or out of the page every other layer. Because of this periodic rotation of the $CO_3^{2-}$ groups, the proper definition of the unit cell (as shown here) necessarily contains a full 6 layers of each $Ca^{2+}$ and $CO_3^{2-}$. This is important to note, since some early studies (and unfortunately a few more recent studies [6-9]) have used different unit cells that do not contain the full symmetry of the $CO_3^{2-}$ layers, and are only based on the morphology of geologic control crystals.

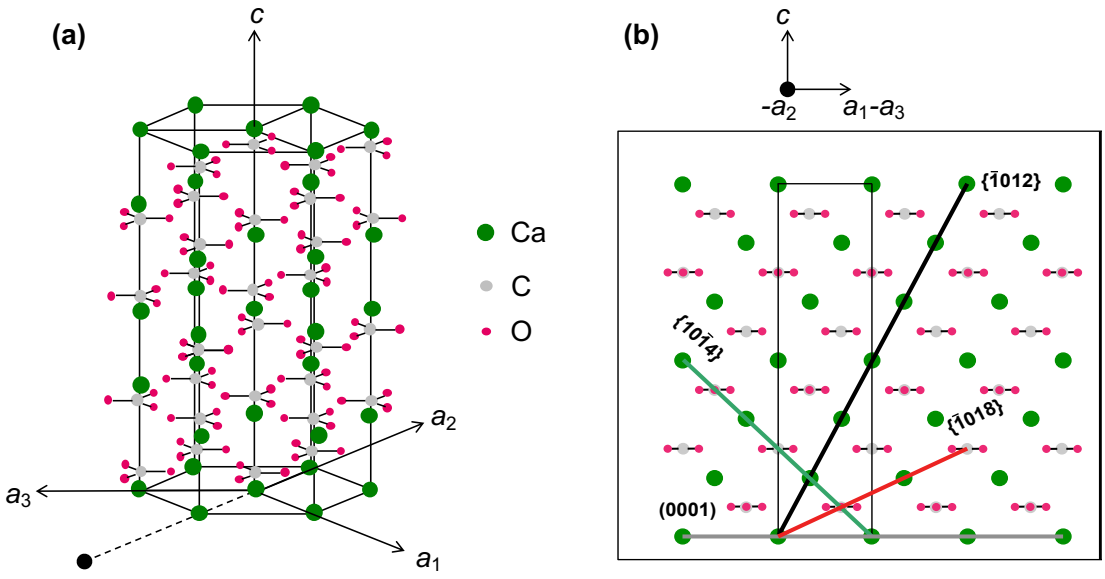


**Figure 2.2:** Schematics of calcite crystal structure. a) A 3D representation of the hexagonal unit cell. b) Cross-sectional view looking down the $a_2$-axis, with out-of-plane atoms projected into the plane of the page.

It is also important to note that the 3 symmetrical *a*-axes of the unit cell are defined as being parallel to the C-O bonds in the $CO_3^{2-}$ groups that make up the "first" $CO_3^{2-}$ layer (*i.e.*, the first layer when stacked vertically along the *c*-axis, starting at the origin of the crystal coordinate system), and pointing in the opposite direction of the vector that starts at the C atom and points towards the O atom.

Also in Figure 2.2b, some important crystallographic planes are labelled. These planes are $\{10\bar{1}4\}$, $(0001)$, $\{\bar{1}018\}$, and $\{\bar{1}012\}$. The $\{10\bar{1}4\}$ planes are important because they have the lowest surface energy, and are thus the natural occurring cleavage planes in geologic control crystals (*e.g.*, facets in Figure 2.1a). The $(0001)$ plane (*i.e.*, the plane that contains the alternating layers of $Ca^{2+}$ and $CO_3^{2-}$ referenced earlier) is important because many biogenic calcite crystals are elongated along the $[0001]$ *c*-axis direction, normal to $(0001)$. Furthermore, the orientation of these biogenic crystals (*e.g.*, in the outer layer of a mollusk or brachiopod shell [10-13]) is such that $(0001)$ is the natural wear surface. The other planes, $\{\bar{1}018\}$ and $\{\bar{1}012\}$, are, in addition to $\{10\bar{1}4\}$, the possible slip planes [14]. Plastic deformation in calcite can occur by normal dislocation glide on $\{10\bar{1}4\}$ and $\{\bar{1}012\}$, and by twinning on $\{\bar{1}018\}$.

Note that here the crystal planes are represented by the full 4-index miller-bravais hexagonal notation $\{hkil\}$. The third index in this notation is redundant, *i.e.*, $i = -(h + k)$. Thus, some authors have chosen to drop the "*i*" index and instead use a condensed 3-index notation [6, 7, 10, 11, 13, 15-19], *i.e.*, such that the cleavage planes (of the full, 6 layer $CaCO_3$ unit cell) are referred to as $\{104\}$ instead of $\{10\bar{1}4\}$. The condensed notation is technically valid, but it makes distinguishing specific planes and directions of the same family difficult. For example, $(10\bar{1}4)$ and $(\bar{1}104)$ each belong to the $\{104\}$ family, but $(\bar{1}104)$ is $(\bar{1}14)$ in the condensed notation—which is not obviously of $\{104\}$ type. Furthermore, converting crystal directions between the two

systems is even more complicated. In the 4-index notation, the crystal direction that is parallel to the $a_1$-axis is $[22\bar{1}0]$, but is $[100]$ in the condensed notation. Hence, I will stick to the 4-index notation here.

### 2.1.3. Elastic properties of calcite

Calcite is highly anisotropic elastically. Its single crystal elastic constants have been determined both experimentally [20] and theoretically [21]. Because of the trigonal symmetry of calcite's structure, there are six independent elastic constants [22]. These are usually reported as the stiffness constants, $C_{ijkl}$, in the condensed Voigt notation, $c_{ij}$. Based on a compilation of reported values included in the theoretical study by Zhang *et al*. [21], the experimentally determined stiffness constants reported by Chen *et al* [20] are close to the mean of all values reported in other studies. The values reported by Chen *et al* are (in GPa):

$c_{11} = 149.4, c_{12} = 57.9, c_{13} = 53.5, c_{14} = -20.2, c_{33} = 85.2,$ and $c_{44} = 34.1.$

In the appendix of Chapter 4, I use these stiffness constants to construct and transform the compliance tensor **S**, in order to calculate Young's modulus ($E_{11} = 1/S_{11}$) for uniaxial loading in any crystallographic direction. In other words, the calculation gives $E(x_1')$, Young's modulus in any direction $x_1'$. Starting with an orthogonal coordinate system with $x_1$ parallel to one calcite *a*-axes and $x_3$ parallel to the *c*-axis, the direction $x_1'$ can be defined by rotating the initial coordinate system about $x_3$ by an angle $\alpha$, and then about the new $x_2'$ by an angle $\beta$ [23]. An illustration of this coordinate system is in Figure 2.3a.

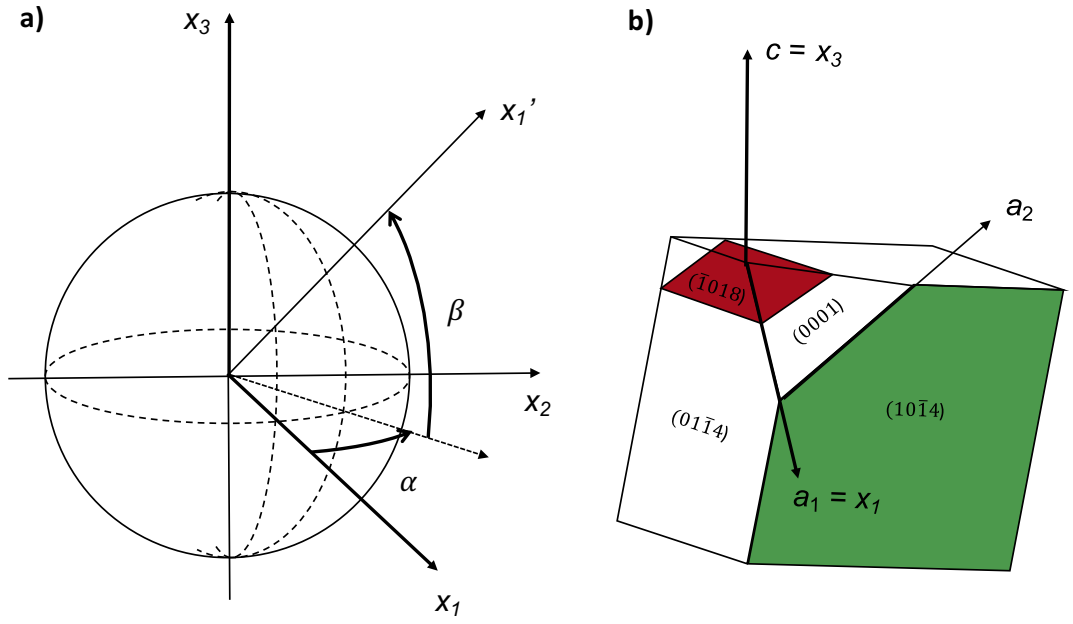


**Figure 2.3:** Schematic illustrating a) the ($\alpha$, $\beta$) coordinate system, and b) its relation to the morphology of a control geologic crystal.

Alongside, in Figure 2.3b, is a labelled schematic of a $\{10\bar{1}4\}$ faceted calcite crystal, with $(0001)$ plane exposed, to facilitate visual comparison between the ($\alpha$, $\beta$) coordinate system and some relevant crystal planes in calcite.

The results of the tensor transformation reveal that the global maximum and minimum Young's moduli are both contained in the spherical "slice" at $\alpha = 30^{\circ}$ (or equivalently, $\alpha = 150$ or $270^{\circ}$), which also happens to be perpendicular to the common zone axis containing the 3 possible slip planes, $\{10\bar{1}4\}$, $\{\bar{1}018\}$, and $\{\bar{1}012\}$, which also happens to be the *a*-axis. For example, see the $a_2$-axis in Figure 2.3b. Within the slice at $\alpha = 30$, 150, or $270^{\circ}$, the global maximum Young's modulus is 144 GPa at $\beta = -23^{\circ}$, and the global minimum is 52 GPa at $\beta = 40^{\circ}$. Neither of these directions are normal to any low-index crystal directions in calcite but, for comparison, $\beta = -27^{\circ}$ is normal to $\{\bar{1}012\}$ (where $E = 141$ GPa), and $\beta = 45^{\circ}$ is normal to $\{10\bar{1}4\}$ (where $E = 53$ GPa). Thus the directions normal to $\{\bar{1}012\}$ and $\{10\bar{1}4\}$ are very close to the directions of highest and lowest Young's modulus, respectively. In comparison, the Young's modulus normal to $(0001)$ is 58 GPa, and the average Young's modulus (simple average over all possible directions) is 74 GPa.

Additionally, Aouni and Wheeler [24] have shown by decomposition of calcite's stiffness tensor that it should display auxetic behavior (*i.e.*, a negative Poisson's ratio) for loading in certain directions. Their calculations show a minimum Poisson ratio of -0.0249, for loading in the direction of $\alpha = 30^{\circ}$ and $\beta = 47^{\circ}$, which is very close to the direction that is normal to $\{10\bar{1}4\}$ (*i.e.*, $\alpha = 30^{\circ}$ and $\beta = 45^{\circ}$).

### 2.1.4. Plastic properties of calcite

Pure geologic calcite is very brittle and tends to fracture before plastically deforming when loaded in most directions at room temperature. Much of the work exploring plastic deformation in calcite has been by compression tests at special orientations,

and often at elevated temperature and/or under confining pressure. Debresser and Spiers summarize much of this work [14]. Although there are apparently a few disparate reports of slip on $\{\bar{1}2\bar{1}0\}$, $\{10\bar{1}0\}$, and $(0001)$ (all at temperatures > 300ºC), the important and consistently reported modes of plastic deformation are slip on $\{10\bar{1}4\}$ along the $<\bar{2}021>$ direction, slip on $\{\bar{1}012\}$ along the $<\bar{2}20\bar{1}>$ or $<0\bar{2}2\bar{1}>$ directions, and mechanical twinning on $\{\bar{1}018\}$ along the $<404\bar{1}>$ direction. The $\{10\bar{1}4\}<\bar{2}021>$ slip and $\{\bar{1}018\}<404\bar{1}>$ twin directions are perpendicular to the $a_2$ zone axis shown in Figure 2.3b, and therefore in the plane of the page in Figure 2.2b. The $\{\bar{1}012\}<\bar{2}20\bar{1}>$ or $<0\bar{2}21>$ slip directions, however, are offset from that zone axis, such that they are in/out of the plane of the page in Figure 2.2b by +/- 30º. For deformation on any of these systems, there is a positive and a negative sense of slip. Slip on the $\{10\bar{1}4\}$ and $\{\bar{1}012\}$ systems can occur in in either sense, but mechanical twinning on $\{\bar{1}018\}$ can only occur in the positive sense, since the carbonate groups have to "flip" or rotate during twinning and can only flip one way.

In this work, in accordance with the natural environments of many biogenic calcites, I am most interested in deformation modes at or near room temperature. DeBresser and Spiers report that at room temperature, mechanical twinning on $\{\bar{1}018\}$ is the easiest deformation mechanism, readily occurring even without confining pressure, and with a critical resolved shear stress (CRSS) of ~10 MPa [14]. In comparison, slip on $\{10\bar{1}4\}$ and $\{\bar{1}012\}$ is rarely observed at room temperature, but by extrapolating values measured at higher temperatures down to room temperature, it seems the CRSS for these systems is above 200 MPa [14].

## 2.2. Indentation hardness measurements

Besides compression testing, another common experimental method that has been used to measure the mechanical properties of calcite is indentation hardness testing.

Here I present a brief background on certain aspects of hardness that are relevant to the main chapters in this thesis.

### 2.2.1. Different definitions of hardness, and microindentation

Although quite different from indentation hardness, a simple and well-known metric that is called "hardness" is Mohs scale of mineral hardness [25]. Mohs scale of hardness is simply based on which common minerals can scratch other common minerals. It is mentioned here only because the Mohs hardness number of 3 is defined by calcite. All that this means is that calcite can scratch Gypsum (2 on Mohs scale) and Talc (1 on Mohs scale), but cannot scratch Flourite (4 on Mohs scale) or Apatite (5 on Mohs scale). In practice, this definition of hardness is only intended to be helpful to field geologists and is of little use to materials scientists. A more useful and quantitative description of hardness is indentation hardness.

The fundamentals of indentation hardness testing are also simple. A typical test involves forcing a sharp, stiff indenter (typically diamond) normal to a flat, planar surface of a sample material, creating a permanent impression on the surface of the sample. Then the size of the impression is determined, and hardness is defined as the ratio between the applied load and some measure of the size of the impression created by the indenter. In a microindentation test, the size of the impression is measured directly by some imaging technique, usually with an optical microscope. Typically, microindentations are made at loads between ~100 and 2,000 mN. In calcite, this results in indentations that are typically ~1-6 $\mu$m deep and ~5-30 $\mu$m in diameter, depending on the geometry of the indenter [6, 9-11, 17, 25-33].

Microindentations can be made with different shaped indenters, and two common indenter shapes are called Vickers [34] and Knoop [33]. These indenters are both 4-sided sharp pyramids, but the angle between adjacent faces is different for each type.

A diagram comparing the shapes of different common pyramidal indenters is in Figure 2.4. The shape of the Vickers indenter (Figure 2.4a) is 4-fold symmetric about the indentation axis, while the Knoop indenter (Figure 2.4b) is only 2-fold symmetric. Furthermore, the angles between opposite indenter faces (and thus the angles between indenter faces and the sample surface during normal loading) are different for each type of indenter. All four edges of a Vickers indenter make an angle of 16º with the sample surface during normal loading, and the angle between all four indenter faces and the sample surface is 22º. For a Knoop indenter, the angle between one set of opposite indenter edges and the sample surface is 3.8º, and that angle is 25º for the other set of opposite edges (the angle between all four faces of the indenter and the sample surface is 25.2º). Traditionally, Vickers and Knoop hardness have been described by a Vickers hardness number (*HV*) or Knoop hardness number (*KHN*), respectively. These numbers (sometimes reported without any units other than *HV* or *KHN*), are defined as the ratio between the applied load (in kgf) and the surface area of the impression (in $mm^2$). A more fundamental measure of hardness is Meyer hardness [35], which is the mean pressure under the indenter during indentation. Meyer hardness $H$ is defined as:

$$H = P/A_c, \tag{2.1}$$

where $P$ is the applied load, and $A_c$ is the "contact area", defined as the surface area of the indentation projected into the plane of the undeformed sample surface. Using the geometric relationship between surface area and contact area for either indenter shape, *HK* or *KHN* can easily be converted to $H$.

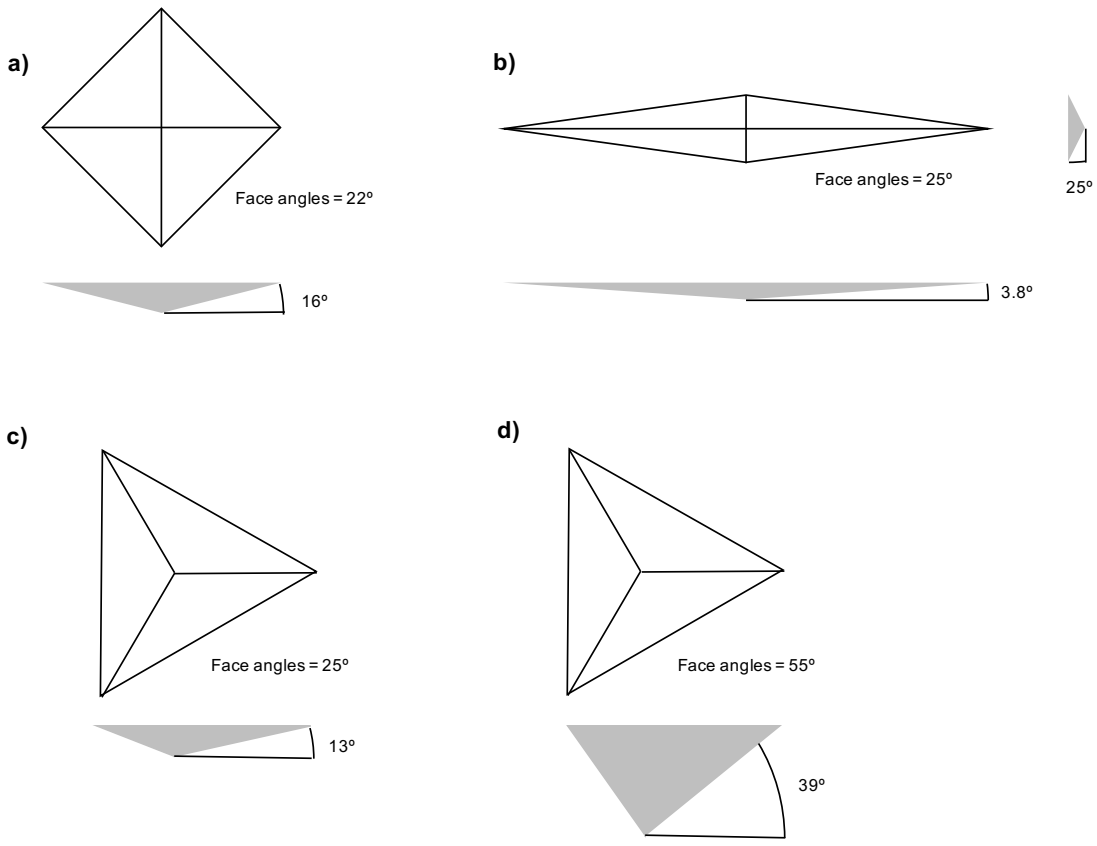


**Figure 2.4**: Schematic of different pyramidal probe geometries. a) Vickers, b) Knoop, c) Berkovich, d) Cube-corner. Relevant angles are labelled. Note that Vickers and Knoop are commonly used in microindentation, and Berkovich and cube-corner are commonly used in nanoindentation.

Meyer hardness provides a quantitative measure of hardness that, in principle, should not depend on the indenter geometry, for indenters with similar depth to area ratios. The deformation induced by the indenter may be accommodated by some combination of plastic deformation (*e.g.*, dislocation glide) in addition to fracture (especially at higher loads). For indentations made with blunt indenters and in the absence of substantial fracture, hardness has been shown to correlate well with yield stress $\sigma_y$, by the simple relationship

$$H = k\sigma_y, \tag{2.2}$$

where $k$ is an empirically determined constant, usually close to 3 [35, 36].

### 2.2.2. Nanoindentation vs. microindentation

A typical microindentation is made open-loop, without any feedback. That is, the applied load is specified, but the resultant displacement of the indenter is not measured. In contrast, there is another technique called "instrumented" (or "depth-sensing") indentation, in which load and displacement of the indenter are measured continuously during indentation. Compared to open-loop microindentation, the main advantages of instrumented indentation is that the resultant load-displacement data can be analyzed to determine the contact area (without imaging), and an elastic modulus for the sample (in addition to hardness) [37]. In practice, this type of indentation is usually done at smaller applied loads (typically < 100 mN, which in calcite typically results in indentations < 1 $\mu$m in depth and < 5 $\mu$m in diameter [13, 15-17, 25, 30, 38-51], depending on the geometry of the indenter). Because of the often sub-micrometer displacements associated with instrumented indentation, the term "nanoindentation" has become nearly synonymous with instrumented indentation, and will also be used that way here.

The foundations of modern methods of nanoindentation as an experimental technique seem to date back to the work of a group at the Baikov Institute of Metallurgy in Moscow in the 1970s [52]. Much of the associated analysis is based on Harding and Sneddon's (1945) [53] solution for elastic contact between a rigid flat punch indenter and an elastically homogeneous, semi-infinite half-space. Practical application of the nanoindentation technique has soared in popularity since Oliver and Pharr outlined their testing method in their famous paper in 1992 [37]. A plot of the number of citations of that paper versus time is included in Figure 2.5 to illustrate this point. Amazingly, the number of citations per year has increased nearly every year and, as of July 2017 the cumulative total number of citations is over 12,100. Thus, the details of the Oliver and Pharr method have already been covered extensively elsewhere, and will not be repeated again in this section. However, before moving on, I will discuss the different indenter shapes commonly used in nanoindentation.

The most commonly used indenter geometry for nanoindentation is the Berkovich indenter (schematically illustrated in Figure 2.4c). In contrast to the Vickers and Knoop geometries commonly used in microindentation, the Berkovich is a 3-sided pyramid. Also, the angle between each face of the indenter and the sample surface during normal loading is 25º. One of the main reasons for using a 3-sided indenter for nanoindentation is that it can more easily be machined to a sharp point at the tip than a 4-sided indenter can be. In reality, no indenter tip is perfectly sharp, and often there is some rounding at the tip. A sharp tip (small radius of rounding) is important because indentations made at depths less than the tip radius may not have a fully formed plastic zone, and thus the hardness measured from such indentations is not the same as that measured at depths where the indenter shape is actually pyramidal [54]. Berkovich indenters with tip radii <150 nm are readily available from modern manufacturers [55], but a similar radius would be much harder to achieve for a four-sided indenter.

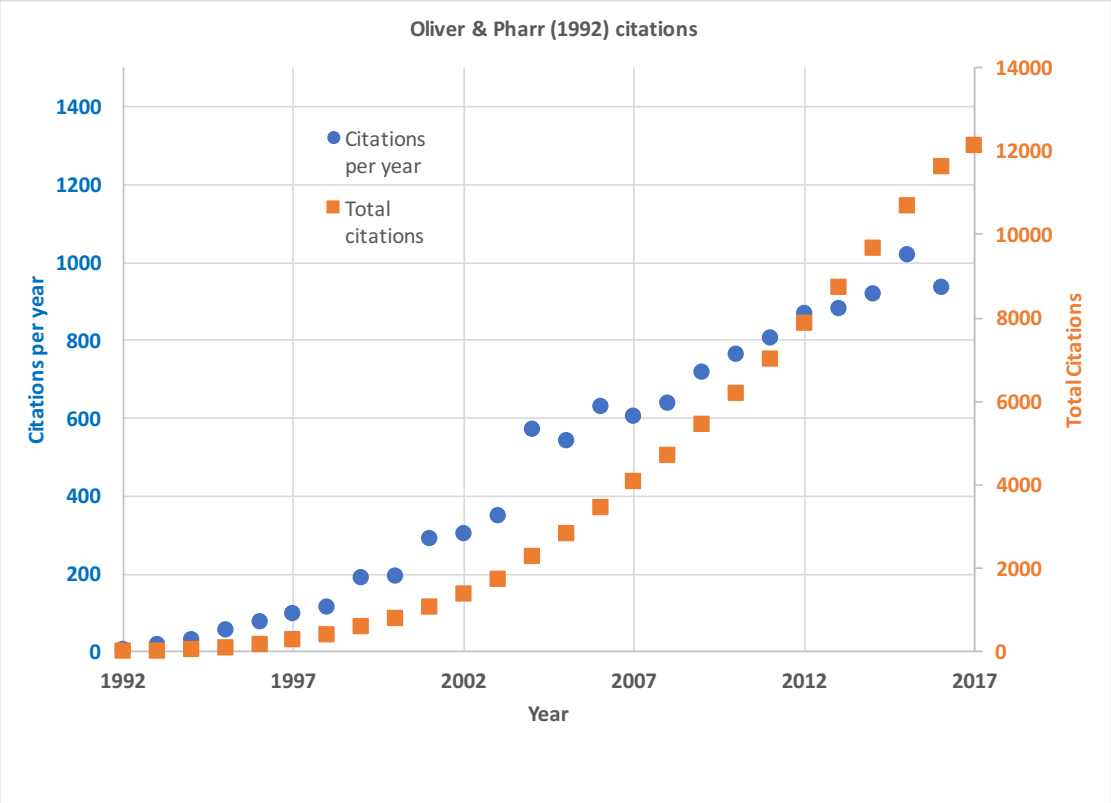


**Figure 2.5**: Plot of Oliver and Pharr citations since its publication in 1992.

The 25º slope of the Berkovich indenter faces results in the same contact area to depth ratio as a Vickers tip [54], that is:

$$A_c = 24.5h_c^2, \tag{2.3}$$

where $h_c$ is the "contact depth," defined as the depth at which the deformed sample surface is in contact with the sides of the indenter (*e.g.*, see Chapter 5).

Probably the next most commonly used indenter in nanoindentation is the cube-corner geometry (see Figure 2.4d). The cube-corner indenter is also a 3-sided pyramid, and so named because it has the same shape as the corner of a cube. The angle between the faces of this indenter and the sample surface during normal indentation is 55º. The higher angle of the cube-corner indenter makes it more likely to create fractures during indentation. Apparently, it also makes it even easier to manufacture to a sharp point, because cube-corner indenters with tip radii as small as 40 nm are readily available [55].

### 2.2.3. Effect of indentation size

A commonly observed phenomenon in indentation measurements is that the measured hardness of many materials decreases with increasing indentation load. This phenomenon is known as the indentation size effect (ISE) [56, 57]. Surprisingly, despite a number of studies reporting load-dependent hardness in calcite over relatively small loading ranges [6, 9, 16, 17, 25, 30, 38, 40, 41, 45, 51], the ISE on calcite has not been explicitly addressed in much detail. However, it has been explored in a number of other materials.

Soft metals tend to show a strong ISE that is especially prominent for small indentation sizes. For example, low-load indentations on Cu show a ~50% decrease in hardness over load ranges of ~0.5 to 5 mN [58] and ~5 to 50 mN [59], followed by a near constant hardness at higher loads. Ionic/covalent single crystals tend to show

smaller ISE's, but across a larger range of loadings. For example, another compound with similar hardness to calcite (tetragonal $KH_2PO_4$), shows a 20% decrease in hardness from 250 to 2,000 mN load [60]. Two softer materials, Sulphur [61] and $MgSO_4$ [62] (each about ¼ the hardness of calcite), show a ~20% decrease in hardness for loads up to some critical load (from 250 to 1,000 mN and 100 to 500 mN, respectively), and quickly reach a steady hardness at higher loads. Aragonite (an orthorhombic $CaCO_3$ polymorph, slightly harder than calcite) shows a ~50% drop in hardness across a large 200x increase in load from 1 to 200 mN [63, 64], and then a ~30% drop from 200 to 2000 mN [63]. And sapphire (which has a similar trigonal crystal structure to calcite, but is ~13x harder) shows a ~30% decrease in hardness over load ranges of 8 to 40 mN [65] and 100 to 2,000 mN [25]. However, contrary to those examples, not all ionic/covalent crystals are alike in their size effects. For example, apatite (another bio-relevant mineral, ~3x harder than calcite) shows only 20% decrease in hardness over each 200x increase in load (*i.e.*, from 1 to 200 mN [66] and 100 to 2000 mN [25]), and quartz (trigonal symmetry, like calcite, but ~8x harder) shows only a 15% decrease in hardness over 100 to 2000 mN load [25]. Also, certain materials have been shown to have nearly no ISE (e.g., fused quartz [59]), or apparently even reverse ISE (*i.e.*, increasing hardness with applied load [67]).

Reports of significant ISE in all of these other materials suggest that it may also be a feature in measurements on calcite. In Chapter 4**,** the effect of ISE in calcite is addressed in detail by comparing reported hardness data over a wide range of indenter loadings.

### 2.2.4. Effect of anisotropy

Attempts have been made to quantify the effects of both plastic [68] and elastic [69] anisotropy on indentation measurements through careful measurements across a

systematic range of crystal orientations. The model introduced by Brookes *et al* [68] focuses on plastic anisotropy, and for certain crystal structures (notably rocksalt, cubic, and some hexagonal structures) it can accurately predict the crystal orientations that have minimum hardness, but it is unable to predict the absolute magnitude of variation in hardness. For example, Brookes *et al* show that two materials with rock-salt structure (LiF and MgO) have minima in hardness at the same relative orientation, but that the difference from the maximum hardness in LiF is ~10%, versus ~100% for MgO. A different model by Vlassak and Nix [69] relates orientation-dependent variations in indentation modulus (measured by depth-sensing indentation) to the elastic anisotropy of the crystal. Their model is not designed to predict variations in hardness, however, Vlassak and Nix's own experimental data does confirm small (< 13%) variations in the hardness of a few cubic metals (W, Al, and Cu), and a larger (~25%) variation in the hardness of a less isotropic HCP metal (Zn).

To date, different degrees in the variation in measured hardness and/or indentation modulus with crystal orientation have been measured on a diverse set of single crystals, including metals and alloys [68-78], hard ceramics [68, 79-91], inorganic compounds [60, 62, 68, 92], semiconductors [93-96], organic compounds [97-99], and natural minerals [6, 9, 13, 26, 33, 61, 63, 64, 66, 68, 100-102]—including a few more recent studies on calcite [6, 9, 13], and on other bio-relevant minerals, namely, apatite (similar crystal structure to calcite, but $CaPO_4$) [66, 102], and aragonite (polymorph of $CaCO_3$ with orthorhombic structure) [63, 64]. Among these studies, most of the largest variations in hardness (20-100%) are associated with lower-symmetry crystal structures (*i.e.*, certain hexagonal [70, 73, 81, 85-87, 91], tetragonal [60, 88], orthorhombic [61, 63, 64, 92, 98], and monoclinic [97] crystals), though there are notable exceptions (*i.e.*, similarly large (20%+) variations in certain cubic crystals [71, 79, 80, 85, 93-95] or surprisingly small (< 20%) variations in some lower symmetry

crystals [66, 76, 77, 83, 102]). In some studies, differences in indentation modulus have also been measured, and have been shown to follow a trend with orientation that is either the same [66, 70, 71, 99, 102, 103], different [64, 73, 96, 98], or opposite [69, 87, 91] to the trend of hardness with orientation—though the reason has not been explained in any detail. Furthermore, the plastic anisotropy of a crystal has been linked to anisotropic surface morphology (*i.e.*, pile-up and/or fracture) surrounding an indentation (both experimentally [6, 9, 26, 58, 64, 66, 76, 77, 83, 84, 95, 98, 102] and/or by simulation [58, 76, 77, 104, 105]), which can provide insight into the nature of plastic slip during indentation.

Even after accounting for ISE, large variations in previously-reported hardness values for pure, defect-free control calcites are unexplained. In Chapter 4, I determine the effect of anisotropy on hardness (and modulus) measured on the important $(0001)$ and $\{10\bar{1}4\}$ planes.

### 2.2.5. Effect of elastic heterogeneities

Another factor affecting instrumented indentation measurements is the effect of elastic heterogeneities in the sample. The most commonly studied case of an elastically heterogeneous sample is that of a thin film on a dissimilar substrate (Figure 2.6a). The most basic way to avoid the effect of the substrate is to make small enough indentations. A basic empirical rule of thumb is to keep the depth of the indent less than 1/10 the film thickness [106], although this has been shown to not always be valid [107]. One of the earliest attempts to model the influence of a substrate was by Doerner & Nix [108], who developed an empirical modification of the definition of reduced modulus to account for the effects of the substrate, assuming a linear transition from film to substrate. Their solution, however, was not widely applicable, as it involved empirical parameters that were specific to their particular material

system. King [109] expanded upon Doerner and Nix's solution to remove the empirical parameter, and generalized it for various flat-ended indenters. In turn, Saha and Nix [107] modified King's solution to be applicable to the more common Berkovich indenter shape. Gao, et al. [110] developed a different type of model that used two weighted functions to describe a smooth transition from film to substrate. In turn, Rar *et al*. ("Song and Pharr") [111] built upon Gao's work to develop a simpler model that works well for compliant films on stiff substrates. From there, Hay and Crawford [112] developed a modification of the model by Rar *et al*. that could also work for stiff films on compliant substrates.

Another example of an elastic heterogeneity that affects nanoindentation measurements is that of indentation near a "vertical" elastic heterogeneity (*i.e*., a boundary that is normal to the surface plane of a sample, which separates two regions of different stiffness, Figure 2.6b). One extreme case of this situation is indentation near the free edge of a sample, where there is no solid material on one side of the vertical boundary. This situation has been studied theoretically, and is referred to as indentation in a "quarter-space" [113, 114]. The effect of dissimilar elastic flexing at this free edge scales with the distance between the center of the indent and the free edge, and for indents sufficiently far away from the free edge the effect on the measured compliance is independent of indentation depth, similar to the compliance associated with flexing of a cantilever beam. Building upon this fact, Jakes *et al*. have developed an experimental method to correct nanoindentation measurements near such elastic heterogeneities [115-117].

Yet another case of an elastic heterogeneity that affects nanoindentation measurements is that of a particle embedded in a dissimilar matrix (Figure 2.6c). Such a scenario exists naturally for many biogenic calcite crystals that exist embedded in an organic matrix as part of a polycrystalline composite structure (*e.g*., a mollusk shell),

and also for synthetic calcite crystals that must be embedded for support during a nanoindentation test. The effect of a dissimilar matrix on the nanoindentation measurement of a particle has been studied theoretically using finite element analysis (FEA) [118-123]. The effect on a measurement analyzed using the standard Oliver and Pharr method is that the measured modulus and hardness will be close to that of the particle at small indentation depths, and then approach that of the matrix at large indentation depths. Using FEA, multiple studies have determined a "particle-dominated" indentation size below which an uncorrected modulus and hardness is within about 10% of that for the particle only [118-123]. This particle-dominated depth is highly dependent on the ratio between the elastic properties of the particle and the matrix, and the size of the particle. Experimentally, a few studies have made measurements on embedded particles to different indentation depths [124, 125], and shown that for certain sized particles embedded in certain matrices, the uncorrected modulus and hardness is nearly independent of depth over some range of indentation depths. When this is true, the modulus and hardness of the particle is equal to that of the measurement at these small depths.

However, when testing small enough particles in dissimilar enough matrices, the uncorrected modulus and hardness may not approach that of the particle, even at the minimum reasonable indentation size (for example, I observe this for measurements on embedded synthetic calcite crystals in Chapter 5). In this case, it is necessary to correct the measurement for the effect of the matrix. Existing experimental techniques to correct such measurements are limited. Notably, existing methods for correcting measurements on thin films should not be expected to work for the case of a particle embedded in a dissimilar matrix, although they have been used for that purpose anyway [42].

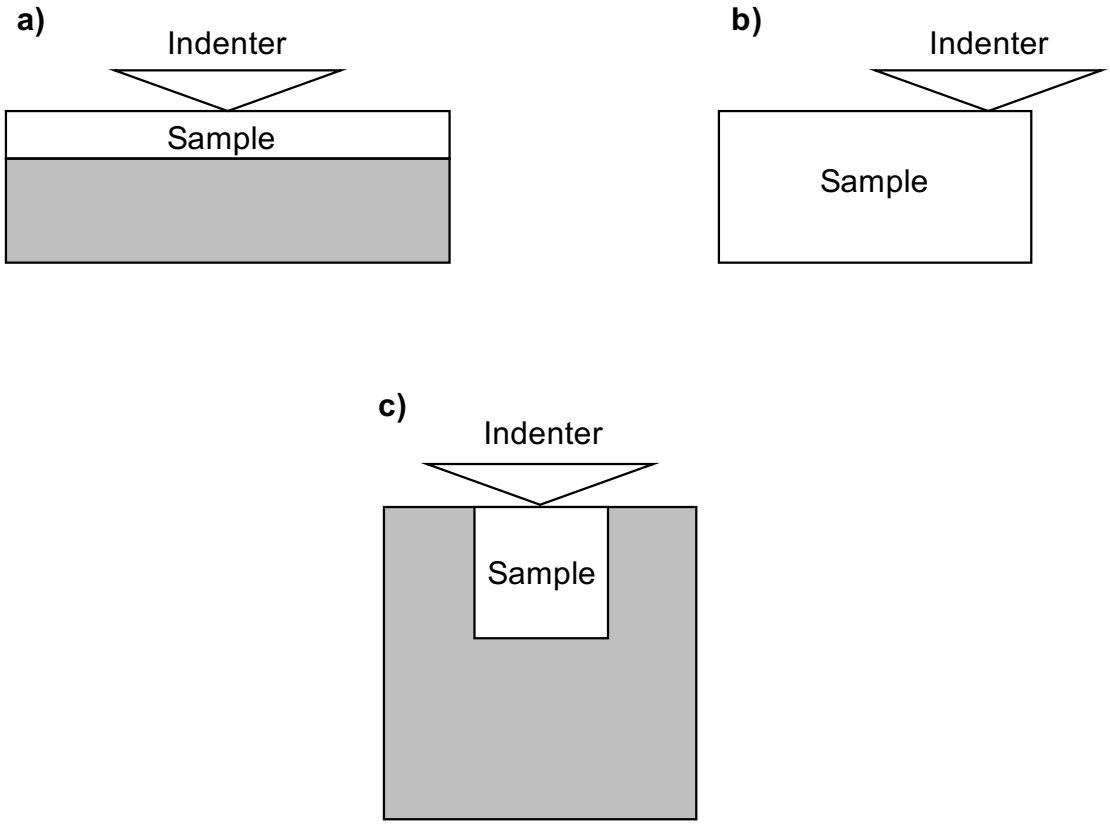


**Figure 2.6:** Schematics of different elastic heterogeneities. a) The commonly studied case of thin-film on substrate, b) indentation near a "vertical" elastic heterogeneity like a free edge, and c) a particle embedded in a dissimilar matrix. Existing methods for correcting measurements on a particle in a matrix are limited.

If there is some range of indentation size within a particle where the effect of the matrix on the measured compliance can be treated as some constant additional compliance, then the basic methodology used by Jakes *et al* [116] to correct for situations like a free edge might also apply for embedded particles. By simple extension of Saint Venant's principle (*i.e.*, that the difference between the effects of two different but statically equivalent loads becomes very small at sufficiently large distances from load), it seems likely that such an indentation size range may exist. However, practical application of the method by Jakes *et al* [116] on materials with unknown hardness requires that multiple indentations be made, and that their contact areas be imaged directly. For small (<100 $\mu$m) embedded particles, making multiple indentations within the particle may be difficult or impossible. Thus, a new method is required to enable accurate measurements to be made on small (< 100 $\mu$m) embedded calcite crystals. Such a method is presented in Chapter 5.

## 2.3. Strengthening mechanisms in calcite

Plastic deformation in crystalline materials occurs by dislocation motion. The yield strength (and thus hardness, see Equation 2.2) of a material increases when dislocation motion is impeded. For a polycrystalline material, the yield strength increases as the grain size decreases by the famous Hall-Petch relationship [126, 127]. This is because dislocations are impeded at grain boundaries. In the absence of grain boundaries, single crystals can also be strengthened by impurities, or other crystallographic defects.

Strengthening of single crystals by impurities generally falls into two categories [128]: (1) Direct blocking of dislocation motion by second-phase particles, or (2) impediment of dislocation motion by the local stress fields associated with misfitting atomic impurities (also known as solid-solution strengthening). Many biogenic calcite

crystals are known to contain both solutes [10, 13, 103, 129, 130] and second phase particles [13, 129, 131], and so both solid solution and second phase strengthening likely play a synergistic role in the increased hardness of biogenic calcite crystals. These strengthening mechanisms have also been explored using synthetic calcite [18, 40, 42-44, 132].

A common solute impurity observed in biogenic calcite crystals is Mg [10, 13, 103, 129, 130]. Synthetic calcite crystals have been grown with varying amounts of Mg substitutions, and the hardness of these crystals has been shown to increase in a manner consistent with solid solution strengthening [18, 19]. Biogenic calcite crystals obtained from the shell of the mollusk *Atrina rigida* contain about 8.4 at.% Mg, and the total increase in hardness (compared to a pure control calcite crystal) is ~60% [13]. The experiments on the synthetic crystals show that 16% increase in hardness is associated with the same (8.4 at.%) amount of Mg in calcite [18, 19]. Thus, the total strengthening in biogenic crystals from *Atrina rigida* cannot be solely due to solid solution strengthening.

Second-phase strengthening in calcite has also been explored synthetically [39, 40, 132]. Many biogenic crystals have been shown to contain large polymer inclusions [13, 129, 131], and are expected to also contain small molecule impurities, although the exact amount of these organic impurities is not well known. Large (> 100 nm) polymer inclusions [42-44] have increased the hardness of synthetic crystals by up to 22% [44], compared to a pure control crystal. In these experiments, the amount of polymer impurity was not precisely controlled, and it is difficult to quantify the strengthening mechanism without knowing how the hardness varies with impurity content. In another study, amino acid inclusions have been shown to increase the hardness (compared to a pure control) by up to 60% [132], approaching that of the biogenic crystals from *Atrina rigida*. In this case, the amount of amino acid inclusion

was varied from 0-7 mol%. By using a simple dislocation-bowing model, the strengthening was shown to correlate with the force required to for dislocations to cut the molecular impurities (details in Appendix Chapter).

High dislocation densities might also be expected to increase hardness. For example, dislocation tangles have been shown to increase the yield strength in plastically deformed metals, through a process often referred to as "strain hardening" [133]. This increase in yield strength has also been shown to translate to increased indentation hardness [134, 135]. Furthermore, high dislocation densities created in calcite crystals by uniaxial compression of (previously defect-free) crystals at elevated temperatures (550-800ºC) have been shown to increase the yield strength of those crystals [136]. However, it is unknown how the dislocation structure of calcite crystals might affect their indentation hardness.

## 2.4. Growth mechanisms of calcite

The driving force for crystallization of calcite from solution is the supersaturation of the solution with respect to $CaCO_3$. A solution is supersaturated with respect to some solid phase $x$, when the supersaturation ratio $S_x$ for that phase is greater than 1 [137]. For $CaCO_3$, the supersaturation ratio is defined as:

$$S_x = \frac{a_{Ca^{2+}} a_{CO^{2-}}}{K_{sp,x}}, \tag{2.4}$$

where $a_i$ is the ionic activity of the $i$th species, and $K_{sp,x}$ is the solubility product of the precipitating $CaCO_3$ phase at zero ionic strength. Supersaturation ($\sigma$) is the natural log of $S$. So, for $CaCO_3$ [138]:

$$\sigma_x = \ln\left(\frac{a_{Ca^{2+}} a_{CO^{2-}}}{K_{sp,x}}\right). \tag{2.5}$$

The product, $a_{Ca^{2+}} a_{CO^{2-}}$, is called the ionic activity product. Ionic activity is related to the concentration of the ions in solution, and thus increasing the concentration of

$Ca^{2+}$ and/or $CO_3^{2-}$ ions in the solution will increase the ionic activity product. Calcite is the least soluble phase of $CaCO_3$, with $K_{sp,calcite} = 3.3\times10^{-9}$, and amorphous calcium carbonate (ACC) is the most soluble phase with $K_{sp,ACC} = 4.0\times10^{-7}$ [2]. Thus ACC, is 121 times more soluble than calcite, and unlikely to survive in solution unless the ionic activity product is well above $K_{sp,ACC}$.

The first step of crystal growth is nucleation [137]. For $S_x > 1$, randomly-formed ionic clusters in solution will eventually reach some critical size, nucleate, and continue to grow. The critical energy for nucleation is related to the free energy of the interface (the surface of the cluster). Thus, "heterogeneous" nucleation (nucleation on an existing surface) has a lower energy barrier and tends to occur before "homogeneous" nucleation. For $S_{ACC} < 1$, the nucleation rate of calcite crystals has been shown to increase with supersaturation [139].

Following nucleation, for $S_{calcite} > 1$ ($\sigma_{calcite} > 0$) and $S_{ACC} < 1$ ($\sigma_{calcite} < 4.8$), calcite crystals tend to continue growth on the low-energy $\{10\bar{1}4\}$ faces by the "classical" mechanisms of spiral growth and/or 2-D nucleation [139]. *In-situ* AFM has shown both of these mechanisms for $\sigma_{calcite}$ in the range of 0.1-1.4 [138]. Spiral growth has the lowest energy barrier, and dominates growth at $\sigma_{calcite} < 0.8$. 2-D nucleation also played a significant role at greater $\sigma_{calcite}$.

In biology, calcite has been shown to grow via "non-classical" mechanisms that involve initial deposition of ACC which then subsequently transforms to calcite, usually either via solid state reconfiguration or via dissolution and reprecipitation [140-142]. Another non-classical growth mechanism (that may also play a role in the growth of some biogenic calcite crystals) is growth via attachment of ACC particles to a growing calcite crystal. For example, growth by ACC particle attachment has been observed by *in-situ* AFM when previously-formed ACC particles are introduced to a growth solution in contact with the $\{10\bar{1}4\}$ face of a pure seed crystal [143]. As

illustrated in Figure 2.7, current theories suggest that the non-classical growth of calcite via ACC particle attachment may occur in a manner that is analogous to classical growth via attachment of at kink sites, but with attachment of large (several nm) ACC particles that subsequently transform to calcite, instead of attachment of single ions only [142, 143]. In this way, $\{10\bar{1}4\}$ faceted calcite crystals can grow even from amorphous precursor particles.

A different non-classical growth mechanism observed in some other materials is growth via attachment of nanocrystalline particles. For example, this kind of growth has been observed for crystals of $TiO_2$ [144], PbSe [145], iron oxide [146], Pt [147], and Au [148]. In these materials, when two nano-crystalline particles attach with slight differences in the orientation of their lattices, dislocations are created at the attachment interface to accommodate the difference in orientation, thus resulting in crystals containing crystallographic defects (see Figure 2.8). It is unknown what effect ACC particle attachment growth may have on the defect structure of calcite crystals, but it seems possible that it may also involve the creation of dislocations.

One way of inducing the formation of ACC particles in solution supersaturated with respect to $CaCO_3$ would be introduce impurities known to stabilize ACC [149]. However, as described in Section 2.3, impurities alone are expected to increase the hardness of calcite, which would make determining the relative effect of a different growth mechanism difficult to separate from the impurity strengthening effect. Another way of inducing the formation of ACC particles would be to increase the supersaturation of a pure growth solution [150]. In Chapter 6, I explore the effect of increasing the initial concentration of $Ca^{2+}$ ions (and thus the initial supersaturation) in a growth solution without impurities on the hardness of $\{10\bar{1}4\}$ faceted calcite crystals grown from that solution. The initial supersaturations span a large range that is expected to transition from growth dominated by classical mechanisms, to growth

involving an ACC precursor. Thus, hardness measurements on these crystals provide insight into the effect of non-classical growth of calcite on its hardness.

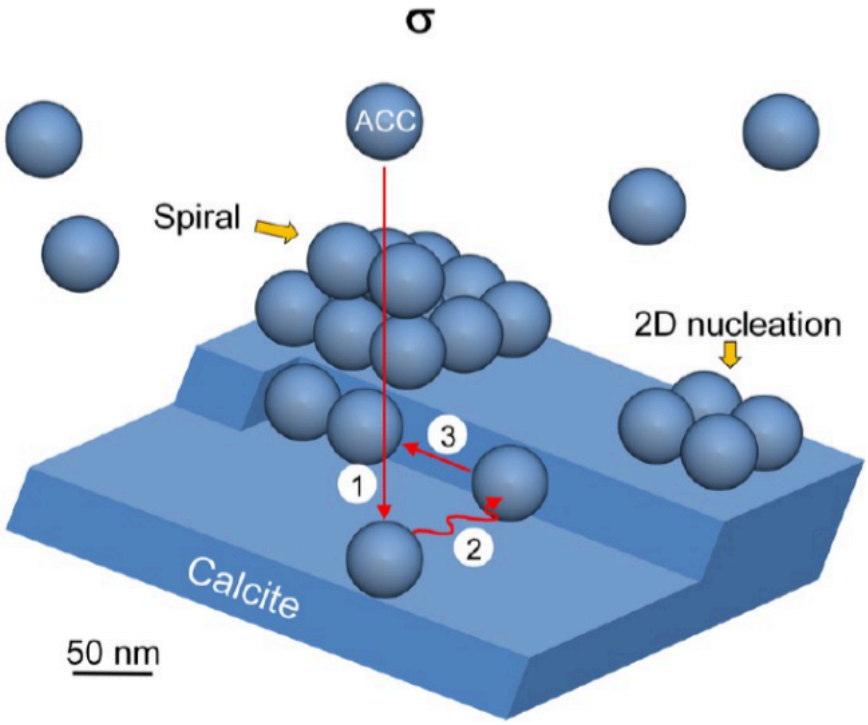


**Figure 2.7**: Schematic of calcite crystal growth via attachment of ACC particles at kink sites on a $\{10\bar{1}4\}$ face. Such ACC particles could be stabilized by impurities, or at high supersaturations.

*Reproduced with permission from: Rodriguez-Navarro, C., *et al*., Direct Nanoscale Imaging Reveals the Growth of Calcite Crystals via Amorphous Nanoparticles. Crystal Growth & Design, 2016. **16**(4): p. 1850-1860

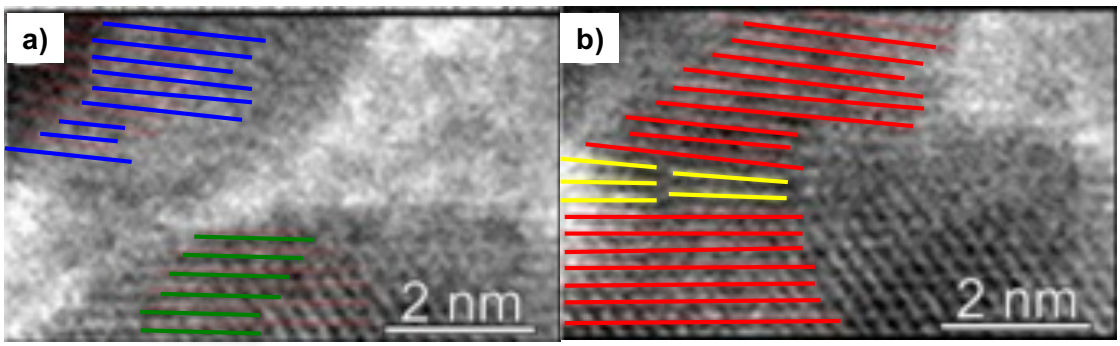


**Figure 2.8**: TEM images of attachment of two particles of iron oxide. a) Two spherical nanocrystal particles (with lattice planes highlighted in blue and green) approach each other. b) The particles attach and form a single crystal (lattice planes highlighted in red), with the difference in orientation of the two particles accommodated by the creation of an edge dislocation (highlighted in yellow). *Reproduced with permission from: Li, D.S., et al., *Direction-Specific Interactions Control Crystal Growth by Oriented Attachment*. Science, 2012. **336**(6084): p. 1014-1018.

## 2.5. REFERENCES


1. Suito, K., et al., *Phase relations of $CaCO_3$ at high pressure and high temperature*. American Mineralogist, 2001. **86**(9): p. 997-1002.

2. Brecevic, L. and A.E. Nielsen, *SOLUBILITY OF AMORPHOUS CALCIUM-CARBONATE*. Journal of Crystal Growth, 1989. **98**(3): p. 504-510.

3. Miers, H.A., *Mineralogy: an introduction to the scientific study of minerals*. 1902: Macmillan and Company, limited.

4. Li, H., et al., *Calcite Prisms from Mollusk Shells (Atrina Rigida): Swiss-cheese-like Organic-Inorganic Single-crystal Composites*. Advanced Functional Materials, 2011. **21**(11): p. 2028-2034.

5. Skinner, A.J., J.P. Lafemina, and H.J.F. Jansen, *STRUCTURE AND BONDING OF CALCITE - A THEORETICAL-STUDY*. American Mineralogist, 1994. **79**(3-4): p. 205-214.

6. Carter, G.M., J.L. Henshall, and R.J. Wakeman, *Knoop-hardness and fracture anisotropy of calcite*. Journal of Materials Science Letters, 1993. **12**(6): p. 407-410.

7. Gallagher, H.G., et al., *A COMPARATIVE-STUDY OF ANISOTROPY IN KNOOP-HARDNESS OF CALCITE AND SODIUM-NITRATE SINGLE-CRYSTALS*. Crystal Lattice Defects and Amorphous Materials, 1987. **16**(1-4): p. 137-143.

8. Joshi, D.R., *HARDNESS ANISOTROPY OF RHOMBOHEDRAL CRYSTALS OF CALCITE - VARIATION OF HARDNESS WITH ORIENTATION*. Crystal Research and Technology, 1993. **28**(1): p. 111-117.

9. Wong, T.Y. and R.C. Bradt, *Microhardness anisotropy of single-crystals of calcite, dolomite and magnesite on their cleavage planes*. Materials Chemistry and Physics, 1992. **30**(4): p. 261-266.

10. Griesshaber, E., et al., *Crystallographic texture and microstructure of terebratulide brachiopod shell calcite: An optimized materials design with hierarchical architecture*. American Mineralogist, 2007. **92**(5-6): p. 722-734.

11. Olson, I.C., et al., *Crystal lattice tilting in prismatic calcite*. Journal of Structural Biology, 2013. **183**(2): p. 180-190.

12. Perez-Huerta, A., M. Cusak, and W. Zhu, *Assessment of crystallographic influence on material properties of calcite brachiopods*. Mineralogical Magazine, 2008. **72**(2): p. 563-568.

13. Kunitake, M.E., et al., *Evaluation of strengthening mechanisms in calcite single crystals from mollusk shells*. Acta Biomaterialia, 2013. **9**(2): p. 5353-5359.

14. DeBresser, J.H.P. and C.J. Spiers, *Strength characteristics of the r, f, and c slip systems in calcite*. Tectonophysics, 1997. **272**(1): p. 1-23.

15. Goetz, A.J., et al., *Tailored order: The mesocrystalline nature of sea urchin teeth*. Acta Biomaterialia, 2014. **10**(9): p. 3885-3898.

16. Li, L. and C. Ortiz, *Pervasive nanoscale deformation twinning as a catalyst for efficient energy dissipation in a bioceramic armour*. Nature Materials, 2014. **13**(5): p. 501-507.

17. Schmahl, W.W., et al., *Hierarchical fibre composite structure and micromechanical properties of phosphatic and calcitic brachiopod shell biomaterials - an overview*. Mineralogical Magazine, 2008. **72**(2): p. 541-562.

18. Kunitake, M.E., S.P. Baker, and L.A. Estroff, *The effect of magnesium substitution on the hardness of synthetic and biogenic calcite*. MRS Communications, 2012. **2**(3): p. 113-116.

19. Kunitake, M.E., S.P. Baker, and L.A. Estroff, *The Effect of Magnesium Substitution on the Hardness of Synthetic and Biogenic Calcite (vol 2, pg 113, 2012)*. Mrs Communications, 2013. **3**(1): p. 79-79.

20. Chen, C.C., et al., *Elasticity of single-crystal calcite and rhodochrosite by Brillouin spectroscopy*. American Mineralogist, 2001. **86**(11-12): p. 1525-1529.

21. Zhao, J.H., et al., *Elasticity of Single-Crystal Calcite by First-Principles Calculations*. Journal of Computational and Theoretical Nanoscience, 2009. **6**(5): p. 1181-1188.

22. Nye, J.F., *Physical properties of crystals: their representation by tensors and matrices*. 1985, Oxford university press.

23. Turley, J. and G. Sines, *The anisotropy of Young's modulus, shear modulus and Poisson's ratio in cubic materials*. Journal of Physics D: Applied Physics, 1971. **4**(2): p. 264.

24. Aouni, N. and L. Wheeler, *Auxeticity of Calcite and Aragonite polymorphs of CaCO3 and crystals of similar structure*. Physica Status Solidi B-Basic Solid State Physics, 2008. **245**(11): p. 2454-2462.

25. Broz, M.E., R.F. Cook, and D.L. Whitney, *Microhardness, toughness, and modulus of Mohs scale minerals*. American Mineralogist, 2006. **91**(1): p. 135-142.

26. Taylor, E.W., *Correlation of the Mohs's scale of hardness with the Vickers's hardness numbers*. Mineralogical Magazine, 1949. **28**: p. 718-721.

27. Barber, D.J. and H.R. Wenk, *Deformation twinning in calcite, dolomite, and other rhombohedral carbonates*. Physics and Chemistry of Minerals, 1979. **5**(2): p. 141-165.

28. Carter, G.M., J.L. Henshall, and R.J. Wakeman, *Influence of surfactants on the mechanical-properties and comminution of wet-milled calcite*. Powder Technology, 1991. **65**(1-3): p. 403-410.

29. Wakeman, R.J., J.L. Henshall, and G.M. Carter, *Solution environment effects on the hardness and toughness of calcite during grinding*. Chemical Engineering Research & Design, 1993. **71**(A4): p. 361-370.

30. Beste, U. and S. Jacobson, *Micro scale hardness distribution of rock types related to rock drill wear*. Wear, 2003. **254**(11): p. 1147-1154.

31. Metzler, R.A., et al., *Composition and Structure of Oyster Adhesive Reveals Heterogeneous Materials Properties in a Biological Composite*. Advanced Functional Materials, 2016. **26**(37): p. 6814-6821.

32. Pandya, J.R. and L.J. Bhagia, *Comparison of knoop and vickers hardness numbers on calcite cleavages*. Indian Journal of Pure & Applied Physics, 1984. **22**(7): p. 439-440.

33. Winchell, H., *The knoop microhardness tester as a mineralogical tool*. American Mineralogist, 1945. **30**(9-10): p. 583-595.

34. Smith, R.L. and G.E. Sandly, *An Accurate Method of Determining the Hardness of Metals, with Particular Reference to Those of a High Degree of Hardness*. Proceedings of the Institution of Mechanical Engineers, 1922. **102**(1): p. 623-641.

35. Tabor, D., *A SIMPLE THEORY OF STATIC AND DYNAMIC HARDNESS*. Proceedings of the Royal Society of London Series a-Mathematical and Physical Sciences, 1948. **192**(1029): p. 247-274.

36. Cheng, Y.T. and C.M. Cheng, *Scaling approach to conical indentation in elastic-plastic solids with work hardening*. Journal of Applied Physics, 1998. **84**(3): p. 1284-1291.

37. Oliver, W.C. and G.M. Pharr, *AN IMPROVED TECHNIQUE FOR DETERMINING HARDNESS AND ELASTIC-MODULUS USING LOAD AND DISPLACEMENT SENSING INDENTATION EXPERIMENTS*. Journal of Materials Research, 1992. **7**(6): p. 1564-1583.

38. Bandini, A., et al., *Effects of intra-crystalline microcracks on the mechanical behavior of a marble under indentation*. International Journal of Rock Mechanics and Mining Sciences, 2012. **54**: p. 47-55.

39. Calvaresi, M., et al., *Morphological and mechanical characterization of composite calcite/SWCNT-COOH single crystals*. Nanoscale, 2013. **5**(15): p. 6944-6949.

40. Giosia, M.D., et al., *Bioinspired Nanocomposites: Ordered 2D Materials Within a 3D Lattice*. Advanced Functional Materials, 2016.

41. Hangen, U.D., *A comparision of nano-hardness and scratch-resistance on Mohs minerals*. Zeitschrift Fur Metallkunde, 2001. **92**(9): p. 1074-1077.

42. Kim, Y.Y., et al., *An artificial biomineral formed by incorporation of copolymer micelles in calcite crystals*. Nature Materials, 2011. **10**(11): p. 890-896.

43. Kim, Y.Y., et al., *Bio-Inspired Synthesis and Mechanical Properties of Calcite-Polymer Particle Composites*. Advanced Materials, 2010. **22**(18): p. 2082-+.

44. Kim, Y.Y., et al., *Structure and Properties of Nanocomposites Formed by the Occlusion of Block Copolymer Worms and Vesicles Within Calcite Crystals*. Advanced Functional Materials, 2016. **26**(9): p. 1382-1392.

45. Lv, J.L., Y.G. Jiang, and D.Y. Zhang, *Structural and Mechanical Characterization of Atrina Pectinata and Freshwater Mussel Shells*. Journal of Bionic Engineering, 2015. **12**(2): p. 276-284.

46. Ma, Y., et al., *Sea urchin tooth design: An "All-Calcite" polycrystalline reinforced fiber composite for grinding rocks*. Advanced Materials, 2008. **20**(8): p. 1555-+.

47. Merkel, C., et al., *Mechanical properties of modern calcite- (Mergerlia truncata) and phosphate-shelled brachiopods (Discradisca stella and Lingula anatina) determined by nanoindentation*. Journal of Structural Biology, 2009. **168**(3): p. 396-408.

48. Muller, W.E.G., et al., *The sponge silicatein-interacting protein silintaphin-2 blocks calcite formation of calcareous sponge spicules at the vaterite stage*. RSC Advances, 2014. **4**(6): p. 2577-2585.

49. Presser, V., et al., *Determination of the elastic modulus of highly porous samples by nanoindentation: a case study on sea urchin spines*. Journal of Materials Science, 2010. **45**(9): p. 2408-2418.

50. Raman, S. and R. Kumar, *Construction and nanomechanical properties of the exoskeleton of the barnacle, Amphibalanus reticulatus*. Journal of Structural Biology, 2011. **176**(3): p. 360-369.

51. Zugner, S., K. Marquardt, and I. Zimmermann, *Influence of nanomechanical crystal properties on the comminution process of particulate solids in spiral jet mills*. European Journal of Pharmaceutics and Biopharmaceutics, 2006. **62**(2): p. 194-201.

52. Bulychev, S.I., et al., *Determining Young's Modulus from the Indenter Penetration Diagram*. Zavod. Lab, 1975. **41**(9): p. 1137-1140.

53. Harding, J.W. and I.N. Sneddon, *THE ELASTIC STRESSES PRODUCED BY THE INDENTATION OF THE PLANE SURFACE OF A SEMI-INFINITE ELASTIC SOLID BY A RIGID PUNCH*. Proceedings of the Cambridge Philosophical Society, 1945. **41**(1): p. 16-26.

54. Fischer-Cripps, A.C., *Nanoindentation*. 2002: Springer.

55. Hysitron, I. *Probe Selection Guide*. 2017]; Available from: https://www.hysitron.com/media/1556/probou-r1f.pdf.

56. Sangwal, K., *Review: Indentation size effect, indentation cracks and microhardness measurement of brittle crystalline solids - some basic concepts and trends*. Crystal Research and Technology, 2009. **44**(10): p. 1019-1037.

57. Bull, S.J., *On the origins and mechanisms of the indentation size effect*. Zeitschrift Fur Metallkunde, 2003. **94**(7): p. 787-792.

58. Wang, Y., et al., *Orientation dependence of nanoindentation pile-up patterns and of nanoindentation microtextures in copper single crystals*. Acta Materialia, 2004. **52**(8): p. 2229-2238.

59. Nix, W.D. and H.J. Gao, *Indentation size effects in crystalline materials: A law for strain gradient plasticity*. Journal of the Mechanics and Physics of Solids, 1998. **46**(3): p. 411-425.

60. Fang, T. and J.C. Lambropoulos, *Microhardness and indentation fracture of potassium dihydrogen phosphate (KDP)*. Journal of the American Ceramic Society, 2002. **85**(1): p. 174-178.

61. Li, H., Y.H. Han, and R.C. Bradt, *Knoop microhardness of single-crystal sulfur*. Journal of Materials Science, 1994. **29**(21): p. 5641-5645.

62. Karan, S. and S.P. Sen Gupta, *Vickers microhardness studies on solution-grown single crystals of magnesium sulphate hepta-hydrate*. Materials Science and Engineering a-Structural Materials Properties Microstructure and Processing, 2005. **398**(1-2): p. 198-203.

63. Han, Y.H., et al., *Knoop microhardness anisotropy of single-crystal aragonite*. Journal of the American Ceramic Society, 1991. **74**(12): p. 3129-3132.

64. Kearney, C., et al., *Nanoscale anisotropic plastic deformation in single crystal aragonite*. Physical Review Letters, 2006. **96**(25).

65. Page, T.F., W.C. Oliver, and C.J. McHargue, *THE DEFORMATION-BEHAVIOR OF CERAMIC CRYSTALS SUBJECTED TO VERY LOW LOAD (NANO)INDENTATIONS*. Journal of Materials Research, 1992. **7**(2): p. 450-473.

66. Saber-Samandari, S. and K.A. Gross, *Micromechanical properties of single crystal hydroxyapatite by nanoindentation*. Acta Biomaterialia, 2009. **5**(6): p. 2206-2212.

67. Sangwal, K., *On the reverse indentation size effect and microhardness measurement of solids*. Materials Chemistry and Physics, 2000. **63**(2): p. 145-152.

68. Brookes, C.A., J.B. Oneill, and B.A.W. Redfern, *Anisotropy in hardness of single crystals*. Proceedings of the Royal Society of London Series a-Mathematical and Physical Sciences, 1971. **322**(1548): p. 73-&.

69. Vlassak, J.J. and W.D. Nix, *Measuring the elastic properties of anisotropic materials by means of indentation experiments*. Journal of the Mechanics and Physics of Solids, 1994. **42**(8): p. 1223-1245.

70. Britton, T.B., et al., *The effect of crystal orientation on the indentation response of commercially pure titanium: experiments and simulations*. Proceedings of the Royal Society a-Mathematical Physical and Engineering Sciences, 2010. **466**(2115): p. 695-719.

71. Kiely, J.D. and J.E. Houston, *Nanomechanical properties of Au (111), (001), and (110) surfaces*. Physical Review B, 1998. **57**(19): p. 12588-12594.

72. Li, T.L., et al., *Indentation Schmid factor and orientation dependence of nanoindentation pop-in behavior of NiAl single crystals*. Journal of the Mechanics and Physics of Solids, 2011. **59**(6): p. 1147-1162.

73. Mante, F., G.R. Baran, and B. Lucas, *Nanoindentation studies of titanium single crystals*. Biomaterials, 1999. **20**(11): p. 1051-1055.

74. Sahin, O., et al., *Vickers microindentation hardness studies of beta-Sn single crystals*. Materials Characterization, 2007. **58**(2): p. 197-204.

75. Wang, W. and K. Lu, *Nanoindentation study on elastic and plastic anisotropies of Cu single crystals*. Philosophical Magazine, 2006. **86**(33-35): p. 5309-5320.

76. Zambaldi, C. and D. Raabe, *Plastic anisotropy of gamma-TiAl revealed by axisymmetric indentation*. Acta Materialia, 2010. **58**(9): p. 3516-3530.

77. Zambaldi, C., C. Zehnder, and D. Raabe, *Orientation dependent deformation by slip and twinning in magnesium during single crystal indentation*. Acta Materialia, 2015. **91**: p. 267-288.

78. Kang, S., et al., *Orientation-dependent indentation modulus and yielding in a high Mn twinning-induced plasticity steel*. Materials Science and Engineering a-Structural Materials Properties Microstructure and Processing, 2012. **532**: p. 500-504.

79. Rowcliffe, D.J. and G.E. Hollox, *Hardness anisotropy, deformation mechanisms and brittle-to-ductile transition in carbides*. Journal of Materials Science, 1971. **6**(10): p. 1270-+.

80. Hannink, R.H.J., D.L. Kohlstedt, and M.J. Murray, *SLIP SYSTEM DETERMINATION IN CUBIC CARBIDES BY HARDNESS ANISOTROPY*. Proceedings of the Royal Society of London Series a-Mathematical and Physical Sciences, 1972. **326**(1566): p. 409-+.

81. Sawyer, G.R., P.M. Sargent, and T.F. Page, *MICROHARDNESS ANISOTROPY OF SILICON-CARBIDE*. Journal of Materials Science, 1980. **15**(4): p. 1001-1013.

82. Li, H. and R.C. Bradt, *KNOOP MICROHARDNESS ANISOTROPY OF SINGLE-CRYSTAL LAB6*. Materials Science and Engineering a-Structural Materials Properties Microstructure and Processing, 1991. **142**(1): p. 51-61.

83. Raynes, A.S., et al., *Fracture-toughness of YBa2Cu3O6+delta single-crystals - Anisotropy and twinning effects*. Journal of Applied Physics, 1991. **70**(10): p. 5254-5257.

84. Jain, A., et al., *LOAD AND DIRECTIONAL EFFECTS ON MICROHARDNESS AND ESTIMATION OF TOUGHNESS AND BRITTLENESS FOR FLUX-GROWN LABO3 CRYSTALS*. Journal of Materials Science, 1994. **29**(14): p. 3847-3856.

85. Maerky, C., et al., *Indentation hardness and fracture toughness in single crystal TiC0.96*. Materials Science and Engineering a-Structural Materials Properties Microstructure and Processing, 1996. **209**(1-2): p. 329-336.

86. Nowak, R., T. Sekino, and K. Niihara, *Surface deformation of sapphire crystal*. Philosophical Magazine a-Physics of Condensed Matter Structure Defects and Mechanical Properties, 1996. **74**(1): p. 171-194.

87. Hay, J.C., et al., *Elastic anisotropy of beta-silicon nitride whiskers*. Journal of the American Ceramic Society, 1998. **81**(10): p. 2661-2669.

88. Chu, F., et al., *Mo5Si3 single crystals: physical properties and mechanical behavior*. Materials Science and Engineering a-Structural Materials Properties Microstructure and Processing, 1999. **261**(1-2): p. 44-52.

89. Gupta, V., et al., *Mechanical characteristics of flux-grown calcium titanate and nickel titanate crystals*. Materials Chemistry and Physics, 2005. **89**(1): p. 64-71.

90. Simunek, A., *Anisotropy of hardness from first principles: The cases of ReB2 and OsB2*. Physical Review B, 2009. **80**(6).

91. Csanadi, T., et al., *Nanoindentation induced deformation anisotropy in beta-Si3N4 ceramic crystals*. Journal of the European Ceramic Society, 2016. **36**(12): p. 3059-3066.

92. Gupte, S.S. and C.F. Desai, *Vickers hardness anisotropy and slip system in zinc (tris) thiourea sulphate crystals*. Crystal Research and Technology, 1999. **34**(10): p. 1329-1332.

93. Watts, D.Y. and A.F.W. Willoughby, *HARDNESS ANISOTROPY OF III-V-SEMICONDUCTING COMPOUNDS AND ALLOYS*. Journal of Applied Physics, 1984. **56**(6): p. 1869-1871.

94. Roberts, S.G., P.D. Warren, and P.B. Hirsch, *Knoop hardness anisotropy on {001} faces of germanium and gallium arsenide*. Journal of Materials Research, 1986. **1**(1): p. 162-176.

95. Ebrahimi, F. and L. Kalwani, *Fracture anisotropy in silicon single crystal*. Materials Science and Engineering a-Structural Materials Properties Microstructure and Processing, 1999. **268**(1-2): p. 116-126.

96. Mosca, D.H., et al., *Mechanical properties of layered InSe and GaSe single crystals*. Journal of Applied Physics, 2002. **91**(1): p. 140-144.

97. Duncanhewitt, W.C., D.L. Mount, and A. Yu, *Hardness anisotropy of acetaminophen crystals*. Pharmaceutical Research, 1994. **11**(5): p. 616-623.

98. Ramos, K.J., D.E. Hooks, and D.F. Bahr, *Direct observation of plasticity and quantitative hardness measurements in single crystal cyclotrimethylene trinitramine by nanoindentation*. Philosophical Magazine, 2009. **89**(27): p. 2381-2402.

99. Kiran, M., et al., *Mechanical Anisotropy in Crystalline Saccharin: Nanoindentation Studies*. Crystal Growth & Design, 2010. **10**(10): p. 4650-4655.

100. Knoop, F., C.G. Peters, and W.B. Emerson, *A sensitive pyramidal-diamond tool for indentation measurements*. Journal of Research of the National Bureau of Standards, 1939. **23**: p. 39-61.

101. Westbrook, J.H. and Jorgense.Pj, *Solution environment effects on the hardness and toughness of calcite during grinding*. American Mineralogist, 1968. **53**(11-1): p. 1899-+.

102. Viswanath, B., et al., *Mechanical properties and anisotropy in hydroxyapatite single crystals*. Scripta Materialia, 2007. **57**(4): p. 361-364.

103. Wang, R.Z., L. Addadi, and S. Weiner, *Design strategies of sea urchin teeth: Structure, composition and micromechanical relations to function*. Philosophical Transactions of the Royal Society of London Series B-Biological Sciences, 1997. **352**(1352): p. 469-480.

104. Chen, H.P., et al., *Multimillion-atom nanoindentation simulation of crystalline silicon carbide: Orientation dependence and anisotropic pileup*. Journal of Applied Physics, 2007. **102**(6).

105. Liu, Y., et al., *Orientation effects in nanoindentation of single crystal copper*. International Journal of Plasticity, 2008. **24**(11): p. 1990-2015.

106. Buckle, H., *Spezifische Anwendungen der Harteprufung nach Vickers mit kleinen Drufkaften*. VDI-Berichte, 1961. **41**: p. 14.

107. Saha, R. and W.D. Nix, *Effects of the substrate on the determination of thin film mechanical properties by nanoindentation*. Acta Materialia, 2002. **50**(1): p. 23-38.

108. Doerner, M.F. and W.D. Nix, *A method for interpreting the data from depth-sensing indentation instruments*. Journal of Materials Research, 1986. **1**(4): p. 601-609.

109. King, R.B., *ELASTIC ANALYSIS OF SOME PUNCH PROBLEMS FOR A LAYERED MEDIUM*. International Journal of Solids and Structures, 1987. **23**(12): p. 1657-1664.

110. Gao, H.J., C.H. Chiu, and J. Lee, *ELASTIC CONTACT VERSUS INDENTATION MODELING OF MULTILAYERED MATERIALS*. International Journal of Solids and Structures, 1992. **29**(20): p. 2471-2492.

111. Rar, A., H. Song, and G.M. Pharr, *Assessment of new relation for the elastic compliance of a film-substrate system*, in *Thin Films: Stresses and Mechanical Properties Ix*, C.S. Ozkan, et al., Editors. 2002, Materials Research Society: Warrendale. p. 431-436.

112. Hay, J. and B. Crawford, *Measuring substrate-independent modulus of thin films*. Journal of Materials Research, 2011. **26**(6): p. 727-738.

113. Gerber, C.E., *Contact Problems For The Elastic Quarter-plane And For The Quarter-space*. Thesis, 1968.

114. Hetényi, M., *A Method of Solution for the Elastic Quarter-Plane*. Journal of Applied Mechanics, 1960. **27**(2): p. 289-296.

115. Jakes, J.E., et al., *Nanoindentation near the edge*. Journal of Materials Research, 2009. **24**(3): p. 1016-1031.

116. Jakes, J.E., et al., *Experimental method to account for structural compliance in nanoindentation measurements*. Journal of Materials Research, 2008. **23**(4): p. 1113-1127.

117. Jakes, J.E. and D.S. Stone, *The edge effect in nanoindentation*. Philosophical Magazine, 2011. **91**(7-9): p. 1387-1399.

118. Cao, Y.Y., P.F. Duan, and J.J. Chen, *Modelling the nanomechanical response of a micro particle-matrix system for nanoindentation tests*. Nanotechnology, 2016. **27**(19): p. 10.

119. Durst, K., M. Goken, and H. Vehoff, *Finite element study for nanoindentation measurements on two-phase materials*. Journal of Materials Research, 2004. **19**(1): p. 85-93.

120. Leggoe, J.W., *Determination of the elastic modulus of microscale ceramic particles via nanoindentation*. Journal of Materials Research, 2004. **19**(8): p. 2437-2447.

121. Low, T.F., C.L. Pun, and W.Y. Yan, *Theoretical study on nanoindentation hardness measurement of a particle embedded in a matrix*. Philosophical Magazine, 2015. **95**(14): p. 1573-1586.

122. Yan, W.Y., C.L. Pun, and G.P. Simon, *Conditions of applying Oliver-Pharr method to the nanoindentation of particles in composites*. Composites Science and Technology, 2012. **72**(10): p. 1147-1152.

123. Yan, W.Y., et al., *Some issues on nanoindentation method to measure the elastic modulus of particles in composites*. Composites Part B-Engineering, 2011. **42**(8): p. 2093-2097.

124. Leisen, D., et al., *A novel and simple approach for characterizing the Young's modulus of single particles in a soft matrix by nanoindentation*. Journal of Materials Research, 2012. **27**(24): p. 3073-3082.

125. Maughan, M.R., M.T. Carvajal, and D.F. Bahr, *Nanomechanical testing technique for millimeter-sized and smaller molecular crystals*. International Journal of Pharmaceutics, 2015. **486**(1-2): p. 324-330.

126. Hall, E.O., *THE DEFORMATION AND AGEING OF MILD STEEL .3. DISCUSSION OF RESULTS*. Proceedings of the Physical Society of London Section B, 1951. **64**(381): p. 747-753.

127. Petch, N.J., *THE CLEAVAGE STRENGTH OF POLYCRYSTALS*. Journal of the Iron and Steel Institute, 1953. **174**(1): p. 25-28.

128. Courtney, T.H., *Mechanical behavior of materials*. 2005: Waveland Press.

129. Perez-Huerta, A., et al., *Material properties of brachiopod shell ultrastructure by nanoindentation*. Journal of the Royal Society Interface, 2007. **4**(12): p. 33-39.

130. Moureaux, C., et al., *Structure, composition and mechanical relations to function in sea urchin spine*. Journal of Structural Biology, 2010. **170**(1): p. 41-49.

131. Li, H.Y., et al., *Calcite Prisms from Mollusk Shells (Atrina Rigida): Swiss-cheese-like Organic-Inorganic Single-crystal Composites*. Advanced Functional Materials, 2011. **21**(11): p. 2028-2034.

132. Kim, Y.-Y., et al., *Tuning hardness in calcite by incorporation of amino acids*. Nature materials, 2016.

133. Mecking, H. and U.F. Kocks, *KINETICS OF FLOW AND STRAIN-HARDENING*. Acta Metallurgica, 1981. **29**(11): p. 1865-1875.

134. Eriksson, C.L., P.L. Larsson, and D.J. Rowcliffe, *Strain-hardening and residual stress effects in plastic zones around indentations*. Materials Science and Engineering a-Structural Materials Properties Microstructure and Processing, 2003. **340**(1-2): p. 193-203.

135. Poole, W.J., M.F. Ashby, and N.A. Fleck, *Micro-hardness of annealed and work-hardened copper polycrystals*. Scripta Materialia, 1996. **34**(4): p. 559-564.

136. De Bresser, J.H.P., *Steady state dislocation densities in experimentally deformed calcite materials: Single crystals versus polycrystals*. Journal of Geophysical Research: Solid Earth, 1996. **101**(B10): p. 22189-22201.

137. Sunagawa, I., *Crystals: Growth, Morphology, & Perfection*. 2005: Cambridge University Press.

138. Teng, H.H., P.M. Dove, and J.J. De Yoreo, *Kinetics of calcite growth: Surface processes and relationships to macroscopic rate laws*. Geochimica Et Cosmochimica Acta, 2000. **64**(13): p. 2255-2266.

139. Verdoes, D., D. Kashchiev, and G.M. Vanrosmalen, *DETERMINATION OF NUCLEATION AND GROWTH-RATES FROM INDUCTION TIMES IN SEEDED AND UNSEEDED PRECIPITATION OF CALCIUM-CARBONATE*. Journal of Crystal Growth, 1992. **118**(3-4): p. 401-413.

140. Addadi, L., S. Raz, and S. Weiner, *Taking Advantage of Disorder: Amorphous Calcium Carbonate and Its Roles in Biomineralization*. Advanced Materials, 2003. **15**(12): p. 959-970.

141. De Yoreo, J.J., et al., *CRYSTAL GROWTH. Crystallization by particle attachment in synthetic, biogenic, and geologic environments*. Science, 2015. **349**(6247): p. aaa6760.

142. Gal, A., et al., *Particle Accretion Mechanism Underlies Biological Crystal Growth from an Amorphous Precursor Phase*. Advanced Functional Materials, 2014. **24**(34): p. 5420-5426.

143. Rodriguez-Navarro, C., et al., *Direct Nanoscale Imaging Reveals the Growth of Calcite Crystals via Amorphous Nanoparticles*. Crystal Growth & Design, 2016. **16**(4): p. 1850-1860.

144. Penn, R.L. and J.F. Banfield, *Imperfect oriented attachment: Dislocation generation in defect-free nanocrystals*. Science, 1998. **281**(5379): p. 969-971.

145. van Huis, M.A., et al., *Low-Temperature Nanocrystal Unification through Rotations and Relaxations Probed by in Situ Transmission Electron Microscopy*. Nano Letters, 2008. **8**(11): p. 3959-3963.

146. Li, D.S., et al., *Direction-Specific Interactions Control Crystal Growth by Oriented Attachment*. Science, 2012. **336**(6084): p. 1014-1018.

147. Ruan, L.Y., et al., *A Rational Biomimetic Approach to Structure Defect Generation in Colloidal Nanocrystals*. Acs Nano, 2014. **8**(7): p. 6934-6944.

148. Lange, A.P., et al., *Dislocation mediated alignment during metal nanoparticle coalescence*. Acta Materialia, 2016. **120**: p. 364-378.

149. Wang, T., M. Antonietti, and H. Colfen, *Calcite mesocrystals: "morphing" crystals by a polyelectrolyte*. Chemistry, 2006. **12**(22): p. 5722-30.

150. Faatz, M., F. Gröhn, and G. Wegner, *Amorphous Calcium Carbonate: Synthesis and Potential Intermediate in Biomineralization*. Advanced Materials, 2004. **16**(12): p. 996-1000.

# CHAPTER 3: METHODS

## 3.1. Nanoindentation

Nanoindentation was used extensively in this work. Most of the nanoindentation was performed at Cornell, using a commercially available nanoindenter (Hysitron Ti-900) equipped with a Berkovich indenter tip (with estimated radius of ~120 nm) and used in both quasi-static and dynamic (nano-DMA) modes. In either mode, load–displacement data are obtained by applying some specified load, and then measuring the resulting displacement of the indenter ("load-controlled"). The maximum possible load of this machine is 10 mN, and the measurements reported in this work were made to maximum loads between 2.5 and 10 mN.

For a quasi-static indentation, the applied load is gradually increased to some specified maximum load at some specified loading rate, then held at that maximum load for some specified hold time, and finally unloaded to zero load at some specified unloading rate. Schematic quasi-static load-displacement data is shown in Figure 3.1a. From these data, the contact stiffness ($S$) at the maximum load of the indentation can be calculated from the slope of a fit to some portion of the unloading data. In general, a dynamic indentation involves the application of some small oscillatory load to the mean load of the indenter during loading (schematic data is shown in Figure 3.1b). From these data, contact stiffness can be calculated across a range of indenter loads and displacements, over the course of a single indentation experiment.

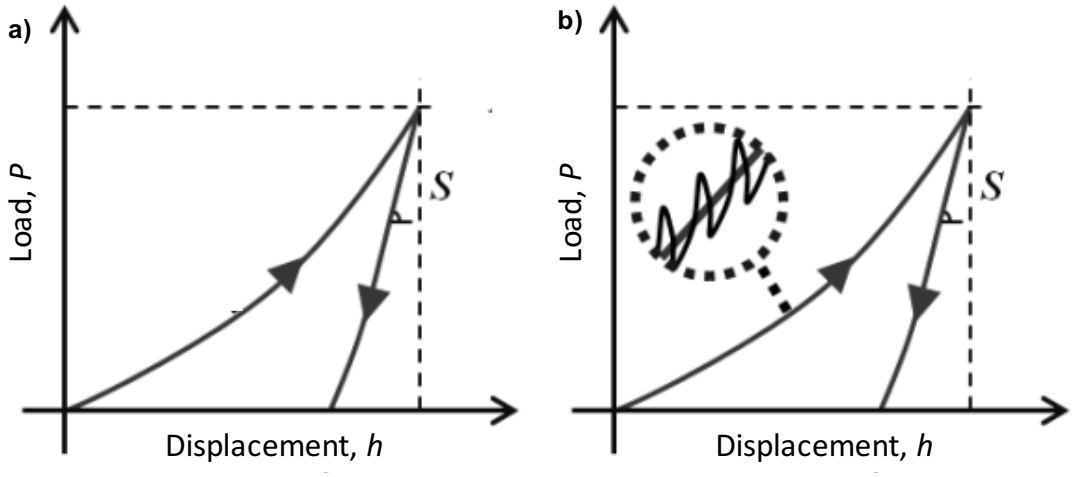


**Figure 3.1:** Schematic load-displacement data for a) a quasi-static indentation with a single loading and unloading at maximum load, and b) a dynamic indentation with oscillatory loads and displacements on loading. For the dynamic indentation, oscillatory data is shown as a zoomed in inset to highlight the small magnitude compared to the mean load-displacement data. Note that, in this work, the dynamic indentations (nanoDMA) actually increased mean load in steps, not continuously.

In this work, quasi static indentations were made with 5 sec loading, holding, and unloading periods, resulting in loading rates between 0.5 and 2 mN/s. Dynamic indentations were made by increasing the mean load of the indenter in 20 equal steps from 1-10 mN, an applying a variable oscillatory load at a frequency of 100 Hz, resulting in small oscillations of ~2 nm. Additional specifics regarding the applied load functions and other experimental details are provided in the individual methods sections of the main Chapters 4-6 here. Whenever indentations were made on large, elastically homogenous samples, data were analyzed according to the standard Oliver and Pharr method [1, 2]. When indentations were made on small (usually < 100 $\mu$m) calcite fully embedded in compliant matrix material, modifications to the standard analysis were made to account for the effect the dissimilar matrix material had on the total measured compliance (as discussed in Chapters 5 and 6).

In the standard analysis, hardness is the previously defined Meyer hardness (Equation 2.1). Additionally, a "reduced modulus" $E_R$ can be defined for a homogeneous isotropic material as

$$\frac{1}{E_R} = \frac{1-\nu_s^2}{E_s^2} + \frac{1-\nu_i^2}{E_i^2}\,, \tag{3.1}$$

where $E$ is Young's modulus and $\nu$ is Poisson's ratio and the subscripts $s$ and $i$ refer to the sample and indenter, respectively. $E_R$ is related to the contact compliance on unloading $C_c$ by

$$E_R = \frac{\sqrt{\pi}}{2C_c\sqrt{A_c}}\,. \tag{3.2}$$

Hence, by determination of $C_c$ and $A_c$, both $H$ and $E_R$ can be calculated using Equations 2.1 and 3.2, respectively. For our diamond Berkovich indenter, $E_i$ and $\nu_i$ are known to equal 1140 GPa and 0.07, respectively. Thus, by plugging those values into Equation 3.1, one can solve for the quantity $E_s/(1-\nu_s^2)$ like so:

$$\frac{E_S}{1-\nu_S^2} = \left(\frac{1}{E_R} - \frac{1-\nu_i^2}{E_i^2}\right)^{-1} . \tag{3.3}$$

This quantity is the plane strain modulus (also referred to as the flexural modulus) of the sample, which we will call "the indentation modulus," and represent with the symbol $F_s$.

In this work, the contact compliance (reciprocal of the contact stiffness) of quasi-static indentations was determined by making a power-law fit to the upper 20-95% of the unloading data and calculating the slope of this fit at maximum load. For dynamic indentations, the contact compliance was determined by analyzing the amplitude of the measured displacement signal $h(\omega)$ using the dynamic model in Oliver and Pharr's paper [1]:

$$\left|\frac{P_{os}}{h(\omega)}\right| = \sqrt{\{(C_c + C_m)^{-1} + K_s - m\omega^2\} + \omega^2 D}, \tag{3.4}$$

where $P_{os}$ is the amplitude of the oscillating force, $\omega$ is the oscillating frequency, $m$ is the oscillating mass, $K_s$ is the spring stiffness, $D$ is the damping coefficient, and $C_m$ is the machine compliance. $P_{os}$ and $\omega$ are applied values; and $m$, $K_s$, $D$, and $C_m$ are calibrated values.

Prior to making any measurements on samples with unknown properties, the nanoindenter had to be carefully calibrated. Two of the most important calibrations are the machine compliance calibration, and the tip area calibration. In practice, the machine compliance needs to be calibrated first, as the tip area cannot be accurately calibrated without knowing the machine compliance. The total measured compliance $C$ includes components from both the elastic deformation of the sample and the elastic flexing of the components that make up the indenter machine. Because this flexing occurs far away from the indentation and in regions of constant cross-sectional area, it is considered to be a constant of the machine an assumed to be independent of indenter

displacement, such that (for a large and homogeneous sample with no elastic heterogeneities) we write:

$$C = C_c + C_m \ , \tag{3.5}$$

where $C_m$ is the machine compliance. This formulation is important because it constitutes the starting point for the corrected nanoindentation method used to measure small particles embedded in a dissimilar matrix presented in Chapter 5.

Calibration of machine compliance was done as described in the Oliver and Pharr method [1, 2]. In short, a series of 25 quasi-static indentations were made in a fused silica calibration standard to maximum loads ranging from 5 to 10 mN, the total measured compliance was plotted versus the reciprocal square root of the applied loading, and the *y*-intercept of a linear fit these data was assumed to be equal to the machine compliance. Note that to use of a plot of this form (*e.g.*, in contrast to using a plot of compliance versus reciprocal square root of *contact area* made in Chapter 5) requires that the sample material has no indentation size effect (ISE), *i.e.*, that the ratio $P/A_c$ is independent of $A_c$. Because fused silica has been shown to display little to no ISE over much larger load ranges [3], the assumption should be valid in this case. This calibration was repeated every few months to ensure it was accurate and unchanging. The calibrated value of machine compliance for our machine was 0.5 nm/mN.

Another important calibration was calibration of the tip area function, $A_c(h_c)$. The tip area function describes the projected contact area ($A_c$) of an indentation at any contact depth ($h_c$) into a sample's surface. The contact area is important because it used to calculate hardness and modulus, and the tip area function is important because it allows for contact area to be calculated without directly measuring the size of a residual impression using some other method. In this work, the tip area was also calibrated according to the Oliver and Pharr method [1, 2]. For this calibration, a series of 100 indentations were made in a standard fused silica sample (with known

modulus) to maximum loads between 0.1 and 10 mN. Because the modulus of the fused silica sample was known (69.6 GPa), the tip area function (contact area as a function of depth) could be determined by analyzing the measured displacement and compliance data as a function of depth. This calibration was repeated every few months to ensure it was accurate. In practice, the tip area function does change slightly over time, as the shape of the indenter tip is gradually worn down. A typical calibrated area function for our Berkovich indenter was:

$$A_c(h_c) = 24.5h_c^2 + 2515h_c + 4799h_c^{1/2}, \quad (3.6)$$

where $h_c$ is in nm and $A_c$ is in nm$^2$. Note that the first term was fixed to $24.5h_c^2$, which is equal to the area function of a perfect Berkovich tip (Equation 2.3). This was done so that for large $h_c$, where this $h_c^2$ term will dominate the form of the function, this area function will approach that of a perfect Berkovich tip. Furthermore, note that this area function closely matches to that of a cone (with the same contact area to depth ratio as a perfect Berkovich indenter) capped with a hemisphere of radius 120 nm—in good agreement with our assumed tip radius of ~120 nm.

Other nanoindentation experiments were performed using a different nanoindenter *in-situ* in a SEM at Hysitron headquarters (Eden Prarie, MN). All relevant details for those experiments are in Chapter 4.

## 3.2. Synthetic calcite growth

In Chapters 5 and 6, synthetic calcite crystals were grown by the ammonium diffusion method [4]. This is a widely used method of growing synthetic calcite in which $(NH_4)_2CO_3$ powder and $CaCl_2$ solution are sealed inside a growth chamber, allowing $NH_3$ and $CO_2$ gas sublimed from the $(NH_4)_2CO_3$ powder to diffuse into the $CaCl_2$ solution, supersaturating the solution with respect to $CaCO_3$. $CaCO_3$ then precipitates from the solution, often forming calcite crystals on any substrate immersed in the

solution. In the absence of any impurities in the growth solution, the growth kinetics and final morphology of crystals are determined by the volume and initial concentration of the $CaCl_2$ solution, and to a lesser degree, the amount of $(NH_4)_2CO_3$ powder and the size of the growth chamber. In this work, two different growth chambers were used: (1) A large glass desiccator, on which a glass top was sealed with vacuum grease, and (2) A small home-made growth chamber consisting of polystyrene petri dish and cap sealed together with a flexible film (Parafilm), which was monitored *in-situ* under an optical microscope. In either setup, the crystals were grown on glass slide substrates. Key experimental details are provided in the individual methods sections of the main Chapters 5 and 6 here. Here, I note some supplemental details about using this growth method successfully.

The cleanliness and smoothness of the substrate on which the crystals grew affected the spacing (space between crystals) and growth rate of crystals. For example, for the in-situ growths, a scratch was made on the glass slide to provide a feature on which the microscope could focus. On the scratch, the spacing between crystals and the final size of crystals was clearly smaller than other crystals on the flat surface of the glass. This is consistent with the reduced barrier for heterogeneous nucleation on rough surfaces [5]. A similar phenomenon was observed in some early experiments where the glass slide was apparently not entirely clean. That is, small, closely spaced crystals were observed in localized streaks across the glass surface. In subsequent growths, the glass slides were carefully cleaned by alternating rinses in ethanol and DI water (with the final rinse being DI water), and then quickly dried with flowing $N_2$ gas. When the glass was carefully cleaned in this manner, the spacing between and final sizes of the resultant crystals were more consistent across the entire substrate.

Obtaining a proper seal on the growth chamber is also important. For the large glass desiccator, this was easily achieved using vacuum grease. For the small

homemade chamber, a good, repeatable seal could also be achieved by careful stretching of a single strip of Parafilm around the outside of the chamber. If the seal was not good, then no crystal growth would occur. That is, in some early experiments, other methods of sealing were attempted (*e.g.*, scotch tape, multiple strips of Parafilm), and no growth at all was observed after 60+ minutes of observation *in-situ*.

### 3.3. Nanoindentation of small crystals

In Chapters 5 and 6, nanoindentation was performed on small (< 100 $\mu$m) synthetic crystals, grown by the method described in Section 3.2. A smooth and flat, horizontal surface is required to make an accurate nanoindentation, but the synthetic crystals grown here had random orientations and sometimes rough or curved surfaces. I created such a surface by covering the crystals in liquid cyanoacrylate glue, allowing the glue to solidify (with crystals embedded inside), then peeling the solidified glue off of the glass substrate, exposing the flat and smooth surface of the crystals that was previously in contact with glass. Then, I indented the crystals on this surface using a dynamic load function, and corrected the measurement for the dissimilar compliance of the embedding material using a new correction method (Chapter 5). Key experimental details are provided in the methods sections of the main Chapters 5 and 6. Here, I discuss some additional lessons learned while developing these methods.

Before deciding on the sample preparation technique and corrected nanoindentation analysis used in Chapters 5 and 6, other methods of making nanoindentation measurements on such small crystals were also considered. The first requirement was to expose a flat and horizontal surface of the crystals. One way of achieving this (*e.g.*, the method used by Kunitake *et al.* [6]) is to embed the crystals in liquid cyanoacrylate glue, allow the glue to solidify and encapsulate the crystals, and then to expose a flat surface of the crystals by polishing down the glue parallel to the

glass substrate. This technique was attempted here, and did work reasonably well a few times for especially large (~100 $\mu$m or larger) crystals, but generally was a very difficult technique to master. Two common failure modes were observed: (1) As the glue approached some critical thickness (approximately 100 $\mu$m), it would tend to curl up at its edges and delaminate from the glass, taking the crystals with it, and (2) any small tilt in the sample during polishing would create thickness gradients in the glue such that one side might be polished through to the glass before the polish on the other side had even reached the surface of the crystals.

Instead, I pursued the mounting method described in a paper by Kim *et al*. [7], in which the crystals "were overlaid with resin and then the slide prised off," leaving a flat face of the crystals without the need for polishing. However, in that paper they do not describe exactly how the glass was removed from the resin. After much trial and error, I've determined a series of steps that works well. Using epoxy or glue (EpoFix, or Krazy Glue work well) and a slightly rough, flexible sheet (a 10 $\mu$m grit polishing paper, or any flexible polyethylene sheet works well):

1) Dab a drop of glue over the area of the slide containing the crystals to be indented
2) Cover with the flexible sheet, lightly press down, and allow to rest until cured
3) Once cured, run under flowing water, and slowly peel the flexible sheet (with cured resin now attached) from the glass

The key to making this work seems to be the use of a slightly rough backing sheet (creating a strong mechanical interlock with the resin), and the use of flowing water (presumably forcing its way between the glass and the glue by capillary action). For comparison, in my experience, neither EpoFix or Krazy Glue can simple be pried off of glass using a razor blade as leverage.

More generally, I imagine this same general technique could be used as an easy method for mounting any small particles in preparation for indentation measurements.

Crystals grown on a flat substrate have the advantage that the surface exposed by peeling is already as flat as the substrate is, but any rough or rounded particle prepared in this way should be so close to the surface of the embedding material that a flat and smooth surface could be easily created by a quick polish with small grit size. Thus, the issue of creating a thickness gradient and/or having the embedding material become so thin that it delaminates should be avoided.

The problem created by embedding crystals for nanoindentation is that the embedded sample is not elastically homogeneous, and so nanoindentation data cannot be analyzed using the standard Oliver and Pharr method [1, 2]. The correction method I introduce in Chapter 5 requires that compliance data be generated for some range of indentation depth. In this work, I use a dynamic loading function, in which compliance is measured near-continuously across many load steps through a 100 Hz oscillation of the indenter. In practice, such compliance versus indentation depth data could also be generated by a single "multiple unload" quasi-static indentation, in which the indenter is loaded and unloaded at various intermediate peak loads, on the way to some global maximum peak load before a final unloading. In some initial experiments, this technique was used and can work just as well, but I prefer dynamic indentations because they could provide a higher density of compliance data for the same amount of time per indentation.

## 3.4. REFERENCES


1. Oliver, W.C. and G.M. Pharr, *An improved technique for determining hardness and elastic-modulus using load and displacement sensing indentation experiments*. Journal of Materials Research, 1992. **7**(6): p. 1564-1583.

2. Oliver, W.C. and G.M. Pharr, *Measurement of hardness and elastic modulus by instrumented indentation: Advances in understanding and refinements to methodology*. Journal of Materials Research, 2004. **19**(1): p. 3-20.

3. Nix, W.D. and H.J. Gao, *Indentation size effects in crystalline materials: A law for strain gradient plasticity*. Journal of the Mechanics and Physics of Solids, 1998. **46**(3): p. 411-425.

4. Ihli, J., et al., *Elucidating Mechanisms of Diffusion-Based Calcium Carbonate Synthesis Leads to Controlled Mesocrystal Formation*. Advanced Functional Materials, 2013. **23**(15): p. 1965-1973.

5. Sunagawa, I., *Crystals: Growth, Morphology, & Perfection*. 2005: Cambridge University Press.

6. Kunitake, M.E., S.P. Baker, and L.A. Estroff, *The effect of magnesium substitution on the hardness of synthetic and biogenic calcite*. MRS Communications, 2012. **2**(3): p. 113-116.

7. Kim, Y.Y., et al., *An artificial biomineral formed by incorporation of copolymer micelles in calcite crystals*. Nature Materials, 2011. **10**(11): p. 890-896.

## CHAPTER 4

*Parts of this chapter to be submitted to *Journal of Materials Science*

# Effect of load and anisotropy on the indentation hardness of calcite single crystals

Joseph D. Carloni[1], Lauren M. Mangano Drenkard[1], Matias Werner[1], Miki E. Kunitake[1], Sanjit Bhowmick[2], Ryan J. Stromberg[2], Thomas J. Wyrobek[2], Lara A. Estroff[1], and Shefford P. Baker[1*]

1. *Cornell University, Department of Materials Science and Engineering, Bard Hall, Ithaca, NY 14853*

2. *Hysitron Inc., 9625 W 76th St, Eden Prairie, MN 55344*

## ABSTRACT

Understanding the mechanical properties of single crystal calcite is important in a wide range of industries and applications. In addition, various types of occlusions in biogenic and synthetic calcite are well known to increase single crystal hardness. Unfortunately, published data, even for nominally pure and defect-free calcite spans a wide range, from ~ 1 to 4 GPa, making quantitative comparisons difficult. Plotting those data *vs*. indentation load reveals a strong indentation size effect and produces a "master curve" for hardness of pure single crystal calcite. To determine if the remaining scatter (~ 1 GPa) could be attributed to anisotropy, nanoindentations were made at a range of azimuthal angles on (0001) and $(10\bar{1}4)$ faces in pure calcite single crystals using Berkovich and cube corner tips, and surface morphology and deformation modes were studied both *post facto* and *in-situ*. Twinning upthrusts at certain angles on the (0001) face caused pileup, cracking, and reduced hardness. In the absence of twinning, the hardness at 2.5 mN load was found to be 2.5 ± 0.07 GPa, independent of orientation, and the indentation modulus was found to vary with the indented face but not azimuthal angle. An elastic analysis reveals that Young's

modulus is not a good surrogate for the indentation modulus. Anisotropy only accounts for a small fraction of the remaining scatter in the published calcite hardness data. The rest (~ 1 GPa at any load) is attributed to experimental error and unreported variations in testing conditions and sample quality.

## 4.1. INTRODUCTION

Calcite (the most thermodynamically stable form of $CaCO_3$) is a common mineral that exists in geology, contained in sedimentary rocks like limestone and shale, and also in biology, for example in the shells, teeth, and spines of marine organisms. The mechanical properties of calcite are important for a number of practical reasons. For example, calcite is an important ingredient in man-made structural materials like concrete and cement [1, 2]; crushed calcite powders are used as low-hardness abrasives or pressed together into pharmaceutical antacid tablets [3]; and the mechanical strength of calcite-containing limestone and shale is important in $CO_2$ sequestration processes used to store greenhouse gas pollutants [4], as well as the hydraulic fracturing processes used to release trapped oil and gas [5].

Another reason the mechanical properties of calcite are interesting is that some biogenic and synthetically-modified single crystals appear to be much stronger than pure crystals of geologic or synthetic origin. Since 1945, we are aware of 42 studies that report the indentation hardness of single crystals of calcite [6-47], including those of biogenic, synthetic, and geologic origin. Hardness values claimed to be upwards of 60% higher than those of pure control crystals have been reported for single crystals of biogenic calcite within the shells of brachiopods [19, 22, 23] and mollusks [20, 31, 33, 38, 39, 41, 42, 47], the teeth [21, 37] and spines [25, 26, 34] of sea urchins, as well as the spicule of a sponge [35]. There is much interest in understanding the mechanisms that could lead to this single-crystal strengthening, and model calcite crystals have been synthesized in a number of studies in order to try to replicate such effects [24, 27, 30, 32, 43-45]. (Note that additional strengthening occurs in hierarchical biogenic structures at length scales that encompass multiple crystals, *e.g.*, hardness measurements with indentation sizes larger than the average grain size (*e.g.* [18, 22,

28, 36, 46, 48-53]). We do not consider such effects here and focus instead on the properties of individual calcite single crystals.)

Unfortunately, it is difficult to interpret the differences in hardness between different calcites because the reference hardness of pure single-crystal calcite is not well known. This situation is illustrated in Figure 4.1, where hardness results for single crystals of biogenic, geologic, and synthetic calcites are shown. Reported hardness values for these "control" calcite single crystals (filled squares in Fig. 4.1) span a wide range, from ~1 to 4 GPa. Control crystals are those expected to be pure and defect free. This includes both large [6-14, 17, 18, 22-24, 26, 28, 29, 33, 36-38, 42, 46] and small [15, 16] geologic crystals, as well as small synthetic crystals [21, 27, 32, 36, 40, 43, 44]. Note that, in Fig. 4.1, the reported Vickers [7-10, 13, 15, 16, 18, 22, 36, 46] or Knoop [6, 9, 11, 12] hardness values (load/indentation surface area) were converted to Meyer hardness values (load/projected indentation area), as is commonly used to report nanoindentation hardness.

By comparison, the reported hardnesses of the biogenic calcites [19-23, 25, 26, 31, 33-35, 37-39, 41, 42, 47] cover a range of ~2–7 GPa (open circles in Fig. 4.1), which is only slightly wider than the range for the control crystals. That some biogenic calcite crystals are harder is not surprising as such crystals have been shown to include solutes [18, 19, 25, 33, 48] that provide solid solution strengthening [30] as well as occluded molecules and second phase particles [19, 33, 54] that impede both dislocation [45] and crack [55] motion.

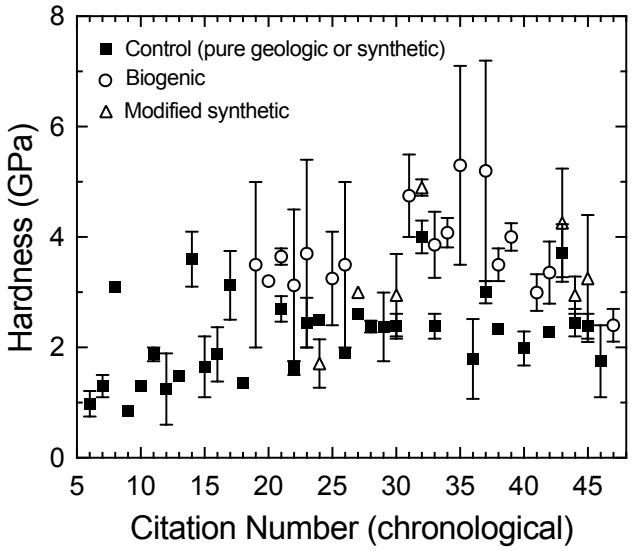


**Figure 4.1:** Single crystal calcite hardness values from 42 publications plotted versus their citation number in the reference list. Each data point represents the average or median hardness (whichever was reported). Error bars represent the reported range. All data presented as Meyer hardness (load/projected area). Biogenic and modified synthetic calcites are generally harder than pure controls, but scatter in all groups is very large making it difficult to interpret strengthening mechanisms.

Finally, in an attempt to mimic and understand the biogenic materials, a number of synthetic crystals have been produced that include biomimetic impurities like solutes [30], small molecules [45], and second phase particles [24, 27, 44], as well as crystals with exotic impurities like carbon nano-tubes [32] and 2D sheets of graphene [43]. The reported hardnesses of these calcites (open triangles in Fig. 4.1) span a range from ~1 to 5 GPa.

While is it not surprising that calcite crystals containing solutes, small molecules, and second phase particles have high and widely varying hardness, the reasons for the large variations in the pure control crystals are not clear. The remaining variations cannot be due to impurities, second phases, grain size, or composite effects. This leaves size effects, anisotropy, and experimental error as possible explanations.

It is well known that the hardness of many materials decreases with increasing indentation load. This phenomenon is known as the indentation size effect (ISE) [56, 57], and has been attributed to an increase in the density of geometrically necessary dislocations with decreasing indentation size [58], surface roughness effects on especially shallow indentations [59], and/or an increase in the tendency towards fracture at higher loads [60, 61]. Surprisingly, despite a number of studies reporting load-dependent hardness in calcite over relatively small load ranges [11, 12, 14-17, 22, 29, 38, 42, 43], the ISE in calcite has not been addressed over a wide range of loads. This problem is particularly important since biogenic and synthetic crystals are often very small (of order 10–100 $\mu$m) and very low load indentations are used to study them [14-17, 21-24, 26-29, 32, 33, 37, 38, 40, 42-44]. The hardness experiments on the pure control calcite single crystals shown in Fig. 4.1 were made at loads ranging from 0.2 to 4900 mN. Hence, it is likely that at least some of the variability among the reported hardnesses of these crystals comes from the ISE.

In addition to the ISE, the anisotropy of calcite single crystals might also be expected to affect the measured hardness. Indeed, variations in measured hardness and/or indentation modulus with crystal orientation have been reported for many single crystals: *e.g.* metals and alloys [62-66], hard ceramics [62, 67-69], inorganic compounds [62, 70-72], organic compounds [73-75], and natural minerals [6, 7, 11, 12, 33, 62, 76-82]—including calcite [11, 12, 33]. Large variations (>20%) in hardness with orientation have been reported for some crystals [63, 69-71, 73, 74, 78-80].

Calcite has a trigonal $R\bar{3}c$ crystal structure and is highly anisotropic. The relevant slip systems are illustrated in Figure 4.2. Plastic deformation at low temperatures (<400°C) occurs by slip on $\{10\bar{1}4\}$ and $\{\bar{1}012\}$ planes and by twinning on $\{\bar{1}018\}$ planes [83]. Uniaxial compression tests have shown that the critical resolved shear stresses (CRSS) for slip on $\{10\bar{1}4\}$ and $\{\bar{1}012\}$ planes increase rapidly with decreasing temperature and, while the room temperature values are not well known, results suggest that the CRSS for each of these slip systems will be near 200 MPa [83]. By contrast, the CRSS for twinning on $\{\bar{1}018\}$ planes at room temperature is less than 10 MPa [83]. It is important to note that, due to the crystal structure, $\{\bar{1}018\}$ twinning is unidirectional—that is, twin shears can only occur in one direction, $<404\bar{1}>^{+}$, since the carbonate groups have to "flip" or rotate during twinning and can only flip one way. Elastic anisotropy in calcite is also large. Based on single crystal elastic constants, calcite has a universal elastic anisotropy index $A^U \approx 2$, ($A^U = 0$ for an isotropic material) which places it among the more anisotropic materials [84]. These large differences in stiffness and CRSS with orientation might be expected to play a role in the measured hardness and indentation modulus.

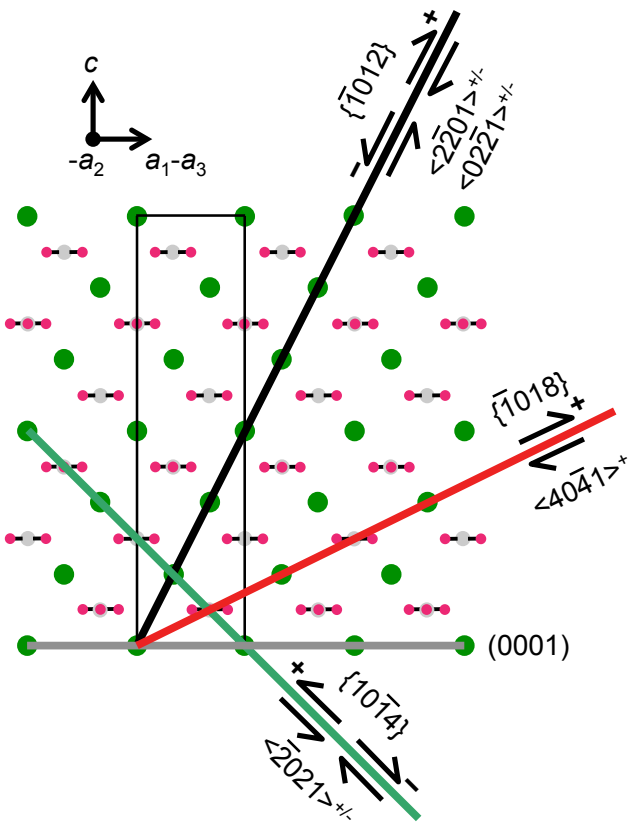


**Figure 4.2:** Schematic of the calcite crystal structure. Large green circles: calcium: small red circles: oxygen; medium grey circles: carbon. The (0001) plane, and example slip planes, $\{10\bar{1}4\}$ (also the natural facet plane), $\{\bar{1}012\}$, and $\{\bar{1}018\}$ (twin plane) are indicated. The unit cell is also outlined. Arrows indicate the direction of shear on each slip plane. $<2\bar{2}01>$ and $<02\bar{2}1>$ slip directions are in/out of the plane of the page by +/- 38°. The $<40\bar{4}1>$ twin direction lies in the plane of the page. $\{\bar{1}012\}<\bar{2}20\bar{1}>$ and $\{10\bar{1}4\}<\bar{2}021>$ slip systems can operate in either direction (+/-) but the $\{\bar{1}018\}<404\bar{1}>$ system can only operate in the positive sense (+).

To date, experimental work exploring the effect of anisotropy on indentation measurements in calcite has been limited and inconsistent. Winchell (1945) used a Knoop indenter at 100 g (980 mN) load to measure hardness on a $\{10\bar{1}4\}$ cleavage plane at three different azimuthal orientations, and found a ~38% variation [6]. Taylor (1949) measured the Vickers hardness of calcite using a 50 g (490 mN) load at a single (random) azimuthal orientation on a $\{10\bar{1}4\}$ cleavage facet, and planes polished perpendicular and parallel (actual orientation unspecified) to the [0001] optical axis, and found a ~28% variation [7]. Later (1992), Wong and Bradt [11] used a Knoop indenter to measure hardness as a function of both azimuthal orientation and load (25–200 g, 220–1960 mN) on a $\{10\bar{1}4\}$ facet and found a small variation (~10%) that matched the symmetry of the indenter and the $\{10\bar{1}4\}$ plane. Shortly afterwards (1993), Carter *et al*. [12] conducted nearly identical experiments at 10–100 g (98–980 mN) but reported large variations (up to 60%) that did not match the indenter/sample symmetry. Recently (2013), Kunitake *et al*. [33] measured nanoindentation hardness as a function of azimuthal orientation on the (0001) face of pure geologic calcite using a 3-sided Berkovich indenter at a load of 2.5 mN and found a small systematic variation (~12%). These authors all attributed variations in hardness to cracking and/or twinning, but no analysis was provided.

Here, we study the effects of indentation load and orientation on the hardness of pure, single crystal calcite. We first characterize the indentation size effect by simply plotting published hardness data as a function of load, finding a substantial ISE that accounts for most of the variation shown in Fig. 4.1. The remaining hardness values fall in a band that is about 1 GPa wide at every load. To determine the extent to which the remaining variability is due to anisotropy, we determined the hardness and indentation modulus as a function of azimuthal angle on both the (0001) and $(10\bar{1}4)$ planes of Iceland spar, a relatively pure and perfect form of calcite, using a Berkovich

indenter, as well as a cube-corner indenter, a more acute angled indenter often used to induce cracking. $\{10\bar{1}4\}$ planes are the naturally occurring cleavage facets, and are thus the most commonly seen and studied, while biological organisms sometimes grow calcite crystals with (0001) planes exposed at the natural wear surface of the structure [18, 33, 36, 85]. We use nanoindentation at low loads (2.5-10 mN) to avoid cracking and focus on plastic deformation mechanisms. Our results thus compare directly with similar measurements used to study small biogenic [19-23, 25, 26, 31, 33-35, 37-39, 41, 42, 47] geologic [14, 17, 22-24, 26, 28, 29, 33, 37, 38, 42] and synthetic calcite crystals [21, 24, 27, 30, 32, 40, 43-45]. We explain in detail the mechanism behind the anisotropy in hardness with azimuthal orientation reported by Kunitake *et al*. on the (0001) face in terms of a unique interaction between the symmetry of the indenter and the orientation of $\{\bar{1}018\}$ twin planes. Higher load measurements made *in-situ* in the SEM allow real-time imaging of these processes. A simple model is developed that qualitatively describes the results. We find *no* variation in hardness or modulus with azimuthal angle on the $(10\bar{1}4)$ face and that, except for the azimuthal angles on (0001) where twin deformation is favorable, the hardness on the (0001) and $(10\bar{1}4)$ faces are the same.

Thus, despite very anisotropic elastic constants and critical resolved shear stresses, careful attention to experimental detail gives a nanoindentation (Meyer) hardness for calcite at 2.5 mN load of 2.5 ± 0.07 GPa, which is independent of orientation outside the range of azimuthal angles on (0001) where twins form. At azimuthal angles were twins form, hardness can be lower by up to 12% (*i.e*., to 2.2 GPa).

## 4.2. INDENTATION SIZE EFFECT

In Figure 4.3a we plot the hardness values reported for pure single crystal control calcites in Fig. 4.1 versus the indentation load used in each study.

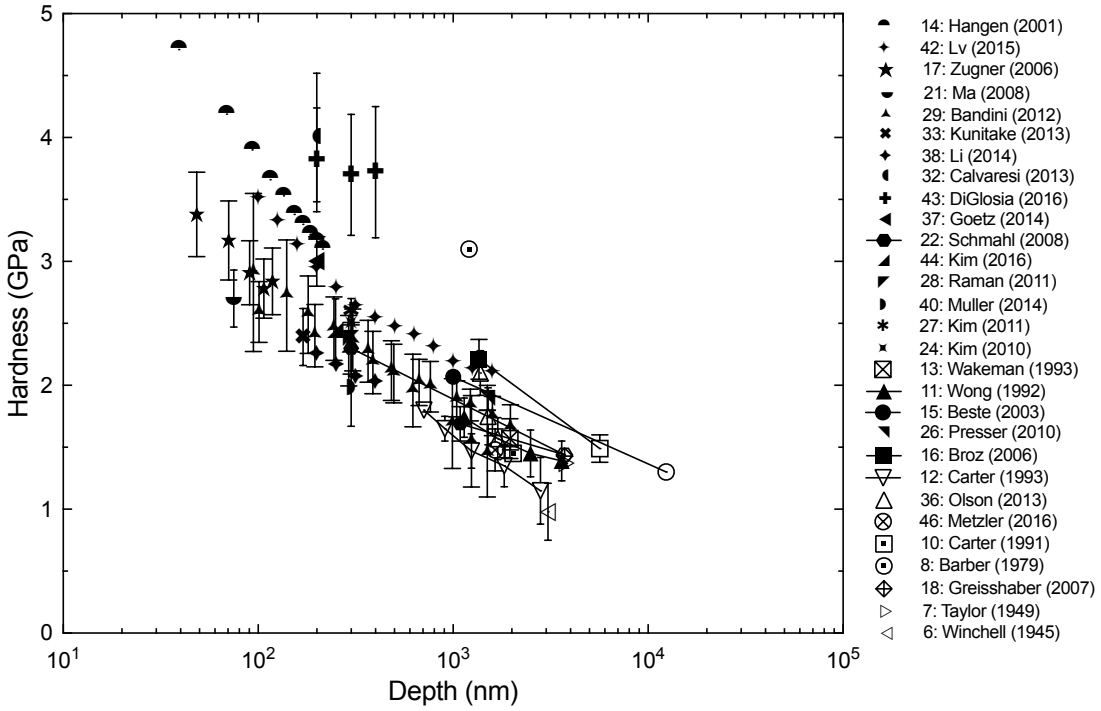


**Figure 4.3a**: Hardness values for 29 pure calcite "control" samples from Fig. 4.1 replotted versus the indenter load used for each measurement. Numbers indicate which reference the data come from. Filled shapes: nanoindentation. Open shapes: microindentation. Vickers or Knoop hardness numbers were converted to Meyer hardness for comparison with nanoindentation. Two very different loads from a single study are connected by a line. The data plotted in this way provide a master curve for the indentation size effect (ISE) in pure single crystal calcite and show that the ISE accounts for the majority (≈ 2.5 GPa) of the scatter in the "control" data in Fig. 4.1. With a few exceptions, the remaining data fall into a ~1 GPa wide band.

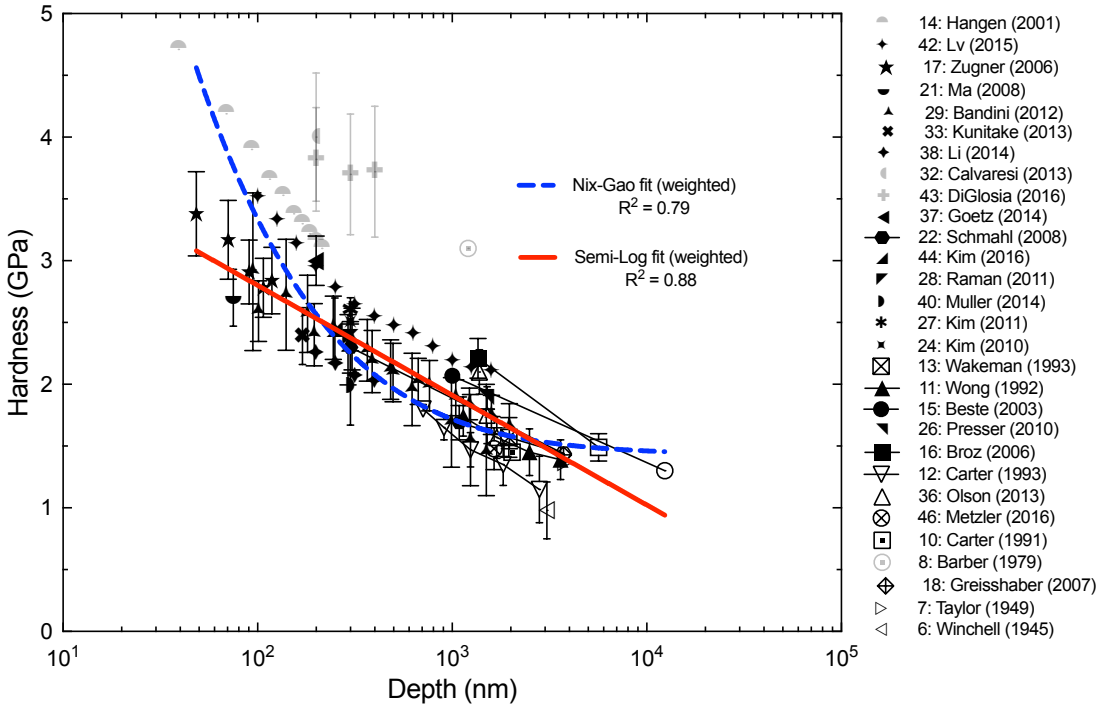


**Figure 4.3b**: The same hardness data in Fig. 4.3a plotted versus indenter depth and with the best fit line for fits to a popular ISE model based on strain-gradient plasticity ("Nix-Gao") [58] and to an empirical semi-log function. Obvious outlier data (Hangen [14], DiGiosia *et al*. [43], Calvaresi, *et al*. [32], and Barber and Wenk [8]) were not included in either fit, and are plotted here with light gray data symbols. Data was weighted by the inverse of the standard deviation squared (data originally reported without standard deviation was given an arbitrary +/-0.5 GPa standard deviation). The Nix-Gao best fit line is $y = 1.43\sqrt{1 + 445/x}$, and the semi-log best fit line is $y = -0.889\log(x) + 4.578$. Note that the empirical semi-log fit seems to provide the best fit to the whole range of data.

This plot include results from bulk geologic calcite [6-14, 17, 18, 22-24, 26, 28, 29, 33, 36-38, 42, 46], small synthetic calcite [21, 27, 32, 36, 40, 43, 44], and small calcite inclusions in limestone [15, 16]. As in Fig. 4.1, hardnesses were converted from the reported Vickers [7-10, 13, 15, 16, 18, 22, 36, 46] or Knoop [6, 9, 11, 12] values to Meyer hardness for direct comparison with the nanoindentation hardness results. Additionally, any nanoindentation data for which the load was not reported (depth only), reported indenter depths were converted to indenter loads by assuming an ideal Berkovich indenter geometry. From this plot, we see that at least part of the overall variation in hardness among these data sets is consistent with an indentation size effect. With few exceptions, the data fall in a band approximately 1 GPa wide that goes from about 3.5 GPa at 0.2 mN to about 1 GPa at 4900 mN.

In Figure 4.3b, two fits to ISE the data from Fig. 4.3a are shown. For these fits, the data is plotted versus indenter depth instead of load, to facilitate comparison to popular ISE models which are often formulated in terms of indenter depth [56, 57]. Similar to Fig. 4.3a, any microindentation data for which depth was not reported (load only) reported indenter depths were converted to indenter loads by assuming an ideal Vickers or Knoop indenter geometry. The Nix-Gao fit is to a model based on a strain gradient plasticity explanation for ISE [58], while the semi-log fit is a purely empirical fit to the data. Comparing these fits, we note that the empirical semi-log fit seems to better describe the data over the entire range.

While the ISE explains much of the variation in hardness reported for pure calcite, the remaining ~1 GPa variation at any given load is still unexplained. The data in Fig. 4.3 come from a variety of crystal orientations. In some reports, indentations were made across a range of specified orientations [6, 7, 11, 12, 33, 38], while in others the crystals were randomly oriented [21, 27, 32, 36, 40, 43, 44]. In the following, we

determine to what extent the remaining hardness variations can be explained by anisotropy effects.

## 4.3. EXPERIMENTS AND RESULTS

Large crystals of Iceland spar from two different sources were cleaved into rhombohedra displaying natural $\{10\bar{1}4\}$ cleavage facets with edges of 1-2 cm in length. Surfaces parallel to (0001) were obtained in samples sourced from Mexico (Carolina Biological Supplies GEO3429B) as described previously [33]. Cleaved rhombohedra were mechanically polished to within ± 1° of (0001) on one corner as shown in Figure 4.2a, starting with a disk grinder, followed by graded $Al_2O_3$ lapping films, and a final 50 nm $Al_2O_3$ powder (Buehler micropolish c-$Al_2O_3$) suspended in a water and 2-methyl-2,4-pentanediol mix (Green Lube, Allied High Tech). Polishing achieved an RMS roughness of ~10 nm, as measured over a $(30\ \mu m)^2$ scan area using indenter SFM. The concentrations of a few impurity atoms known to substitute for Ca in calcite (Mg, Mn, and Fe) were measured on separate small pieces using inductively coupled plasma mass spectrometry (ICP-AES). The concentrations of Mn and Fe were each extremely small (0.01 and 0.03 at%, respectively), and the Mg concentration was also small, at 0.16 at%. The $(10\bar{1}4)$ surfaces indented in this study were the $\{10\bar{1}4\}$ cleavage facets of rhombohedra cleaved from crystals sourced from Brazil (Ward's Science 470225-122). Because $\{10\bar{1}4\}$ planes have very low surface energy in calcite, they can be nearly atomically smooth upon fracture. Even without polishing, these as-cleaved rhombohedra had surface roughness < 10 nm RMS as measured over a $(30\ \mu m)^2$ area using indenter SFM. The Mg concentration in the (10-14) sample was measured using WDS, and found to be similar to that in the (0001) sample, at 0.22 +/- 0.04 at%.

Four sets of nanoindentation experiments were performed. **On the (0001) face:** (1) indentations were made at different azimuthal orientations using a Berkovich indenter at maximum loads of 2.5 and 9-10 mN, (2) an indentation load series from 2.5 to 10 mN in 0.5 mN load steps was made at fixed azimuthal angle, also using the Berkovich indenter, and (3) a cube-corner indenter was used to make indentations to a maximum load of 20 mN while observing the indentation process *in-situ* in a scanning electron microscope (SEM). **On the $(10\bar{1}4)$ face,** (4) indentations were made at different azimuthal orientations using the Berkovich indenter at maximum loads of 2.5 and 10 mN.

All Berkovich indentations were performed using a Hysitron Triboindenter (TI-900). The shape of the indenter tip was calibrated using the Oliver and Pharr method on fused silica [86]. The radius at the indenter tip was approximately 120 nm. Except for the indentations to a maximum load of 10 mN on the $(10\bar{1}4)$ face, all Berkovich indentations were performed in quasi-static mode. Each quasi-static indentation was load controlled, with a 5 s ramp to maximum load, a 5 s hold at maximum load, and 5 s ramp back down to zero load. Hardness and modulus were calculated according to the Oliver and Pharr method [86] by fitting a power law to the unloading data between 20 and 95% of the maximum load and using the slope of this fit at the maximum load as the contact stiffness. The 10 mN indentations on the $(10\bar{1}4)$ face were performed in dynamic "nano-DMA" mode. For these indentations, the mean applied load was increased in 20 discrete load steps from 1-10 mN over the course of 70 seconds. In addition, a small sinusoidal loading at 100 Hz was applied with the amplitude varied so as to maintain a dynamic displacement of approximately 3 nm. Hardness and modulus were calculated using a dynamic model [86] to analyze the amplitude of the displacement signal to calculate the contact stiffness. In all cases, for modulus we report the quantity $E_s/(1-\nu_s^2)$, which is the plane strain or "flexural" modulus of the

sample. Here, we will simply refer to this quantity as the "indentation modulus," and use the symbol $F_s$.

Surface topography scans were performed using two scanning force microscopy (SFM) methods. In the first, the same Berkovich tip that was used to make the indentations was scanned across the surface to create an SFM image before and after most indentations. We refer to this method as "indenter SFM". In the second, a commercial atomic force microscope (AFM) was used to obtain high resolution images of indentations. For these experiments, a Digital Instruments DI 3100 AFM equipped with a SiN tip (Olympus Corporation) was used in tapping mode. In addition, images were obtained of select Berkovich indentations using scanning electron microscopy (LEO 1550 FESEM). Prior to imaging in this SEM, samples were coated with Au-Pd (to prevent charging).

Indentations using a cube-corner indenter were made using a PI 85 SEM PicoIndenter (Hysitron Inc., Minneapolis, MN) installed in a Versa 3D FIBSEM (FEI Company, Hillsboro, OR). *In-situ* real-time SEM images of the indentation process were obtained, along with load-displacement data. The samples tested *in-situ* were uncoated (to prevent affecting the natural evolution of cracks and pile-up), so to prevent charging the SEM was run were imaged at a low acceleration voltage with a low current. Additional SEM images of these cube-corner indentations were made after the indenter was removed.

### 4.3.1. (0001) specimen preparation

A large calcite crystal was cleaved into rhombohedra displaying natural {10-14} cleavage facets with edges of 1-2 cm in length. These rhombohedra were mechanically polished on the (0001) plane to within ± 1° using a disk grinder followed by graded $Al_2O_3$ lapping films and a final 50 nm $Al_2O_3$ powder (Buehler micropolish c-$Al_2O_3$)

suspended in a water and 2-methyl-2,4-pentanediol mix (Green Lube, Allied High Tech). Polishing achieved an RMS roughness of ~10 nm, as measured over a 30 μm square scan area using indenter SFM.

### 4.3.2. (0001) azimuthal indentation series

Berkovich indentations were performed on the prepared (0001) facet at different azimuthal orientations as shown in Figure 4.4a and b. The azimuthal angle ($\phi$) was defined as the angle between the edges of the residual indentation and the edges of the crystal defined by the intersections of $\{10\bar{1}4\}$ planes with the polished (0001) plane, which correspond with the *a*-axis directions of the crystal ($<2\bar{1}\bar{1}0>$ directions). $\phi$ was defined to be zero when the edges of the indentation were parallel to the edges of the (0001) facet (*i.e.* parallel to the *a*-axes) and the corners of the indentation were pointing towards the corners of the (0001) facet (*i.e.*, toward $<40\bar{4}0>$). $\phi$ was defined to increase in magnitude with clockwise rotation of the indenter. The full symmetry of the (0001) face is contained within azimuthal angles between 0-60°, but to check for possible alignment effects, the angle was varied from 0-120° in 10° increments. At each angle, an array of 9 indentations was made using a maximum load of 2.5 mN. At this load, indentation depths were at least 10× the RMS roughness of the surface, and are thus not expected to be significantly affected by the roughness. This low load was selected to minimize the chance of fracture and to obtain hardness values that would be directly comparable with nanoindentation results from biologic and synthetic calcites [19-27, 30-35, 37-39, 41-45, 47], which are typically available only as small (10–100 $\mu$m) crystals. Additional sets of indentations were made using maximum loads of 9 mN (3 per angle at azimuthal angles between 0-60º in 20º increments) and at 10 mN (6 each at 0 and 60º).

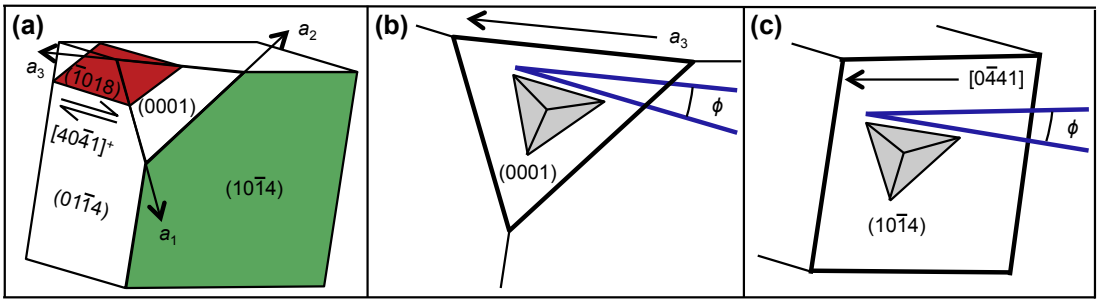


**Figure 4.4:** a) Schematic of a calcite single crystal showing $\{10\bar{1}4\}$ cleavage facets, a ground and polished (0001) surface, one of three equivalent $\{\bar{1}018\}$ planes, and the $a_1$, $a_2$, and $a_3$ directions. The $(\bar{1}018)$ twin plane intersects the (0001) plane along a line that is parallel to the $a_2$-axis. b) Schematic showing how the azimuthal angle, $\phi$, for Berkovich indentations is defined on the (0001) plane. c) Schematic showing how $\phi$ is defined on the $(10\bar{1}4)$ plane.

The calculated hardness and modulus are plotted as a function of $\phi$ in Figure 4.5. The data are nearly symmetric about $\phi = 60°$, indicating good alignment of the indenter axis and sample normal. At both 0 and 60º, the hardness measured at 10 mN is lower (2-6%) than that measured at 2.5 mN, in agreement with the ISE shown in Fig. 4.3. At each load, the hardness is maximum (≈ 2.4-2.5 GPa) near the 60° orientation and minimum (≈ 2.2-2.3 GPa) near the symmetrically equivalent 0° and 120° orientations. The indentation modulus follows the opposite trend. At both 0 and 60º, the indentation modulus at 10 mN is similar to that at 2.5 mN (≈ 81 GPa at 0º and ≈ 70 GPa at 60º). The variations with $\phi$ are approximately 12% and 17% in hardness and modulus, respectively.

The surface topography of the residual indentations in the (0001) face varied significantly with $\phi$. Figure 4.6 shows indenter SFM images of 10 mN indentations at $\phi = 0$ and 60°. The indentations made at $\phi = 0°$ (Fig. 4.6a) show significant pile-up at the edges of the residual indentations (103 nm from the flat sample surface to the peak, compared to a final indentation depth of 279 nm). The pile-up is comprised of three distinct features. From the outside in, there is a step up that is aligned with the crystallographic *a* axes, followed by a raised flat plateau, followed by a slope leading up to the peak of the pileup. The alignment of the outermost step with the *a*-axes indicates a crystallographic origin for this behavior. In contrast, indentations made at $\phi = 60°$ showed no sign of pile-up (Fig. 4.6b).

SEM images of the residual indentations emphasize the crystallographic nature of the pileup and reveal that it is also associated with cracking. Figure 4.7a shows indentations made to 9 mN at $\phi = 0, 20, 40$, and 60º. Fig. 4.7b shows the orientation relationship between the indenter and the (0001) face schematically. The pileup evident in Fig. 4.6a is also visible at $\phi = 0º$ in Fig. 4.7a and deceases with increasing $\phi$. The visible steps on the surface outside the indent remain parallel to the *a*-axes as $\phi$

increases. These are indicated by dashed white lines in Fig. 4.7c. Significant cracking is associated with the pileup and decreases, along with the pileup, from $\phi = 0°$ to $\phi = 60°$. These are not the typical radial cracks that emanate from the corners of indentations [87], but rather form in pairs that connect the crystallographic surface step at the outside of the indentation with the interior of the indentation. The solid white lines in Fig. 4.7c trace these prominent cracks.

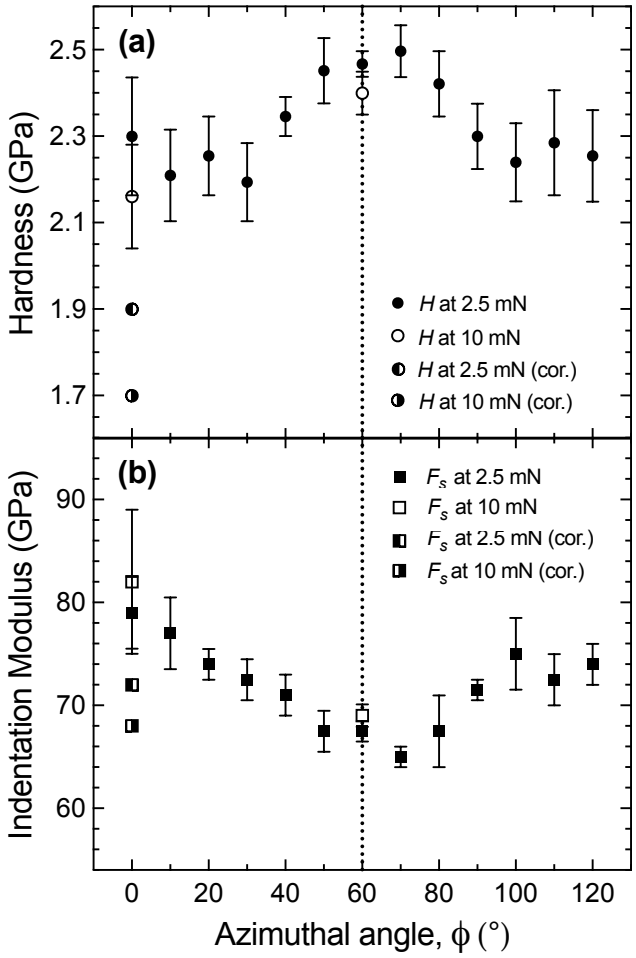


**Figure 4.5:** a) Hardness ($H$), and b) indentation modulus ($F_s$), as a function of azimuthal angle $\phi$ on the (0001) face. Calculated Oliver-Pharr hardness and modulus values from indentations made to 2.5 mN maximum load at $\phi = 0$-120º are plotted as filled symbols (mean of 9 at each angle), and from indentations made to 10 mN at $\phi = 0$º and 60º are plotted as open symbols (mean of 6 at each angle). Error bars represent one standard deviation. The data are symmetric about the vertical dashed line at $\phi = 60$º, as expected from the symmetries of the indenter tip and the (0001) face of calcite. Values after correcting the contact area for pile-up from 2.5 and 10 mN indentations at $\phi = 0$º (see Fig. 4.10) are plotted as corresponding half-filled symbols.

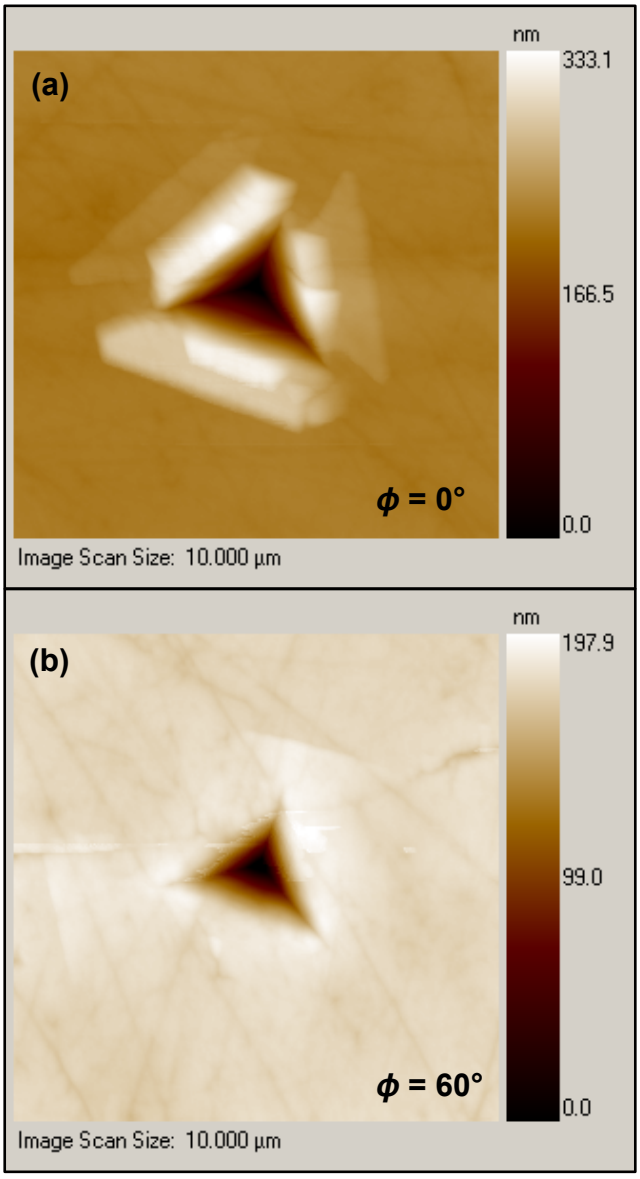


**Figure 4.6:** Indenter SFM scans of 10 mN indentations on the (0001) face made at a) $\phi = 0$ and b) $\phi = 60$ degrees. Significant pile-up is observed at $\phi = 0°$.

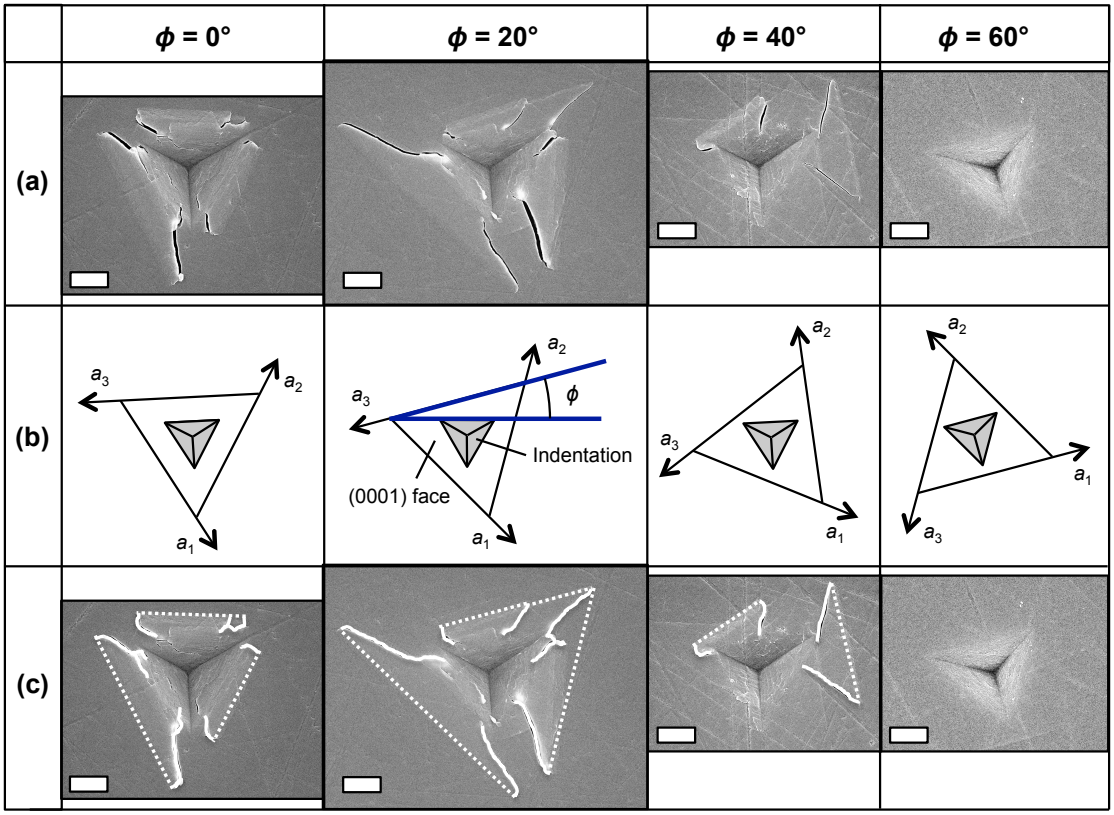


**Figure 4.7:** a) SEM images of indentations made at 10 mN load on the (0001) face at azimuthal angles $\phi = 0, 20, 40,$ and 60°. b) Schematics showing the orientations of the residual indentations with respect to the polished (0001) face of the crystal at each azimuthal angle. c) SEM images from a) with cracks (solid lines) and surface steps at the outer edge of the pileup (dashed lines) traced. The surface steps are aligned with the *a*-axis directions and the cracks connect the indentations to the ends of the surface steps.

### 4.3.3. (0001) indentation load series

To determine the load dependence of the pile-up and fracture for indentations with azimuthal angles near $\phi = 0°$, indentations were made with the Berkovich indenter on the (0001) face at $\phi = 0°$ at applied loads ranging from 2.5 to 10 mN in 0.5 mN increments, with 3 indentations at each load. Each indentation in this series was imaged using SEM and the total crack length associated with each indentation was measured by tracing all visible cracks in each image. Example images of residual indentations at 2.5 and 10 mN without and with crack tracing are shown in Figures 4.8a and b and Fig's 4.8c and d, respectively. The average crack length per indentation is plotted versus applied indentation load in Figure 4.9. The total crack length and the scatter in the crack length data both increase with indentation load.

The surface topographies measured by AFM from representative indentations at 2.5 and 10 mN are shown in Figure 4.10. Line-profile traces were taken from the corner to the center of the opposite edge for all three edges of each residual indentation. The locations of these scans are shown in Fig's 4.10a and c and the corresponding height versus distance data are plotted in Fig's 4.10b and d. Small arrows indicate the steps that are aligned with the *a*-axes at the outer edge of the pileup, as seen in Fig's 4.6, 4.7, and 4.8. The pileups at all loads have similar shapes and features, but are taller and wider at the higher load. No fracture threshold is visible in this load range, but the trend in the data suggest that there might be one at about 1.5 mN.

Consistent with Fig. 4.5, cracking is associated with significantly reduced hardness. The average hardness (not shown) decreases with applied load from ~2.3 GPa at 2.5 mN to ~2.0 GPa at 10 mN. While the magnitude of the decrease is in good agreement with the ISE shown in Fig. 4.3, the values are at the bottom of the reported band.

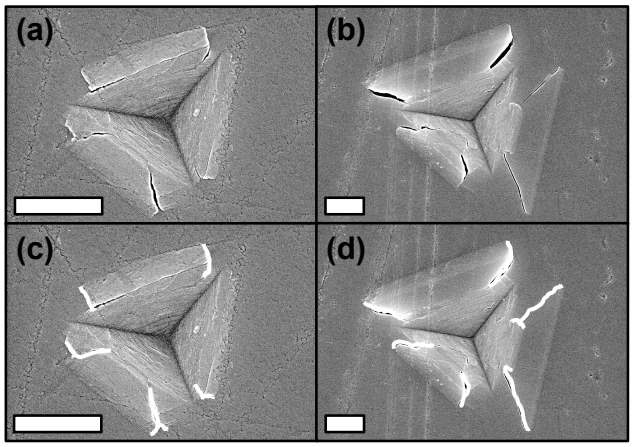


**Figure 4.8:** SEM images of indentations made at (a) 2.5 and (b) 10 mN load. c) and d) traces of the cracks from these same images.

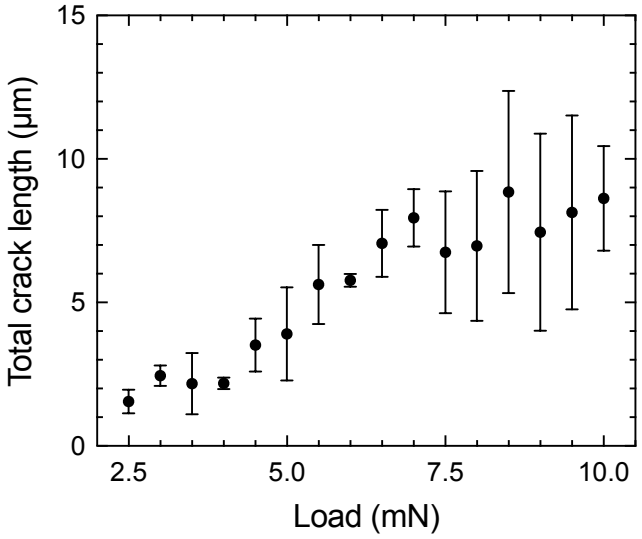


**Figure 4.9:** Average crack length per indentation traced from 3 indentations made at each load.

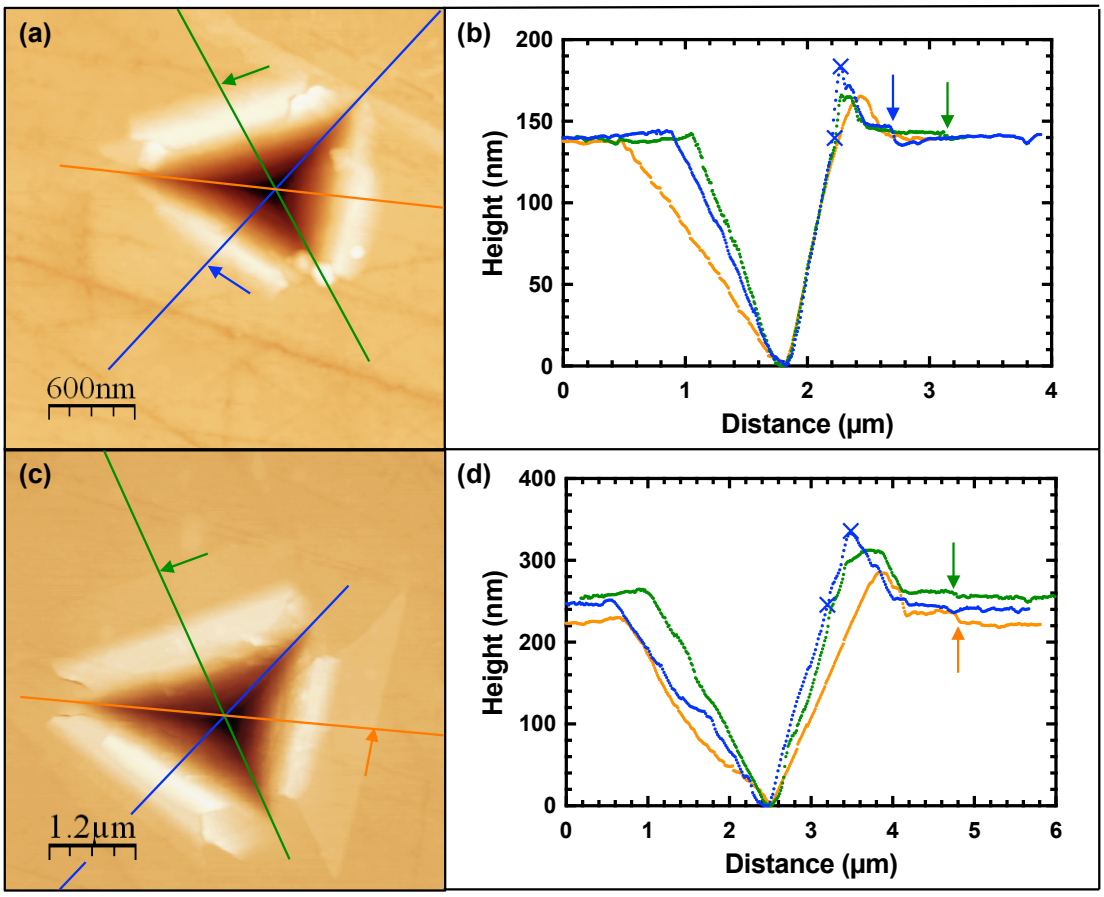


**Figure 4.10:** AFM images of indentations made at a) 2.5 and c) 10 mN load. b) and d) show height *vs*. distance for scans along the lines indicated in a) and c). Arrows indicate the locations of the crystallographic surface steps at the outermost edges of the pileups.

### 4.3.4. (0001) *in-situ* indentation

To determine when and how cracking and pile-up form during indentation, we performed indentations on the (0001) face using a cube corner indenter in a setup that allowed us to obtain SEM images of the indentation process *in-situ*. The more acute cube-corner geometry (compared to Berkovich) produces a slightly different stress state [88] but allows for a better view of the surface during indentation *in-situ* in the SEM. Load-displacement data were recorded in sync with the real-time SEM video. *In-situ* indentations were performed in load control, with a 40 s ramp to a maximum load of 20 mN, a 5 s hold at 20 mN load, and 5 s ramp back down to zero load. Ten indentations each were performed at $\phi = 0°$ and $\phi = 60°$.

Load-displacement data, along with still images from the video, from an *in-situ* indentation at $\phi = 0°$ are shown for different time steps in Figure 4.11. Arrows in Fig. 4.11a point to the load-displacement curve at the same time time-stamp as the SEM images in Fig's 4.11b and c. In the video (available online), no obvious cracking is visible up to ~13 mN load (Fig. 4.11b). Between ~14-15 mN load (Fig. 4.11c), a large crack appears, accompanied by an upthrust of material on each side of the crack. It is evident that the formation of this crack (circled in Fig. 4.11c) correlates with a jump in the load-displacement data (circled in Fig. 4.11a). Similar jumps in the load-displacement data (indicated by asterisks in Fig. 4.11a) are due to the formation of similar cracks outside the field of view. Fig. 4.11d shows the indenter at final depth (after unloading), with the large crack from Fig. 4.11c having reached its final length. An SEM image of the residual indentation (Fig. 4.11e) reveals features similar to those seen in residual Berkovich indentations at $\phi = 0°$ (Fig's 4.6-8, and 4.10), including pileup that terminates at surface steps parallel to the *a*-axes and cracks that extend from the indentation to that surface step.

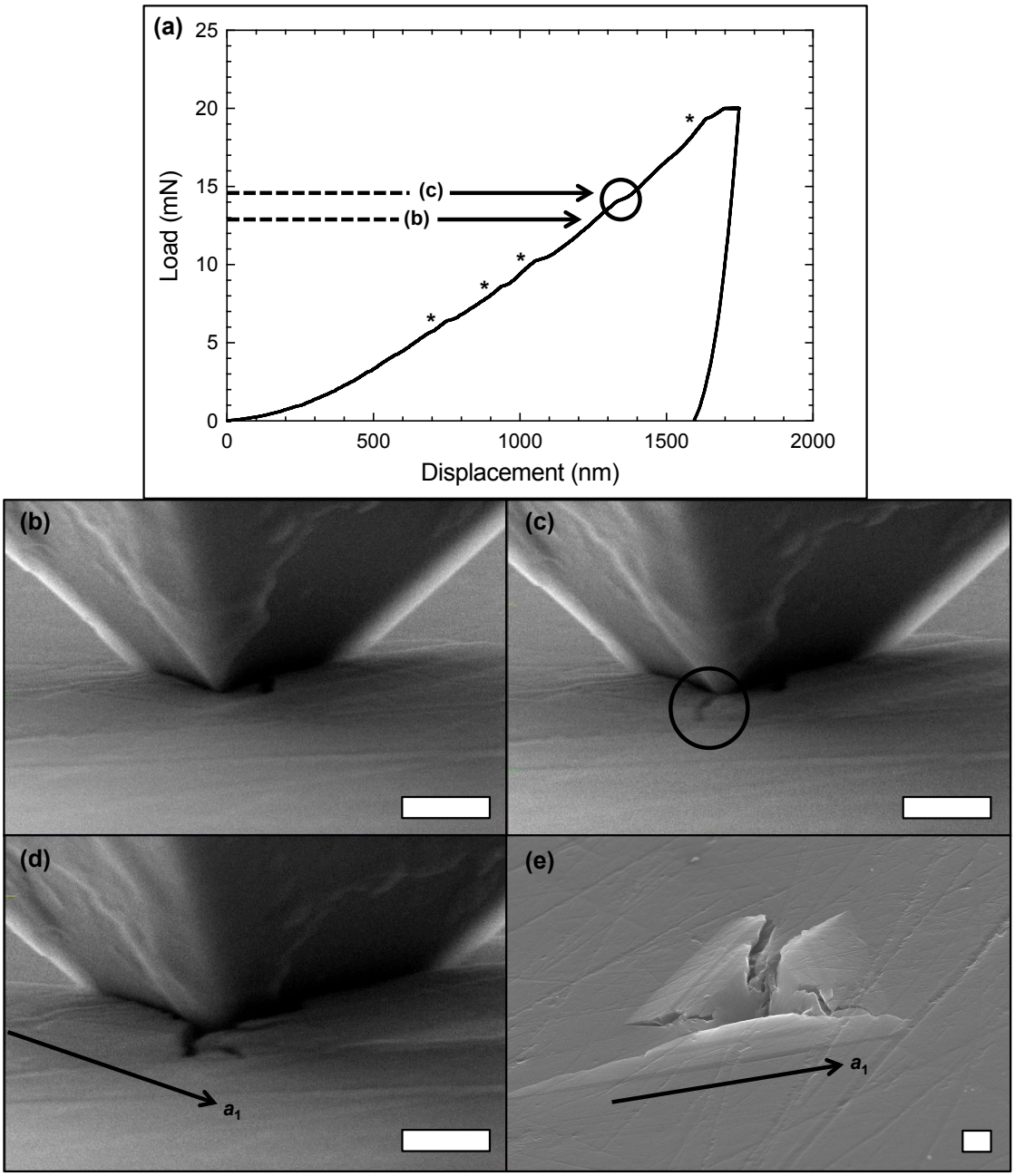


**Figure 4.11:** *In-situ* SEM of cube-corner indentation on (0001) at azimuthal angle $\phi$ = 0°. a) Load-displacement data and corresponding SEM images of indentation b) before any obvious cracking, and c) right after formation of crack at ~14 mN. d) Full extent of cracking at final depth. e) SEM of residual indentation. Black arrows in d) and e) show the same crystal direction.

Load-displacement data, along with still images from the video of an *in-situ* indentation, at $\phi = 60°$ are shown in Figure 4.12. Arrows in Fig. 4.12a point to the load-displacement curve at the same time time-stamp as the SEM images in Fig's 4.12b and c. Changes in surface morphology are more subtle than in Fig. 4.11. However, between 12-13 mN (Fig. 4.12c) a small pile-up appears, along with barely visible cracks, correlated with a jump in the load-displacement data (circled in Fig. 4.12c). As before, other jumps in the load-displacement data (marked by asterisks) are associated with the formation of surface features outside the field of view. Fig. 4.12d shows the indenter at final depth (after unloading), with the small pile-up from Fig. 4.12c having reached its final extent. An SEM image of this residual indentation (shown in Fig. 4.12e) reveals behavior that was not seen in Berkovich indentations at $\phi = 60°$, which showed neither pileups nor cracking. Instead, like the indentations at $\phi = 0°$, pileups (although subtle), which terminate at surface steps parallel to the *a*-axes and are bounded by cracks that extend from the surface step to the indentation, form around the indentation. However, because of the orientation, in this case the pileup emanates from the corners of the indenter rather than the edges.

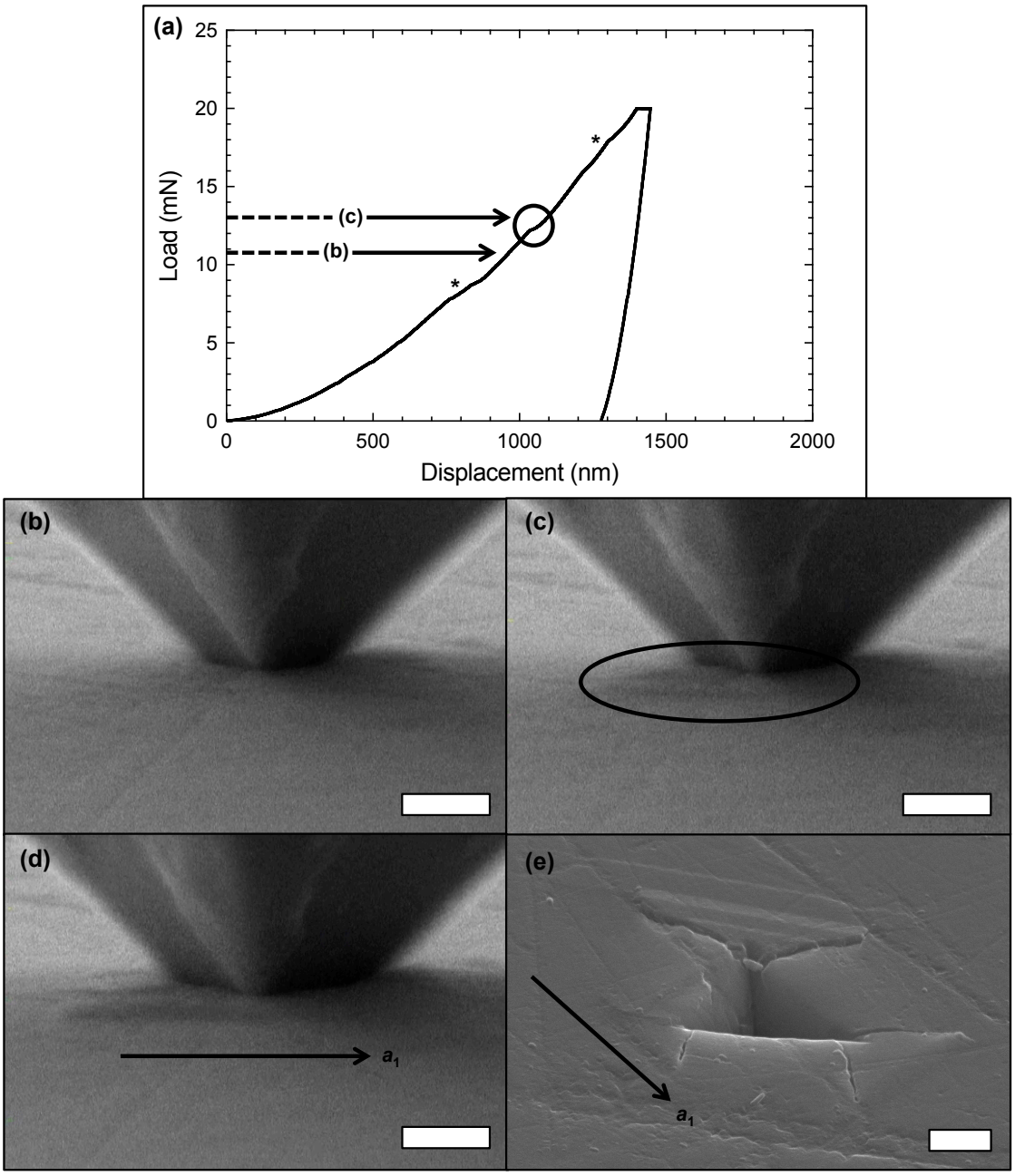


**Figure 4.12:** *In-situ* SEM of cube-corner indentation on (0001) at azimuthal angle $\phi$ = 60˚. a) Load-displacement data and corresponding SEM images of indentation b) before any obvious cracking, and c) right after formation of pileup at ~13 mN. d) Full extent of pile-up at final depth. e) SEM of residual indentation. Black arrows in d) and e) show the same crystal direction.

### 4.3.5. $(10\bar{1}4)$ specimen preparation

Because $\{10\bar{1}4\}$ planes have the lowest surface energy in calcite, they can be nearly atomically smooth upon fracture. Even without polishing, the as-cleaved rhombohedra had surface roughness < 10 nm RMS as measured over a $(30\ \mu m)^2$ area using indenter SFM. Thus, we just used the as-cleaved $(10\bar{1}4)$ faces for indentation experiments.

### 4.3.6. $(10\bar{1}4)$ azimuthal indentation series

For Berkovich indentations on the $(10\bar{1}4)$ facet, the azimuthal angle, $\phi$, was defined as zero when one edge of a residual indentation was parallel to the $[0\bar{4}41]$ direction and as increasing with clockwise rotation of the indenter, as illustrated in Fig. 4c. $\phi$ was varied from 0 to 120° in 10° increments. The full symmetry between the indenter and the $(10\bar{1}4)$ facet is contained within azimuthal angles of 21-81°, but the full 120° of the symmetry of the indenter probe was used to check for possible alignment effects. At each angle, an array of 5 indentations was made to a maximum load of 2.5 mN. As on the (0001) face, this load generates indentations to depths greater than 10 times the RMS surface roughness. A set of dynamic load indentations was made across the same range of azimuthal orientations to a maximum load of 10 mN to determine the effect of applied load on these measurements.

Calculated hardness and modulus for indentations made on the $(10\bar{1}4)$ face at both 2.5 and 10 mN load are plotted as a function of $\phi$ in Figure 4.13. Both are nearly constant with azimuthal orientation. The hardness at 10 mN is slightly (~4%) lower than that at 2.5 mN, consistent with the ISE in Fig. 4.3. The average modulus is 86 GPa, about 23% higher than the lowest value on (0001), and the average hardness at 2.5 mN is 2.5 GPa, about 12% higher than the lowest value on (0001).

As before, the surface topography was measured after these indentations by indenter SFM. Representative images of 10 mN load indents are shown in Figure 4.14.

No signs of pile up or fracture surrounding the residual indentations were seen at any azimuthal orientation.

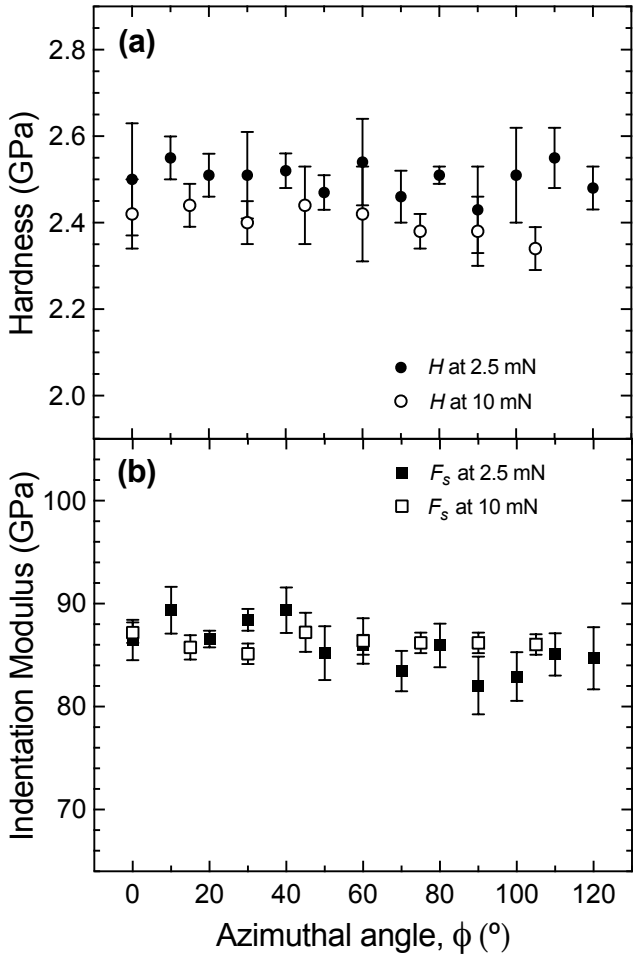


**Figure 4.13:** The hardness ($H$) and indentation modulus ($F_s$) measured on the $(10\bar{1}4)$ face, plotted *vs*. azimuthal angle. Hardness at select azimuthal angles was measured at both 2.5 and 10 mN.

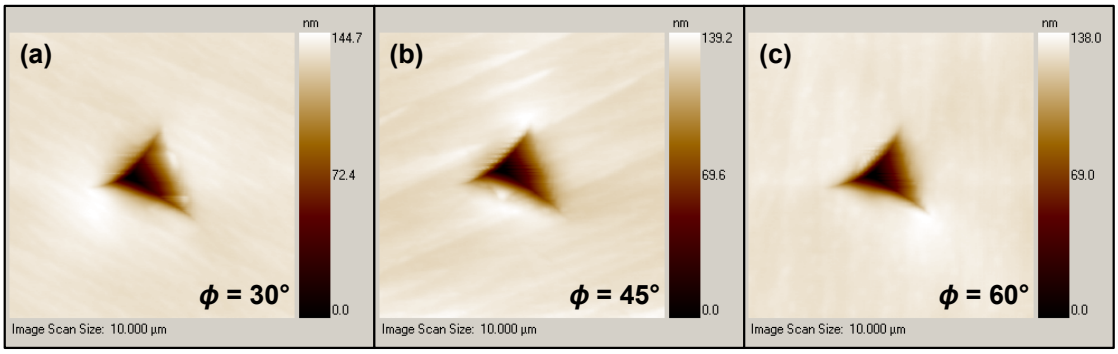


**Figure 4.14:** Indenter SFM scans of the 10 mN indentations made on the $(10\bar{1}4)$ face at $\phi$ = a) 30, b) 45, and c) 60 degrees. Note that no pile-up or cracking is observed at any angle.

## 4.4. DISCUSSION

We showed that the largest fraction (≈ 3 GPa) of the reported variation in the hardness of pure single crystal calcite (Fig. 4.1) is due to the indentation size effect (Fig. 4.3), but that large variations (≈ 1 GPa) remain at a given load. Indentations on the (0001) face show a small (≈ 0.3 GPa) but systematic variation in hardness (Fig. 4.5) with azimuthal angle $\phi$ that is clearly related to a specific interaction between the indenter geometry and the slip systems in the material (Fig's 4.6-8, and 4.10-12). Indentations on the $(10\bar{1}4)$ face show no systematic variation with azimuthal angle. We briefly discuss the ISE, focus in detail on the mechanisms responsible for orientation effects (or lack thereof), and comment briefly on the role of experimental errors in calcite hardness measurements.

### 4.4.1 Indentation size effect

By simply converting published hardness values for pure, defect free, single crystal calcite to Meyer hardness (load/projected area) and plotting as a function of load or depth (Fig. 4.3), we see that, with only a few exceptions (Hangen [14], DiGiosia *et al*. [43], Calvaresi, *et al*. [32], and Barber and Wenk [8]), the data all follow a uniform trend. These include results from bulk geologic [6-14, 17, 18, 22-24, 26, 28, 29, 33, 36-38, 42, 46] and synthetic [21, 27, 32, 36, 40, 43, 44] calcite, and calcite inclusions in limestone [15, 16], which were tested by microindentation using Vickers [7-10, 13, 15, 16, 18, 22, 36, 46] or Knoop [6, 9, 11, 12] indenters, and nanoindentation using a Berkovich indenter [14-17, 21-24, 26-29, 32, 33, 37, 38, 40, 42-44] covering nearly four orders of magnitude in load. The data and fits in Fig. 4.3 thus constitute a "master curve" for the reference hardness of pure single crystal calcite.

Ignoring the outliers ([8, 14, 32, 43]), the data in Fig. 4.3 show a decrease in hardness from ~3.5 GPa at 0.2 mN, to ~1 GPa at 4,900 mN (a ~70% decrease).

Although the magnitude of the ISE is strongly dependent on material (*e.g.* fused quartz shows little to no ISE across a similar load range [58]), the ISE shown in Fig. 4.3 is similar in scale to that in other similar materials. For example, using data reported in two different studies [78, 80] the hardness of aragonite (an orthorhombic $CaCO_3$ polymorph), shows a decrease in hardness between 1 and 2,000 mN of ~60%. For comparison, Qian *et al*., [89] determined the hardness of Cu, stainless steel, NiTi, fused silica, and Si and found total drops in hardness of approximately 80%, 50%, 20%, 25%, and 20%, respectively, in the range from 1 to 5000 mN. They suggest that the ISE may be related to pileup and thus correlated to the *Y/E* (yield stress to modulus) ratio of the material, such that a lower ratio results in a larger total decrease. Indeed, NiTi, fused silica, and Si all have relatively high *Y/E* ratios (> 0.1), and show relatively small total decreases (< 25%). The *Y/E* ratio of calcite (which we estimate to be ~0.01) is similar to that of Cu and stainless steel, which show larger total decreases in hardness of approximately 80% and 50%, respectively. Thus, the magnitude of the ISE that we show for calcite (~70%) in Fig. 4.3 appears to be reasonable.

### 4.4.2. Role of $\{\bar{1}018\}$ twins in deformation, hardness, and indentation modulus on the (0001) face

The presence of the surface step parallel to the *a*-axis direction at the edge of the pileup for indentations on the (0001) face (Fig's 4.6-8, 4.10, 4.11e, 4.12e) indicates that the pileup occurs by slip on a particular slip system. We show that this system is the $\{\bar{1}018\}\langle 404\bar{1}\rangle$ twin system.

For three-sided indenters, at both $\phi = 0°$ and $\phi = 60°$, the *a*-axes lie simultaneously in the sample surface plane, the planes of all three indenter faces, and all three slip planes: $\{\bar{1}018\}$, $\{\bar{1}012\}$, and $\{10\bar{1}4\}$. That is, an edge of an indentation, which is nominally the line of intersection of the sample surface with one of the indenter faces,

is also parallel to the intersection of the $\{\bar{1}012\}$ and $\{10\bar{1}4\}$ slip planes and the $\{\bar{1}018\}$ twin planes with the sample surface. This situation is illustrated in Figure 4.15a, which is a schematic cross-section looking in the $+a_2$-axis direction showing the relationships of the indenter faces at $\phi = 0°$ and edges at $\phi = 60°$ with the slip planes, twin plane, and free surface, on the side of the indentation that faces an (0001)/$\{10\bar{1}4\}$ edge (Fig. 4.4). The situation is the same at each of the three indenter faces and edges.

This configuration leads directly to an explanation for the azimuth-dependent indentation results shown in Fig's 4.5-7, 4.11 and 4.12. It is well known that the stress field under an indenter tip includes a large hydrostatic compressive component [90-92]. At the 0° azimuthal orientation, the $\{\bar{1}018\}$ twin system is ideally oriented with respect to the faces of either indenter to relax that hydrostatic pressure by forming twins that allow blocks of material to move out from under the indenter towards the free surface, as shown schematically in Fig. 4.15b. Note that this configuration produces a step in the surface along the intersection with the $\{\bar{1}018\}$ plane parallel to the $a_2$-axis, just as we see in Fig's 4.6-8, 4.10, and 4.11.

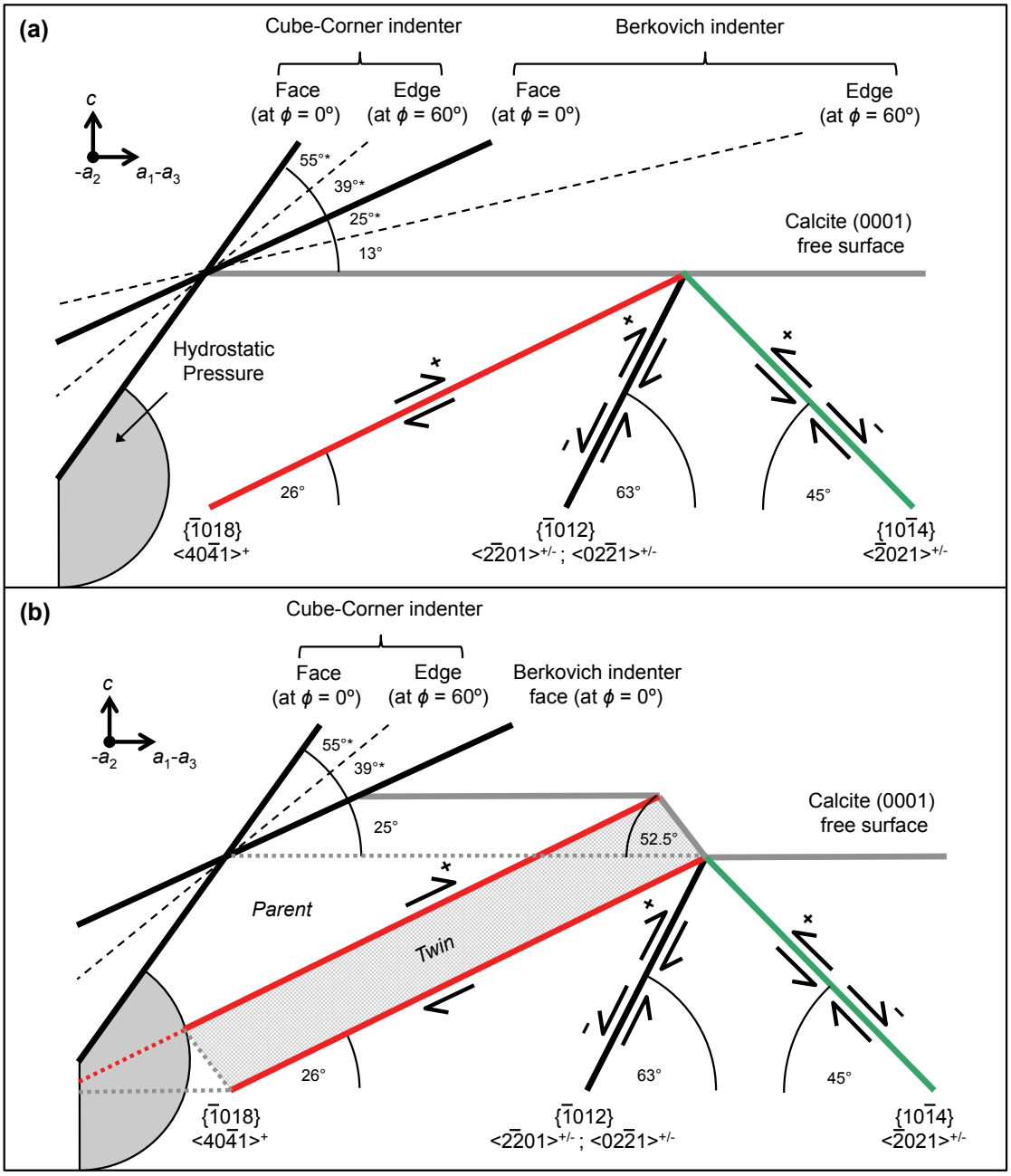


**Figure 4.15:** a) Schematic cross-section of indentation on (0001) showing relative orientations of slip systems and indenter faces (at $\phi = 0°$) and edges (at $\phi = 60°$) between the indenter and the nearest (0001)/$\{10\bar{1}4\}$ facet edges. b) Same as (a) showing how $\{\bar{1}018\}$ twinning can move material to the surface to relieve the stress under the indenter.

The upthrust of material from below the indenter also accounts for the cracking that we see at $\phi = 0°$. Since the indenter face is triangular, a wedge-shaped volume is extruded up from beneath the indenter, as can be seen in Fig's 4.6-8, 4.10, and 4.11. This can only happen if cracks form along the edges of the upthrust material as shown in Figure 4.16a. Indeed, as shown in Fig. 4.9, the overall crack length increases with indentation load and thus simply with the size of the upthrust volume. The *in-situ* experiments reveal how the pileup forms. In the videos, the pile-up (and associated cracks) forms in discrete spurts that are associated with jumps in the load-displacement data. As the indenter sinks in, the accumulated upthrusts lead to the observed pileup.

Analysis of the pileup provides further detail. AFM line scans from 0° indentations made at 2.5 and 10 mN (from Fig. 4.10) are shown at higher magnification in Figure 4.17. The general shape of the two pile-ups is the same. Both consist of a series of sloped regions separated by relatively flat regions (Fig. 4.17a and b). The angles that the sloped regions make with the flat surface were 10–22˚, as determined by fitting straight lines to those regions ($R^2 > 0.98$). Since the twin angle with the surface is 52.5° (Fig. 4.15b), the piled-up surface must be comprised of some distribution of twins separated by untwinned parent material, as illustrated in Figure 4.17c. For example, a regular array of equally sized twins separated by a distance 1.76 times the twin width would create a ~10° incline. Thus, we can estimate that about 36–63% of the volume of the material in the steep regions is twinned, and about 22–38% in the pileups overall.

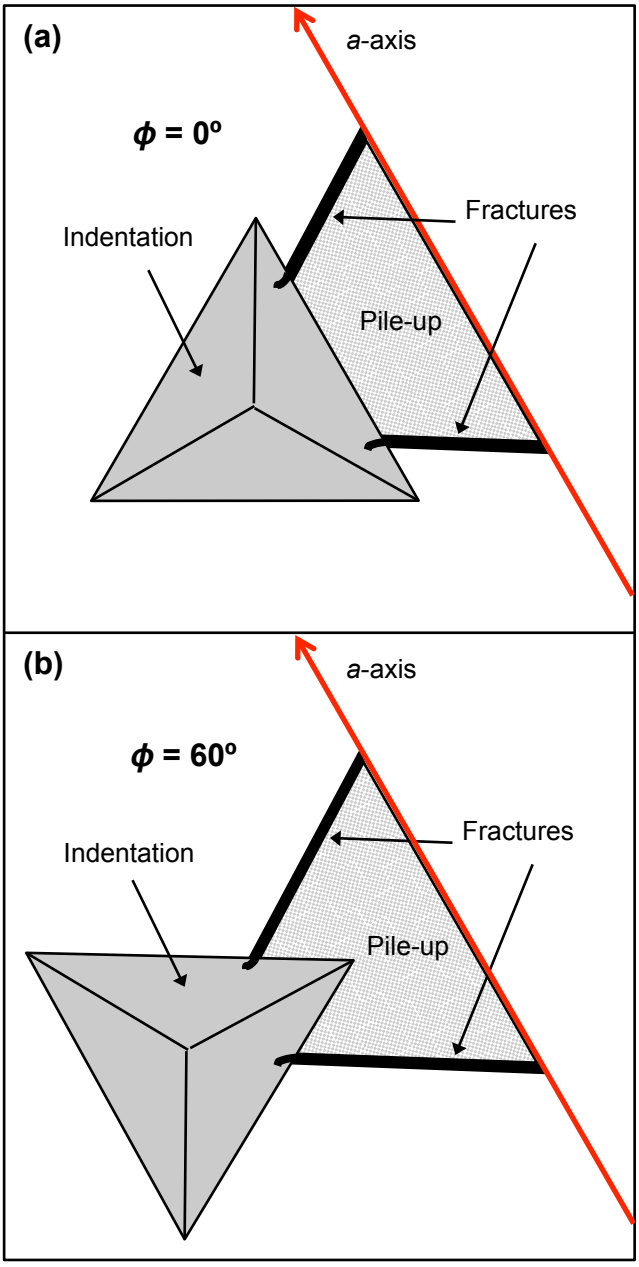


**Figure 4.16:** Schematics showing how upthrust twinning at a) $\phi = 0^{\circ}$ and b) $\phi = 60^{\circ}$ must be accommodated by cracking.

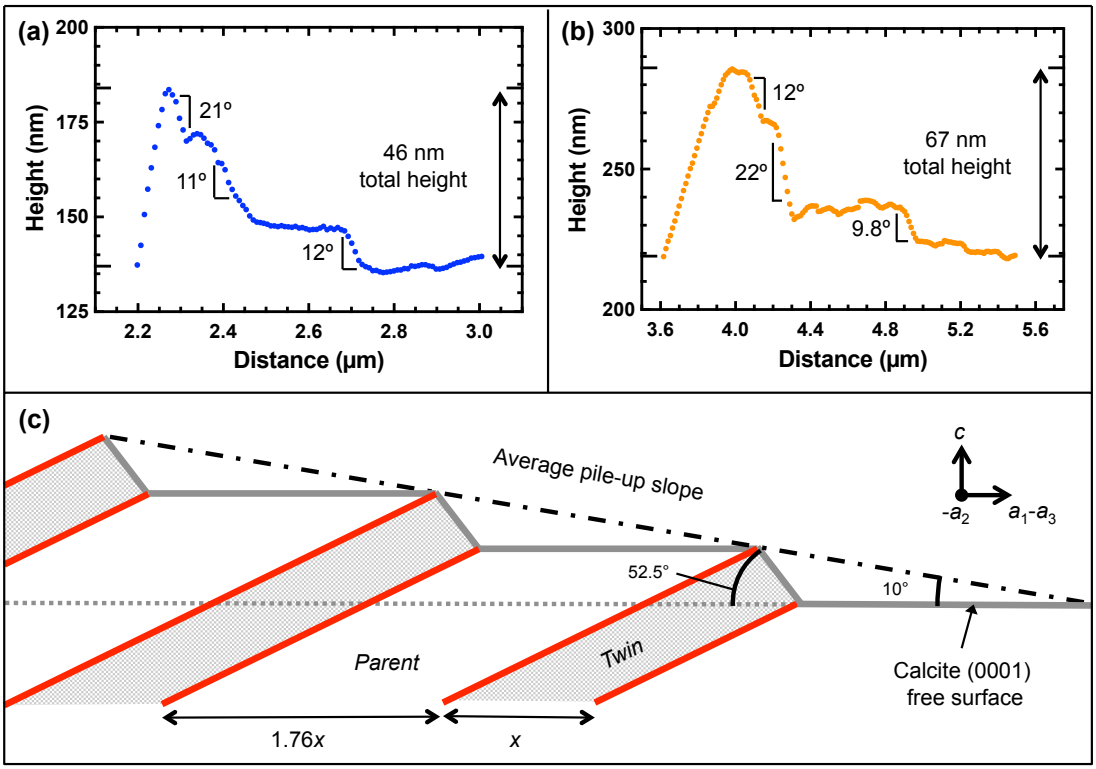


**Figure 4.17:** Magnified AFM line scans from indentations made at a) 2.5 and b) 10 mN load from Fig. 4.7. c) Schematic showing how the measured slopes could be created by an array of twins.

In contrast, Berkovich indentations made at $\phi = 60°$ on the (0001) face show no pileup, no cracks, and no crystallographic steps at either 2.5 or 10 mN load. This can also be easily understood by again considering the orientations of the slip planes adjacent to the indentation, but this time looking at the opposite side of the indentation, *i.e*. the side that faces the corner where two $\{10\bar{1}4\}$ faces meet the (0001) face (Fig. 4.4) as shown in Figure 4.18. In this case we are looking along the indenter faces at $\phi = 60°$ and perpendicular to the indenter edges at $\phi = 0°$. In this case, the $\{\bar{1}018\}$ system cannot efficiently relieve the hydrostatic stress of the indentation. Instead, slip on the more difficult $\{10\bar{1}4\}$ and $\{\bar{1}012\}$ planes must occur. Although the $\{10\bar{1}4\}$ plane appears to be favorably oriented for a similar upthrust, the fact that the CRSS is 20x higher than that on $\{\bar{1}018\}$ must prevent this. Since there is no twinning and no upthrust, there is no pileup and no cracking.

The influence of the twin planes is emphasized in Fig. 4.12e, where twinning, pileup (albeit small), and cracking are seen, even at the 60° orientation, after a 20 mN indentation with the cube corner indenter. Crystallographically, the pileup morphology is identical to the situation at 0°, but the pileup, twins, and cracks are now in front of the edges of the indenter (corners of the indentation) rather than the faces (edges of the indentation), as shown schematically in Figure 4.16b. As evident in Fig. 4.15, while the Berkovich indenter edge angle is apparently low enough to prevent upthrusts due to twinning from forming (Fig's 4.6 and 4.7), the edges of the cube corner indenter make a much higher angle with the sample surface, allowing twins to form in front of the indentation corners (Fig. 4.12e and Fig. 4.16b).

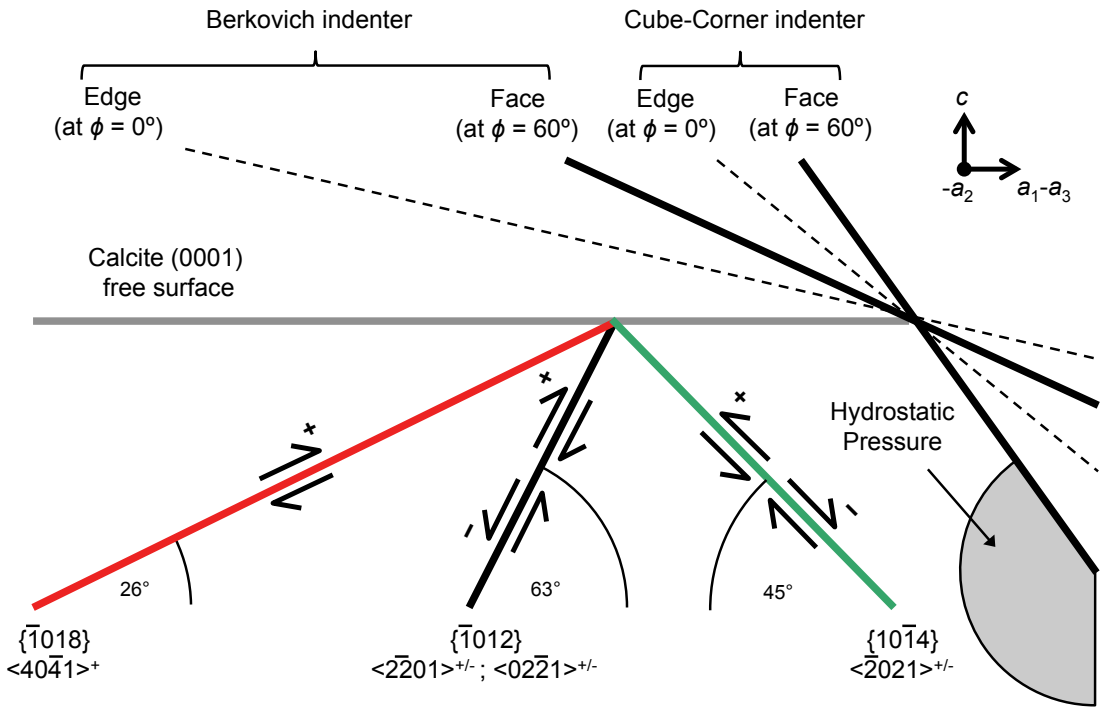


**Figure 4.18:** Schematic cross-section of indentation on (0001) showing relative orientations of slip systems and indenter faces ($\phi = 60^{\circ}$) and edges ($\phi = 0^{\circ}$) between the indenter and the facet corner formed by the intersection of the (0001)/$\{10\bar{1}4\}$ facet edges. Note that the slip on $\{\bar{1}018\}$ could *not* twin material towards the free surface.

The variation in hardness with azimuthal angle $\phi$ shown in Fig. 4.5 can now be understood as follows: At $\phi = 0°$, all three indenter faces are oriented such that the hydrostatic pressure of the indentation can be partially relieved by simple upthrust of the material by $\{\bar{1}018\}$ twinning. Because the CRSS for $\{\bar{1}018\}$ twinning is much less ($\approx$ 1/20) than the CRSS values for the remaining $\{10\bar{1}4\}$ and $\{\bar{1}012\}$ slip systems [83], this reduces the total force needed to achieve a certain amount of indentation deformation, and thus the hardness, compared to $\phi = 60°$, where significant twinning does not occur. These simple twin shears cannot provide all of the deformation required to form the indentation since extensive 3-D plasticity is required. This, in turn, requires dislocation motion on the much more difficult $\{10\bar{1}4\}$ and $\{\bar{1}012\}$ slip systems, and since this deformation occurs in parallel with twinning, the overall reduction in hardness is small.

Crack formation is correlated with the reduction in hardness, but it is not clear what role the cracks that we see (Fig's 4.7 and 4.8) play in the hardness variations shown in Fig. 4.5. It is important to realize that these cracks are *not* the typical cracks that are associated with indentation processes [87, 93]. It is well known that there is a load threshold for indentation cracking in brittle materials that arises because of the differences in the rate of growth of plastic work and fracture energy with indentation size [94, 95]. Such indentation cracks are driven by the stresses surrounding the indentation and have typical shapes and locations that depend on the properties of the material being indented, the shape of the indenter, and other factors [87]. Although our cracks appear somewhat similar to typical radial indentation cracks [93], they are not: They have either no or a very low threshold, and increase steadily with increasing load (Fig. 4.9), while radial cracks typically have a marked initiation threshold [94, 95]; they do not emerge at indentation corners where the stresses that lead to radial cracks are highest [90]; and they form on loading (Fig's 4.11 and 4.12, video online) while

radial cracks typically form on unloading [93]. Furthermore, they are orientation dependent in that they do not appear at $\phi = 60°$, yet the cracks that we see at $\phi = 0°$ are not facetted, as they would be if a low-energy cleavage plane was facilitating fracture [11]. Thus, it appears that the indentation loads imposed in these experiments are well below the threshold for normal indentation fracture, even for the cube corner indentations at 20 mN. Instead cracks form simply to accommodate the twins. We attribute the scatter in the data, which is larger near $\phi = 0°$ than $\phi = 60°$ to the variability in the extent of twinning, pileup, and cracking among indentations at the same load (Fig. 4.5).

Although small (≈ 12%), the variation in hardness we see with the three-sided Berkovich indenter is undoubtedly larger than would be seen at similar loads with a four-sided Vickers or Knoop indenter. While the face angles for these indenters are similar, only one face at a time is perfectly oriented for twinning. However, it is interesting to note that, for the Berkovich indenter, significant twinning occurs (Fig. 4.6) and the hardness is significantly reduced (Fig. 4.5) over a range of azimuthal angles spanning at least ± 15° from $\phi = 0°$. For a Vickers indenter, two faces are 15° from the ideal orientation every 30° in $\phi$. Whether this allows enough displacement to form $\{\bar{1}018\}$ twin upthrusts at those orientations is unknown. But because only part of the indentation can twin and because the effects occur over a range in $\phi$, little azimuthal variation would be expected.

Finally, we note that the trend in indentation modulus is the opposite of that in hardness (Fig. 4.5). Because cracks increase compliance, the modulus variation must be an artifact. Due to pileup, the contact area between the indenter and the sample is larger near $\phi = 0°$ than is predicted by the Oliver and Pharr analysis, leading to increased contact stiffness, which is then interpreted as an increased modulus. For determining contact area, the important dimension of the pile-up here is the horizontal

distance from where the surface profile inside the residual indentation meets the original sample surface, to the peak of the pile-up (*e.g.*, the distance between the X's in Fig. 4.10b and d). At 2.5 and 10 mN (Fig's 4.10a and b), the average of these distances for the three pile-up lobes is 83 and 285 nm, respectively. By approximating the contact perimeter as a semi-ellipse [96] we estimate that the true contact areas are 21 and 33% greater than the Oliver-Pharr calculated contact areas, and that the true moduli are 9 and 13% lower, at 2.5 and 10 mN, respectively. The corrected values at $\phi$ = 0° are 72 and 68 GPa (half-filled squares in Fig. 4.5), close to the average value of 69-70 GPa measured at $\phi$ = 60° where there is no pile-up and no need for contact area correction. We expect that the effect of correcting all contact areas would be to reduce the variation in modulus with $\phi$, such that the average modulus measured at any $\phi$ on the (0001) face would be ~68-72 GPa. Correcting the contact area also affects the hardness. At 2.5 and 10 mN, the corrected hardnesses at $\phi$ = 0° are 17 and 25% lower (half-filled circles in Fig. 4.5). Hence, the effect of correcting all contact areas would be to significantly *increase* the variation in hardness with $\phi$ .

### 4.4.3. Deformation, hardness, and indentation modulus on the $(10\bar{1}4)$ face

In contrast to the 3-fold rotational symmetry of the (0001) face, the $(10\bar{1}4)$ face of calcite has no rotational symmetry. Hence, the orientation of the slip systems relative to each indenter face is unique at all azimuthal angles, regardless whether a 3- or 4-sided indenter is used. Furthermore, the Burgers vectors for two of the three twin systems are parallel to the $(10\bar{1}4)$ face so only the $(\bar{1}018)$ plane can twin in the way described above (Figure 4.4a).

Accordingly, we see no evidence of pile-up or fracture at any azimuthal angle for Berkovich indentations the $(10\bar{1}4)$ face, and our hardness and modulus results (Fig. 4.13) show no significant variation with $\phi$. Interestingly, the average value of hardness

across all azimuthal angles on $(10\bar{1}4)$ matches the average hardness measured at the 60° orientation on (0001), for which $\{\bar{1}018\}$ twinning is suppressed. Furthermore, in the absence of pileup, the modulus artifact seen for indentations on the (0001) face does not appear for indentations on the $(10\bar{1}4)$ face.

### 4.4.4 Comparison of hardness on the (0001) and $(10\bar{1}4)$ faces

To describe the plastic anisotropy in our results, we develop a simple model based on concepts proposed by Daniels and Dunn [97] and elaborated by Brookes, O'Neill, and Redfern [62]. The stress state under an indenter is quite inhomogeneous and complex. However, for the upthrusts that we see (Fig's 4.6 & 4.10) a slip system that allows rotation about an axis parallel to the edge of the indentation (*i.e.* to both the adjacent indenter face and the sample surface) is required. The $\{\bar{1}018\}$ twin system provides this uniquely at all three indenter faces when $\phi = 0°$. We assume that there is an effective resolved stress, $\tau_{\text{eff}}$, at which this slip system operates and that this stress varies as the cosine of the angle between the edge of the indentation and the rotation axis, which is, according to our definition, just $\phi$. Thus, slip occurs when some measure of the local applied stress, $\sigma$, satisfies $\tau_{\text{eff}} = \sigma\cos(\phi)$ [62, 97]. Although $\sigma$ is very inhomogeneous, we know that it is simply proportional to $H$ at every point. We can then write,

$$H = H^* - S\cos(\phi), \tag{4.1}$$

where $H^*$ and $S$ are fitting parameters.

Separate fits of Equation 4.1 to the hardness data at 2.5 mN on the (0001) face between $\phi$ = 0-60° and $\phi$ = 60-120° are shown in Figure 4.19 and return $S = 0.51$, and $H^* = 2.7$ or 2.8 GPa, respectively.

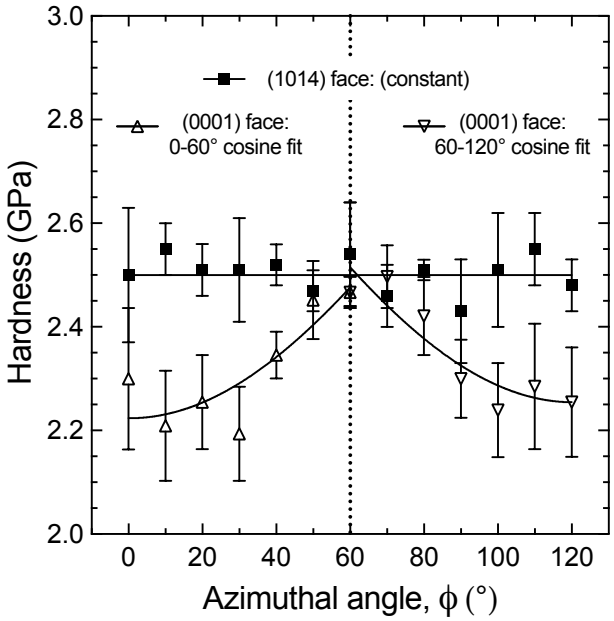


**Figure 4.19:** Plot comparing hardness on the (0001) and $(10\bar{1}4)$ faces as a function of $\phi$. $H(\phi)$ on (0001) is well described by a simple form relating the twin directions to the indenter geometry (Fit of Eq. 4.1 to the data shown). $H \neq f(\phi)$ on the $(10\bar{1}4)$ face; average value shown. In the absence of twinning the hardness is independent of both face and azimuth.

The hardness data at 2.5 mN on the $(10\bar{1}4)$ face are also reproduced in Fig. 4.19. Since there are no orientations with extensive $\{\bar{1}018\}$ twinning on this face, we simply represent those data with a horizontal line at the average hardness value of 2.5 GPa. The fits to the (0001) hardness data intersect the constant $(10\bar{1}4)$ hardness at $\phi = 60°$. Hence, we conclude that, at 2.5 mN, calcite has a hardness of 2.5 ± 0.07 GPa, that is independent of orientation and mostly determined by deformation on the $\{10\bar{1}4\}$ and $\{\bar{1}012\}$ slip systems, except for "special" indenter/crystal orientations where slip on $\{\bar{1}018\}$ planes is facilitated.

### 4.4.5. A comment on the indentation modulus

The measured indentation modulus is ~23% higher on the $(10\bar{1}4)$ face (86 +/- 2 GPa) than on the (0001) face (70 +/-2 GPa at $\phi = 60°$). In general, the indentation modulus for contact between a Berkovich diamond and an anisotropic single crystal is some complicated and unknown function of the elastic constants [65]. For comparison, we calculated Young's modulus as a function of orientation (see Appendix, Section 4.8 for details) using reported elastic constants for calcite [98]. Interestingly, the calculated Young modulus perpendicular to $\{10\bar{1}4\}$ planes (53 GPa) is actually ~9% *lower* than that perpendicular to (0001) (58 GPa). Although this may seem counterintuitive, the indentation modulus is determined by deformation in all directions in the crystal and the model by Vlassak, *et al*., shows that the indentation modulus does not necessarily scale with the Young modulus, especially for highly anisotropic crystals [65]—and calcite is certainly anisotropic; the Poisson ratio is even negative in certain crystal directions close to the normal to $\{10\bar{1}4\}$ [99]. This illustrates that Young's modulus is not a good surrogate for the indentation modulus. Indeed, the indentation moduli are much closer to the average of Young's modulus

over all directions, which is 74 GPa. (Note that the Young moduli normal to both $\{10\bar{1}4\}$ and (0001) are much lower than the maximum value in calcite, 144 GPa.)

### 4.4.6. Interpreting the calcite hardness literature

As discussed in the introduction, after the ISE is accounted for, a consistent ~1 GPa range in reported hardness at any given load or depth remains (Fig. 4.3). Our present results (Fig. 4.19) suggest that, at least for a Berkovich indenter at relatively low loads, anisotropy accounts for only a small fraction (0.3 GPa, ~33%) of the remaining variation. The reasoning above suggests that variations will be even smaller for Vickers or Knoop indenter geometries. What then, accounts for the remaining variations beyond the ISE in Fig. 4.3? Three obvious choices are additional experimental variables, fracture, and experimental errors.

We have made the assumption, based on the descriptions in the published papers, that the material in the studies compiled in Fig. 4.3 is consistently pure, defect-free calcite. Additional variables such as temperature and load rate are well known to affect hardness results, but all the tests in Fig. 4.3 were performed at room temperature, and while load rates are rarely recorded, we presume that common experimental rates were used. As described above, fracture occurs during indentation of brittle materials above a threshold load. It is conceivable that fracture generates additional hardness anisotropy, but this topic is beyond the scope of the present paper. Finally, it is well-known that indentation results are prone to errors [100]. For imaging tests (*e.g.* Vickers, Knoop), accurate measurement of the residual indentation area becomes more difficult as indentation size decreases since the resolution of the imaging system is constant. For depth-sensing nanoindentation tests, a variety of calibration errors (tip shape and machine compliance) [100], as well as additional compliance in the sample mount (as shown in Chapter 5), can play a significant role.

With these points in mind, we can speculate about the quality of the data Fig. 4.3. While we may not know the sources of errors in those studies, there is at least enough data that potential outliers can be identified.

## 4.5. SUMMARY AND CONCLUSIONS

Published values for the hardness of single-crystal calcite are widely scattered, for both pure and defect free crystals (1–4 GPa) and for biogenic or synthetic crystals with occlusions known to strengthen the material (2–7 GPa). As a result, it has been difficult to make quantitative statements about the strength of calcite or of the effectiveness of possible strengthening mechanisms. By plotting the results of 42 studies reporting the hardness of pure, defect free calcite as a function of the load used in those studies, we are able to show that the majority of the scatter in those data can be explained by the indentation size effect. These data provide a "master curve" for the hardness of calcite varies from about 3.5 GPa at 0.2 mN indentation load to about 1 GPa at 4900 mN indentation load.

We hypothesized that the remaining 1 GPa of variation at any given load in this literature might be due to anisotropy effects, as calcite is very anisotropic and orientation in hardness tests is only rarely controlled or reported. We conducted nanoindentation tests as a function of azimuthal angle $\phi$ on both $(10\bar{1}4)$ and (0001) faces at various loads using both Berkovich and cube corner tips and found that the nominal hardness and indentation modulus vary significantly with $\phi$ on the (0001) face but that there was no $\phi$ dependence on the $(10\bar{1}4)$ face. Careful examination of the surface topography both *post facto* and *in-situ* during indentation, along with an analysis of the geometry and available slip systems allowed us to conclude that there are particular orientations on the (0001) face where $\{\bar{1}018\}$ twinning is facilitated, leading to lower hardness, pileup, and cracking. When corrected for pileup effects, the

variations in hardness with $\phi$ are even larger, but the variations in the indentation modulus are eliminated. At $\phi$ angles where twinning does not occur on the (0001) face, the hardness is the same as that measured at any $\phi$ on the $(10\bar{1}4)$ face, where twinning was never observed. Thus, despite a high degree of anisotropy, careful attention to experimental detail gives a nanoindentation (Meyer) hardness for calcite at 2.5 mN load of 2.5 ± 0.07 GPa, independent of orientation, outside the range of azimuthal angles where twins form.

The indentation modulus on the $(10\bar{1}4)$ face (86 +/-2 GPa) is 23% *higher* than that on the (0001) face at angles where twins do not appear (70 +/- 2 GPa), but Young's modulus values calculated from elastic constants are lower on the $(10\bar{1}4)$ face (53 GPa) than on the (0001) face (58 GPa), indicating that the indentation modulus is not a good surrogate for the Young modulus. The largest Young's modulus (144 GPa) is much higher than either of these calculated values.

Our measured anisotropy effect accounts for only about a third of the reported scatter that remains in the published calcite hardness data once the indentation size effect is taken into account. We thus conclude that the remaining variations are due to experimental error, or unreported differences in testing conditions or sample quality. Careful experimentation, using the master curve to account for the effects of load (ISE), and paying attention to changes in deformation mechanism (twinning) should allow researchers to make much more quantitative analysis based on calcite hardness data.

## 4.6. ACKNOWLEDGMENTS

This work was supported by the National Science Foundation (NSF) via the Materials World Network grant (DMR-1210304). We also acknowledge support from NSF (DMR 0845212), the J.D. Watson Investigator Program (NYSTAR Contract #C050017), the Cornell Center for Materials Research (CCMR), a Materials Research Science and Engineering Center of the National Science Foundation (DMR 1120296), the GI Bill (Chapter 33), Hysitron Inc., and Engineering Learning Initiatives (Cornell College of Engineering). The authors would like to thank Ryan Major, Oden Warren, and Syed Asif of Hysitron, Inc. for helpful discussions regarding the *in-situ* experiments.

## 4.7. REFERENCES


1. De Muynck, W., N. De Belie, and W. Verstraete, *Microbial carbonate precipitation in construction materials: A review*. Ecological Engineering, 2010. **36**(2): p. 118-136.

2. Matschei, T., B. Lothenbach, and F.P. Glasser, *The role of calcium carbonate in cement hydration*. Cement and Concrete Research, 2007. **37**(4): p. 551-558.

3. Carretero, M.I. and M. Pozo, *Clay and non-clay minerals in the pharmaceutical and cosmetic industries Part II. Active ingredients*. Applied Clay Science, 2010. **47**(3-4): p. 171-181.

4. Bachu, S., *Sequestration of CO2 in geological media: criteria and approach for site selection in response to climate change*. Energy Conversion and Management, 2000. **41**(9): p. 953-970.

5. Gale, J.F.W., R.M. Reed, and J. Holder, *Natural fractures in the Barnett Shale and their importance for hydraulic fracture treatments*. AAPG Bulletin, 2007. **91**(4): p. 603-622.

6. Winchell, H., *The knoop microhardness tester as a mineralogical tool*. American Mineralogist, 1945. **30**(9-10): p. 583-595.

7. Taylor, E.W., *Correlation of the Mohs's scale of hardness with the Vickers's hardness numbers*. Mineralogical Magazine, 1949. **28**: p. 718-721.

8. Barber, D.J. and H.R. Wenk, *Deformation twinning in calcite, dolomite, and other rhombohedral carbonates*. Physics and Chemistry of Minerals, 1979. **5**(2): p. 141-165.

9. Pandya, J.R. and L.J. Bhagia, *Comparison of knoop and vickers hardness numbers on calcite cleavages*. Indian Journal of Pure & Applied Physics, 1984. **22**(7): p. 439-440.

10. Carter, G.M., J.L. Henshall, and R.J. Wakeman, *Influence of surfactants on the mechanical-properties and comminution of wet-milled calcite*. Powder Technology, 1991. **65**(1-3): p. 403-410.

11. Wong, T.Y. and R.C. Bradt, *Microhardness anisotropy of single-crystals of calcite, dolomite and magnesite on their cleavage planes*. Materials Chemistry and Physics, 1992. **30**(4): p. 261-266.

12. Carter, G.M., J.L. Henshall, and R.J. Wakeman, *Knoop-hardness and fracture anisotropy of calcite*. Journal of Materials Science Letters, 1993. **12**(6): p. 407-410.

13. Wakeman, R.J., J.L. Henshall, and G.M. Carter, *Solution environment effects on the hardness and toughness of calcite during grinding*. Chemical Engineering Research & Design, 1993. **71**(A4): p. 361-370.

14. Hangen, U.D., *A comparision of nano-hardness and scratch-resistance on Mohs minerals*. Zeitschrift Fur Metallkunde, 2001. **92**(9): p. 1074-1077.

15. Beste, U. and S. Jacobson, *Micro scale hardness distribution of rock types related to rock drill wear*. Wear, 2003. **254**(11): p. 1147-1154.

16. Broz, M.E., R.F. Cook, and D.L. Whitney, *Microhardness, toughness, and modulus of Mohs scale minerals*. American Mineralogist, 2006. **91**(1): p. 135-142.

17. Zugner, S., K. Marquardt, and I. Zimmermann, *Influence of nanomechanical crystal properties on the comminution process of particulate solids in spiral jet mills*. European Journal of Pharmaceutics and Biopharmaceutics, 2006. **62**(2): p. 194-201.

18. Griesshaber, E., et al., *Crystallographic texture and microstructure of terebratulide brachiopod shell calcite: An optimized materials design with hierarchical architecture*. American Mineralogist, 2007. **92**(5-6): p. 722-734.

19. Perez-Huerta, A., et al., *Material properties of brachiopod shell ultrastructure by nanoindentation*. Journal of the Royal Society Interface, 2007. **4**(12): p. 33-39.

20. Lee, S.W., G.H. Kim, and C.S. Choi, *Characteristic crystal orientation of folia in oyster shell, Crassostrea gigas*. Materials Science & Engineering C-Biomimetic and Supramolecular Systems, 2008. **28**(2): p. 258-263.

21. Ma, Y., et al., *Sea urchin tooth design: An "All-Calcite" polycrystalline reinforced fiber composite for grinding rocks*. Advanced Materials, 2008. **20**(8): p. 1555-+.

22. Schmahl, W.W., et al., *Hierarchical fibre composite structure and micromechanical properties of phosphatic and calcitic brachiopod shell biomaterials - an overview*. Mineralogical Magazine, 2008. **72**(2): p. 541-562.

23. Merkel, C., et al., *Mechanical properties of modern calcite- (Mergerlia truncata) and phosphate-shelled brachiopods (Discradisca stella and Lingula anatina) determined by nanoindentation*. Journal of Structural Biology, 2009. **168**(3): p. 396-408.

24. Kim, Y.Y., et al., *Bio-Inspired Synthesis and Mechanical Properties of Calcite-Polymer Particle Composites*. Advanced Materials, 2010. **22**(18): p. 2082-+.

25. Moureaux, C., et al., *Structure, composition and mechanical relations to function in sea urchin spine*. Journal of Structural Biology, 2010. **170**(1): p. 41-49.

26. Presser, V., et al., *Determination of the elastic modulus of highly porous samples by nanoindentation: a case study on sea urchin spines*. Journal of Materials Science, 2010. **45**(9): p. 2408-2418.

27. Kim, Y.Y., et al., *An artificial biomineral formed by incorporation of copolymer micelles in calcite crystals*. Nature Materials, 2011. **10**(11): p. 890-896.

28. Raman, S. and R. Kumar, *Construction and nanomechanical properties of the exoskeleton of the barnacle, Amphibalanus reticulatus*. Journal of Structural Biology, 2011. **176**(3): p. 360-369.

29. Bandini, A., et al., *Effects of intra-crystalline microcracks on the mechanical behavior of a marble under indentation*. International Journal of Rock Mechanics and Mining Sciences, 2012. **54**: p. 47-55.

30. Kunitake, M.E., S.P. Baker, and L.A. Estroff, *The effect of magnesium substitution on the hardness of synthetic and biogenic calcite*. MRS Communications, 2012. **2**(3): p. 113-116.

31. Schneider, A.S., et al., *Hierarchical super-structure identified by polarized light microscopy, electron microscopy and nanoindentation: Implications for the limits of biological control over the growth mode of abalone sea shells*. Bmc Biophysics, 2012. **5**.

32. Calvaresi, M., et al., *Morphological and mechanical characterization of composite calcite/SWCNT-COOH single crystals*. Nanoscale, 2013. **5**(15): p. 6944-6949.

33. Kunitake, M.E., et al., *Evaluation of strengthening mechanisms in calcite single crystals from mollusk shells*. Acta Biomaterialia, 2013. **9**(2): p. 5353-5359.

34. Lemloh, M.L., et al., *Low Mg/Ca ratio alters material properties in sea urchin larvae skeleton*. Bioinspired Biomimetic and Nanobiomaterials, 2013. **2**(1): p. 28-34.

35. Muller, W.E.G., et al., *The enzyme carbonic anhydrase as an integral component of biogenic Ca-carbonate formation in sponge spicules*. Febs Open Bio, 2013. **3**: p. 357-362.

36. Olson, I.C., et al., *Crystal lattice tilting in prismatic calcite*. Journal of Structural Biology, 2013. **183**(2): p. 180-190.

37. Goetz, A.J., et al., *Tailored order: The mesocrystalline nature of sea urchin teeth*. Acta Biomaterialia, 2014. **10**(9): p. 3885-3898.

38. Li, L. and C. Ortiz, *Pervasive nanoscale deformation twinning as a catalyst for efficient energy dissipation in a bioceramic armour*. Nature Materials, 2014. **13**(5): p. 501-507.

39. Metzger, T.H., et al., *Nanostructure of Biogenic Calcite and Its Modification under Annealing: Study by High-Resolution X-ray Diffraction and Nanoindentation*. Crystal Growth & Design, 2014. **14**(10): p. 5275-5282.

40. Muller, W.E.G., et al., *The sponge silicatein-interacting protein silintaphin-2 blocks calcite formation of calcareous sponge spicules at the vaterite stage*. RSC Advances, 2014. **4**(6): p. 2577-2585.

41. Fitzer, S.C., et al., *Ocean acidification alters the material properties of Mytilus edulis shells*. Journal of the Royal Society Interface, 2015. **12**(103).

42. Lv, J.L., Y.G. Jiang, and D.Y. Zhang, *Structural and Mechanical Characterization of Atrina Pectinata and Freshwater Mussel Shells*. Journal of Bionic Engineering, 2015. **12**(2): p. 276-284.

43. Giosia, M.D., et al., *Bioinspired Nanocomposites: Ordered 2D Materials Within a 3D Lattice*. Advanced Functional Materials, 2016.

44. Kim, Y.Y., et al., *Structure and Properties of Nanocomposites Formed by the Occlusion of Block Copolymer Worms and Vesicles Within Calcite Crystals*. Advanced Functional Materials, 2016. **26**(9): p. 1382-1392.

45. Kim, Y.-Y., et al., *Tuning hardness in calcite by incorporation of amino acids*. Nature materials, 2016.

46. Metzler, R.A., et al., *Composition and Structure of Oyster Adhesive Reveals Heterogeneous Materials Properties in a Biological Composite*. Advanced Functional Materials, 2016. **26**(37): p. 6814-6821.

47. Chen, G.W., et al., *Vertically oriented structure and its fracture behavior of the Indonesia white-pearl oyster*. Journal of the Mechanical Behavior of Biomedical Materials, 2017. **66**: p. 211-223.

48. Wang, R.Z., L. Addadi, and S. Weiner, *Design strategies of sea urchin teeth: Structure, composition and micromechanical relations to function*. Philosophical Transactions of the Royal Society of London Series B-Biological Sciences, 1997. **352**(1352): p. 469-480.

49. Beniash, E., et al., *Elevated level of carbon dioxide affects metabolism and shell formation in oysters Crassostrea virginica*. Marine Ecology Progress Series, 2010. **419**: p. 95-108.

50. Lee, S.W., et al., *Mechanical characteristics and morphological effect of complex crossed structure in biomaterials Fracture mechanics and microstructure of chalky layer in oyster shell*. Micron, 2011. **42**(1): p. 60-70.

51. Dickinson, G.H., et al., *Interactive effects of salinity and elevated CO2 levels on juvenile eastern oysters, Crassostrea virginica*. Journal of Experimental Biology, 2012. **215**(1): p. 29-43.

52. Ivanina, A.V., et al., *Interactive effects of elevated temperature and CO2 levels on energy metabolism and biomineralization of marine bivalves Crassostrea virginica and Mercenaria mercenaria*. Comparative Biochemistry and Physiology a-Molecular & Integrative Physiology, 2013. **166**(1): p. 101-111.

53. Lombardi, S.A., et al., *Shell Hardness and Compressive Strength of the Eastern Oyster, Crassostrea virginica, and the Asian Oyster, Crassostrea ariakensis*. Biological Bulletin, 2013. **225**(3): p. 175-183.

54. Li, H.Y., et al., *Calcite Prisms from Mollusk Shells (Atrina Rigida): Swiss-cheese-like Organic-Inorganic Single-crystal Composites*. Advanced Functional Materials, 2011. **21**(11): p. 2028-2034.

55. Aizenberg, J. and G. Hendler, *Designing efficient microlens arrays: lessons from Nature*. Journal of Materials Chemistry, 2004. **14**(14): p. 2066-2072.

56. Sangwal, K., *Review: Indentation size effect, indentation cracks and microhardness measurement of brittle crystalline solids - some basic concepts and trends*. Crystal Research and Technology, 2009. **44**(10): p. 1019-1037.

57. Bull, S.J., *On the origins and mechanisms of the indentation size effect*. Zeitschrift Fur Metallkunde, 2003. **94**(7): p. 787-792.

58. Nix, W.D. and H.J. Gao, *Indentation size effects in crystalline materials: A law for strain gradient plasticity*. Journal of the Mechanics and Physics of Solids, 1998. **46**(3): p. 411-425.

59. Kim, J.Y., et al., *Influence of surface-roughness on indentation size effect*. Acta Materialia, 2007. **55**(10): p. 3555-3562.

60. Swain, M.V. and M. Wittling, *Indentation size effects for ceramics: Is there a fracture mechanics explanation?* Fracture Mechanics of Ceramics, Vol 11: R-Curve Behavior, Toughness Determination, and Thermal Shock, ed. R.C. Bradt, et al. Vol. 11. 1996, New York: Plenum Press Div Plenum Publishing Corp. 379-387.

61. Quinn, G.D., *Indentation size effect for glasses: Yes, there is a fracture contribution*. Active Materials, Nanoscale Materials, Composites, Glass and Fundamentals, ed. R.C. Bradt, et al. Vol. 14. 2005, New York: Springer. 149-171.

62. Brookes, C.A., J.B. Oneill, and B.A.W. Redfern, *Anisotropy in hardness of single crystals*. Proceedings of the Royal Society of London Series a-Mathematical and Physical Sciences, 1971. **322**(1548): p. 73-&.

63. Kiely, J.D. and J.E. Houston, *Nanomechanical properties of Au (111), (001), and (110) surfaces*. Physical Review B, 1998. **57**(19): p. 12588-12594.

64. Mante, F., G.R. Baran, and B. Lucas, *Nanoindentation studies of titanium single crystals*. Biomaterials, 1999. **20**(11): p. 1051-1055.

65. Vlassak, J.J. and W.D. Nix, *Measuring the elastic properties of anisotropic materials by means of indentation experiments*. Journal of the Mechanics and Physics of Solids, 1994. **42**(8): p. 1223-1245.

66. Zambaldi, C., C. Zehnder, and D. Raabe, *Orientation dependent deformation by slip and twinning in magnesium during single crystal indentation*. Acta Materialia, 2015. **91**: p. 267-288.

67. Hay, J.C., et al., *Elastic anisotropy of beta-silicon nitride whiskers*. Journal of the American Ceramic Society, 1998. **81**(10): p. 2661-2669.

68. Raynes, A.S., et al., *Fracture-toughness of YBa2Cu3O6+delta single-crystals - Anisotropy and twinning effects*. Journal of Applied Physics, 1991. **70**(10): p. 5254-5257.

69. Rowcliffe, D.J. and G.E. Hollox, *Hardness anisotropy, deformation mechanisms and brittle-to-ductile transition in carbides*. Journal of Materials Science, 1971. **6**(10): p. 1270-+.

70. Gupte, S.S. and C.F. Desai, *Vickers hardness anisotropy and slip system in zinc (tris) thiourea sulphate crystals*. Crystal Research and Technology, 1999. **34**(10): p. 1329-1332.

71. Fang, T. and J.C. Lambropoulos, *Microhardness and indentation fracture of potassium dihydrogen phosphate (KDP)*. Journal of the American Ceramic Society, 2002. **85**(1): p. 174-178.

72. Karan, S. and S.P. Sen Gupta, *Vickers microhardness studies on solution-grown single crystals of magnesium sulphate hepta-hydrate*. Materials Science and Engineering a-Structural Materials Properties Microstructure and Processing, 2005. **398**(1-2): p. 198-203.

73. Duncanhewitt, W.C., D.L. Mount, and A. Yu, *Hardness anisotropy of acetaminophen crystals*. Pharmaceutical Research, 1994. **11**(5): p. 616-623.

74. Ramos, K.J., D.E. Hooks, and D.F. Bahr, *Direct observation of plasticity and quantitative hardness measurements in single crystal cyclotrimethylene trinitramine by nanoindentation*. Philosophical Magazine, 2009. **89**(27): p. 2381-2402.

75. Kiran, M., et al., *Mechanical Anisotropy in Crystalline Saccharin: Nanoindentation Studies*. Crystal Growth & Design, 2010. **10**(10): p. 4650-4655.

76. Knoop, F., C.G. Peters, and W.B. Emerson, *A sensitive pyramidal-diamond tool for indentation measurements*. Journal of Research of the National Bureau of Standards, 1939. **23**: p. 39-61.

77. Westbrook, J.H. and Jorgense.Pj, *Solution environment effects on the hardness and toughness of calcite during grinding*. American Mineralogist, 1968. **53**(11-1): p. 1899-+.

78. Han, Y.H., et al., *Knoop microhardness anisotropy of single-crystal aragonite*. Journal of the American Ceramic Society, 1991. **74**(12): p. 3129-3132.

79. Li, H., Y.H. Han, and R.C. Bradt, *Knoop microhardness of single-crystal sulfur*. Journal of Materials Science, 1994. **29**(21): p. 5641-5645.

80. Kearney, C., et al., *Nanoscale anisotropic plastic deformation in single crystal aragonite*. Physical Review Letters, 2006. **96**(25).

81. Viswanath, B., et al., *Mechanical properties and anisotropy in hydroxyapatite single crystals*. Scripta Materialia, 2007. **57**(4): p. 361-364.

82. Saber-Samandari, S. and K.A. Gross, *Micromechanical properties of single crystal hydroxyapatite by nanoindentation*. Acta Biomaterialia, 2009. **5**(6): p. 2206-2212.

83. DeBresser, J.H.P. and C.J. Spiers, *Strength characteristics of the r, f, and c slip systems in calcite*. Tectonophysics, 1997. **272**(1): p. 1-23.

84. Ranganathan, S.I. and M. Ostoja-Starzewski, *Universal elastic anisotropy index*. Physical Review Letters, 2008. **101**(5).

85. Perez-Huerta, A., M. Cusak, and W. Zhu, *Assessment of crystallographic influence on material properties of calcite brachiopods*. Mineralogical Magazine, 2008. **72**(2): p. 563-568.

86. Oliver, W.C. and G.M. Pharr, *An improved technique for determining hardness and elastic-modulus using load and displacement sensing indentation experiments*. Journal of Materials Research, 1992. **7**(6): p. 1564-1583.

87. Lawn, B. and R. Wilshaw, *Indentation fracture - Principles and applications*. Journal of Materials Science, 1975. **10**(6): p. 1049-1081.

88. Jang, J. and G.M. Pharr, *Influence of indenter angle on cracking in Si and Ge during nanoindentation*. Acta Materialia, 2008. **56**(16): p. 4458-4469.

89. Qian, L.M., et al., *Comparison of nano-indentation hardness to microhardness*. Surface & Coatings Technology, 2005. **195**(2-3): p. 264-271.

90. Chiang, S.S., D.B. Marshall, and A.G. Evans, *The response of solids to elastic plastic indentation. 1. Stresses and residual-stresses*. Journal of Applied Physics, 1982. **53**(1): p. 298-311.

91. Johnson, K.L., *Correlation of indentation experiments*. Journal of the Mechanics and Physics of Solids, 1970. **18**(2): p. 115-&.

92. Mata, M., O. Casals, and J. Alcala, *The plastic zone size in indentation experiments: The analogy with the expansion of a spherical cavity*. International Journal of Solids and Structures, 2006. **43**(20): p. 5994-6013.

93. Lawn, B.R., A.G. Evans, and D.B. Marshall, *Elastic-plastic indentation damage in ceramics - The median-radial crack system*. Journal of the American Ceramic Society, 1980. **63**(9-10): p. 574-581.

94. Lankford, J. and D.L. Davidson, *Crack-initiation threshold in ceramic materials subject to elastic-plastic indentation*. Journal of Materials Science, 1979. **14**(7): p. 1662-1668.

95. Pharr, G.M., D.S. Harding, and W.C. Oliver, *Measurement of fracture-toughness in thin-films and small volumes using nanoindentation methods*. Mechanical Properties and Deformation Behavior of Materials Having Ultra-Fine Microstructures, ed. M. Nastasi, D.M. Parkin, and H. Gleiter. Vol. 233. 1993, Dordrecht: Kluwer Academic Publ. 449-461.

96. Kese, K.O., Z.C. Li, and B. Bergman, *Method to account for true contact area in soda-lime glass during nanoindentation with the Berkovich tip*. Materials Science and Engineering a-Structural Materials Properties Microstructure and Processing, 2005. **404**(1-2): p. 1-8.

97. Daniels, F.W. and C.G. Dunn, *The effect of orientation on knoop hardness of single crystals of zinc and silicon ferrite*. Transactions of the American Society for Metals, 1949. **41**: p. 419-442.

98. Chen, C.C., et al., *Elasticity of single-crystal calcite and rhodochrosite by Brillouin spectroscopy*. American Mineralogist, 2001. **86**(11-12): p. 1525-1529.

99. Aouni, N. and L. Wheeler, *Auxeticity of Calcite and Aragonite polymorphs of CaCO3 and crystals of similar structure*. Physica Status Solidi B-Basic Solid State Physics, 2008. **245**(11): p. 2454-2462.

100. Oliver, W.C. and G.M. Pharr, *Measurement of hardness and elastic modulus by instrumented indentation: Advances in understanding and refinements to methodology*. Journal of Materials Research, 2004. **19**(1): p. 3-20.

## 4.8. APPENDIX: YOUNG'S MODULUS CALCULATIONS

Calcite has trigonal crystal symmetry and thus 6 independent elastic constants, which have been determined both experimentally [98], and by theoretical calculations [102]. We here calculate the anisotropic Young modulus as a function orientation using Hooke's law in tensor form [103]. To our knowledge, this calculation has not been correctly reported for calcite (in a recent study, hexagonal symmetry was incorrectly assumed [104]).

Young's modulus of a single crystal in a direction $x_1$' is just the inverse of the compliance in that direction [103]. That is:

$$E(x_1') = 1 / S_{11}', \tag{4.2}$$

where $E(x_1')$ is Young's modulus in the $x_1$' direction and $S_{11}$' is the compliance in that same direction. The orthogonal coordinate system in which calcite elastic constants are typically reported has $x_1$ parallel to one of the $a$-axes, $x_3$ parallel to [0001], and $x_2$ such that a right-handed system is formed [98]. To calculate $E(x_1')$, we transform the compliance tensor from the crystal coordinate system to a new coordinate system containing $x_1$' by rotating the original coordinate system about $x_3$ by an angle $\alpha$ and then about the new $x_2$' by an angle $\beta$ (as in, *e.g.*, [105]). Thus, any direction $x_1$' in the crystal can be defined with respect to an $a$-axis by the angles $\alpha$ and $\beta$.

Using the stiffness constants ($C_{ij}$) reported by Chen, *et al*. [98], we first invert the stiffness tensor to determine the compliance constants ($S_{ij}$), then transform the compliance tensor through every combination of the rotation angles $\alpha$ (from 0-360 degrees) and $\beta$ (from 0-180 degrees), in 1 degree increments using functions built into the Mathematica software (*Wolfram Research*) (results verified at several directions using analytical expressions derived by Nye [103] and Ting [106]). The values of Young's modulus calculated using Eq. 4.2 are plotted as a 3D surface in $x_1, x_2, x_3$

coordinates in Figure 4.20 where the radial distance between the origin and this surface represents the magnitude of $E(x_1')$ in that direction.

The stiffest directions in uniaxial loading occur at $\alpha$ = 30º, 60º, and 120º in the $+x_3$ domain and at $\alpha$ = -30º, -60º, and -120º in the $-x_3$ domain. A cross section from Fig. 4.21 showing the $x_1'$-$x_3$ plane at $\alpha$ = 30º is shown in Figure 4.21. The maximum (144 GPa) and minimum (52 GPa) values of the Young modulus of calcite are contained in this plane at $\beta$ = -23º and $\beta$ = +40º, respectively. For comparison, the directions normal to $\{\bar{1}012\}$ and $\{10\bar{1}4\}$ planes also lie in this plane at $\beta$ = -27º and $\beta$ = +45º, having 141 and 53 GPa, respectively. Thus, directions normal to the $\{10\bar{1}4\}$ facets are very close to the direction of the lowest Young's modulus in calcite. By comparison, the Young's modulus normal to (0001) is also relatively low, at 58 GPa. The average over all directions is 74 GPa.

A compilation of literature values for the elastic constants in calcite by Zhao [102] shows that the reported values vary by up to ~30% between studies. However, the general trend (*i.e.*, the ratios between different elastic constants in any one report) is fairly consistent. Thus, we expect that the form of Young's modulus with orientation should be very close to that shown in Fig's 4.20 and 4.21, although the magnitudes may vary slightly. We chose the constants reported by Chen, *et al*. because they are close to the mean values (averaged across studies).

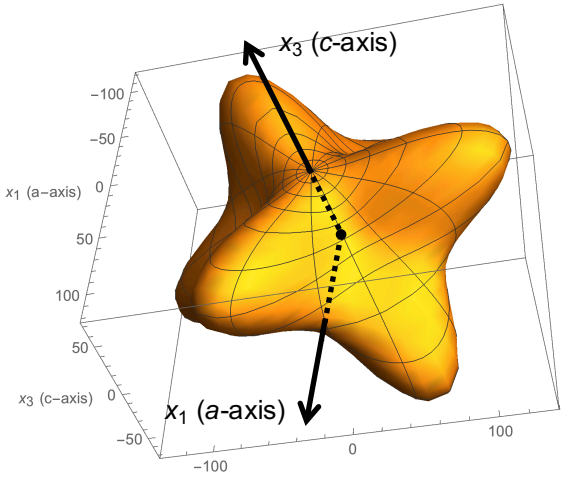


**Figure 4.20:** 3D plot of Young's modulus. $\alpha$ and $\beta$ are polar coordinates used in calculations: $\alpha$ is the angle between $x_1$ and $x_1$' for clockwise rotations about the -$x_3$ axis. $\beta$ is the angle between $x_1$' and $x_1$" for subsequent clockwise rotations about the $-x_2$' axis.

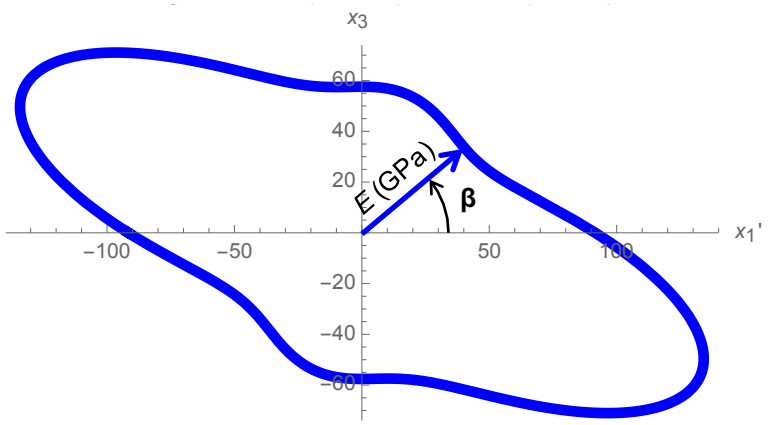


**Figure 4.21:** Cross section of the 3D Young's modulus plot in Fig. 4.20 at $\alpha = 30^{\circ}$. The maximum and minimum moduli are contained in this plane (*i.e.*, 144 GPa at $\beta = -23^{\circ}$ and 52 GPa at $\beta = +40^{\circ}$.

## 4.9. APPENDIX: REFERENCES


98. Chen, C.C., et al., *Elasticity of single-crystal calcite and rhodochrosite by Brillouin spectroscopy*. American Mineralogist, 2001. **86**(11-12): p. 1525-1529.

101. Zhao, J.H., et al., *Elasticity of Single-Crystal Calcite by First-Principles Calculations*. Journal of Computational and Theoretical Nanoscience, 2009. **6**(5): p. 1181-1188.

102. Nye, J.F., *Physical properties of crystals: their representation by tensors and matrices*. 1985, Oxford university press.

103. Fu, J., F. Bernard, and S. Kamah-Bernard, *First-principles calculations of typical anisotropic cubic and hexagonal structures and homogenized moduli estimation based on the Y-parameter: Application to CaO, MgO, CH and Calcite CaCO3*. Journal of Physics and Chemistry of Solids, 2017. **101**: p. 74-89.

104. Turley, J. and G. Sines, *The anisotropy of Young's modulus, shear modulus and Poisson's ratio in cubic materials*. Journal of Physics D: Applied Physics, 1971. **4**(2): p. 264.

105. Ting, T.C.T., *Explicit Expression of the Stationary Values of Young's Modulus and the Shear Modulus for Anisotropic Elastic Materials*. Journal of Mechanics, 2011. **21**(4): p. 255-266.

## CHAPTER 5

*Parts of this chapter to be submitted to *Journal of Materials Research*

# Measuring the elastic modulus and hardness of particles within a dissimilar matrix using instrumented indentation

Joseph D. Carloni, John L. Mason, Teresa E. Jordan, Chung-Yuen Hui, Lara A. Estroff, and Shefford P. Baker

*Cornell University, Department of Materials Science and Engineering, Bard Hall, Ithaca, NY 14853*

## ABSTRACT

The standard method used to calculate hardness and modulus from an instrumented indentation requires that the sample is large and homogeneous, but many interesting samples do not fit these criteria. Here, we focus on the case of a small particle embedded in a dissimilar matrix. Previous simulations have shown that measurement of such a particle is affected by the matrix material. Experimental methods to account for this effect have been limited, and one existing method requires that the sample material has hardness that is independent of the indentation size. However, for most materials, the hardness does depend on indentation size, often referred to as the indentation size effect (ISE). We suggest a new correction method that does not require that the sample has no ISE. In this new method, the initial error associated with the correction is eliminated through the analysis of an iterative series of plots of the data generated from the instrumented indentation. The efficacy of this method is demonstrated through corrected experimental measurements on small embedded particles of calcite, a material that has been demonstrated to show ISE. These corrected measurements closely match measurements on a bulk calcite control sample, proving that the proposed method can work.

## 5.1. INTRODUCTION

Instrumented indentation techniques, such as nanoindentation, can accurately measure indenter loads and displacements during the indentation, usually in order to calculate the mechanical properties of the sample being indented. To determine the hardness and modulus of the sample, the load-displacement data are often analyzed using the method developed by Oliver & Pharr [1, 2]. This method allows the indentation contact compliance and contact area (and, in turn, the indentation modulus and hardness) to be calculated directly from the measured indenter loads and displacements that have been generated from a properly-calibrated indenter machine. However, the fundamental equations governing this analysis assume that the sample being indented is an elastically homogeneous, semi-infinite half-space [3]—a condition that is clearly not met in real experiments. Nonetheless, application of the Oliver-Pharr analysis is reasonably accurate when a small indentation is made on a large, homogeneous sample—such that the effect of the finite geometry of the sample can be ignored. However, when measuring small volumes of material, sometimes the minimum experimentally-practical indentation size is large enough effect of the elastic heterogeneities at the sample boundaries *cannot* be ignored.

One of the most widely studied examples of the effect of an elastic heterogeneity on an instrumented indentation is the case of a thin film on a dissimilar substrate. A number of models have been developed that describe the transition from measuring the properties of the film to that of the substrate, which occurs with increasing displacement of the indenter into the surface of the film [4-9]. Implicit to these models is the assumption that the only heterogeneous boundary is a horizontal one between the film and substrate, *i.e.*, that the lateral extent of the film is large with respect to the indentation size. Inspired by the interesting mechanical properties of small grains of natural minerals like calcite, here we are interested in the more general case where the

material of interest may be near both horizontal and vertical elastic boundaries. Specifically, we are interested in the extreme case where such boundaries are nearby on all sides, which we will refer to as an embedded particle. For the mineral calcite, this situation exists for (often micrometer-sized) crystals that are naturally embedded in biogenic composites like the teeth and shells of marine organisms [10-14], or naturally embedded as one of the many possible mineral constituents that make up sedimentary rocks like limestone and shale [15, 16]. Synthetically, a similar situation exists because lab-grown calcite crystals need to be embedded in some mounting material prior to indentation testing, in order to properly-orient a suitably flat and smooth surface, or to create such a surface by polishing [17-23]. In any case, indentation measurement of these kinds of embedded particles is expected to be significantly affected by the surrounding matrix material for large enough indentation size, though any possible effect has been ignored in many experiments.

The effect of a dissimilar matrix on the nanoindentation measurement of a particle has been studied theoretically using finite element simulations (FEA) [24-29]. Generally, these studies show that the measured hardness and modulus is some combination of the properties of the particle and the matrix. Experimental techniques to correct for this effect are limited, and generally rely on simply making small enough indentations that the effect of the matrix is minimal. Jakes, *et al*. [30, 31] have determined that the effect of some other types of elastic heterogeneities can be described by some constant additional compliance that does not depend on indentation size. In this case, the problem becomes simplified, and more robust solutions can be developed. However, the experimental methods suggested by Jakes, *et al*. have some shortcomings, for example, either requiring that multiple indentation on the same sample be made, or requiring that the hardness of the sample does not depend on

indentation depth. Either of these requirements are not suitable for many types of samples, including the embedded particles we are interested in here.

Here we analyze the effect of dissimilar matrix material surrounding an indented particle on the calculation of indentation contact compliance and contact area by the usual Oliver and Pharr method. We express the difference between the actual measured values and those that would be expected for a large and homogeneous sample in terms of an additional "matrix compliance" that is due to dissimilar elastic displacements occurring within the matrix material. We note that this matrix compliance may be nearly constant over some range of indentation sizes, and can thus be treated in a similar way as the elastic heterogeneities considered by Jakes, *et al*. Building upon the correction method proposed by Jakes, *et al*., we suggest an improved method that does not require multiple indentations or hardness to be constant with depth.

## 5.2. THE STANDARD ANALYSIS, AND NEW CORRECTIONS

### 5.2.1. The standard analysis

In an indentation experiment, a load $P$ is applied to an indenter, forcing it into the sample a displacement $h_s$ and creating a residual indentation on the sample surface. The Meyer hardness $H$ of the sample is defined as

$$H = \frac{P}{A_c}, \tag{5.1}$$

where $A_c$ is the contact area of the residual indentation projected into the surface plane. In an instrumented indentation, the load $P$ and total displacement of the indenter $h$ are measured continuously, and the $P$-$h$ data are subsequently analyzed to determine $A_c$, and therefore $H$ and other quantities. In the standard method developed by Oliver and Pharr [1, 2] it is assumed that the deformation on unloading is fully

elastic and the compliances of the indenter and the sample material sum such that a "reduced modulus" $E_R$ can be defined for a homogeneous isotropic material as

$$\frac{1}{E_R} = \frac{1-v_s^2}{E_s} + \frac{1-v_i^2}{E_i} . \tag{5.2}$$

where $E$ is Young's modulus and $v$ is Poisson's ratio and the subscripts $s$ and $i$ refer to the sample and indenter, respectively.

Assuming further that the contact on unloading can be modeled using Sneddon's solutions for an elastic contact between a flat punch and an isotropic, homogeneous, semi-infinite half-space [3], $E_R$ is related to the contact compliance on unloading, $C_c = dh_s/dP$, and $A_c$ by

$$E_R = \frac{\sqrt{\pi}}{2C_c\sqrt{A_c}} . \tag{5.3}$$

Hence, by determination of $C_c$ and $A_c$ from $P$-$h$ data, both $H$ and $E_R$ can be calculated using Equations 5.1 and 5.3, respectively. If $E_i$ and $v_i$ are known, then one can solve for the plane strain modulus of the sample, $E_s/(1-v_s^2)$, from

$$\frac{E_s}{1-v_s^2} = \left(\frac{1}{E_R} - \frac{1-v_i^2}{E_i}\right)^{-1} . \tag{5.4}$$

Here, we will simply refer to this quantity as the "indentation modulus."

Oliver and Pharr showed that the total elastic compliance of the indentation, $C = dh/dP$, can be determined using either quasi-static or dynamic indentation methods [1, 2]. For a quasi-static indentation, $C$ is just the inverse of the slope of the unloading data, and for a dynamic indentation, $C$ can be calculated from the amplitude of the load and displacement signals. A dynamic measurement has the added benefit of measuring $C$ across a range of $h$ from a single indentation.

In either case, $C$ includes components from both the elastic deformation of the sample and the elastic flexing of the components that make up the indenter machine. Since these compliances are in series, we write:

$$C = C_c + C_m \ , \tag{5.5}$$

where $C_m$ is the machine compliance. Combining equations 5.3 and 5.5 yields:

$$C = \frac{\sqrt{\pi}}{2E_R\sqrt{A_c}} + C_m \ . \tag{5.6}$$

Thus, a plot of $C$ *vs.* $1/\sqrt{A_c}$ should be a straight line with slope equal $\sqrt{\pi}/2E_R$, and *y*-intercept equal $C_m$ [4]. Making such a plot from experimentally determined $C$ and $A_c$ is one way to calculate $C_m$. $C_m$ is usually considered to be a calibration constant of the machine, and is subtracted from all future measurements. Thus, it follows that a plot of $C - C_m$ *vs.* $1/\sqrt{A_c}$ from measurements made on any sample that meets the assumptions of the Oliver and Pharr method, should reveal a straight line with slope equal $\sqrt{\pi}/2E_R$, and zero *y*-intercept.

The contact compliance, $C_c$, can be found using Eq. 5.5. To find $A_c$, we first determine the contact depth $h_c$, which is the depth along the indenter axis to which the indenter is in contact with the sample (see Figure 5.1a). Building upon Sneddon's solution for the shape of the surface outside the area of contact of a conical indenter [3], Oliver and Pharr [1] have shown that the contact depth, $h_c$, is given by:

$$h_c = h_s - \varepsilon P C_c \ , \tag{5.7}$$

where $\varepsilon$ is a constant related to the indenter geometry (*e.g.*, $\varepsilon = 0.75$ for a Berkovich indenter). Since

$$h_s = h - P C_m \ , \tag{5.8}$$

and incorporating Eq. 5.6, we have

$$h_c = h - P(C_m + \varepsilon C_c) \ , \tag{5.9}$$

$A_c$ is then determined from the calibrated "area function," $A_c = f(h_c)$, for the particular indenter tip used [1, 2].

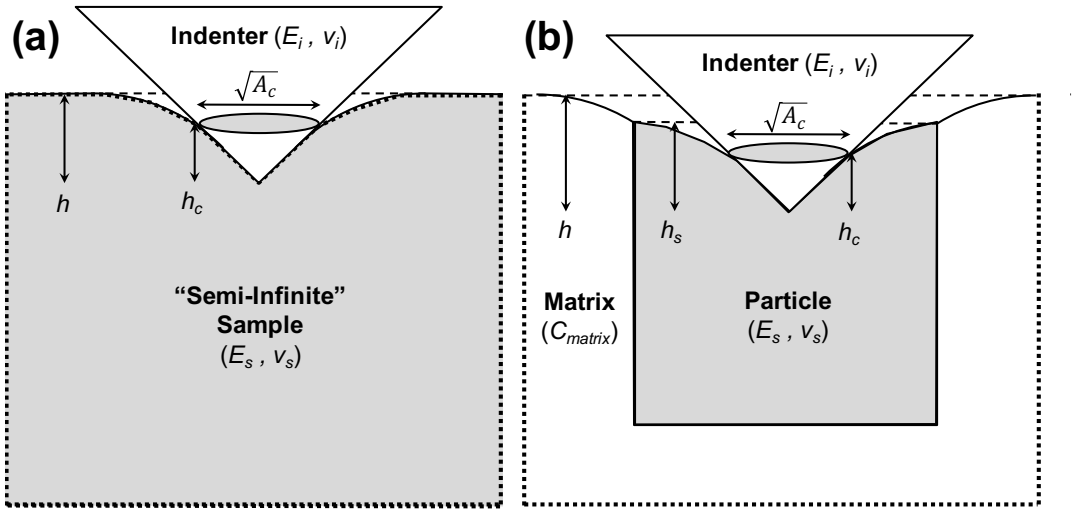


**Figure 5.1**: Schematics showing an indentation into a) a "semi-infinite" half-space of homogeneous material, and b) a particle surrounded by a dissimilar matrix material. Note, indentation size is exaggerated for clarity.

In summary, given accurate calibration values for the area function and $C_m$, $C_c$ and $A_c$, and thus $H$ and $E_s/(1-\nu_s^2)$, can be calculated directly from measured indentation load-displacement data. A significant advantage of this method is that it obviates the need for imaging indentations so that mechanical properties can be obtained quickly and from indentations that would be otherwise too small to study efficiently, as in nanoindentation.

### 5.2.2. Indentation of particles in dissimilar matrices

There are many cases where it is desirable to study the mechanical properties of a small particle embedded in a dissimilar matrix. For example, one might want to obtain the mechanical properties of the individual constituents of a microscale composite [10-16]. Alternatively, one might want to measure the mechanical properties of particles that are only available in microscopic sizes. A convenient way to accomplish this is to embed the particles in a matrix material, polish down to the particles and indent them. For example, this technique has been used to prepare synthetic calcite crystals for indentation measurement [17-23].

However, in such cases, the assumption of an isotropic, homogeneous, elastic half space required by the Oliver-Pharr method [1, 2] may not be valid. Consider the case where a self-similar indenter is used to make an indentation with contact diameter $\sqrt{A_c}$ near the center of a small, roughly equiaxed, particle of diameter *D* embedded in a dissimilar matrix material as shown in Figure 5.1b. For a small enough indentation ($\sqrt{A_c} \ll D$), the stresses, and therefore displacements, at the particle boundary will be small and the reduced modulus (Eq. 5.3) includes the properties of the indenter tip and the particle (subscript *s* refers to the particle in Eq. 5.2). We refer to this as $E_{R,p}$. For a large enough indentation ($\gg D$), the particle becomes a small defect on the indenter and the reduced modulus includes the properties of the indenter tip and the matrix. We

refer to this as $E_{R,MAT}$ (subscript $s$ refers to the matrix in Eq. 5.2). At intermediate indentation sizes, the analysis is expected to return values that represent some convolution of particle and matrix properties.

We derive a simple formulation for the nominal contact compliance returned by the Oliver and Pharr analysis, $C - C_m$ (from Eq. 5.5), using dimensional analysis. Assuming that the form of the Sneddon solution applies throughout, we could, in general, write

$$C - C_m = \frac{\sqrt{\pi}}{2E_{R,p}\sqrt{A_c}} f\left(\frac{\sqrt{A_c}}{D}, \frac{E_{R,p}}{E_{R,MAT}}\right) , \tag{5.10}$$

but we do not know the form of the function $f$. Instead, we construct a solution in parts. For $\sqrt{A_c} \gg D$ the solution is simply

$$C - C_m = \frac{\sqrt{\pi}}{2E_{R,\mathrm{MAT}}\sqrt{A_c}} \tag{5.11}$$

This is shown in Figure 5.2, where, in accordance with Eq. 5.6, we show a schematic plot of the nominal contact compliance, $C - C_m$ *vs.* $1/\sqrt{A_c}$ for the case of a stiff particle in a compliant matrix. At large $\sqrt{A_c}$, the data follow a line with slope $\sqrt{\pi}/2E_{R,MAT}$. For $\sqrt{A_c} < D$ we consider that the indenter indents the particle while the particle indents the matrix. These occur in series so we can write

$$C - C_m = \frac{\sqrt{\pi}}{2E_{R,p}\sqrt{A_c}} + \frac{1}{2E_{R,MAT}D} g\left(\frac{E_{R,p}}{E_{R,MAT}}\right) , \tag{5.12}$$

where we again assume that the contact between the particle and the matrix follows the form of the Sneddon solution. We again don't know the form of the function $g$, but we have assumed that it is independent of load. This is equivalent to assuming that there is a load range where the magnitude but not the form of the distribution of stresses along the particle/matrix interface varies with load. In this case, the second term on the right hand side of Eq. 5.12 is a constant and can be treated as an additional

linear compliance $C_{MAT}$, which we call "matrix compliance". The total measured compliance $C$ then becomes

$$C = C_c + C_m + C_{MAT} \ , \tag{5.13}$$

so

$$C - C_m = \frac{\sqrt{\pi}}{2E_{R,p}\sqrt{A_c}} + C_{MAT} \ . \tag{5.14}$$

This can be seen at smaller values of $\sqrt{A_c}$ in Fig. 5.2, where data plotted as $C - C_m$ vs. $1/\sqrt{A_c}$ fall on a straight line with an intercept of $C_{MAT}$. Finally, between the regions represented by Eq's 5.11 and 5.12 (*i.e.*, where $\sqrt{A_c} \approx D$), we expect there must be some smooth transition, which we represent by a dotted line in Fig. 5.2.

The key conclusion of our dimensional analysis is that, to the extent that there is a load range where $C_{MAT}$ can be treated as constant, then a plot of $C - C_m$ *vs.* $1/\sqrt{A_c}$ should be linear, with intercept $C_{MAT}$. If it were possible to obtain $\sqrt{A_c}$ and $C$ from the $P$–$h$ data, then with knowledge of $C_m$, such a plot would make it possible to determine $C_{MAT}$ and thus the correct contact compliance, $C_c$, from Eq. 5.11. This would then make it possible to obtain $H$ and $E_s/(1-\nu_s^2)$ for the particle using Equations 5.1, 5.3 and 5.4.

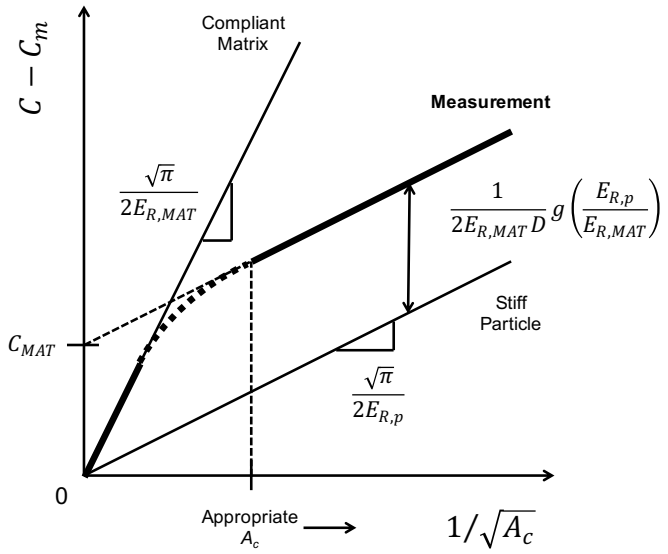


**Figure 5.2**: Schematic illustrating possible behavior of compliance versus the reciprocal square root of contact area over a large range of contact areas. The dashed lines labeled "stiff particle" and "compliant matrix" represent the expected bounds of the function. The solid line labeled "measurement" illustrates the interpretation discussed in Section 5.2.2. Note that the solid line is approximately linear below small enough contact areas.

Unfortunately, this is not the case. For nonzero $C_{MAT}$, Eq. 5.8 becomes:

$$h_s = h - PC_m - PC_{MAT} \ . \tag{5.15}$$

If an attempt is made to find $C_c$ based on Eq. 5.5 (that is by neglecting $C_{MAT}$), an incorrect value, $h_c{}'$, (primed symbols in the following indicate false calculated values) for the contact depth will be calculated. The value will be

$$h_c{}' = h_c + (1-\varepsilon)PC_{MAT} \ . \tag{5.16}$$

If the actual contact area, hardness, and reduced modulus are $A_c$, $H$, and $E_R$, respectively, and we assume a simple self-similar tip shape given by

$$A_c = kh_c^2 \ , \tag{5.17}$$

where $k$ is a geometric constant (*e.g.*, $k = 24.5$ for a Berkovich indenter), neglecting $C_{MAT}$ yields false uncorrected values for these quantities given by:

$$A_c{}' = A_c\left[1 + \frac{\sqrt{\pi}}{2}\sqrt{k}(1-\varepsilon)\frac{HC_{MAT}}{E_R C_c}\right] , \tag{5.18}$$

$$H' = \frac{H}{\left[1+\frac{\sqrt{\pi}}{2}\sqrt{k}(1-\varepsilon)\frac{HC_{MAT}}{E_R C_c}\right]^2} , \tag{5.19}$$

and

$$E_R{}' = \frac{E_R}{\left(1+\frac{C_{MAT}}{C_c}\right)\left[1+\frac{\sqrt{\pi}}{2}\sqrt{k}(1-\varepsilon)\frac{HC_{MAT}}{E_R C_c}\right]} , \tag{5.20}$$

respectively.

The error in the uncorrected values increases with increasing $C_{MAT}$, and for some constant $C_{MAT}$, increases with decreasing $C_c$. Since $C_c$ decreases with increasing $A_c$ (Eq. 5.3), the error in these values should increase with increasing $A_c$. Hence, as expected, shallower indentations should be less affected by $C_{MAT}$. But, to avoid such errors altogether, we consider ways in which to determine $C_{MAT}$, and subtract it from measured displacements.

### 5.2.3. The correction method

Based on the above, we find ourselves in the situation where, if we had $A_c$ we could calculate $C_{MAT}$ and obtain the properties of the particle, but, following conventional methods, $C_{MAT}$ is needed to calculate $A_c$. Jakes *et al*. [31] suggested two solutions to this problem: 1. Make multiple indentations, each to a different maximum load, and measure $A_c$ directly in a second imaging step. Or, 2. Assume $H$ does not depend on $A_c$, and use a similar plot (that they call a "SYS plot") to calculate $C_c$ [33, 34]. The first suggestion is not practical for small embedded particles both because there may not be enough room on the particle's surface to make multiple indents and because $C_{MAT}$ may not be the same in each location on the particle's surface. The second suggestion is also not ideal, because of an assumption inherent to the derivation of the SYS plot.

In short, the derivation of the SYS plot (in terms of our variable names) is to start with Equation 5.14, replace $A_c$ with $P/H$, and to rearrange the equation such that it becomes clear that a plot of $C\sqrt{P}$ *vs*. $\sqrt{P}$ will yield a straight line with slope equal $C_m + C_{MAT}$, a quantity that could be subtracted from $C$ to determine $C_m$. However, in order to replace $A_c$ with $P/H$ in this way, it must be true that $H$ does not depend on $A_c$. This is a troubling assumption to make, since the point of the measurement is typically to *obtain* $H$, and, for most materials, $H$ *does* depend on $A_c$—a phenomenon generally referred to as the "Indentation Size Effect" [35]. Here, we suggest an alternative approach that doesn't require imaging or assumptions about hardness, instead we simply calculate $A_c'$ (Eq. 5.18) and use this value to obtain a first estimate of the matrix compliance $C_{MAT}'$. We then use this value to obtain an improved value for the contact area, $A_c''$. Further iterations may be made when possible and as necessary to obtain more accurate values.

From this data, a plot of $C - C_m$ *vs.* $1/\sqrt{A_c'}$ would be similar to the desired plot of $C - C_m$ *vs.* $1/\sqrt{A_c}$ , but shifted along the *x*-axis by some amount $1/\sqrt{A_c'} - 1/\sqrt{A_c}$ . Thus, the *y*-intercept of this plot will also be shifted away from $C_{MAT}$, instead taking on some other value that we will call $C_{MAT}'$. It could be true that this initial $C_{MAT}'$ is close enough to $C_{MAT}$ that the difference is negligible. In any case, so long as the magnitude of this difference is less than the magnitude of the actual $C_{MAT}$, then $C - C_m - C_{MAT}'$ will at least be closer to $C_c$, than is $C - C_m$. Hence, a new plot of $C - C_m - C_{MAT}'$ *vs.* $1/\sqrt{A_c''}$ could be generated (where $A_c''$ is calculated like $A_c'$, but using $C - C_m - C_{MAT}'$ instead of $C - C_m$). As such, an iterative series of plots like $C - C_m - \sum C_{MAT}'$ *vs.* $1/\sqrt{A_c''}$ (where the previous sum $C - C_m - \sum C_{MAT}'$ is always used to calculate $A_c''$) should eventually converge to a plot with zero *y*-intercept—and the total value of $\sum C_{MAT}'$ over all iterations would be the actual value of $C_{MAT}$. The number of iterations necessary to converge upon this solution should be related to the magnitude of $A_c'/A_c$, and for $A_c'/A_c$ close enough to unity, we expect the plot might converge in very few iterations.

In detail, we propose the following method to calculate $C_{MAT}$:

1. Obtain $P$–$h$ data from either a single dynamic indentation or a number of quasi-static indentations at different maximum loads near the center of a particle embedded in a matrix as shown in Fig. 5.1b.
2. Use $C_c' = C - C_m$, along with the tip shape function, to calculate $h_c'$ and $A_c'$, for a range of $h$ and $A_c$.
3. Plot $C_c'$ *vs.* $1/\sqrt{A_c'}$ and fit a straight line to the data. If the fit is good, we assume that we are on that portion of the curve in Fig. 5.2 where $C_{MAT}$ is constant. The *y*-intercept gives our first estimate of the matrix compliance, $C_{MAT}'$.

4. Now use Eq. 5.13 (using $C_{MAT}{}'$ in place of $C_{MAT}$), along with the tip shape function, to calculate a new contact area $A_c{}''$ as before, but now using $C_c{}'' = C - C_m - C_{MAT}{}'$.
5. Plot $C_c{}''$ *vs.* $1/\sqrt{A_c{}''}$, fit a straight line to the data and calculate the new *y*-intercept (the new $C_{MAT}{}'$). If the new *y*-intercept is closer to zero than the previous one, then further iterations can be expected to converge to an intercept of zero. The sum of the intercepts converges to the actual $C_{MAT}$. That is $C_{MAT} = \sum C_{MAT}{}'$ (see below).
6. If $C_{MAT}{}'$ from step 5 is not close to zero, then repeat steps 4 and 5, using $C_c{}''' = C - C_m - \sum C_{MAT}{}'$. Otherwise,
7. Assume $C_{MAT}$ equal to $\sum C_{MAT}{}'$, calculate $C_c$ from $C - C_m - C_{MAT}$, and then $H$ and $E_s/(1 - \nu_s^2)$ can be calculated for the particle as above.

This method is based on only two assumptions: (1) that $C_{MAT}$ is constant over the range of $A_c$ measured, and (2) that the calculation of $\sum C_{MAT}{}'$ converges to $C_{MAT}$ over some number of iterations. The experiments and results in the following sections will test the accuracy of this method on small crystals of the mineral calcite embedded in relatively compliant matrices.

## 5.3. EXPERIMENTS AND RESULTS

To test the efficacy of the proposed method, indentations were made in small (≈ 50 $\mu$m) calcite crystals embedded in more compliant matrices. Two systems were studied: synthetic crystals embedded in cyanoacrylate glue, and geologic calcite inclusions in a concretionary mudstone, a type of shale with high organic content. As a reference, identical indentations were made in a bulk single crystal of Iceland spar, a very high quality calcite of geologic origin. Indentations were performed using a commercially available nanoindenter (TI-900, Hysitron Inc. Minneapolis, MN) equipped with a

Berkovich diamond tip. Prior to these experiments, the tip area function and machine compliance were calibrated using a standard fused silica sample, as in the Oliver-Pharr method [1, 2]. In Chapter 4, we showed that there is an indentation size effect (ISE) in calcite that can be well described by a "master" curve of hardness versus indentation depth, created by fitting extensive literature data collected at a wide range of loads. The hardness results obtained here are compared with that master curve.

### 5.3.1. Bulk geologic calcite

In preparation for indentation, a single crystal geologic (Iceland spar*)* calcite was cleaved along its natural $\{10\bar{1}4\}$ cleavage planes into a rhombohedron approximately 1 cm on each side. By using the indenter tip as a scanning force probe, the surface roughness over a 10 $\mu$m scan on an exposed $(10\bar{1}4)$ facet was measured to be less than 10 nm RMS.

The crystal was then indented using a dynamic loading function. The mean applied load was increased in 15 discrete load steps from 2.5-10 mN over the course of 60 seconds. In addition, a small sinusoidal loading at 100 Hz was applied with the amplitude varied so as to maintain a dynamic displacement of approximately 3 nm. The crystal was indented 5 times at each of 8 different azimuthal orientations, for a total of 40 indentations. Despite the general mechanical anisotropy of calcite, the difference in the average measured modulus and hardness between these different orientations on the (10-14) face was within the standard deviation of the measurements at a single orientation on this face (Chapter 4). The resulting data were analyzed using the methods described in Section 5.2. Hardness and indentation modulus data are shown as a function of indenter displacement in Figure 5.3a and a plot of $C - C_m$ *vs.* $1/\sqrt{A_c}$ is shown in Figure 5.3b. As expected, the uncorrected indentation modulus is constant with displacement, and a fit of a line to the of $C - C_m$

*vs*. $1/\sqrt{A_c}$ is excellent with a negligibly small *y*-intercept (zero to two significant figures). Also, the uncorrected hardness decreases slightly between the minimum and maximum applied load, consistent with the expected ISE. The calculated values of $H$ and $E_s/(1-\nu_s^2)$ at the minimum and maximum indentation depths, averaged over all 40 indentations, are tabulated in Table 5.1.

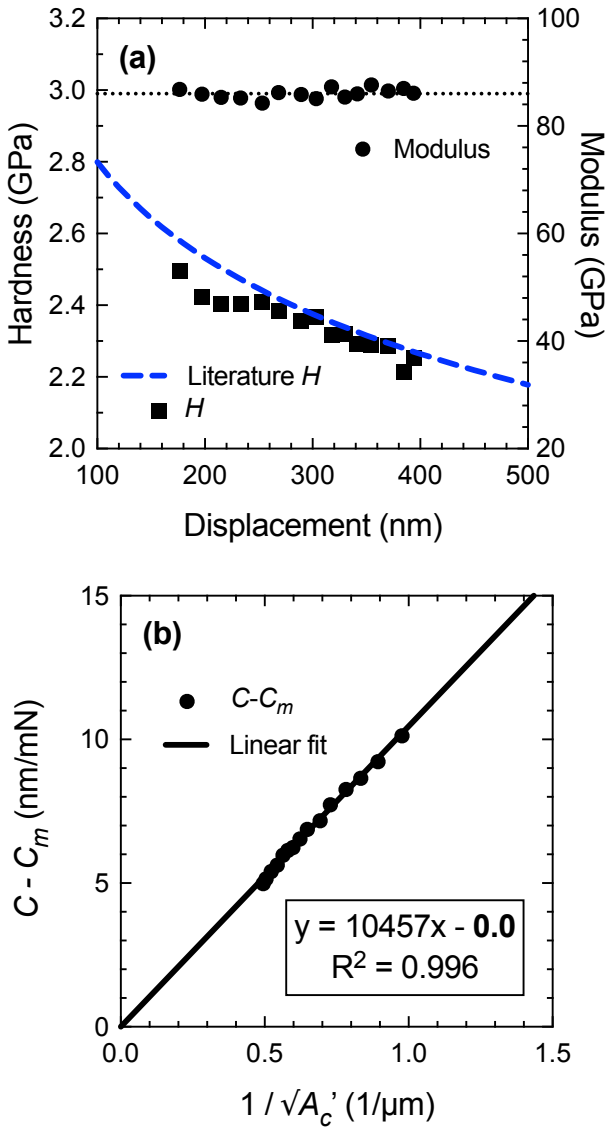


**Figure 5.3**: Data from a representative dynamic indentation onto the $(10\bar{1}4)$ face of a ~1 cm equiaxed rhombohedron of geologic calcite (Iceland spar). a) Measured indentation modulus and hardness as a function of indenter displacement into the sample, $h_s = h - PC_m$. The black dotted line shows the average indentation modulus measured on $(10\bar{1}4)$ geologic calcite, and the blue dashed line shows the fit to literature hardness data from Chapter 4. b) Plot of $C - C_m$ *vs.* $1/\sqrt{A_c}$ with linear fit. These plots show the expected behavior for indentations in calcite.

**Table 5.1**: The average indentation modulus and hardness at each 2.5 mN and 10 mN load from dynamic indentations in bulk geologic calcite (Iceland spar), small synthetic calcite embedded in a cyanoacrylate matrix, and small grains of calcite within an organic-rich shale rock (a concretionary mudstone).

| | Bulk geologic calcite $(10\bar{1}4)$ face | | Small synthetic calcite grains in cyanoacrylate matrix (random orientations) | | Small calcite grains in organic-rich shale (random orientations) | |
|---|---|---|---|---|---|---|
| | 2.5 mN | 10 mN | 2.5 mN | 10 mN | 2.5 mN | 10 mN |
| Modulus before correction (GPa) | 87 +/- 1.7 | 88 +/- 1.7 | 56 +/- 4.5 | 40 +/- 4.7 | 80 +/-5 | 72 +/- 4.0 |
| Hardness before correction (GPa) | 2.5 +/- 0.1 | 2.4 +/- 0.1 | 2.4 +/- 0.2 | 2.2 +/- 0.3 | 2.6 +/- 0.3 | 2.3 +/- 0.2 |
| Modulus after correction (GPa) | N/A | N/A | 92 +/- 8.4 | 93 +/- 9.7 | 85 +/- 7.4 | 86 +/- 7.8 |
| Hardness after correction (GPa) | N/A | N/A | 2.5 +/- 0.2 | 2.4 +/- 0.3 | 2.6 +/- 0.3 | 2.3 +/- 0.2 |
| Matrix compliance (nm/mN) | 0.0 +/- 0.0 | | 5.7 +/- 1.1 | | 1.0 +/- 0.6 | |

### 5.3.2. Synthetic calcite crystals in cyanoacrylate embedding medium

Synthetic calcite crystals were precipitated over the course of ≈ 12 hours onto a glass slide from an initially 15 mM $CaCl_2$ solution that was supersaturated with $CO_2$ gas sublimated from $NH_4CO_3$ powder, via the "Ammonium Diffusion Method" [36]. The resultant single crystals were, on average, equiaxed rhombohedra of about 50 $\mu$m along each edge. The crystals nucleated on the glass substrate at a range of orientations but, in all cases, a flat and smooth surface existed on the "bottom" facet of the crystal where it was attached to the glass.

To prepare the crystals for nanoindentation, we followed the procedure illustrated in Figure 5.4. First, the glass slide (with crystals attached) was coated with a liquid cyanoacrylate-embedding medium (Fig. 5.4a). Next, the unsolidified cyanoacrylate was then "sandwiched" with a thin mylar sheet coated with resin containing aluminum oxide particles ("5 $\mu$m alumina lapping film" Allied Products, Rancho Dominguez, CA) (Fig. 5.4b). After solidification of the embedding medium, the mylar sheet was peeled off of the glass slide. Because of its roughness, the mylar sheet formed a strong mechanical bond to the embedding medium, and the medium delaminated from the smooth glass during peeling. The calcite crystals remained embedded, so we were left with crystals surrounded by a cyanoacrylate matrix exposing the flat and smooth surface where they grew on the glass slide (Fig. 5.4c).

Indentations were made only on exposed surfaces of calcite crystals having rhombohedral geometry similar to that of a $\{10\bar{1}4\}$ face of calcite, in an attempt to match the $(10\bar{1}4)$ orientation of our geologic control. Surface scans made using the indenter tip as a scanning force probe showed a roughness of less than 10 nm RMS. As can be seen in Figure 5.5, the interface between a crystal and the surrounding embedding medium could easily be distinguished in the surface scans.

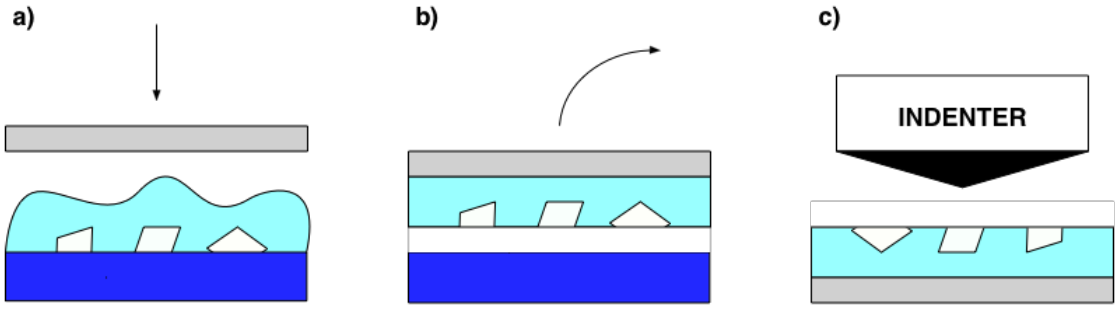


**Figure 5.4**: Method for preparing small synthetic crystals for nanoindentation: (a) Crystals grown on glass slide are embedded in cyanoacrylate to which an abrasive-coated mylar sheet is attached. (b) The mylar sheet with attached particles and embedding medium is peeled from the glass. (c) The sample is turned over exposing smooth flat growth surfaces for nanoindentation.

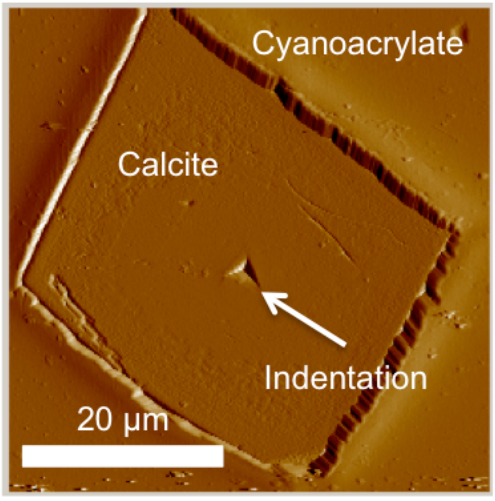


**Figure 5.5**: Scanning force image created using the indenter tip as scanning force probe of a small synthetic calcite crystal embedded in a cyanoacrylate matrix. The boundary between a rhombohedral, seemingly $\{10\bar{1}4\}$, face of the crystal and the surrounding cyanoacrylate matrix as well as an indentation placed in the center of this crystal are visible.

Indentations using the dynamic loading scheme described above were made at the centers of 15 different crystals. The resulting data were analyzed using the methods described in Section 5.2. The results for a representative indent are shown in Figure 5.6. Note that the uncorrected indentation modulus values decrease with increasing indenter displacement (Fig. 5.6a), and are below the average value measured on the bulk geologic control (dashed line) as expected due to the compliant matrix. Also note that both the uncorrected and corrected hardnesses decrease slightly between the minimum and maximum applied load, consistent with the expected ISE (Fig. 5.6b). A plot of $C_c{}'$ *vs.* $1/\sqrt{A_c{}'}$ (Fig. 5.6c) is well described by a linear fit with a *y*-intercept of 5.2 nm/mN, which represents the value of $C_{MAT}{}'$. A linear fit to $C_c{}''$ *vs.* $1/\sqrt{A_c{}''}$ (Fig. 5.6d) is also good with a very small *y*-intercept (-0.2 nm/mN). Hence, we set $C_{MAT}$ equal to $C_{MAT}{}' + C_{MAT}{}''$ (no further iterations needed) and correct the measurement for $C_{MAT}$. After correction, the calculated indentation modulus (Fig. 5.6a) and hardness (Fig. 5.6b) are both constant with displacement, and closely match the average values we measured for the bulk geologic sample. The calculated values of $H$, $E_s/(1-\nu_s^2)$, and $C_{MAT}$ averaged over all 15 indentations are tabulated in Table 5.1.

The cyanoacrylate embedding material surrounding the crystals was also indented using the dynamic loading function. The modulus and hardness did not vary significantly with depth and was on the order of 1 GPa and 100 MPa, respectively.

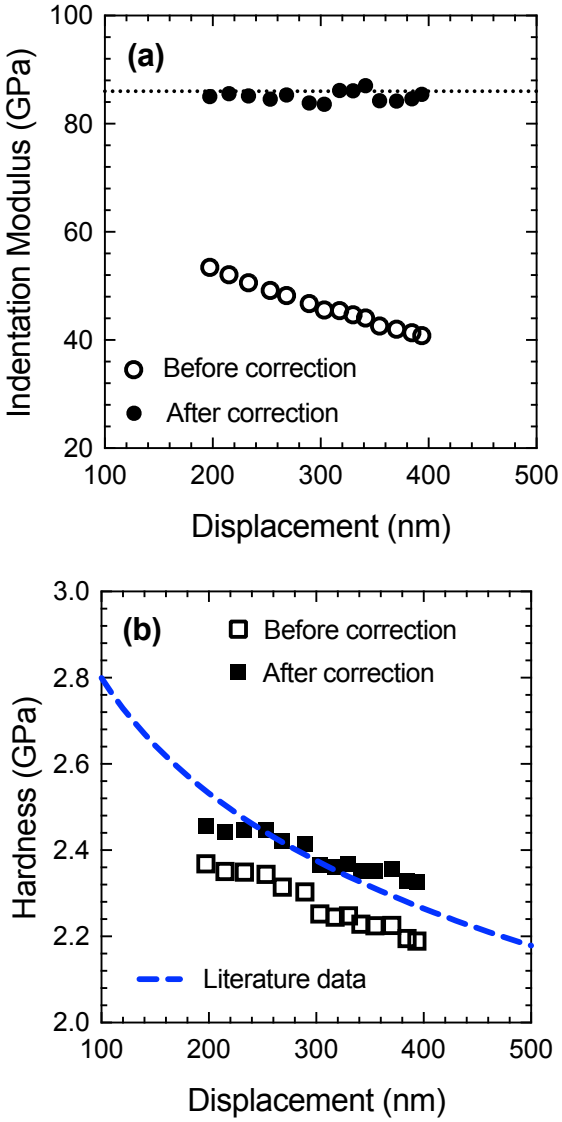


**Figure 5.6**: Data from a representative indentation onto a $\{10\bar{1}4\}$ face of a ~50 $\mu$m equiaxed rhombohedron of synthetic calcite embedded in a cyanoacrylate matrix. Un-corrected and corrected a) indentation modulus, and b) hardness, as a function indenter displacement. As in Fig. 5.3, the dotted black line shows the average indentation modulus on $(10\bar{1}4)$ geologic calcite, and the blue dashed line shows the fit to literature hardness data from Chapter 4. After correction, the indentation modulus is constant with depth and closely matches the average value measured on the control (in contrast, hardness is not strongly affected by matrix compliance).

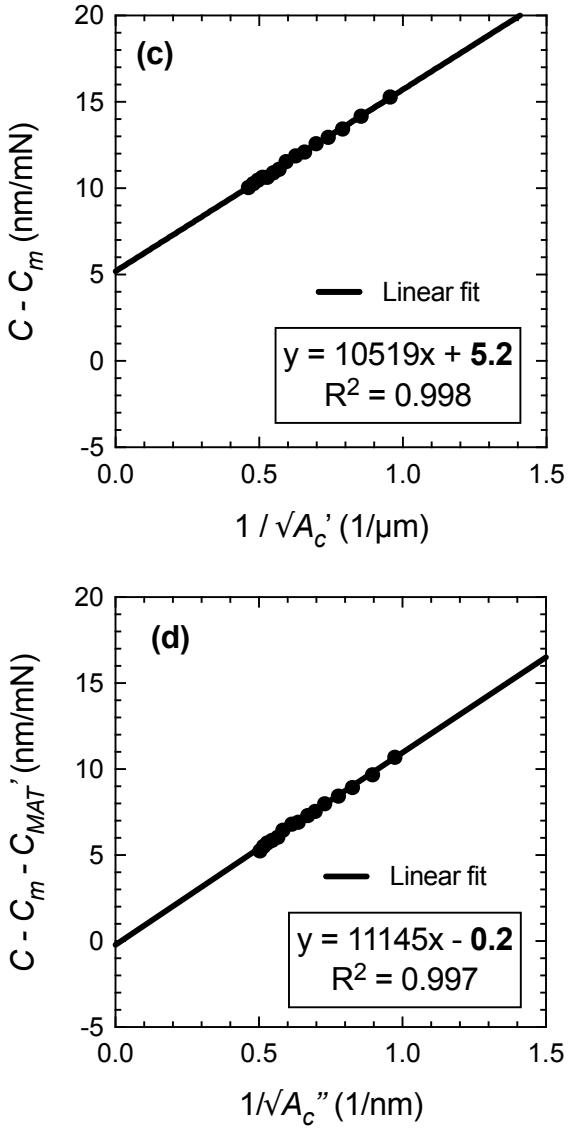


**Figure 5.6 (cont.)**: c) Plot of $C'$ *vs.* $1/\sqrt{A_c{}'}$. The data are well described by a linear fit with a *y*-intercept of 5.2 nm/mN, which we take to be an estimate of the matrix compliance, $C_{MAT}{}'$. d) A new plot of $C''$ *vs.* $1/\sqrt{A_c{}''}$ with linear fit. The *y*-intercept is now negligibly small, therefore we set $C_{MAT} = C_{MAT}{}' + C_{MAT}{}''$ in order to make the corrections shown in parts a and b.

### 5.3.3. Calcite particles in shale rock

A rock sample of a concretionary mudstone outcrop was obtained from a Marcellus shale quarry in Seneca Falls, NY. Concretionary mudstone is a heterogeneous composite material containing nanometer to micrometer-sized mineral grains and relatively compliant occluded organic material. This particular sample contained many calcite grains on the order of 50 $\mu$m across. A 1 cm cube was cut from the sample using a diamond saw, and the cut cube was embedded in Bakelite and mechanically polished using silicon carbide paper, down to 1 $\mu$m grit size, resulting in a roughness of approximately 1 $\mu$m RMS. Because of the extreme brittleness of certain heterogeneous constituents of the shale, a finer polish was not possible using conventional polishing methods. In order to achieve a roughness more suitable for nanoindentation, following Loucks, *et al*. [37], we milled the surfaces of our samples using an argon ion beam operated at 500-1000 V accelerating voltage and 70-80 mA of current for a total of 75 minutes. During milling, the sample was continuously rotated 360º azimuthally, and the angle of the beam was incrementally decreased from 30º to 10º above parallel. The ion milling obtained an average surface roughness of ≈ 100 nm RMS, with roughness as low as ≈ 30 nm RMS in calcite grains (as determined using indenter tip surface scans).

The samples were then coated with ≈ 1 nm of Au-Pd in order to obtain a conductive surface for imaging in SEM. Grains of calcite were identified using SEM (Fig. 5.7a) and EDS, and their locations with respect to the sample boundaries were recorded. These same calcite grains were then located using the microscope in the nanoindenter, and their exact locations were verified using indenter tip surface scans (Fig. 5.7b). Dynamic load indentations were made at the centers of 20 of these grains. The resulting data were analyzed using the methods described in Section 5.2 and shown in Figure 5.8 and Table 5.1.

The crystallographic orientation of the calcite grains in shale is unknown and may be completely random. Calcite is mechanically anisotropic so we can only expect our measurements of indentation modulus to fall within a range between its stiffest and most compliant orientations. Furthermore, the hardness has been shown to vary significantly between calcites of different origin and impurity concentration [14, 18, 22, 23]). Thus, we do not know what modulus and hardness to expect *a priori*— though the moduli and hardnesses of the calcites measured here do tend to closely match that of our relatively pure controls.

Before correction, indentations in 10 relatively small (~50 $\mu$m) calcite grains that were surrounded by organic material returned modulus measurements that decreased with increasing indenter displacement, and were at or below the lower end of the expected range for range for randomly oriented calcite. After correction, these measurements were similar to those made on calcite controls, as shown in Fig. 5.8. The other 10 grains of calcite in the shale were much larger than 50 $\mu$m and/or not obviously surrounded by organic material, had zero calculated matrix compliance, and returned modulus values that were close to that measured on our controls (on average, 78 +/- 4 GPa).

The organic material surrounding some of the calcite grains was also indented with a similar loading function. The modulus and hardness did not vary significantly with depth and were on the order of 10 GPa and 500 MPa, respectively.

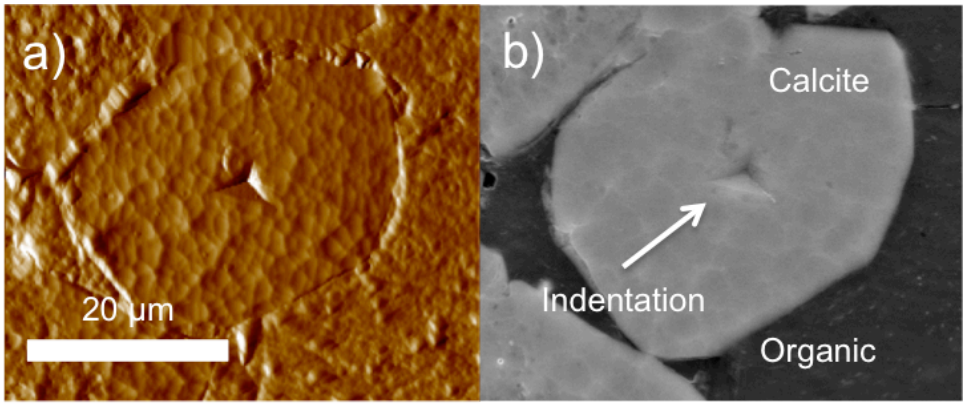


**Figure 5.7**: a) Scanning force probe and b) SEM images of a small grain of calcite of unknown crystallographic orientation in shale (concretionary mudstone) surrounded by naturally occurring organic material. The boundary between the crystal and the surrounding organic matrix as well as an indentation placed in the center of this crystal are also visible.

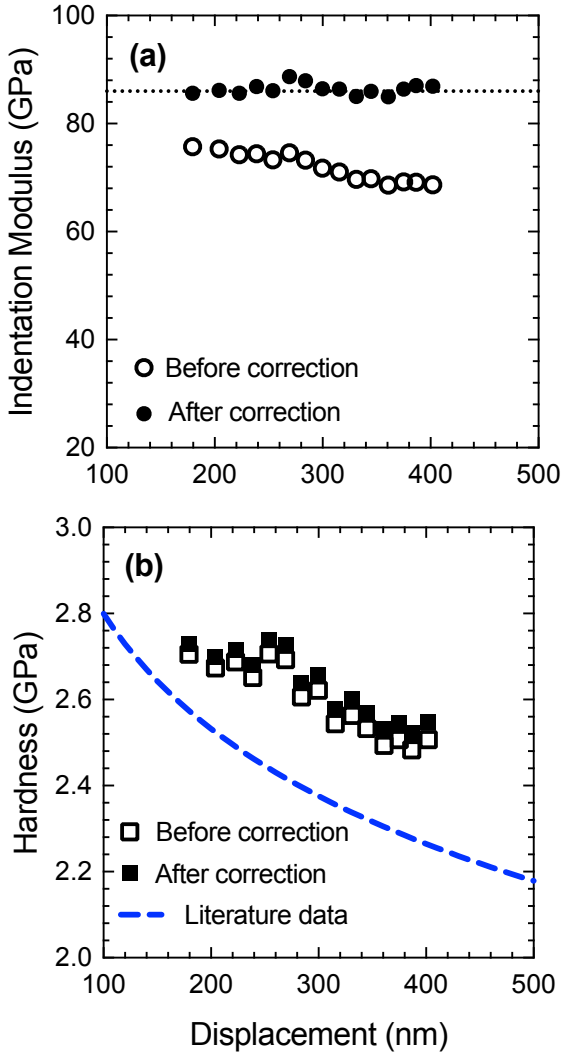


**Figure 5.8**: Data from a representative indentation in shale. a) The measured indentation modulus is plotted as a function of indenter displacement, before and after correction for the calculated matrix compliance. As in Fig's 5.3 and 5.6, the dotted black line shows the average indentation modulus on the $(10\bar{1}4)$ geologic calcite control, and the blue dashed line shows the fit to literature hardness data from Chapter 4. After correction, the indentation modulus is constant with depth and closely matches the average value measured on the control (in contrast, hardness is not strongly affected by matrix compliance).

## 5.4. DISCUSSION

We have tested the efficacy of the correction proposed in Section 5.2 via our experiments in Section 5.3. Some assumptions were made in the development of the correction, and these assumptions will be discussed in more detail here. We will also discuss the meaning of our results, as well as put them in the context of previous work done in this area of study.

### 5.4.1. Constant matrix compliance assumption

The experimental results presented in Section 5.3 show that the new correction method proposed here can indeed work. That is, the corrected modulus measured on our embedded calcite crystals matches that of the bulk calcite crystal. This suggests that the assumptions associated with our analysis are valid, at least for the samples explored here. The main assumptions were: (1) that $C_{MAT}$ is nearly constant over the range of $A_c$ measured, and (2) that $\sum C_{MAT}{}'$ should converge to $C_{MAT}$ over some number of iterations.

The first assumption has been considered elsewhere. Gerber [38], based on the work of Hetenyi [39], considered measured compliance for an indentation on an elastic "quarter-space" and found that the additional compliance due to the free edge could be treated as a constant. Jakes, *et al*. [30] extended this analysis to the more general case where some dissimilar material bounds the edge, and came to the conclusion that this effect could be treated in the same way as the quarter space problem when the radius of the indentation is small with respect to the distance from the edge—*i.e*., in accordance with Saint Venant's principle. Additionally, their experiments show that, in certain cases, this critical radius could even approach that of being equal with the distance to the edge, suggesting widespread applicability. Furthermore, they used a model by Stone, *et al*. [40] to simulate whether the effect of

a dissimilar substrate on an indentation of a thin film could also be treated as some constant compliance that sums with the contact compliance, and concluded that it could when the radius of the contact was less approximately than the film thickness—generally a more stringent criteria, but still widely applicable.

We note that in Jakes' work, the criterion for which the constant additional compliance approximation is valid (*i.e.*, the critical value of the ratio $\sqrt{A_c}/D$) has not been exactly defined, but only approximated. Here, we do not try to exactly define this ratio either, but instead we simply assume that if the $C_c$ *vs.* $1/\sqrt{A_c}$ data fall on a straight line, then $C_{MAT}$ is constant. To check for curvature in the $C_c$ *vs.* $1/\sqrt{A_c}$ data, we occasionally adjusted the range of the data in $A_c$ used to make the linear fit (*e.g.*, comparing the fit to the data from the 5 largest values of $A_c$ to the fit to the data from the 5 lowest values of $A_c$). In all cases, the slope of the fits were not significantly different (data not shown), indicating that $C_{MAT}$ was indeed constant across the whole range of $\sqrt{A_c}/D$ that was measured. If indentations were made to large enough $\sqrt{A_c}/D$ where $C_{MAT}$ was not constant, then the slope of a linear fit to $C_c$ *vs.* $1/\sqrt{A_c}$ would vary depending on the range of the data used to make the fit.

### 5.4.2. Error in calculated contact area ($A_c'$)

The second main assumption that our correction is based on is that the calculation of $\sum C_{MAT}'$ should converge to $C_{MAT}$ over some number of iterations. This is related to the effect that the magnitude of the ratio $A_c'/A_c$ has on a plot of $C_c'$ *vs.* $1/\sqrt{A_c'}$. In Section 5.2.3, we explain that the error in the calculated contact area is expected to decrease over iterative subtraction of $C_{MAT}'$, but here we consider exactly how that should work.

Compared to a plot of $C_c'$ *vs.* $1/\sqrt{A_c}$, $C_c'$ plotted *vs.* $1/\sqrt{A_c'}$ should be shifted along the *x*-axis by the amount $1/\sqrt{A_c'} - 1/\sqrt{A_c}$. For $A_c'/A_c$ greater than unity,

$1/\sqrt{A_c{}'} - 1/\sqrt{A_c}$ is negative, and vice versa. Rearranging Equation 5.18, and substituting values as needed:

$$\frac{A_c{}'}{A_c} = \left[1 + \sqrt{k}(1-\varepsilon)HC_{MAT}\sqrt{A_c}\right], \tag{5.21}$$

Hence, it is obvious that $A_c{}'/A_c$ is greater than unity for any positive $C_{MAT}$. We also note that, for any physically reasonable value of negative $C_{MAT}$ (*e.g.*, compliant particle in stiff matrix), $A_c{}'/A_c$ is less than unity. (Though certain negative values of $HC_{MAT}\sqrt{A_c}$ input in Equation 5.21 lead to $A_c{}'/A_c$ greater than unity, these values represent the un-physical scenario where $C_c + C_{MAT} \leq 0$.)

Having established that $1/\sqrt{A_c{}'} - 1/\sqrt{A_c}$ is always negative for positive $C_{MAT}$, we now consider exactly how that will affect the plot of $C_c{}'$ plotted *vs.* $1/\sqrt{A_c{}'}$. In general, negative $1/\sqrt{A_c{}'} - 1/\sqrt{A_c}$ means that all values of $C_c{}'$ plotted *vs.* $1/\sqrt{A_c{}'}$ will be shifted along the *x*-axis closer to the origin than when plotted *vs.* $1/\sqrt{A_c}$ . Expanding upon Eq. 5.21 to solve for the magnitude of $1/\sqrt{A_c{}'} - 1/\sqrt{A_c}$ yields

$$\frac{1}{\sqrt{A_c{}'}} - \frac{1}{\sqrt{A_c}} = \frac{-\sqrt{k}(1-\varepsilon)HC_{MAT}\sqrt{A_c}}{1+\sqrt{k}(1-\varepsilon)HC_{MAT}\sqrt{A_c}}. \tag{5.22}$$

This shows that the magnitude of the shift $1/\sqrt{A_c{}'} - 1/\sqrt{A_c}$ will be less for greater $A_c$. That is, the magnitude of the shift will be less for $C_c{}'$ data plotted close to the origin. One consequence of this is that the slope of the $C_c{}'$ data plotted *vs.* $1/\sqrt{A_c{}'}$ will be greater than that of the $C_c{}'$ data plotted *vs.* $1/\sqrt{A_c}$. Another consequence is that, since $1/\sqrt{A_c{}'} - 1/\sqrt{A_c}$ is not linear *vs.* $1/\sqrt{A_c}$, the non-linear behavior of the shift $1/\sqrt{A_c{}'} - 1/\sqrt{A_c}$ could drive the plot of $C_c{}'$ data *vs.* $1/\sqrt{A_c{}'}$ away from linearity (even for constant $C_{MAT}$). However, the functional form of Equation 5.22 suggests that $1/\sqrt{A_c{}'} - 1/\sqrt{A_c}$ *vs.* $1/\sqrt{A_c}$ should be *nearly* linear, except for especially small $A_c$. Thus, if $C_c{}'$ data plotted *vs.* $1/\sqrt{A_c}$ is linear (*e.g.*, constant $C_{MAT}$), then that same $C_c{}'$ plotted *vs.* $1/\sqrt{A_c{}'}$ should also be linear, in most cases.

To illustrate what this might look like, we've generated model data for an ideal indentation made over loads ranging 1-10 mN. Our model simply uses the error equations introduced in Section 5.2.2 (Eq's 5.18-5.20) to simulate the quantity $A_c{}'$ measured at some load $P$, given inputs of $H$, $E_s/(1-\nu_s^2)$, and $C_{MAT}$. We input $H$ = 2.5 GPa and $E_s/(1-\nu_s^2)$ = 90 GPa (to approximate that of the calcite crystals tested here). To exaggerate the difference $1/\sqrt{A_c{}'} - 1/\sqrt{A_c}$, we input $C_{MAT}$ = 100 nm/mN, approximately 20x that measured in our experiments. These model data are shown in Figure 5.9. In this model we see that the data plotted *vs.* $1/\sqrt{A_c{}'}$ are still linear ($R^2 >$ 0.98) even for an extreme value of $C_{MAT}$.

The ultimate consequence of the shift caused by the magnitude of the ratio $A_c{}'/A_c$ is that the plot of $C_c{}'$ *vs.* $1/\sqrt{A_c{}'}$ will have a larger *y*-intercept than that of $C_c{}'$ *vs.* $1/\sqrt{A_c}$. Thus, the initial value of $C_{MAT}{}'$ will be greater than $C_{MAT}$. Hence, the next plot of $C_c{}''$ *vs.* $1/\sqrt{A_c{}''}$ will be over-accounting for the effect of the matrix, such that $C_c{}''$ is less than $C_c$, and $A_c{}''/A_c$ is less than unity. Thus, the *y*-intercept of this plot (the new $C_{MAT}{}'$) will be negative, and $\sum C_{MAT}{}'$ will be less than $C_{MAT}$. Further iteration will switch between $\sum C_{MAT}{}'$ being less than or greater than $C_{MAT}$, eventually converging on the actual value of $C_{MAT}$.

It follows that the only way these iterations would *not* converge is if the difference $C_{MAT}{}' - C_{MAT}$ after the first iteration is greater than the magnitude of $C_{MAT}$. In which case, the magnitude of $C_{MAT}{}'$ would just steadily increase, switching between negative and positive. Because of the difference in slope between $C_c{}'$ plotted *vs.* $1/\sqrt{A_c{}'}$ and $C_c{}'$ plotted *vs.* $1/\sqrt{A_c}$, determining the exact criteria for which these plots diverge is complicated. However, by simple trigonometry, $C_{MAT}{}' - C_{MAT}$ should be roughly equal $1/\sqrt{A_c{}'} - 1/\sqrt{A_c}$ times the slope of $C_c{}'$ plotted *vs.* $1/\sqrt{A_c}$, that is, $\sqrt{\pi}/2E_R$. Thus, the plot would diverge only when:

$$\left(\frac{\sqrt{k}(1-\varepsilon)HC_{MAT}\sqrt{A_c}}{1+\sqrt{k}(1-\varepsilon)HC_{MAT}\sqrt{A_c}}\right)\left(\frac{\sqrt{\pi}}{2E_R}\right) > C_{MAT}\ , \tag{5.23}$$

For a Berkovich indenter, this simplifies to the following relationship:

$$C_{MAT}(1.1H - E_R) - 1.24HE_RC_{MAT} > 0\ , \tag{5.24}$$

which can only be true for positive $(1.1H - E_R)$ or, more generally, materials with extremely high hardness to modulus ratio ($> 0.9$). And even for positive $(1.1H - E_R)$, Eq. 5.24 would only be true if $1.24HE_RC_{MAT} < C_{MAT}(1.1H - E_R)$ too.

Thus, we've shown that for most practical material systems, $\sum {C_{MAT}}'$ should indeed converge to $C_{MAT}$ over some number of iterations. The number of iterations before convergence is dependent on the magnitude of the initial difference ${C_{MAT}}' - C_{MAT}$. In our experiments, this difference was small enough that only a single iteration was necessary.

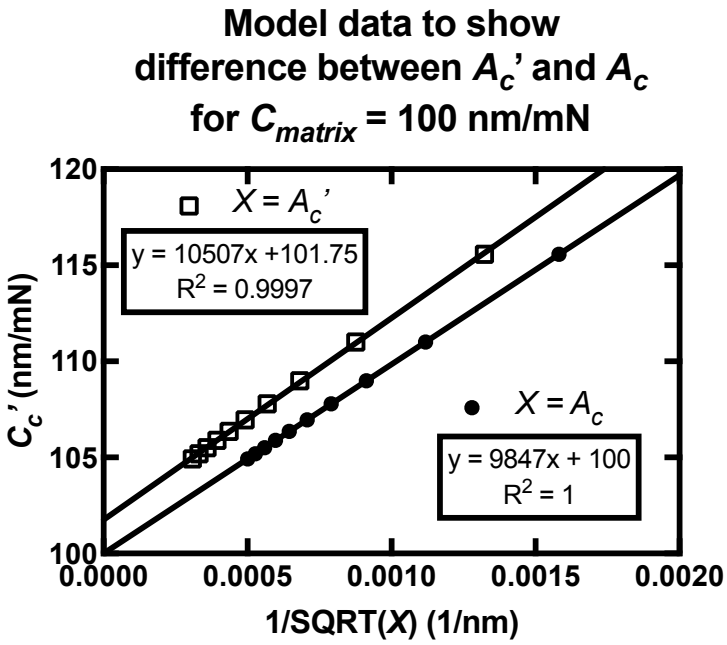


**Figure 5.9**: Model data to show the difference between plotting $C_c'$ *vs*. the uncorrected and actual contact area for a large matrix compliance. Note that the difference between the two sets is not very large. The ultimate effect is that the *y*-intercept of the plot using the uncorrected area is larger than the actual matrix compliance.

### 5.4.3. Relating matrix compliance to physical properties

Here we relate the magnitude of $C_{MAT}$ to the measured modulus of our matrix materials. In our model, $C_{MAT}$ is just the contact compliance for indentation of the matrix material using the particle as an indenter. This contact compliance is not exactly equivalent to Sneddon's solution of a flat-punch indenter because of the additional constraints associated with the particle being firmly embedded at some depth into the matrix. However, we do assume that $C_{MAT}$ scales with Sneddon's solution, such that:

$$C_{MAT} \approx \frac{1}{2E_{R,MAT}\sqrt{A}}. \tag{5.25}$$

where $A$ is some unknown quantity with units of area, which describes the interface between the particle and the matrix. Since we have measured the moduli and average $C_{MAT}$ for each of the samples tested here, we can solve for $A$. For the synthetic crystals in cyanoacrylate, $A$ is ~22500 $\mu$m$^2$, and for the natural crystals embedded in organic-rich shale, $A$ is ~1480 $\mu$m$^2$. These values correspond to the surface area of a hemisphere with radius equal 60 $\mu$m and 15 $\mu$m, respectively. This is very close to the size of the crystal in each case. Maybe the lower value of $A$ for the natural crystals can be explained by the fact that the matrix organic material may not surround each of those crystals equally on all sides, as it does in the synthetically embedded crystals. For example, if each crystal were partially in contact with other stiff minerals at one side and/or underneath its surface, then it would make sense for the total matrix compliance to be less than if the crystal was uniformly surrounded by compliant matrix material.

### 5.4.4. Comparison to other work

Previous work investigating the indentation measurement of a particle in a dissimilar matrix has been limited. A few studies have explored this situation theoretically using

finite element simulations (FEA) [24-29]. The results of these studies show that the measured hardness and modulus calculated using the standard Oliver and Pharr method are some combination of the properties of the particle and the matrix, with the effect of the matrix being greater at larger indentation size. Leggoe *et al*. [26] analyze their FEA results in terms of the particle making a "secondary" indentation into the matrix, and determine that the compliance of this secondary indentation can be described by Sneddon's solution, multiplied by some correction factor that depends on the shape of the particle. This result is consistent with our analysis in Section 4.3. Numerous FEA studies (Durst *et al*. [25], Low *et al*. [27], Yan *et al*. [28, 29], and Cao *et al*. [24]) each find a "particle-dominated" indentation size, below which uncorrected measured values are reasonably close (within 5-10%) of the actual properties of the particle. Durst *et al*. [25] and Low *et al*. [27] focus on the measurement of hardness, while Yan *et al*. [28, 29] and Cao *et al*. [24] explore both modulus and hardness. Consistent with our results here, the results of these studies indicate that the matrix has a much greater effect on measured modulus than on hardness.

Based upon the concept of a particle-dominated indentation size, Liesen *et al*. [41] proposed an experimental method to correct indentation measurements made on small particles embedded in a more compliant matrix. Their method involves plotting uncorrected modulus measurements as a function of depth, and extrapolating to zero depth, similar to models used for indentation measurements of thin-films on dissimilar substrates [4]. The sample used by Liesen *et al*. [41] consisted of hard ceramic particles of 2-3 mm in diameter embedded in epoxy and polished to expose a flat surface of the particles.

Maughan *et al*. [42] proposed a method for mounting small (~ 1 mm) crystalline particles in preparation for nanoindentation measurements. Similar to the mounting method used here (Figure 5.4), their method involves orienting pre-existing flat

surfaces of particles (*i.e.*, without polishing) but is instead based on gently dipping the particle into the mounting adhesive, so as to avoid the need for any peeling step. Because of the precision required to mount a particle in this way, they explain that it is not practically useful for particles < 250 $\mu$m in diameter. In contrast, we have demonstrated that the simple peeling method used here can effectively mount crystals that are < 50 $\mu$m in diameter.

Jakes, *et al*. have mostly developed their indentation correction model in terms of the effect of a single elastic discontinuity that intersects the surface place of the sample perpendicularly, but they have also applied their model to a few situations which could be described as a particle embedded in a matrix (*i.e.*, nearby elastic discontinuities in all directions) [30]. For those examples, they use what they refer to as a SYS plot, which inherently involves assuming that the hardness does not depend on indentation size. As described in Section 5.2.3, this assumption is troubling because hardness does depend on indentation size in many materials [35]. It is not clear what effect the constant hardness assumption had on the accuracy of their corrected data.

Finally, we note that much more work has been focused on the similar, but different case of thin films on dissimilar substrates. Similar to the concept of a particle-dominated indentation size, the most basic way to avoid the effect of the substrate is to make small enough indentations. A basic empirical rule of thumb is to keep the depth of the indent less than 1/10 the film thickness [43], although this has been shown to not always be valid [8]. One of the earliest attempts to model the influence of a substrate was by Doerner & Nix [4], who developed an empirical modification of the definition of reduced modulus to account for the effects of the substrate, assuming a linear transition from film to substrate. Since then, a number of improved models, usually based on a similar empirical concept, have been introduced [5-9]. In all cases, such models are different than the Jakes model (and the alternative

method proposed here) in a few key ways. For one, the thin film models were designed and evaluated specifically for the sample geometry of a thin film, *i.e.*, a sample is laterally large with respect to the indentation size such that its finite extent can be ignored, unlike the geometry of small particle. Also, the thin film models describe the full transition from measuring the properties of the film to that of the substrate, including the measurement at indentation sizes where the effect of the substrate cannot be considered a constant additional compliance. For these reasons, the thin film models are not directly comparable to any model based on a constant additional compliance, and thus should not be expected to apply to analysis of the types of measurements we are interested in here. However, in cases where the indentation size on a film is small enough to be treated as a constant additional compliance, the method proposed here has the advantage over existing thin film models that it does not require *a priori* knowledge of the elastic properties of the substrate.

## 5.5. SUMMARY AND CONCLUSIONS

The commonly used method of Oliver & Pharr to calculate the hardness and modulus of a sample from an instrumented indentation measurement is only accurate when a small indentation is made on a large and homogeneous sample. If this same analysis is used for indentations in on other types of samples, such as a particle embedded in dissimilar matrix, the measured hardness and modulus are not equal to those of the particle alone, but are also affected by the properties of the matrix. Previous simulation work has shown that the effect of the matrix on such measurements is greater for greater mismatch between the properties of the particle and the matrix, but the complicated nature of these simulations do not lend themselves to a practical experimental solution to remove the effect of the matrix. Based on the assumption

that, for small enough relative indentation size, the effect certain elastic heterogeneities within a sample can be treated as some constant additional compliance that sums with the compliance measured during an instrumented indentation, Jakes, *et al*. have introduced simple experimental methods by which that constant additional compliance can be calculated and removed from the measurement. However, the most convenient of these methods (that which does not require multiple indentations to be made), requires that the sample material has no indentation size effect (ISE), a requirement that is not met by many materials of interest.

In this work, we extend and modify the method introduced by Jakes so that it can be accurately applied to embedded particle samples where the particle displays an ISE. We use simple dimensional analysis to show that the effect of the matrix in this scenario should be some constant additional compliance (like that considered by Jakes), which we call "matrix compliance." Here we suggest making linear fits to an iterative series of plots of measured compliance and assumed contact area data in order to account for the error in the calculated matrix compliance that is associated with the ISE. The efficacy of this new method is proven through experiments in bulk and embedded samples of calcite, a common and important material that we have shown to display a strong ISE (Chapter 4).

Unlike hardness, indentation modulus is not expected to vary with indentation size in pure materials. Our experiments in calcite show that the modulus measured using the unmodified Oliver & Pharr method on particles of calcite embedded in a more compliant matrix decreases with indentation size and is lower than the modulus measured on a bulk calcite control. After correction, the modulus measurements in the embedded calcite do not vary with indentation size and also match that of the bulk control. Hardness, which is less affected by the matrix material, shows ISE before correction, and retains ISE after correction. Thus, we have demonstrated that this

method does indeed work on a material with ISE. Furthermore, simple analysis of the calculated values of matrix compliance shows that this quantity is related to the size of the particle and the modulus of the matrix material.

Like Jakes' method, our approach is based on the assumption that the matrix compliance is independent of indentation size below some critical indentation size. While analysis of our data suggests that this assumption is true for the indentation sizes used here, the dimensional limits of this assumption remain an unanswered question. Further analysis of these limits may be well-suited to finite element analysis.

## 5.6. ACKNOWLEDGMENTS

This work was supported by the National Science Foundation (NSF) via the Materials World Network grant (DMR-1210304). Support for the experiments on shale was provided by the American Chemical Society Petroleum Research Fund via PRF grant-in-aid #52282-ND8, and in part by Cornell University's David R. Atkinson Center for a Sustainable Future (ACSF). Some work was performed in Cornell Center for Materials Research shared facilities (supported by NSF DMR-1120296), and also in Cornell NanoScale Facility. Many thanks to Seneca Stone Corp. for allowing us access to their Marcellus exposures, and to Hysitron, Inc. for providing the Baker group with the nanoindenter.

## 5.7. REFERENCES


1. Oliver, W.C. and G.M. Pharr, *AN IMPROVED TECHNIQUE FOR DETERMINING HARDNESS AND ELASTIC-MODULUS USING LOAD AND DISPLACEMENT SENSING INDENTATION EXPERIMENTS*. Journal of Materials Research, 1992. **7**(6): p. 1564-1583.

2. Oliver, W.C. and G.M. Pharr, *Measurement of hardness and elastic modulus by instrumented indentation: Advances in understanding and refinements to methodology*. Journal of Materials Research, 2004. **19**(1): p. 3-20.

3. Sneddon, I.N., *The relation between load and penetration in the axisymmetric boussinesq problem for a punch of arbitrary profile*. International Journal of Engineering Science, 1965. **3**(1): p. 47-57.

4. Doerner, M.F. and W.D. Nix, *A method for interpreting the data from depth-sensing indentation instruments*. Journal of Materials Research, 1986. **1**(4): p. 601-609.

5. King, R.B., *ELASTIC ANALYSIS OF SOME PUNCH PROBLEMS FOR A LAYERED MEDIUM*. International Journal of Solids and Structures, 1987. **23**(12): p. 1657-1664.

6. Gao, H.J., C.H. Chiu, and J. Lee, *ELASTIC CONTACT VERSUS INDENTATION MODELING OF MULTILAYERED MATERIALS*. International Journal of Solids and Structures, 1992. **29**(20): p. 2471-2492.

7. Rar, A., H. Song, and G.M. Pharr, *Assessment of new relation for the elastic compliance of a film-substrate system*, in *Thin Films: Stresses and Mechanical Properties IX*, C.S. Ozkan, et al., Editors. 2002, Materials Research Society: Warrendale. p. 431-436.

8. Saha, R. and W.D. Nix, *Effects of the substrate on the determination of thin film mechanical properties by nanoindentation*. Acta Materialia, 2002. **50**(1): p. 23-38.

9. Hay, J. and B. Crawford, *Measuring substrate-independent modulus of thin films*. Journal of Materials Research, 2011. **26**(6): p. 727-738.

10. Ma, Y., et al., *Sea urchin tooth design: An "All-Calcite" polycrystalline reinforced fiber composite for grinding rocks*. Advanced Materials, 2008. **20**(8): p. 1555-+.

11. Perez-Huerta, A., M. Cusak, and W. Zhu, *Assessment of crystallographic influence on material properties of calcite brachiopods*. Mineralogical Magazine, 2008. **72**(2): p. 563-568.

12. Schmahl, W.W., et al., *Hierarchical fibre composite structure and micromechanical properties of phosphatic and calcitic brachiopod shell biomaterials - an overview*. Mineralogical Magazine, 2008. **72**(2): p. 541-562.

13. Merkel, C., et al., *Mechanical properties of modern calcite- (Mergerlia truncata) and phosphate-shelled brachiopods (Discradisca stella and Lingula anatina) determined by nanoindentation*. Journal of Structural Biology, 2009. **168**(3): p. 396-408.

14. Kunitake, M.E., et al., *Evaluation of strengthening mechanisms in calcite single crystals from mollusk shells*. Acta Biomaterialia, 2013. **9**(2): p. 5353-5359.

15. Ulm, F.J., et al., *Statistical indentation techniques for hydrated nanocomposites: Concrete, bone, and shale*. Journal of the American Ceramic Society, 2007. **90**(9): p. 2677-2692.

16. Bennett, K.C., et al., *Instrumented nanoindentation and 3D mechanistic modeling of a shale at multiple scales*. Acta Geotechnica, 2015. **10**(1): p. 1-14.

17. Kim, Y.Y., et al., *Bio-Inspired Synthesis and Mechanical Properties of Calcite-Polymer Particle Composites*. Advanced Materials, 2010. **22**(18): p. 2082-+.

18. Kim, Y.Y., et al., *An artificial biomineral formed by incorporation of copolymer micelles in calcite crystals*. Nature Materials, 2011. **10**(11): p. 890-896.

19. Kunitake, M.E., S.P. Baker, and L.A. Estroff, *The effect of magnesium substitution on the hardness of synthetic and biogenic calcite*. Mrs Communications, 2012. **2**(3): p. 113-116.

20. Calvaresi, M., et al., *Morphological and mechanical characterization of composite calcite/SWCNT-COOH single crystals*. Nanoscale, 2013. **5**(15): p. 6944-6949.

21. Giosia, M.D., et al., *Bioinspired Nanocomposites: Ordered 2D Materials Within a 3D Lattice*. Advanced Functional Materials, 2016.

22. Kim, Y.-Y., et al., *Tuning hardness in calcite by incorporation of amino acids*. Nature materials, 2016.

23. Kim, Y.Y., et al., *Structure and Properties of Nanocomposites Formed by the Occlusion of Block Copolymer Worms and Vesicles Within Calcite Crystals*. Advanced Functional Materials, 2016. **26**(9): p. 1382-1392.

24. Cao, Y.Y., P.F. Duan, and J.J. Chen, *Modelling the nanomechanical response of a micro particle-matrix system for nanoindentation tests*. Nanotechnology, 2016. **27**(19): p. 10.

25. Durst, K., M. Goken, and H. Vehoff, *Finite element study for nanoindentation measurements on two-phase materials*. Journal of Materials Research, 2004. **19**(1): p. 85-93.

26. Leggoe, J.W., *Determination of the elastic modulus of microscale ceramic particles via nanoindentation*. Journal of Materials Research, 2004. **19**(8): p. 2437-2447.

27. Low, T.F., C.L. Pun, and W.Y. Yan, *Theoretical study on nanoindentation hardness measurement of a particle embedded in a matrix*. Philosophical Magazine, 2015. **95**(14): p. 1573-1586.

28. Yan, W.Y., C.L. Pun, and G.P. Simon, *Conditions of applying Oliver-Pharr method to the nanoindentation of particles in composites*. Composites Science and Technology, 2012. **72**(10): p. 1147-1152.

29. Yan, W.Y., et al., *Some issues on nanoindentation method to measure the elastic modulus of particles in composites*. Composites Part B-Engineering, 2011. **42**(8): p. 2093-2097.

30. Jakes, J.E., et al., *Nanoindentation near the edge*. Journal of Materials Research, 2009. **24**(3): p. 1016-1031.

31. Jakes, J.E., et al., *Experimental method to account for structural compliance in nanoindentation measurements*. Journal of Materials Research, 2008. **23**(4): p. 1113-1127.

32. Jakes, J.E. and D.S. Stone, *The edge effect in nanoindentation*. Philosophical Magazine, 2011. **91**(7-9): p. 1387-1399.

33. Stone, D.S., K.B. Yoder, and W.D. Sproul, *HARDNESS AND ELASTIC-MODULUS OF TIN BASED ON CONTINUOUS INDENTATION TECHNIQUE AND NEW CORRELATION*. Journal of Vacuum Science & Technology a-Vacuum Surfaces and Films, 1991. **9**(4): p. 2543-2547.

34. Joslin, D.L. and W.C. Oliver, *A NEW METHOD FOR ANALYZING DATA FROM CONTINUOUS DEPTH-SENSING MICROINDENTATION TESTS*. Journal of Materials Research, 1990. **5**(1): p. 123-126.

35. Nix, W.D. and H.J. Gao, *Indentation size effects in crystalline materials: A law for strain gradient plasticity*. Journal of the Mechanics and Physics of Solids, 1998. **46**(3): p. 411-425.

36. Ihli, J., et al., *Elucidating Mechanisms of Diffusion-Based Calcium Carbonate Synthesis Leads to Controlled Mesocrystal Formation*. Advanced Functional Materials, 2013. **23**(15): p. 1965-1973.

37. Loucks, R.G., et al., *MORPHOLOGY, GENESIS, AND DISTRIBUTION OF NANOMETER-SCALE PORES IN SILICEOUS MUDSTONES OF THE MISSISSIPPIAN BARNETT SHALE*. Journal of Sedimentary Research, 2009. **79**(11-12): p. 848-861.

38. Gerber, C.E., *Contact Problems For The Elastic Quarter-plane And For The Quarter-space*. Thesis, 1968.

39. Hetényi, M., *A Method of Solution for the Elastic Quarter-Plane*. Journal of Applied Mechanics, 1960. **27**(2): p. 289-296.

40. Stone, D.S., *Elastic rebound between an indenter and a layered specimen: Part I. Model*. Journal of Materials Research, 1998. **13**(11): p. 3207-3213.

41. Leisen, D., et al., *A novel and simple approach for characterizing the Young's modulus of single particles in a soft matrix by nanoindentation*. Journal of Materials Research, 2012. **27**(24): p. 3073-3082.

42. Maughan, M.R., M.T. Carvajal, and D.F. Bahr, *Nanomechanical testing technique for millimeter-sized and smaller molecular crystals*. International Journal of Pharmaceutics, 2015. **486**(1-2): p. 324-330.

43. Buckle, H., *Spezifische Anwendungen der Harteprufung nach Vickers mit kleinen Drufkaften*. VDI-Berichte, 1961. **41**: p. 14.

## CHAPTER 6

*Parts of this chapter planned to be submitted for publication

# Crystallization via an Amorphous Precursor Mechanically Strengthens Synthetic Calcite Single Crystals

Joseph D. Carloni, Matias Werner, Miki E. Kunitake, Lara A. Estroff, and Shefford P. Baker

*Cornell University, Department of Materials Science and Engineering, Bard Hall, Ithaca, NY 14853*

## ABSTRACT

Many biogenic calcite crystals are harder than pure and defect-free control calcite crystals, however, the origins of this strengthening are poorly understood. Biogenic calcite crystals are known to contain impurities and also to grow via non-classical growth mechanisms. While other studies have demonstrated the strengthening effects of impurities in synthetic calcite, to date, the effect of growth mechanism on hardness has not been investigated. Here, we test the relationship between the solution supersaturation and growth kinetics of calcite crystals, and the mechanical properties of the resulting crystals. *In-situ* observations of crystal growth from impurity-free solution as a function of supersaturation suggest that growth from the highest supersaturation solutions (90-1,000 mM $CaCl_2$) may occur via the formation of an amorphous precursor phase and/or particle attachment. Crystals grown from relatively low supersaturation solutions (10-15 mM) have an average hardness of 2.5 GPa, as measured by nanoindentation, that match that of a pure and defect free control, while those grown from the highest supersaturation solutions have an increase in average hardness of up to 44%. The increase in hardness for crystals grown via an amorphous precursor might be related to an increased density of crystallographic defects

introduced during growth. These results have important implications for better understanding the origins of strengthening in biogenic calcite and can inform the synthetic growth of harder minerals.

## 6.1. INTRODUCTION

The mechanical strength of biominerals (*e.g.*, calcite, $CaCO_3$) is of interest because living organisms successfully employ these inherently soft and brittle materials towards structural purposes by exploiting a hierarchical set of strengthening mechanisms. For example, the teeth, shells, and spines of many marine organisms (*e.g.*, sea urchins [1-6], brachiopods [7-10], and mollusks [11-25]) contain, or are entirely composed of, calcite. The polycrystalline and/or composite nature of these structures provides some strengthening, compared to a single crystal of calcite [26-28]. Additionally, small-scale mechanical testing (by nanoindentation) indicates that even the single crystals of calcite that make up these structures can be upwards of 60% harder than a pure and defect-free "control" calcite crystal measured at similar indentation size (Chapter 4). Hence, biogenic structures made of calcite exhibit strengthening at multiple length scales, even at the level of single crystals.

When discussing strengthening of a material, it is necessary to compare to some "control" state of that material. Relatively large and optically transparent, geologic single crystals, known as Iceland spar, are commonly used as control calcite crystals [30]. The optical transparency of Iceland spar crystals is related to the high degree of purity and crystallographic perfection of such crystals. Because of these characteristics, these crystals display smooth and flat facets of the naturally low-energy $\{10\bar{1}4\}$ cleavage planes, in the shape of a rhombohedron. Crystals of similar morphology, but usually of smaller size, can be reproduced synthetically by growth from solution at low supersaturation (*e.g.*, [31, 32]). Furthermore, we have recently shown that the hardness of such synthetic crystals is the same as that of Iceland spar crystals (Chapters 4 and 5). Hence, either Iceland spar, or synthetic calcite grown from low supersaturation solutions, can serve as good control crystals to compare to strengthened calcites.

Biogenic calcite crystals are different from control calcite in a variety of ways. One important difference is purity. Biogenic calcite crystals have been shown to contain inorganic and/or organic impurities [1, 4, 7, 20, 33]. Such impurities can act to block dislocation motion and increase the hardness of single crystals [34]. Calcite crystals containing a range of additives have also been grown synthetically, and their hardnesses measured by nanoindentation. For example, synthetic single crystals of calcite have been strengthened by the incorporation of $Mg^{2+}$, long-chain polymers, and small-molecule amino acids [35-38]. Hence, it is well established that impurities can strengthen calcite crystals, and probably play a significant role in the total strengthening observed in biogenic calcite. However, it is still not clear if impurities are the sole cause of strengthening in biogenic calcites, or if there might be other ways to strengthen calcite.

Besides impurities, another known difference between biogenic and pure control calcite is the growth mechanism. In contrast to "classical" ion-by-ion growth (*e.g.*, spiral growth via screw dislocations or 2-D nucleation of islands), which dominates during growth of pure calcite crystals at low supersaturations [39, 40], many biogenic calcite crystals are known to grow via an amorphous precursor phase (amorphous calcium carbonate, ACC) [41-45]. The subsequent transformation of the ACC to calcite has been proposed to go through either a solid state transformation[42-46] or a dissolution-reprecipitation pathway [47, 48]. Of importance to the current work, the initial formation of the ACC phase has been proposed to occur via attachment of ACC particles, possibly mediated by impurities [49-51].

Particle-attachment based growth mechanisms could have an effect on the mechanical properties of the resulting crystals due to the introduction of defects during growth. For a variety of synthetic single-crystal materials that formed via particle attachment without impurities (namely $TiO_2$ [52], PbSe [53], iron oxide [54], Pt [55],

and Au [56]), high-resolution TEM images have provided direct evidence of the creation of dislocations and/or twin boundaries at the attachment interface. High dislocation densities (*e.g.,* those induced by strain hardening [57]) are known to increase hardness. Thus, it seems possible that growth via particle attachment could increase hardness [16, 58], though to the best of our knowledge, this principle has not yet been demonstrated.

In this work, we have designed a synthetic experiment to test the possibility of tuning the hardness of calcite crystals without introducing impurities, by only varying the crystallization pathway by changing calcium concentration in the growth solution. The growth rates of the resultant crystals are measured *in-situ* under an optical microscope. Nanoindentation is used to measure the hardness and modulus of the resultant calcite crystals. To the best of our knowledge, this is the first report of linking the growth mechanism to the hardness of calcite crystals.

## 6.2. EXPERIMENTAL

### 6.2.1. *In-situ* growth experiments

Calcite crystals were precipitated onto glass slides from $CaCl_2$ solutions supersaturated with respect to $CaCO_3$ via the "ammonium diffusion method" [59]. A stock $CaCl_2$ solution (1,000 mM) was prepared by dissolving $CaCl_2$ powder (96% pure anhydrous, Acros Organics) into DI water. Lower concentration $CaCl_2$ solutions (as low as 10 mM) were created by diluting small batches of the stock solution with additional DI water. Most of the growth experiments were performed within a small, home-made chamber. This small polystyrene growth chamber (90 mm diameter and 20 mm tall; 12.7 mL volume) was optically transparent, to allow observation of the growth *in-situ* under an optical microscope, as illustrated schematically in Figure 6.1.

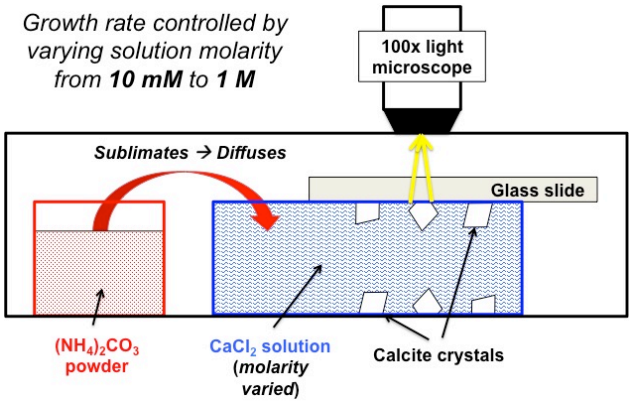


**Figure 6.1**: Schematic of *in-situ* growth setup. The $CaCl_2$ solution is supersaturated with respect to $CaCO_3$, via the "ammonium diffusion method." Heterogeneous nucleation and growth is observed and recorded *in-situ* via an optical microscope at 100x total magnification. The initial $CaCl_2$ concentration of the solution is varied from 10-1,000 mM.

Two smaller polystyrene dishes (35 mm diameter, 15 mm tall; 14.4 mL volume, 9.6 $cm^2$ surface area), one containing 0.5 g $(NH_4)_2CO_3$ powder (ACS reagent grade, Sigma Aldrich) and the other containing 3 mL $CaCl_2$ solution were placed within the growth chamber, and a glass slide was positioned across the $CaCl_2$ dish in such a way that only the bottom (under) side of the glass was in contact with the solution. Before positioning the glass slide, it was scratched with a diamond scribe near the center of the side that was to be placed in contact with the solution, in order to provide a clear feature on which to focus the microscope. Each growth experiment was started by sealing the growth chamber with a flexible film (Parafilm), and hence allowing the diffusion of $NH_3$ and $CO_2$ gas from the $(NH_4)_2CO_3$ powder into the $CaCl_2$ solution, raising the pH of the solution, and supersaturating it with respect to $CaCO_3$.

The initial concentration of the $CaCl_2$ solution in these experiments was varied from 10 mM to 1 M across five different concentrations (10, 90, 270, 810, and 1000 mM). Before the start of each growth experiment, the microscope (Leica DM EP) was adjusted to focus on the bottom side of the glass slide (using the scratch as a landmark), so as to observe the nucleation and growth of heterogeneously nucleated crystals only. In some trial experiments, we moved the microscope stage in *x* and *y* to view different portions of the slide at different times in the growth, and we confirmed that the growth proceeded in a similar way even in locations far from the scratch (except very close to the edge of the glass, where there was higher nucleation density). Hence, to allow for consistent measurement of individual crystals for the entire duration of their growth, the field of view remained fixed on the same area (near the scratch) in subsequent growths. Two of these fixed field of view recordings were performed for growths from solutions of each initial $Ca^{2+}$ concentration, to check for repeatability. Videos of these growths, using a 10x objective (100x total magnification), were recorded using a 1080p resolution camera installed above the

lens of the microscope (Leica MC120 HD). Recording was started at the time the growth chamber was sealed. The growth was observed real time via a live feed of the video, and the videos were later analyzed to compare the growth rates of calcite crystals in each experiment. In order to produce crystals of roughly the same size, each growth was stopped when the crystals grew to a size of ~25 $\mu$m on any visible edge, as estimated from the live video feed. For all initial $Ca^{2+}$ concentrations, this occurred within 80-90 minutes after sealing the chamber. At that point, the growth was stopped by removing the seal from the chamber, and immediately rinsing the glass slide with DI water and ethanol. Ultimately, this technique produced hundreds of randomly-oriented crystals evenly coating each glass slide.

The videos from these growth experiments were analyzed to determine the growth kinetics. Screenshots of the videos were taken at regular time intervals, and these images were further analyzed using ImageJ. From these screenshots, the projected (2D) areas of selected crystals were determined by tracing the outline of the crystal (using the "trace" tool) and calculating the area within the trace (using the "measure" tool).

### 6.2.2. *Ex-situ* growth experiments

In addition to the *in-situ* growths, three more growths were performed *ex-situ* in a larger, glass desiccator growth chamber (~10 L) sealed with vacuum grease. The same amounts of $(NH_4)_2CO_3$ powder and $CaCl_2$ solution were used as the *in-situ* growths (0.5 g and 3 mL, respectively), and a glass slide was positioned in the $CaCl_2$ dish in a similar manner. These growths were at similar initial $Ca^{2+}$ concentrations to some of the *in-situ* growths (*i.e.*, 15, 100, and 175 mM), to facilitate comparison between the sets. In contrast though, the *ex-situ* growths were instead allowed to continue for 24 hours before removing the seal and rinsing the slide. As such, the final crystal size was

not controlled in these experiments, and the crystals presumably grew until depleting the supply of $Ca^{2+}$ from the solution. Similar to the *in-situ* growths, these growths produced hundreds of randomly-oriented crystals evenly coating each glass slide.

### 6.2.3. Estimating supersaturation

We make an estimate for the initial supersaturation of our growth systems by assuming 5 mM $CO_3^{2-}$, pH = 8.5, and a $Ca^{2+}$ concentration equal to the initial $Ca^{2+}$ concentration of our solution. Inputting these values into the software package Visual MINTEQ (v3.1, J.P Gustafsson), we calculate $\sigma_{calcite} = 4.3$ for 10 mM $Ca^{2+}$, up to $\sigma_{calcite} = 6.5$ for 1,000 mM $Ca^{2+}$. These values are plotted (along with the same calculation at higher pH, to show sensitivity to pH) in Figure 6.2. The solubility limit of ACC, $\sigma_{calcite} = 4.8$, is indicated by a dashed line.

### 6.2.4. Nanoindentation measurements

The hardness and modulus of selected calcite crystals grown here were measured using a commercially available nanoindenter (Hysitron Ti-900) equipped with a Berkovich tip (with tip radius ~120 nm). A flat and smooth surface of the sample that is parallel to its substrate is required to make an accurate nanoindentation measurement. In general, the randomly-oriented calcite crystals grown here did not naturally display such surfaces. In Chapter 5, we developed a mounting and analysis technique that allows for accurate nanoindentation measurements to be made on small (< 100 $\mu$m) crystals similar to those grown here. In this work, the same technique is applied.

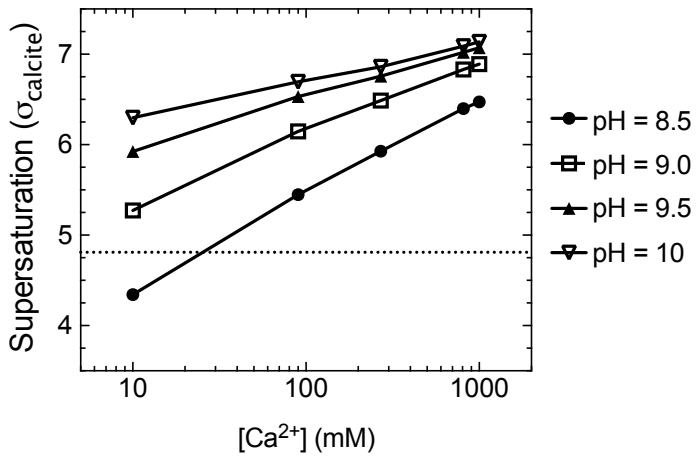


**Figure 6.2**: Supersaturations with respect to calcite plotted as a function of pH and [$Ca^{2+}$], calculated in MINTEQ, assuming 5 mM $CO_3^{2-}$, chosen as a reasonable estimate for our system in the early stages of growth.

For the mounting, in short: Crystals were embedded in glue on their original glass substrates, the glue was allowed to solidify and encapsulate the crystals, and then the solidified glue was peeled away from the glass, exposing the flat and smooth surface on which they initially grew (see Chapter 5). The embedded crystals were then mounted on the stage of the nanoindenter. This process was repeated for selected samples from both *in-situ* and *ex-situ* growths. Prior to indenting a crystal, the sample surface was scanned using the indenter tip as a SFM probe. From these scans, the boundaries of the crystal could be clearly distinguished from the surrounding embedding material, and the roughness on the crystal surface was measured to be <10 nm RMS over a 10 $\mu$m square.

For the testing and analysis, in short: For each crystal tested, a dynamic load function that increased from 2.5-10 mN in 0.5 mN steps was applied to create an indentation in the center of the crystal. The contact compliance at each load step was calculated by analyzing the amplitude of the displacement signal with a dynamic model [60]. These compliances were plotted versus the reciprocal square root of the calculated contact area in order to determine the effect of the embedding material on the measurement (the "matrix compliance"). Then the matrix compliance was subtracted from the measured compliances and displacements, and hardness and modulus were calculated from these corrected data (Chapter 5). As in previous chapters, for modulus we report the quantity $E_s/(1-\nu_s^2)$, which is the plane strain or "flexural" modulus of the sample. Here, we will simply refer to this quantity as the "indentation modulus."

From the *in-situ* growth experiments, samples grown at 10, 90, and 1000 mM were embedded for measurement. From the *ex-situ* growths, samples grown at 15, 100, and 175 mM were embedded for measurement. Within each sample, there were bundles of smaller crystals (<25 $\mu$m on edge) interspersed between larger crystals (always > 25

$\mu$m on edge). For consistency, only the larger crystals in each sample were considered for nanoindentation measurement. From each sample, 10 to 15 of these larger crystals (10 from each *in-situ* sample, and 15 from each *ex-situ* sample), covering some range of different crystal orientations, were selected to be measured.

At 2.5 mN load, the corrected contact depths ranged from 125-160 nm (with corresponding contact areas of 0.7-1.1 $\mu m^2$), and at 10 mN load the corrected contact depths ranged from 290-360 nm (with corresponding contact areas of 2.9-4.1 $\mu m^2$). The minimum load of 2.5 mN was chosen because it resulted in corrected contact depths of at least 120 nm, thus beyond the radius of rounding at the tip of our Berkovich indenter. At 10 mN, the maximum indentation diameter was < 1/10 the diameter of any tested crystal, thus we assume the indentations are small enough that the matrix compliance can be assumed to be constant (as in Chapter 5). Even after correction for matrix compliance, most indentations showed at least a slight size effect in hardness between 2.5 and 10 mN load (usually ~5% decrease), consistent with our findings in Chapter 4 (examples in Figure 6.3). There was no significant size effect in modulus, as expected. For consistency, we compare the measured values of hardness and modulus at 2.5 mN load only.

**a)**

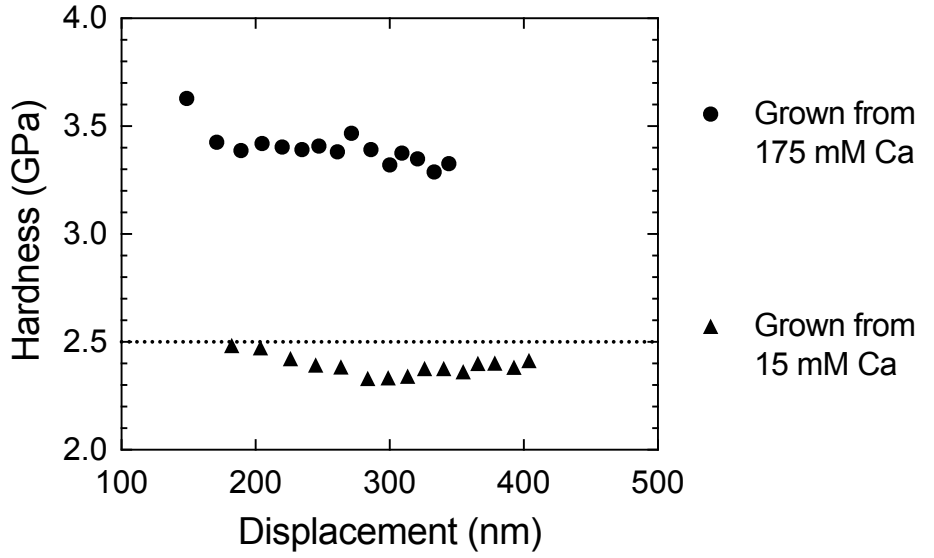


**b)**

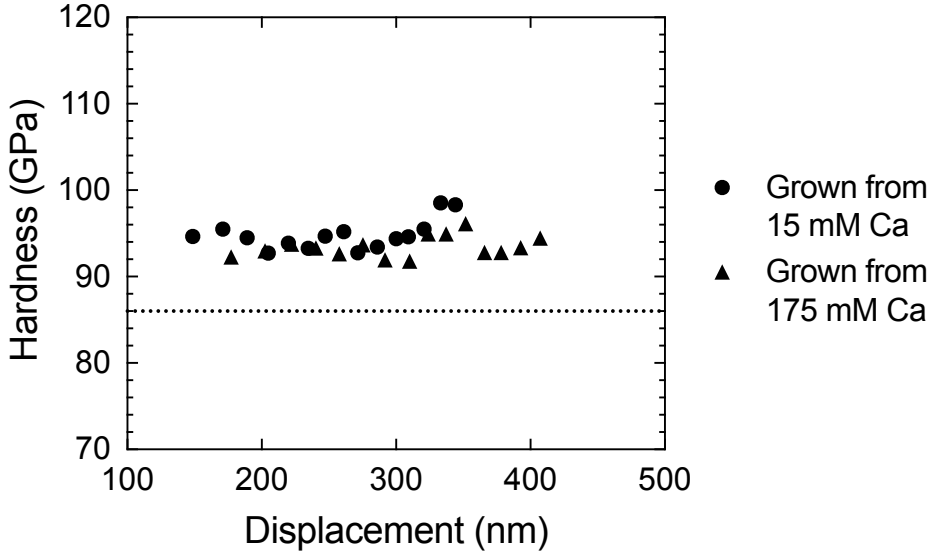


**Figure 6.3**: Example corrected a) hardness and b) modulus data versus indenter displacement from indentations on crystals grown from 15 mM and 175 mM initial $Ca^{2+}$ concentrations. Note that there is a small size effect in hardness, such that hardness decreases with increasing displacement (consistent with results in Chapter 5).

The size of the plastic deformation zone can be estimated by modeling the deformation zone as an expanding spherical cavity [61]. This leads to the following well-known relation:

$$\frac{c}{R} = \left(\frac{2E}{3\sigma_{ys}}\right)^{1/3} \quad (4)$$

where $c$ is the radius of the plastic zone, $R$ is the radius of the indentation, and $E$ and $\sigma_{ys}$ are the elastic modulus and yield strength of the material, respectively. Assuming the hardness is roughly 2.8x the yield strength in calcite [35], and inputting the average indentation modulus of Iceland spar calcite on the $(10\bar{1}4)$ face from Chapter 5 (87 GPa), we find $c/R = 4.1$. Thus, based on our average measured contact area at 2.5 mN load (~1.0 $\mu$m$^2$, or equivalently 1.1 $\mu$m diameter), we estimate that these indentations are plastically deforming a fraction of the crystal with diameter less than or equal to ~4.5 $\mu$m.

## 6.3. RESULTS

### 6.3.1. *In-situ* observation of crystal growth

We determined the effect of the initial concentration of $Ca^{2+}$ in the growth solution on the growth kinetics of calcite crystals. Each growth experiment involved a characteristic sequence of events, consistent with known theories of crystal nucleation and growth: Some initial incubation time before any crystals were visible on the glass surface, followed by a quick "burst" in which many crystals appeared on the glass all at once, then followed by a gradual increase in size of these crystals (see Figure 6.4). The initial incubation time and subsequent growth rates of calcite crystals were similar for each experiment performed at the same starting concentration of the growth solution, but varied between different concentrations.

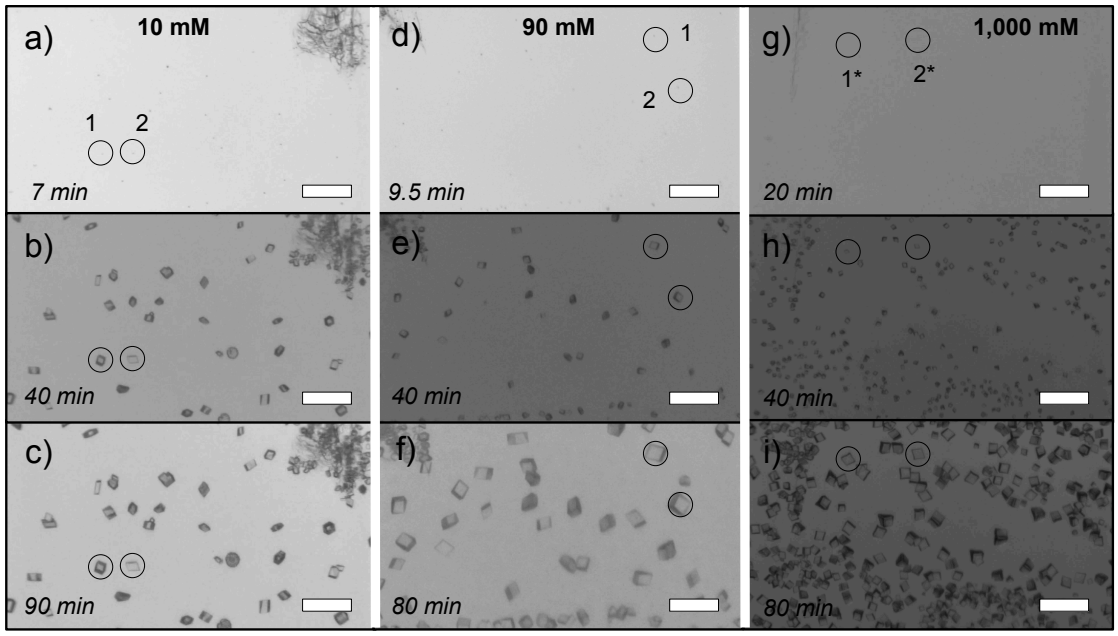


**Figure 6.4**: Screenshots of the growth experiments from $CaCl_2$ solutions with initial $Ca^{2+}$ concentrations of a-c) 10 mM, d-f) 90 mM, and g-i) 1,000 mM. The first image in each series (a,d, and g) shows the first appearance of crystals (dark spots) on the glass surface, the time for which increases with concentration (note: for 1,000 mM, the first appearance of crystals is not obvious because of the cloudy solution, hence the asterisks). The second image in each set shows crystals size at 40 min, and the third image in each set shows the final crystal size (shortly before growth was stopped). The scratch (used as landmark for focusing the microscope) is visible in each set (in the top right corner for a-c, and the top left corner for d-f and g-i). Note the consistent size of crystals within each set, and the difference in crystal size between each set. The circled crystals (labeled 1 and 2) were the ones that we tracked growth rates for from these videos (*i.e.*, 2 of the total 4 crystals tracked for that initial solution concentration).

During the initial incubation period, the growth solution would gradually become cloudy, especially at the higher solution concentrations. Eventually, many small (the smallest size easily measured in the videos, ~ 3-4 $\mu$m diameter) dark spots would appear on the glass slide in a single burst (all within a span of about 30 seconds), and then these spots would continue to grow to become larger calcite crystals. Within the 730 by 410 $\mu$m field of view of the video, tens of these spots would appear during this initial nucleation burst (examples in Fig. 6.4a,d,g). The total time elapsed before this initial burst increased with the initial $Ca^{2+}$ concentration of the solution.

Following the initial incubation period, we tracked the size and shape of the crystals to determine their growth rates as a function of initial $Ca^{2+}$ concentration. The majority of crystals at all concentrations are calcite, which can be distinguished from the other $CaCO_3$ polymorphs (aragonite and vaterite) by its characteristic faceted rhombohedral morphology. For the growths from higher solution concentrations (generally > 90 mM), we note that the edges of the calcite crystals tend to bow inward (*e.g.* Fig. 6.4f,i), consistent with the "hopper" morphology often observed for crystals grown at high rates [39]. Within any sample, the calcite crystals that appeared at the same time and were evenly spaced, seemed to grow at a similar rate (*i.e.*, had similar sizes at the same point in the growth). By focusing on crystals that grew such that a $\{10\bar{1}4\}$ facet is near parallel to the glass surface, we could estimate the average edge length and growth rate by measuring the projected area of the crystal. The square root of the projected area of such crystals is proportional to the average length of the edges bounding the $\{10\bar{1}4\}$ faces that are parallel to the glass. Assuming that all $\{10\bar{1}4\}$ faces grow at an equal rate, the rate of change of this average length divided by two should be proportional to the average growth rate normal to each $\{10\bar{1}4\}$ face of the crystal.

The final sizes of all crystals at the time growths were stopped (after 80-90 minutes) ranged from 20-30 $\mu$m on edge (see Figure 6.5a). Because the subsequent nanoindentation measurements only measure the mechanical properties of some fraction of each crystal (see Section 6.2.4), further analysis of the growth kinetics focused on the early stages of crystal growth. For the first 20 minutes of growth following the initial incubation time (*i.e.*, after the crystals reached a measurable size, the sizes of selected crystals were measured every 2 minutes (Figure 6.5b). During these first 20 minutes, the crystals grown from solutions with lower initial concentrations of $Ca^{2+}$ grew to larger sizes. At the two extremes: the crystals grown from the initially 1,000 mM $Ca^{2+}$ solution reached an average size of only ~10 $\mu$m on edge, and the crystals grown from the initially 10 mM $Ca^{2+}$ solution reached an average size of nearly 15 $\mu$m on edge.

To provide a more quantitative comparison of the different growth experiments, the data in Fig. 6.5b (average edge length *vs.* time) were fit using non-linear regression in a software program (GraphPad Prism 7). A second-order polynomial provided the best fit for the data from each growth experiment except for the 810 mM initial $Ca^{2+}$ growth, which was best fit by a straight line. The "initial time" ($x$-intercept) and "initial rate" ($y$'/2 at $x$ = initial time) were calculated from each of the fits (all values tabulated in Table 6.1). On average, the initial time increases with increasing initial $Ca^{2+}$ concentration, and the initial rate decreases with increasing initial $Ca^{2+}$ concentration (Figure 6.6).

**a)**

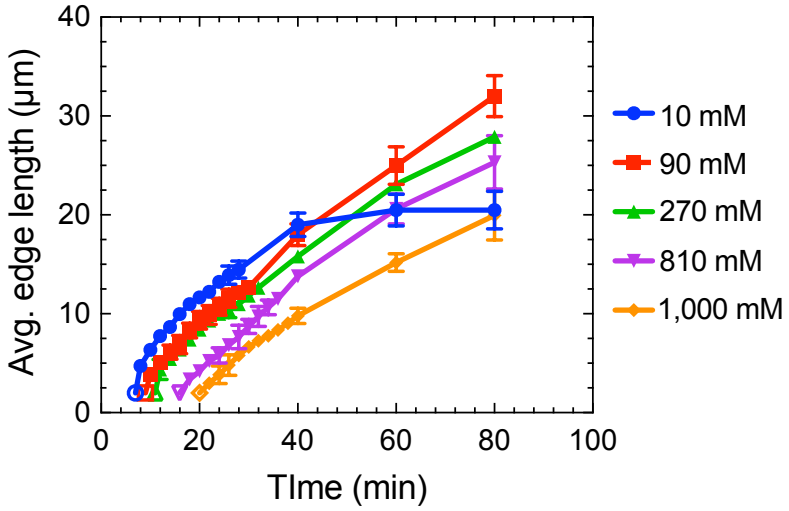


**b)**

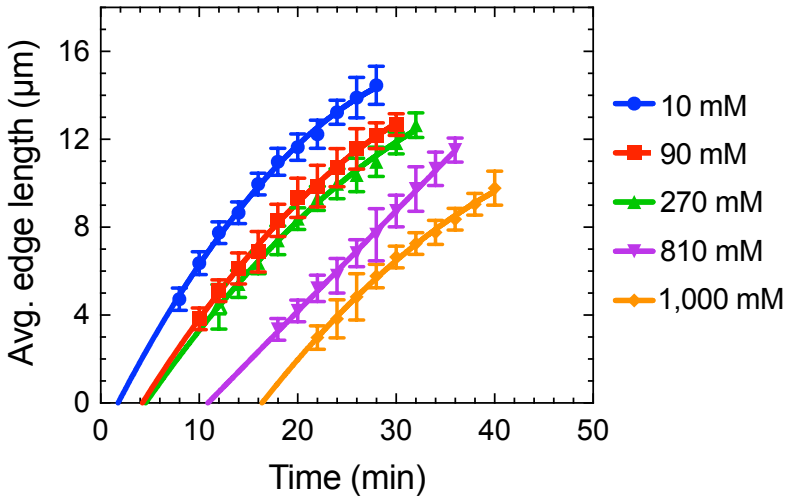


**Figure 6.5**: Plots showing the average measured sizes of crystals grown from solutions with different initial $Ca^{2+}$ concentrations. The average edge length is the square root of the measured area. The size at each time point is the average of all 4 crystals measured from that initial solution concentration, and the error bars are the standard deviations. a) All size measurements for the total 80 minutes of growth with data points connected as a guide to the eye, and b) zoom in on the same size data for the first 20 minutes of growth with polynomial best fit lines shown.

**Table 6.1**: Values calculated from fits to edge length *vs*. time data (Fig. 6.5b).[a]

| | 10 mM | 90 mM | 270 mM | 810 mM | 1000 mM |
|---|---|---|---|---|---|
| $B_0$ | -1.6 | -3.2 | -3.1 | -5.0 | -11.1 |
| $B_1$ | 0.90 | 0.78 | 0.71 | 0.46 | 0.79 |
| $B_2$ | -0.012 | -0.008 | -0.007 | 0 (linear) | -0.007 |
| $R^2$ | 0.998 | 0.998 | 0.997 | 0.998 | 0.997 |
| Initial time (min)[b] | 1.8 | 4.2 | 4.6 | 9.5 | 16.4 |
| Initial rate (nm/s)[c] | 7.2 +/- 0.69 | 5.9 +/- 0.72 | 5.4 +/- 1.1 | 3.8 +/- 0.59 | 4.7 +/-0.81 |

[a] Best-fit coefficients for fits to $y = B_0 + B_1 x + B_2 x^2$, and corresponding $R^2$ value indicating goodness of fit.

[b] "Initial time" is the *x*-intercept.

[c] "Initial rate" is *y*'/2 at *x* = initial time. The error bars on the rates are calculated based on the error bars on measured edge lengths. Derivative (*y*') is divided by two to be comparable with growth rate normal to $\{10\bar{1}4\}$ faces (as described in text).

**a)**

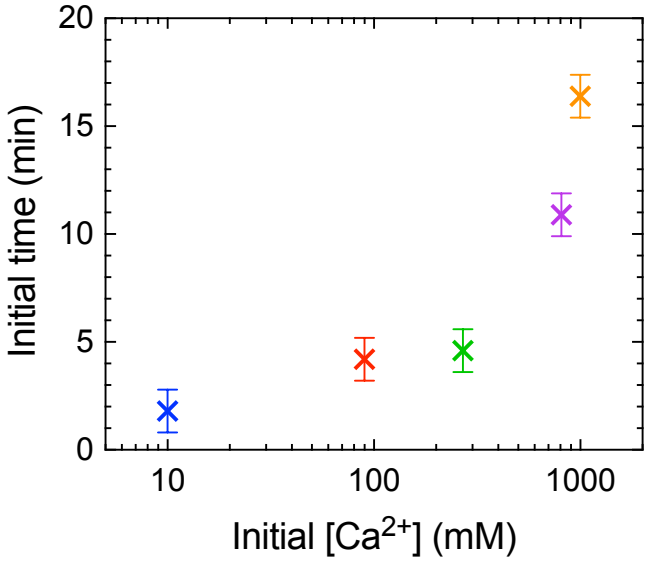


**b)**

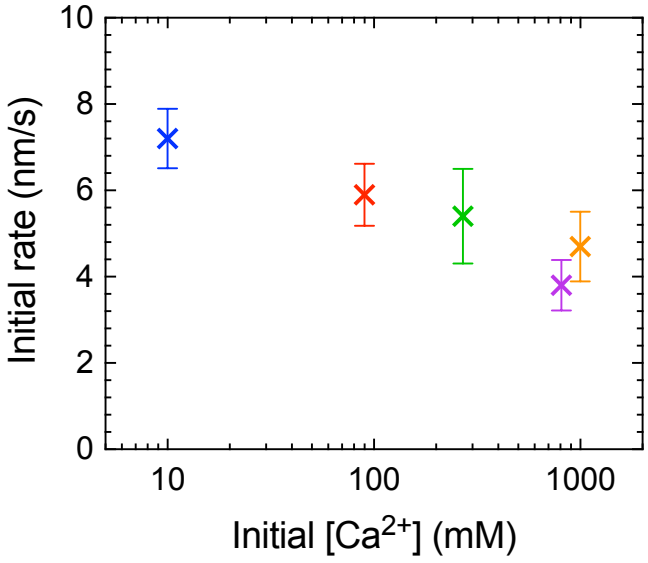


**Figure 6.6**: Plots of a) initial time, and b) initial rates of *in-situ* crystal growth versus the initial $Ca^{2+}$ concentrations of the solutions from which the crystals grew. These values were calculated from the fits to the data in Figure 6.5 (more info in Table 6.1). Note that the initial time increases rapidly with the initial $Ca^{2+}$ concentration, but the initial rate does not increase.

### 6.3.2. Crystals grown *ex-situ*

The *ex-situ* growth experiments were allowed to grow for a full 24 hours. Thus, the crystals grown at higher initial $Ca^{2+}$ concentrations had more time to grow, and reached larger final sizes (Figure 6.7). The crystals grown from 15 mM $Ca^{2+}$ reached a maximum size of approximately 25 $\mu$m (the same size at which the *in-situ* growths were stopped), while the crystals grown from 100 mM initial $Ca^{2+}$ grew to as large as 50 $\mu$m, and the crystals from 175 mM initial $Ca^{2+}$ grew to nearly 75 $\mu$m. The crystals from 15 mM initial $Ca^{2+}$ had the characteristic faceted rhombohedral morphology, while the crystals from 100 mM initial $Ca^{2+}$ had a hopper morphology, similar to what we started to observe happen in the higher solution concentrations *in-situ*. The crystals grown at 175 mM initial $Ca^{2+}$ had even more extremely bowed edges, taking on a star-like morphology, while still extinguishing light under cross-polarizers as single crystals (data not shown).

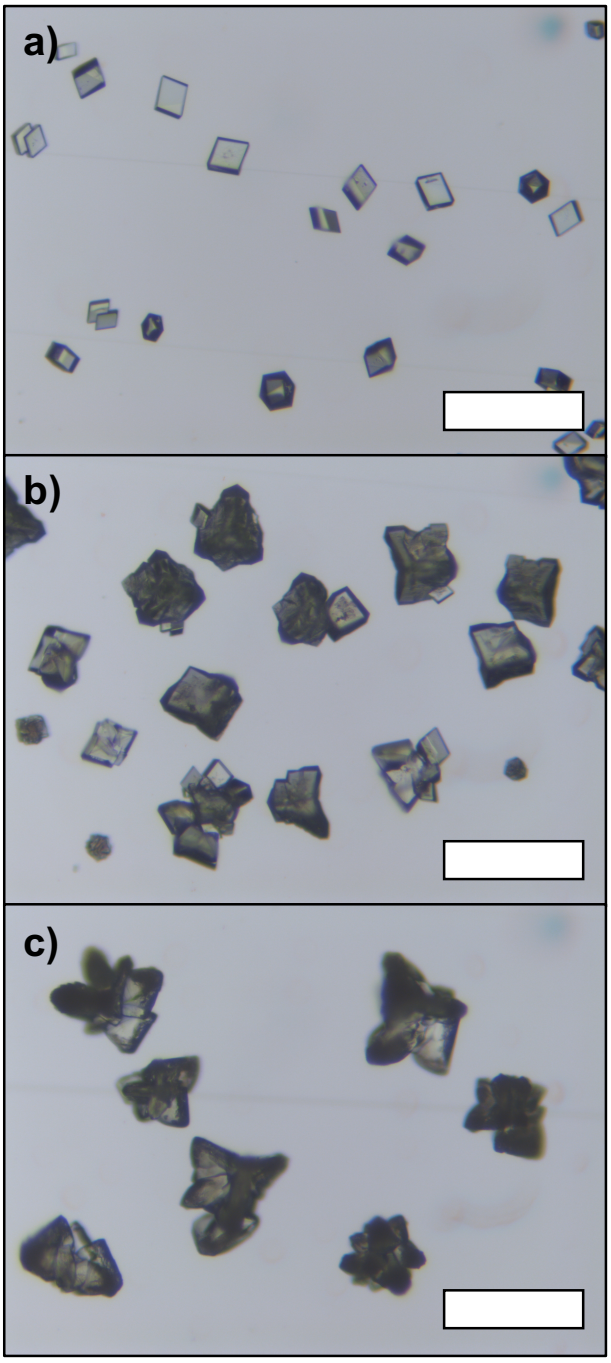


**Figure 6.7**: Optical microscope images of the final morphologies of crystal grown *ex-situ* for 24 hours from initial $Ca^{2+}$ concentrations of a) 15 mM, b) 100 mM, and c) 175 mM. Note the characteristic hopper morphology of the crystals grown from 100 and 175 mM initial $Ca^{2+}$ concentration.

### 6.3.3. Hardness and modulus measurements

The corrected hardness and indentation modulus measured for each crystal is plotted versus the initial $Ca^{2+}$ concentration of the solution from which it grew in Figures 6.8a and b, respectively. The average values measured on crystals grown from similar initial $Ca^{2+}$ concentrations are similar, regardless if the crystals were grown *in-situ* or *ex-situ*. For reference, we compare these measurements to the average values of hardness and indentation modulus measured on the $(10\bar{1}4)$ face of a pure geologic Iceland spar calcite crystal using the same loading function (from Chapter 5).

On average, the hardness of crystals grown from high initial $Ca^{2+}$ concentrations are higher than those grown from low initial $Ca^{2+}$ concentrations. The average hardness of crystals grown from either 10 or 15 mM initial $Ca^{2+}$ (2.6 and 2.5 GPa, respectively) is similar to the average hardness of Iceland spar (2.5 GPa). In contrast, the average hardness of crystals grown from 1,000 mM initial $Ca^{2+}$ is 3.6 GPa, 44 % higher than 2.5 GPa.

In contrast, the average indentation moduli of crystals grown from high initial $Ca^{2+}$ concentrations are lower than those grown from low initial $Ca^{2+}$ concentrations. In particular, the average indentation modulus of crystals grown from 1,000 mM initial $Ca^{2+}$ is 79 GPa, 15% lower than the average indentation modulus measured on crystals from 10 mM initial $Ca^{2+}$ (93 GPa). For comparison, the average indentation modulus on the $(10\bar{1}4)$ face of Iceland spar is 87 GPa.

**a)**

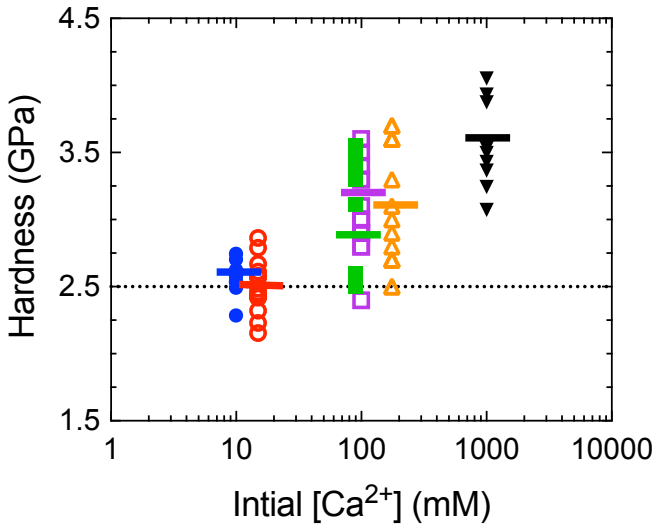


**b)**

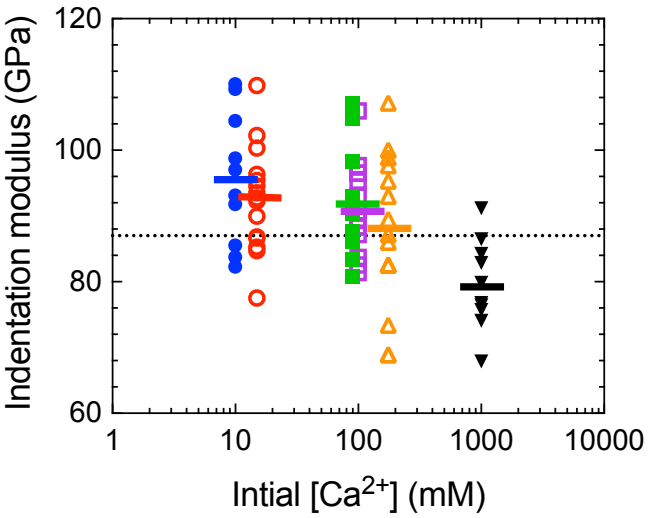


**Figure 6.8**: The corrected a) hardness and b) indentation modulus measured for each crystal at 2.5 mN load, plotted versus the initial $Ca^{2+}$ concentration of the solution from which it grew. Values measured on crystals grown from *in-situ* growth experiments are plotted with filled data symbols, and values measured on crystals grown *ex-situ* are plotted with open symbols. The horizontal dashed lines in a) and b) represent the average hardness or modulus (respectively) measured on the $(10\bar{1}4)$ face of a pure geologic Iceland spar calcite crystal.

## 6.4. DISCUSSION

### 6.4.1. Effect of solution concentration on growth kinetics

Calcite is the least soluble phase of $CaCO_3$, with $K_{sp,calcite} = 3.3 \times 10^{-9}$, and amorphous calcium carbonate (ACC) is the most soluble phase with $K_{sp,ACC} = 4.0{\times}10^{-7}$ [62]. Thus ACC, is 121 times more soluble than calcite, and unlikely to form in solution unless the ionic activity product is well above $K_{sp,ACC}$, *i.e.*, $\sigma_{calcite} \gg 4.8$. In the absence of ACC ($\sigma_{calcite} < 4.8$), calcite growth typically occurs by "classical," ion-by-ion growth mechanisms.

In the context of classical growth theory [39], the growth rate is expected to always increase with the supersaturation of the solution, the exact form of this relationship depending on the specific growth mechanism, *e.g.*, continuous "adhesive growth", 2-D island nucleation, or spiral growth via screw dislocations. Here we observe the opposite trend: That is, with increase of the initial $Ca^{2+}$ concentration (presumably increasing the initial supersaturation) there is both an increase in the initial incubation time, and a decrease in the subsequent growth rate. To help understand these observations, first we consider some features of the ammonium diffusion growth method used here.

The ammonium diffusion method has been widely applied to grow calcite crystals, and many aspects of this method have been described in detail elsewhere [59]. In short, the $(NH_4)_2CO_3$ powder spontaneously sublimates into $NH_3$ and $CO_2$ gas, and these gases diffuse into the $CaCl_2$ solution. The dissolved $CO_2$ gas forms carbonate and bicarbonate in the solution, and the ratio of these ions is determined by the pH of the solution (more carbonate at higher pH). Simultaneously, the $NH_3$ gas increases the pH of the solution, and thus the $Ca^{2+}$ ions combine with carbonate to supersaturate the solution with respect to $CaCO_3$. Thus, the concentration of $CO_3^{2-}$, and hence the

magnitude of $\sigma$, are related to the rate of diffusion of the $NH_3$ and $CO_2$ gases into the $CaCl_2$ solution.

Ihli, *et al*. have characterized many of the features related to the ammonium diffusion growth method for initial $CaCl_2$ concentrations ranging from 10-50 mM [59]. Notably, they measure pH, and $Ca^{2+}$ and $CO_3^{2-}$ concentrations *in-situ* over time, but not the growth rate (change in crystal size over time) that we measured here. Thus, we can compare and contrast our results. For one, they also show an increase in "induction time" (time before detectable formation of $CaCO_3$ precipitate, determined by transmission of light through the solution) with increasing $Ca^{2+}$ concentration, which matches the trend in initial incubation time that we observe here (Fig. 6.6a). Additionally, they calculate the supersaturation as a function of time and show that, coincident with the induction point, the supersaturation of the solution rapidly increases to a maximum level that is proportional to the initial $Ca^{2+}$ concentration, and is above the solubility of ACC ($i.e.$, $\sigma_{calcite} > 4.8$), even for initial $Ca^{2+}$ concentration as low as 10 mM.

Because Ihli, *et al*. use a much large volume of growth solution (70 mL vs. 3 mL) and a much larger growth chamber (2.6 L vs. 12.7 mL) than we use in the *in-situ* experiments here, the supersaturation in our system is most likely different than theirs. We have estimated the initial supersaturations of our system by making a conservative estimate for the initial concentration of $CO_3^{2-}$ (Fig. 6.2). Based on these estimates, it is clear that growth from this system at the higher initial $Ca^{2+}$ concentrations (> 15 mM) used here likely occurs at supersaturation levels near or above the threshold level for ACC formation.

We hypothesize that the formation of ACC particles before and during the growth of the larger calcite crystals may explain the non-classical trend in initial incubation times and growth rates that we observe here. For example, calcite has been shown to

grow after an initial formation of ACC and/or vaterite, especially at relatively high supersaturations [62-64]. Thus, the increase in initial incubation times with initial $Ca^{2+}$ concentration we measure here might be related to an increased tendency to form such ACC particles before calcite at the higher supersaturations. Additionally, in the presence of ACC particles, calcite growth has been shown to proceed via particle attachment, which may occur in parallel with classical ion-by-ion processes, thus maintaining the faceted calcite morphology (like the crystals we observe here) [50, 65]. The rate laws describing the growth of calcite via particle attachment are not known [65]. However, it has been shown that the average size of ACC particles in supersaturated solution increases with supersaturation [66], and it has been shown that the rate of crystal growth by oriented particle attachment decreases with increasing particle size [67]. Tying these pieces of evidence together, it seems that the observation here (growth rate of calcite crystals not increasing with supersaturation) is consistent with growth occurring via attachment of ACC particles.

Finally, we also note that the solution stoichiometry (ratio of $Ca^{2+}$ to $CO_3^{2-}$ ions) for growth via ammonium diffusion is not constant. Ihli *et al*. show that the $Ca^{2+}$ concentration steadily decreases (because the finite supply of $Ca^{2+}$ is depleted as $CaCO_3$ precipitates), and the $CO_3^{2-}$ concentration steadily increases (as the excess of $NH_3$ and $CO_2$ gas continue their slow, surface controlled diffusion into the growth solution) [59]. This creates a situation where the ratio of $Ca^{2+}$/ $CO_3^{2-}$ must be constantly decreasing during growth. $Ca^{2+}$/ $CO_3^{2-}$ ratios not equal 1 have been shown to result in slower growth rates of calcite by spiral growth (at low $\sigma$) [68-72], but it is not clear what effect this ratio might have on the growth rate of calcite via particle attachment.

### 6.4.2. Effect of initial $Ca^{2+}$ concentration on hardness

The key result here is that the average indentation hardness of the calcite crystals increases with the initial $Ca^{2+}$ concentration of the pure $CaCl_2$ solution from which they grew. In Chapter 4, we show that there is an indentation size effect (ISE) in calcite, such that the measured hardness decreases as the indentation size increases, and that due to the anisotropy of the slip and twin systems in calcite, there is a small (~12 %) decrease in hardness for indentations made at special orientations where mechanical twins can form, and a relatively large difference in indentation modulus (~23 %) between measurements on different crystal planes. Since we only compare the hardness measured at one load (2.5 mN), we expect that the ISE should not play a role in our comparisons. Furthermore, since measurements were made across multiple (10 to 15) randomly-oriented crystals from each growth condition, we expect that any anisotropy effects should average out in a similar way for each sample set. Thus, crystal anisotropy probably contributes to at least some of the variation within any set of measurements on crystals from one initial $Ca^{2+}$ concentration, but should not explain the variations in the averages between the different sets. Also, the indentations were corrected for the effect of the compliant matrix in which they had to be embedded prior to indentation, so we expect the measured values to represent the properties of the crystals only.

The indentations on these crystals were analyzed at low enough maximum load (2.5 mN) that they are below the cracking threshold in calcite at most crystal orientations (*e.g.*, see similar indentations in Chapters 4 and 5), so we expect the measured hardnesses to primarily be a measure of resistance to plastic deformation. In a crystalline material like calcite, plastic deformation occurs by dislocation slip. Thus, an increased hardness means an increased resistance to dislocation slip. Indentation experiments on certain biogenic [29] and synthetic [35, 36, 38, 73-76] single crystals

of calcite have also shown an increased hardness, compared to a pure control crystal measured at the same load. However, to the best of our knowledge, existing reports of increased hardness in calcite crystals can all be explained by the presence of impurities within the crystals. Here, we grew crystals from a $CaCl_2$ solution, in the absence of any impurities, thus the cause of this increase in hardness cannot be the usual impurity strengthening mechanism, as described elsewhere [35-38]. Instead, the strengthening must be explained by other crystallographic defects that can impede dislocation motion. For example, high dislocation densities and/or the presence of voids could impede the motion of geometrically necessary dislocations generated during indentation, and increase the measured hardness.

Since the growth rates of crystals measured here do not increase with the initial $Ca^{2+}$ concentration in the solutions from which they grew, defects in these crystals cannot simply be remnants of classical growth mechanisms at higher growth rates. For example, in the regime of supersaturations where growth is dominated by spiral dislocations and/or 2D nucleation, growth at higher rates is associated with increased density of kinks on the growing crystal surface (which may be incorporated into the final crystal), as well as an increased tendency to occlude small pockets of the growth solution liquid within the crystal [39]. But since the defects in our crystals apparently do not track with growth rate, then where do the defects come from? Since we have established that the supersaturations in our growth experiments (especially those with initial $Ca^{2+}$ concentration > 15 mM) are likely above the threshold for ACC formation ($\sigma_{calcite} = 4.8$), and thus also beyond the regime where classical ion-by-ion growth should dominate, we consider how non-classical growth by particle attachment might create crystallographic defects.

Prevailing theories to describe non-classical growth of calcite suggest that growth by attachment of large (> 10 nm) ACC particles may occur simultaneously with ion-

by-ion growth [50, 65]. One theory is that under certain conditions ACC particles in solution migrate towards a growing surface of a calcite crystal, diffusion and surface tension will favor its movement towards growing steps and kinks on the crystal surface, where the ACC particle will land and crystallize in alignment with the lattice of the growing crystal [50]. In this way, faceted calcite crystals can form even when grown via an amorphous precursor, and *in-situ* AFM of a growing calcite facet exposed to ACC particles has provided direct evidence for this type of behavior [65]. Because of the faceted morphology of the crystals grown here, we speculate that this kind of particle attachment growth may be occurring here.

Growth by attachment of nanocrystalline particles has been demonstrated to generate dislocations to accommodate any difference in orientation between adjacent particles [52-56]. It is unknown how the attachment of amorphous ACC particles could also create defects, but it has been suggested as a possibility [16, 58]. Determining the exact mechanism for defect creation is difficult since the exact mechanism controlling the transformation from ACC to calcite after attachment is not known, and may involve a solid-state transformation and/or an interface-coupled dissolution-reprecipitation mechanism [50]. We can imagine ways in which either could cause defects: (1) The change in density associated with a solid state transformation would have to leave gaps between the initially spherical ACC particles, and it is not clear how those would be filled. Or (2) if there was any poorly crystalline intermediate involved in dissolution-reprecipitation [77] then dislocations or voids might have to accommodate any difference in orientation that occurred during this process. The decrease in the average modulus of the crystals grown at higher initial $Ca^{2+}$ concentrations (especially those grown at 1,000 mM initial $Ca^{2+}$), is consistent with the accumulation of voids. As a rough estimate (using the rule of mixtures), the percent decrease in modulus of a crystal containing voids (compared to the same

crystal without voids) should be equal to the volume fraction of voids. This calculation suggests that the crystals grown from 1,000 mM initial $Ca^{2+}$ might contain ~15% void space on average.

## 6.5. CONCLUSION

By using straightforward solution growth of calcite, we have demonstrated that the hardness of synthetic calcite crystals can be increased by simply increasing the supersaturation of the growth solution. Of particular importance, unlike in other studies of synthetic calcite, the calcite is grown without the addition of any impurities, and still exhibits increased hardness as compared to controls. Our results show that the average hardness of calcite crystals increases with the initial supersaturation of the solution from which they grow, from an average hardness that closely matches that of an Iceland spar control at low initial supersaturation, to a 44% increase in hardness at the highest initial supersaturation. Since we have not added impurities to the growth solution, the strengthening must be explained by other crystallographic defects that can impede dislocation motion (*e.g.*, dislocation tangles and/or voids). The decrease in the average indentation modulus of the crystals grown at the higher initial supersaturations is consistent with the inclusion of such crystallographic defects. Furthermore, *in-situ* observation of the growth of these crystals shows that the growth kinetics (especially the initial incubation time) change with initial supersaturation in a way that is consistent with non-classical mechanisms of growth that involve the formation of ACC particles before calcite growth. Based on these results, we speculate that growth via ACC may lead to the incorporation of crystallographic defects within pure calcite crystals, in such a way that increases hardness and/or reduces modulus. These results have important implications towards better understanding the origins of the increased hardness of many biogenic and synthetic calcite crystals.

## 6.6. ACKNOWLEDGMENTS

This work was supported by the National Science Foundation (NSF) via the Materials World Network grant (DMR-1210304). We also acknowledge support from NSF (DMR 0845212), the J.D. Watson Investigator Program (NYSTAR Contract #C050017), the Cornell Center for Materials Research (CCMR), a Materials Research Science and Engineering Center of the National Science Foundation (DMR 1120296), the GI Bill (Chapter 33), and Hysitron, Inc.

## 6.7. REFERENCES


1. Wang, R.Z., L. Addadi, and S. Weiner, *Design strategies of sea urchin teeth: Structure, composition and micromechanical relations to function*. Philosophical Transactions of the Royal Society of London Series B-Biological Sciences, 1997. **352**(1352): p. 469-480.

2. Ma, Y., et al., *Sea urchin tooth design: An "All-Calcite" polycrystalline reinforced fiber composite for grinding rocks*. Advanced Materials, 2008. **20**(8): p. 1555-+.

3. Goetz, A.J., et al., *Tailored order: The mesocrystalline nature of sea urchin teeth*. Acta Biomaterialia, 2014. **10**(9): p. 3885-3898.

4. Moureaux, C., et al., *Structure, composition and mechanical relations to function in sea urchin spine*. Journal of Structural Biology, 2010. **170**(1): p. 41-49.

5. Presser, V., et al., *Determination of the elastic modulus of highly porous samples by nanoindentation: a case study on sea urchin spines*. Journal of Materials Science, 2010. **45**(9): p. 2408-2418.

6. Lemloh, M.L., et al., *Low Mg/Ca ratio alters material properties in sea urchin larvae skeleton*. Bioinspired Biomimetic and Nanobiomaterials, 2013. **2**(1): p. 28-34.

7. Griesshaber, E., et al., *Crystallographic texture and microstructure of terebratulide brachiopod shell calcite: An optimized materials design with hierarchical architecture*. American Mineralogist, 2007. **92**(5-6): p. 722-734.

8. Schmahl, W.W., et al., *Hierarchical fibre composite structure and micromechanical properties of phosphatic and calcitic brachiopod shell biomaterials - an overview*. Mineralogical Magazine, 2008. **72**(2): p. 541-562.

9. Perez-Huerta, A., et al., *Material properties of brachiopod shell ultrastructure by nanoindentation*. Journal of the Royal Society Interface, 2007. **4**(12): p. 33-39.

10. Merkel, C., et al., *Mechanical properties of modern calcite- (Mergerlia truncata) and phosphate-shelled brachiopods (Discradisca stella and Lingula anatina) determined by nanoindentation*. Journal of Structural Biology, 2009. **168**(3): p. 396-408.

11. Beniash, E., et al., *Elevated level of carbon dioxide affects metabolism and shell formation in oysters Crassostrea virginica*. Marine Ecology Progress Series, 2010. **419**: p. 95-108.

12. Lee, S.W., et al., *Mechanical characteristics and morphological effect of complex crossed structure in biomaterials Fracture mechanics and microstructure of chalky layer in oyster shell*. Micron, 2011. **42**(1): p. 60-70.

13. Dickinson, G.H., et al., *Interactive effects of salinity and elevated CO2 levels on juvenile eastern oysters, Crassostrea virginica*. Journal of Experimental Biology, 2012. **215**(1): p. 29-43.

14. Ivanina, A.V., et al., *Interactive effects of elevated temperature and CO2 levels on energy metabolism and biomineralization of marine bivalves Crassostrea virginica and Mercenaria mercenaria*. Comparative Biochemistry and Physiology a-Molecular & Integrative Physiology, 2013. **166**(1): p. 101-111.

15. Lombardi, S.A., et al., *Shell Hardness and Compressive Strength of the Eastern Oyster, Crassostrea virginica, and the Asian Oyster, Crassostrea ariakensis*. Biological Bulletin, 2013. **225**(3): p. 175-183.

16. Olson, I.C., et al., *Crystal lattice tilting in prismatic calcite*. Journal of Structural Biology, 2013. **183**(2): p. 180-190.

17. Metzler, R.A., et al., *Composition and Structure of Oyster Adhesive Reveals Heterogeneous Materials Properties in a Biological Composite*. Advanced Functional Materials, 2016. **26**(37): p. 6814-6821.

18. Lee, S.W., G.H. Kim, and C.S. Choi, *Characteristic crystal orientation of folia in oyster shell, Crassostrea gigas*. Materials Science & Engineering C-Biomimetic and Supramolecular Systems, 2008. **28**(2): p. 258-263.

19. Schneider, A.S., et al., *Hierarchical super-structure identified by polarized light microscopy, electron microscopy and nanoindentation: Implications for the limits of biological control over the growth mode of abalone sea shells*. Bmc Biophysics, 2012. **5**.

20. Kunitake, M.E., et al., *Evaluation of strengthening mechanisms in calcite single crystals from mollusk shells*. Acta Biomaterialia, 2013. **9**(2): p. 5353-5359.

21. Li, L. and C. Ortiz, *Pervasive nanoscale deformation twinning as a catalyst for efficient energy dissipation in a bioceramic armour*. Nature Materials, 2014. **13**(5): p. 501-507.

22. Metzger, T.H., et al., *Nanostructure of Biogenic Calcite and Its Modification under Annealing: Study by High-Resolution X-ray Diffraction and Nanoindentation*. Crystal Growth & Design, 2014. **14**(10): p. 5275-5282.

23. Fitzer, S.C., et al., *Ocean acidification alters the material properties of Mytilus edulis shells*. Journal of the Royal Society Interface, 2015. **12**(103).

24. Lv, J.L., Y.G. Jiang, and D.Y. Zhang, *Structural and Mechanical Characterization of Atrina Pectinata and Freshwater Mussel Shells*. Journal of Bionic Engineering, 2015. **12**(2): p. 276-284.

25. Chen, G.W., et al., *Vertically oriented structure and its fracture behavior of the Indonesia white-pearl oyster*. Journal of the Mechanical Behavior of Biomedical Materials, 2017. **66**: p. 211-223.

26. Dunlop, J.W.C. and P. Fratzl, *Biological Composites*. Annual Review of Materials Research, 2010. **40**(1): p. 1-24.

27. Ji, B. and H. Gao, *Mechanical Principles of Biological Nanocomposites*. Annual Review of Materials Research, 2010. **40**(1): p. 77-100.

28. Meyers, M.A., et al., *Biological materials: Structure and mechanical properties*. Progress in Materials Science, 2008. **53**(1): p. 1-206.

30. Miers, H.A., *Mineralogy: an introduction to the scientific study of minerals*. 1902: Macmillan and Company, limited.

31. Aizenberg, J., A.J. Black, and G.M. Whitesides, *Control of crystal nucleation by patterned self-assembled monolayers*. Nature, 1999. **398**(6727): p. 495-498.

32. Addadi, L., et al., *A CHEMICAL-MODEL FOR THE COOPERATION OF SULFATES AND CARBOXYLATES IN CALCITE CRYSTAL NUCLEATION - RELEVANCE TO BIOMINERALIZATION*. Proceedings of the National Academy of Sciences of the United States of America, 1987. **84**(9): p. 2732-2736.

33. Li, H.Y., et al., *Calcite Prisms from Mollusk Shells (Atrina Rigida): Swiss-cheese-like Organic-Inorganic Single-crystal Composites*. Advanced Functional Materials, 2011. **21**(11): p. 2028-2034.

34. Courtney, T.H., *Mechanical behavior of materials*. 2005: Waveland Press.

35. Kim, Y.-Y., et al., *Tuning hardness in calcite by incorporation of amino acids*. Nature materials, 2016.

36. Kim, Y.Y., et al., *An artificial biomineral formed by incorporation of copolymer micelles in calcite crystals*. Nature Materials, 2011. **10**(11): p. 890-896.

37. Kunitake, M.E., S.P. Baker, and L.A. Estroff, *The Effect of Magnesium Substitution on the Hardness of Synthetic and Biogenic Calcite (vol 2, pg 113, 2012)*. Mrs Communications, 2013. **3**(1): p. 79-79.

38. Kim, Y.Y., et al., *Structure and Properties of Nanocomposites Formed by the Occlusion of Block Copolymer Worms and Vesicles Within Calcite Crystals*. Advanced Functional Materials, 2016. **26**(9): p. 1382-1392.

39. Sunagawa, I., *Crystals: Growth, Morphology, & Perfection*. 2005: Cambridge University Press.

40. Teng, H.H., P.M. Dove, and J.J. De Yoreo, *Kinetics of calcite growth: Surface processes and relationships to macroscopic rate laws*. Geochimica Et Cosmochimica Acta, 2000. **64**(13): p. 2255-2266.

41. Addadi, L., S. Raz, and S. Weiner, *Taking advantage of disorder: Amorphous calcium carbonate and its roles in biomineralization*. Advanced Materials, 2003. **15**(12): p. 959-970.

42. DeVol, R.T., et al., *Nanoscale Transforming Mineral Phases in Fresh Nacre*. Journal of the American Chemical Society, 2015. **137**(41): p. 13325-13333.

43. Gong, Y.U.T., et al., *Phase transitions in biogenic amorphous calcium carbonate*. Proceedings of the National Academy of Sciences of the United States of America, 2012. **109**(16): p. 6088-6093.

44. Politi, Y., et al., *Transformation mechanism of amorphous calcium carbonate into calcite in the sea urchin larval spicule*. Proceedings of the National Academy of Sciences of the United States of America, 2008. **105**(45): p. 17362-17366.

45. Radha, A.V., et al., *Transformation and crystallization energetics of synthetic and biogenic amorphous calcium carbonate*. Proceedings of the National Academy of Sciences of the United States of America, 2010. **107**(38): p. 16438-16443.

46. Killian, C.E., et al., *Mechanism of Calcite Co-Orientation in the Sea Urchin Tooth*. Journal of the American Chemical Society, 2009. **131**(51): p. 18404-18409.

47. Aizenberg, J., et al., *Direct fabrication of large micropatterned single crystals*. Science, 2003. **299**(5610): p. 1205-1208.

48. Lee, J.R.I., et al., *Structural development of mercaptophenol self-assembled monolayers and the overlying mineral phase during templated CaCO3 crystallization from a transient amorphous film*. Journal of the American Chemical Society, 2007. **129**(34): p. 10370-10381.

49. De Yoreo, J.J., et al., *CRYSTAL GROWTH. Crystallization by particle attachment in synthetic, biogenic, and geologic environments*. Science, 2015. **349**(6247): p. aaa6760.

50. Gal, A., et al., *Particle Accretion Mechanism Underlies Biological Crystal Growth from an Amorphous Precursor Phase*. Advanced Functional Materials, 2014. **24**(34): p. 5420-5426.

51. Gal, A., S. Weiner, and L. Addadi, *A perspective on underlying crystal growth mechanisms in biomineralization: solution mediated growth versus nanosphere particle accretion*. CrystEngComm, 2015. **17**(13): p. 2606-2615.

52. Penn, R.L. and J.F. Banfield, *Imperfect oriented attachment: Dislocation generation in defect-free nanocrystals*. Science, 1998. **281**(5379): p. 969-971.

53. van Huis, M.A., et al., *Low-Temperature Nanocrystal Unification through Rotations and Relaxations Probed by in Situ Transmission Electron Microscopy*. Nano Letters, 2008. **8**(11): p. 3959-3963.

54. Li, D.S., et al., *Direction-Specific Interactions Control Crystal Growth by Oriented Attachment*. Science, 2012. **336**(6084): p. 1014-1018.

55. Ruan, L.Y., et al., *A Rational Biomimetic Approach to Structure Defect Generation in Colloidal Nanocrystals*. Acs Nano, 2014. **8**(7): p. 6934-6944.

56. Lange, A.P., et al., *Dislocation mediated alignment during metal nanoparticle coalescence*. Acta Materialia, 2016. **120**: p. 364-378.

57. Mecking, H. and U.F. Kocks, *KINETICS OF FLOW AND STRAIN-HARDENING*. Acta Metallurgica, 1981. **29**(11): p. 1865-1875.

58. Zhang, H.Z., J.J. De Yoreo, and J.F. Banfield, *A Unified Description of Attachment-Based Crystal Growth*. Acs Nano, 2014. **8**(7): p. 6526-6530.

59. Ihli, J., et al., *Elucidating Mechanisms of Diffusion-Based Calcium Carbonate Synthesis Leads to Controlled Mesocrystal Formation*. Advanced Functional Materials, 2013. **23**(15): p. 1965-1973.

60. Oliver, W.C. and G.M. Pharr, *AN IMPROVED TECHNIQUE FOR DETERMINING HARDNESS AND ELASTIC-MODULUS USING LOAD AND DISPLACEMENT SENSING INDENTATION EXPERIMENTS*. Journal of Materials Research, 1992. **7**(6): p. 1564-1583.

61. Mata, M., O. Casals, and J. Alcala, *The plastic zone size in indentation experiments: The analogy with the expansion of a spherical cavity*. International Journal of Solids and Structures, 2006. **43**(20): p. 5994-6013.

62. Brecevic, L. and A.E. Nielsen, *SOLUBILITY OF AMORPHOUS CALCIUM-CARBONATE*. Journal of Crystal Growth, 1989. **98**(3): p. 504-510.

63. Rodriguez-Blanco, J.D., S. Shaw, and L.G. Benning, *The kinetics and mechanisms of amorphous calcium carbonate (ACC) crystallization to calcite, via vaterite*. Nanoscale, 2011. **3**(1): p. 265-71.

64. Spanos, N. and P.G. Koutsoukos, *The transformation of vaterite to calcite: effect of the conditions of the solutions in contact with the mineral phase*. Journal of Crystal Growth, 1998. **191**(4): p. 783-790.

65. Rodriguez-Navarro, C., et al., *Direct Nanoscale Imaging Reveals the Growth of Calcite Crystals via Amorphous Nanoparticles*. Crystal Growth & Design, 2016. **16**(4): p. 1850-1860.

66. Zou, Z.Y., et al., *On the Phase Diagram of Calcium Carbonate Solutions*. Advanced Materials Interfaces, 2017. **4**(1): p. 5.

67. Penn, R.L., K. Tanaka, and J. Erbs, *Size dependent kinetics of oriented aggregation*. Journal of Crystal Growth, 2007. **309**(1): p. 97-102.

68. Nehrke, G., et al., *Dependence of calcite growth rate and Sr partitioning on solution stoichiometry: Non-Kossel crystal growth*. Geochimica Et Cosmochimica Acta, 2007. **71**(9): p. 2240-2249.

69. Nielsen, L.C., D.J. DePaolo, and J.J. De Yoreo, *Self-consistent ion-by-ion growth model for kinetic isotopic fractionation during calcite precipitation*. Geochimica Et Cosmochimica Acta, 2012. **86**: p. 166-181.

70. Perdikouri, C., et al., *An Atomic Force Microscopy Study of the Growth of a Calcite Surface as a Function of Calcium/Total Carbonate Concentration Ratio in Solution at Constant Supersaturation*. Crystal Growth & Design, 2009. **9**(10): p. 4344-4350.

71. Stack, A.G. and M.C. Grantham, *Growth Rate of Calcite Steps As a Function of Aqueous Calcium-to-Carbonate Ratio: Independent Attachment and Detachment of Calcium and Carbonate Ions*. Crystal Growth & Design, 2010. **10**(3): p. 1409-1413.

72. Wolthers, M., et al., *Calcite growth kinetics: Modeling the effect of solution stoichiometry*. Geochimica Et Cosmochimica Acta, 2012. **77**: p. 121-134.

73. Calvaresi, M., et al., *Morphological and mechanical characterization of composite calcite/SWCNT-COOH single crystals*. Nanoscale, 2013. **5**(15): p. 6944-6949.

74. Giosia, M.D., et al., *Bioinspired Nanocomposites: Ordered 2D Materials Within a 3D Lattice*. Advanced Functional Materials, 2016.

75. Kim, Y.Y., et al., *Bio-Inspired Synthesis and Mechanical Properties of Calcite-Polymer Particle Composites*. Advanced Materials, 2010. **22**(18): p. 2082-+.

76. Kunitake, M.E., S.P. Baker, and L.A. Estroff, *The effect of magnesium substitution on the hardness of synthetic and biogenic calcite*. Mrs Communications, 2012. **2**(3): p. 113-116.

77. Rodriguez-Navarro, C., et al., *Formation of amorphous calcium carbonate and its transformation into mesostructured calcite*. CrystEngComm, 2015. **17**(1): p. 58-72.

# CHAPTER 7: SUGGESTIONS FOR FUTURE WORK

The work presented in this dissertation was undertaken with the intent to understand mechanical deformation and strengthening mechanisms in calcite single crystals. Successful strides were made towards this goal through the work described in the main chapters (4-6), as well as through the previously published collaborative work described in the Appendix chapter. The conclusions to each of those studies are included in their respective chapters. Here, I provide a compilation of some of the remaining questions, and provide suggestions for previous work to help answer those questions.

## 7.1. Variation among control calcites

In Chapter 4, I show that there is significant scatter in the reported hardness of (presumably pure and defect free) control calcites found in the literature, even after accounting for an indentation size effect. I also show that the mechanical anisotropy of the crystal may contribute to this scatter, but it seems that anisotropy can only account for some fraction of the scatter at any given load or depth. What then, accounts for the remaining variations? One of the assumptions inherent to my analysis is that all the control samples that other authors have described as "pure" and/or "optically clear" natural or geologic calcite crystals represent more or less the same pure material. However, it is unknown if this assumption is valid. Because detailed descriptions (other than the hardness) of many of these control calcites is lacking, it is not possible to determine if these calcites are really of the same purity and perfection from published data alone. A detailed study of the impurity and defect content of many commonly available natural calcites would provide a good baseline. Otherwise, more detailed descriptions (origin, size, impurity content, *etc*.) of calcites used as controls in future studies would be helpful.

## 7.2. Origin / mechanism of indentation size effect

In Chapter 4, I show that the reported hardness values for control calcites show a significant indentation size effect (ISE). While the existence of an ISE has been reported for many different materials and is generally well known, mechanistic descriptions are lacking in many cases. Some of the most successful descriptions of ISE for low-load indentations in many materials are based on strain-gradient plasticity. The fits to the entire range of ISE data in Chapter 4 show that the data is better described by a purely empirical semi-log fit than by a popular ISE model based on strain gradient plasticity [1]. Assuming that the large amount of scatter in the data does not obscure the form of the fit, these fits to the data suggests that the ISE in calcite may not be caused by strain gradient plasticity, at least not across such a large range of indentation sizes. It's also not clear what effect the anisotropic deformation due to mechanical twinning in calcite might have on ISE. Future work to more carefully quantify and explain the ISE in calcite may help answer these questions. For example, indentation across a large range of indentation sizes on the same calcite sample at specific crystal orientations would be helpful. At least, any future studies on calcite should clearly describe the indentation size, and only compare to the hardness of calcite measured at that same indentation size.

## 7.3. Experimental bounds of indentation correction method

In Chapter 5, I show that an accurate nanoindentation measurement of hardness and modulus can be made on a particle embedded in a more compliant matrix by applying an iterative correction method. Like the method proposed by Jakes, *et al*. [2, 3] for other types of elastic heterogeneities in nanoindentation samples, my method requires that the additional compliance due to the matrix is constant, *i.e*., independent of indentation size over some range of indentation size. Basic analysis of my measured

and corrected data seems to suggest that this assumption is reasonable for the ratio of indentation size to particle size explored here, but the upper and lower limits to this ratio have not been clearly defined. Performing similar experiments on more extreme sample configurations (*e.g.*, smaller/stiffer particles and/or more compliant matrices) might help to empirically define these boundaries. Furthermore, comparison to FEA simulations might also be helpful.

One of the main advantages of my method to that of Jakes, *et al*. [2, 3] is that it does not implicitly assume that the sample shows no ISE. My results on calcite over a small (7.5 mN) load range show that the expected ISE is indeed retained after correction. However, the ISE over this load range is relatively small and thus the full extent of the advantages of my method are not clear. Similar experiments over larger load ranges and/or on a material with even more dramatic ISE may be enlightening.

Even though the bounds of the correction method are not clear, it is clear that the effect of surrounding material is strong in many cases. Thus, it is important that future researchers are at least careful to consider and note any possible effect of surrounding material when reporting indentation data, and to correct it whenever possible.

### 7.4. Defect structure in pure calcites

Previous work has established that impurities are an important strengthening mechanism in many biogenic calcites. In Chapter 6, I show that the hardness of synthetic calcites can be increased without adding impurities to the crystals. It seems that this increase in hardness must be due to the existence of crystallographic defects within the crystals, but the exact nature of these defects is not clear. Further study of calcite crystals grown at high supersaturations would help explain. For example, electron microscopy might help identify the nature of any dislocation and/or void structure. *In-situ* imaging, of both crystal growth and deformation, would be especially

helpful in elucidating the mechanism of defect formation and the mechanism of strengthening, respectively.

### 7.5. Further strengthening single crystals

In the collaborative work included in the Appendix chapter, we show that the strength of calcite crystals can be increased by the incorporation of single-molecule amino acid impurities in the crystal. Furthermore, we show that this strengthening can be described in terms of the force required for a mobile dislocation in the crystal to tear apart the covalent bonding in the molecule. Thus, this kind of impurity strengthening is governed by the force to move a dislocation in the crystal (related to the shear modulus of the crystal) and the strength of the bonding in the impurity molecule. Using the strengthening equation presented in that paper, it would be interesting to explore other crystal / impurity combinations. For example, impurities with stronger bonding should impart greater strengthening than those with weaker bonding. Likewise, impure crystals with greater shear moduli should display greater strengthening (compared to a pure control crystal), than would impure crystals lower shear moduli.

Another avenue to explore would be to combine strengthening by crystallographic defects (*e.g.*, dislocation tangles and/or voids) with impurity strengthening. In this dissertation, I have shown how either feature can increase the hardness of calcite to similar levels. It is not clear what the effect of combining these features might be. One way to explore this in calcite might be to grow crystals in the presence of impurities at high supersaturation. Again, it would also be interesting to explore these features in other crystal / impurity systems.

## 7.6. REFERENCES


1. Nix, W.D. and H.J. Gao, *Indentation size effects in crystalline materials: A law for strain gradient plasticity*. Journal of the Mechanics and Physics of Solids, 1998. **46**(3): p. 411-425.

2. Jakes, J.E., et al., *Nanoindentation near the edge*. Journal of Materials Research, 2009. **24**(3): p. 1016-1031.

3. Jakes, J.E., et al., *Experimental method to account for structural compliance in nanoindentation measurements*. Journal of Materials Research, 2008. **23**(4): p. 1113-1127.

## APPENDIX CHAPTER

*This chapter is collaborative work already published in *Nature Materials* (2016), with supplementary data and full derivations not included here

# Tuning Hardness in Calcite by Incorporation of Amino Acids

Yi-Yeoun Kim[1], Joseph D. Carloni[3], Beatrice Demarchi[2], David Sparks[4], David Reid[5], Miki E. Kunitake[3], Chiu C. Tang[6], Melinda J. Duer[5], Colin L. Freeman[4], Boaz Pokroy[7], Kirsty Penkman[2], John Harding[4], Lara A. Estroff[3,8], Shefford P. Baker[3] and Fiona C. Meldrum[1]

1: School of Chemistry, University of Leeds, Woodhouse Lane, Leeds, LS8 2PA, UK.

2: BioArCh, Departments of Chemistry and Archaeology, University of York, York YO10 5DD, UK

3: Department of Materials Science and Engineering, Cornell University, 329 Bard Hall, Ithaca, NY 14853, USA

4: Department of Materials Science and Engineering, Sir Robert Hadfield Building, Mappin St, Sheffield S1 3JD, UK

5: Department of Chemistry, University of Cambridge, Lensfield Rd, Cambridge CB2 1EW, UK

6: Diamond Light Source, Harwell Science and Innovation Campus, Didcot, Oxfordshire, OX11 0DE, UK.

7: Department of Materials Science and Engineering and the Russell Berrie Nanotechnology Institute, Technion Israel Institute of Technology Haifa 32000, Israel

8: Kavli Institute at Cornell for Nanoscale Science, Ithaca, NY

****My contributions to this paper:**
Miki Kunitake and I performed the nanoindentation experiments (Fig. 6A); Shefford Baker and I analyzed the strengthening mechanism (Fig. 6B-E, Eq. 1)

## ABSTRACT

Structural biominerals are inorganic/ organic composites that exhibit remarkable mechanical properties. However, the structure-property relationships of even the simplest building unit – mineral single crystals containing embedded macromolecules – remain poorly understood. This article investigates the origin of the superior hardness of biogenic calcite by creating "model biominerals" from calcite single crystals containing glycine (0-7 mol%) or aspartic acid (0-4 mol%). Lattice distortions in these crystals were analyzed using x-ray diffraction and molecular dynamics simulations, while SS-NMR showed that the amino acids are incorporated as individual molecules. Nanoindentation hardness increased with amino acid content, reaching values equivalent to their biogenic counterparts. Finally, a dislocation pinning model reveals that the enhanced hardness is determined by the force required to cut covalent bonds in the molecules.

## INTRODUCTION

Biominerals such as bones, teeth and seashells are characterized by properties optimized for their functions. Despite being formed from brittle minerals and flexible polymers, nature demonstrates that it is possible to generate materials with strengths and toughnesses appropriate for structural applications.(*1*) At one level, the mechanical properties of these hierarchically structured materials are modeled as classical composites consisting of a mineral phase embedded in an organic matrix.(*2*) However, the single crystal mineral building blocks of biominerals are also composites, containing both aggregates of biomacromolecules as large as 20 nm(*3, 4*) and inorganic impurities.(*5, 6*) While it should be entirely possible to employ this simple biogenic strategy in materials synthesis,(*7, 8*) the strengthening and toughening mechanisms that result from these inclusions are still poorly understood.(*9, 10*) This work addresses this challenge by analyzing hardening mechanisms in a simple model biomineral system: calcite single crystals containing known amounts of amino acids. We report synthetic calcite crystals with hardnesses equivalent to those of their biogenic counterparts, and offer a detailed explanation for the observed hardening.

Since plastic deformation in single crystals occurs by the motion of dislocations, hardness is enhanced by features that inhibit dislocation motion. The mechanisms by which guest species may harden ionic single crystals generally fall into two categories. Second phase particles directly block dislocation motion, requiring a dislocation to either cut through (shear) a particle or bypass it by a diffusive process to keep going.(*11*) Solutes (point defects) do not directly block dislocation motion, but the stress fields of the dislocations interact with those associated with misfitting solutes, retarding dislocation motion.(*11*) To fully understand the hardening mechanisms of single crystal biominerals, one must determine the relationship between the hardness and the concentrations of the different types of guest species. For example, the effect

of $Mg^{2+}$ substitutionals has been determined, and was shown to be consistent with solute strengthening.(*12*) Determination of the hardening mechanism of occluded organic additives has proven far more challenging. While species ranging from small molecules,(*13, 14*) to peptides(*15*) and proteins,(*16, 17*) to nanoparticles(*8, 18, 19*) and fibers,(*20, 21*) have been incorporated in calcite, the effect of these inclusions on mechanical properties is not yet known. Occlusion of 200 nm latex particles within calcite single crystals was shown to reduce their hardness,(*7*) while in a pioneering study, the incorporation of polymeric micelles having sizes comparable to those of the protein occlusions in biominerals was shown to increase hardness.(*8*) However, due to an inability to control the number of micelles occluded, it was not possible to quantitatively characterize their hardening effect.

The present study describes a model system – created by the incorporation of the amino acids aspartic acid (Asp) and glycine (Gly) within calcite – in which we can precisely *tune* the compositions of our single crystal composites over a wide range, and thus finally determine the origin of the hardening effects of small organic molecules. By application of x-ray diffraction and molecular dynamics simulations to characterize the local and global distortions of the crystal lattice, NMR to demonstrate that the amino acids are present as individual species within the crystal, nanoindentation to determine the hardness, and a dislocation pinning model, we show that the enhanced hardness is determined by the force required to cut a single covalent bond. This analysis provides strong evidence that the occluded molecules function more like second-phase particles than as point defects.

## RESULTS

### Incorporation of Asp and Gly in Calcite Single Crystals

Calcite was precipitated in the presence of Asp or Gly using the ammonium diffusion method,(*22*) and the crystals were characterised using SEM and optical microscopy (Figure 1). Crystals were 20-50 $\mu$m in size and took the form of perfect rhombohedra at low additives concentrations, and at higher concentrations transitioned to elongated particles with highly roughened sides, which were capped at each apex with three, smooth {104} faces. (*23*) The amounts of amino acids occluded within these crystals were determined using reverse-phase high-pressure liquid chromatography (HPLC) after dissolution of the crystals. All samples were bleached before dissolution to remove surface-bound amino acids. (*24, 25*) The relationship between the initial concentration of amino acid in the reaction solution ($[AA]_{Sol}$) and the mole fraction of amino acids incorporated ($[AA]_{Inc}$) was determined by holding $[Ca^{2+}]$ = 10 mM whilst varying the amino acid concentration (Figure 2a). Looking first at Asp, there is a roughly linear relationship between $[Asp]_{Sol}$ and $[Asp]_{Inc}$ until $[Asp]_{Sol}$ = 50 mM and $[Asp]_{Inc}$ = 3.9 mol%, after which point $[Asp]_{Inc}$ reduces. The incorporation of Gly shows a similar strong correlation with $[Gly]_{Sol}$, but is less efficient, with lower occlusion levels observed for equivalent values of $[AA]_{Sol}$ ($[Gly]_{Inc}$ = 1.1 mol% at 50 mM Gly). However, while Asp occlusion reaches a maximum at ≈ 3.9 mol%, Gly occlusion continues to increase, reaching values as high as 6.9 mol% at 400 mM Gly. These values are far higher than those obtained in a previous study of amino acid incorporation in calcite,(*13*) highlighting the importance of the growth conditions in achieving occlusion. Higher Gly concentrations were not examined due to strong growth inhibition under those conditions.

**Figure 1**. **Crystal Morphologies**. Representative SEM images showing calcite crystals precipitated with different conditions of $[AA]_{sol}$ and initial $[Ca]_{sol}$ = 10 mM. (A to C) $[Asp]_{sol}$ = (A) 5 mM (B) 20 mM (C) 50 mM. (D to E) $[Gly]_{sol}$ = (D) 10 mM (E) 100 mM (F) 200 mM.

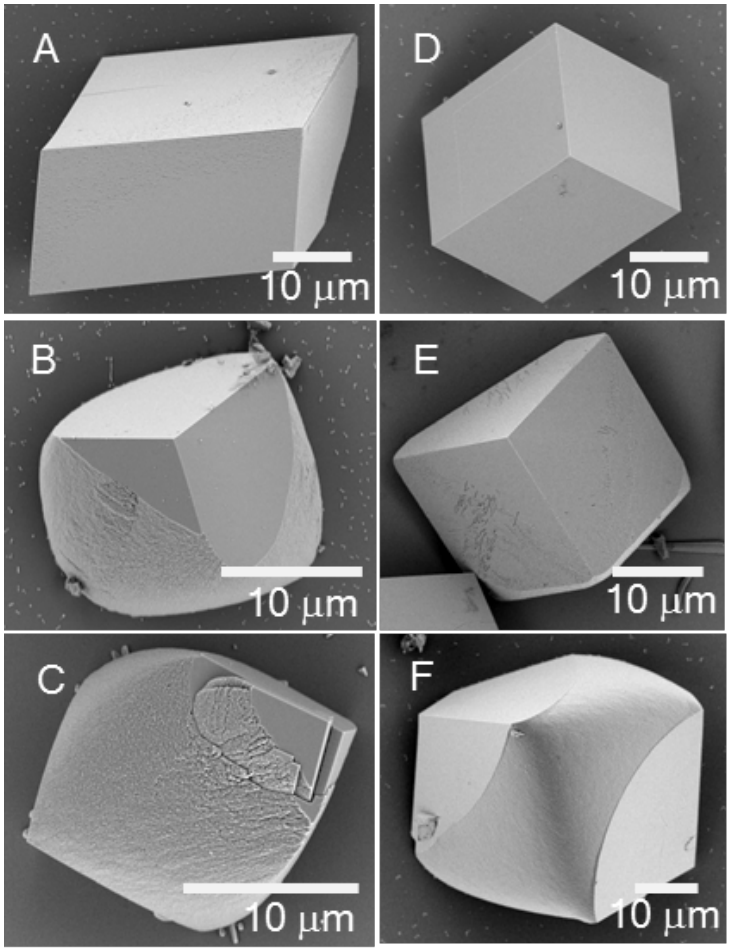

A measure of the efficiency of amino acid occlusion was also obtained from the distribution coefficient, $D = [AA]_{inc}/[AA]_{sol}$, where the high values of D at low solution concentrations of Asp serve to emphasise the far more efficient occlusion of Asp than Gly (Figure 2b). This trend can be attributed to the charge on the Asp molecule, and its greater hydrophilicity.(*26, 27*) The effect of the growth rate on amino acid occlusion was also investigated for Asp by precipitating calcite at $[Ca^{2+}]$ = 2–100 mM at a fixed initial $[Asp]_{Sol}$ = 10 mM (data not shown). Incorporation was strongly dependent on the growth rate, increasing from 0.4 mol % at $[Ca^{2+}]$ = 2 mM to 1.9 mol % at $[Ca^{2+}]$ = 50 mM (Figure 2c). This effect is additionally seen in the increase of D with crystal growth rate and $[Ca^{2+}]$(Figure 2d) and is fully consistent with an occlusion mechanism based upon binding to step edges, where the density of step edges increases with supersaturation.(*28*)

## Effects of Incorporated Amino Acids on the Lattice Structure

Previous studies utilizing synchrotron high-resolution powder diffraction (PXRD) have shown that occlusion of organic molecules in both biogenic and synthetic calcium carbonates give rise to lattice distortions.(*13, 29*) In the present study, the effects of the occluded amino acid on the crystal lattice were studied using synchrotron PXRD and the diffraction patterns were modelled using full pattern analysis by Rietveld refinement as well as line profile analysis. Occlusion of both Asp and Gly resulted in anisotropic lattice expansion, where the lattice distortions were about an order of magnitude greater along the *c*-axis than the *a*-axis (Figures 3a and 3b). Both amino acids caused similar degrees of distortion along the *c*-axis at low incorporation levels, while the strains in Gly are higher than those in Asp at values of $[AA]_{Inc}$ exceeding 1 mol%, reaching 0.3% at $[Asp]_{inc}$ = 3.9 mol% and 0.5% at $[Gly]_{inc}$

= 6.9 mol%. Gly again caused somewhat more distortion along the *a*-axis at higher levels of occlusion.

Analysis of the broadening (FWHM) of the full spectra and individual PXRD peaks showed that the domain sizes falls in the ranges 200 to > 1000 nm (Asp/calcite) and 500 to > 1000 nm (Gly/calcite) (data not shown). The degree of broadening varied across the different lattice planes, being greatest for the (006) planes, and in common with the lattice distortions, Gly had a greater effect than Asp at equivalent values of $[AA]_{Inc}$ (Figures 3c, 3d and S5). The broadening generally increased with increasing $[Asp]_{Inc}$, before levelling-off above 1 mol% occlusion, while for many of the lattice planes $[Gly]_{Inc}$ reached a maximum at ≈ 2-4 mol%, before decreasing again. This trend was particularly clear for the (006) planes. The consequence of this behaviour is that all of the diffraction peaks from the crystals occluding 6.9 mol% Gly have comparable broadening levels (Figure 3d). It is also notable that the maximum of the peak broadening occurs at the same value of $[Gly]_{inc}$ at which the lattice distortions begin to saturate.

Occlusion of individual amino acids within calcite gives rise to inhomogeneous distortions throughout the lattice, which increase the average lattice parameter. This observation is consistent with a model in which, as $[AA]_{inc}$ increases, the strain fields around the molecules begin to overlap, and the strain inhomogeneity decreases as the macrostrains continue to increase (Figures 3e and 3f). Our data raise the possibility that the Gly molecules may be sufficiently close to each other at the higher occlusion levels that the local strain fields around them begin to overlap. Our PXRD data provides no evidence for segregation of amino acids within the lattice at higher concentrations, with the exception of crystals grown at $[Asp]_{sol}$ = 100 mM.

**Figure 2**. **Occlusion of aspartic acid and glycine**. (A) The amount of amino acid occluded within the $CaCO_3$ crystals, $[AA]_{inc}$, as a function of the initial concentration of amino acid in solution, $[AA]_{sol}$, for Asp and Gly at $[Ca^{2+}]_{sol}$ = 10 mM. (B) The distribution coefficients for Asp and Gly in calcite as a function of the initial $[AA]_{sol}$ at $[Ca^{2+}]$ = 10 mM. The insets show sub-section of the respective graphs. (C) The amount of Asp occluded as a function of $[Ca^{2+}]_{sol}$ at an initial $[Asp]_{sol}$ = 10 mM. (D) The distribution coefficient of Asp in calcite at and initial $[Asp]_{Sol}$ = 10 mM.

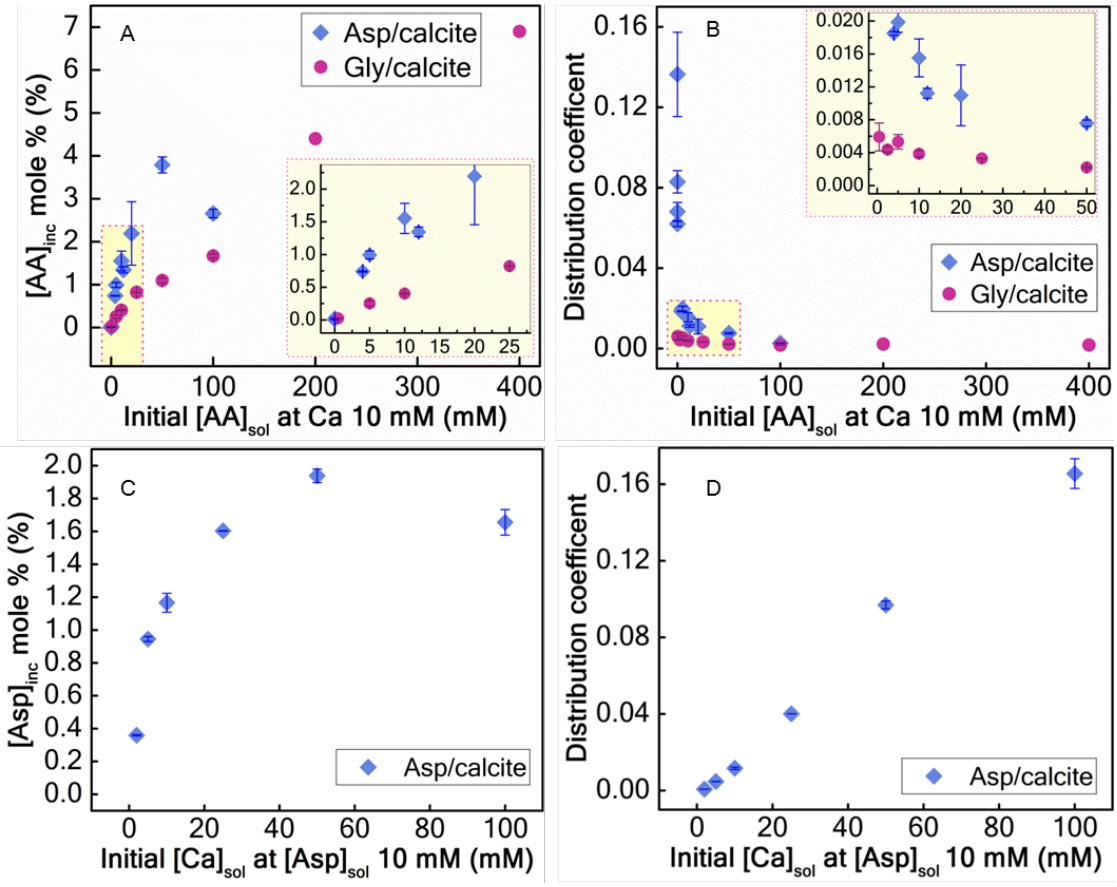

**Figure 3**. **XRD analysis**. (A and B) Lattice distortions arising from the incorporation of aspartic acid and glycine in calcite, (A) along the *c*-axis and (B) the *a*-axis. (C and D) XRD peak broadening (FWHM) due to strains induced by (C) aspartic acid and (D) glycine incorporation. The inhomogeneous strains show a maximum with (E) aspartic acid (F) glycine while the macrostrain continues to increase, as is consistent with overlapping of the strain fields associated with the individual molecules as the spacings between the molecules become smaller.

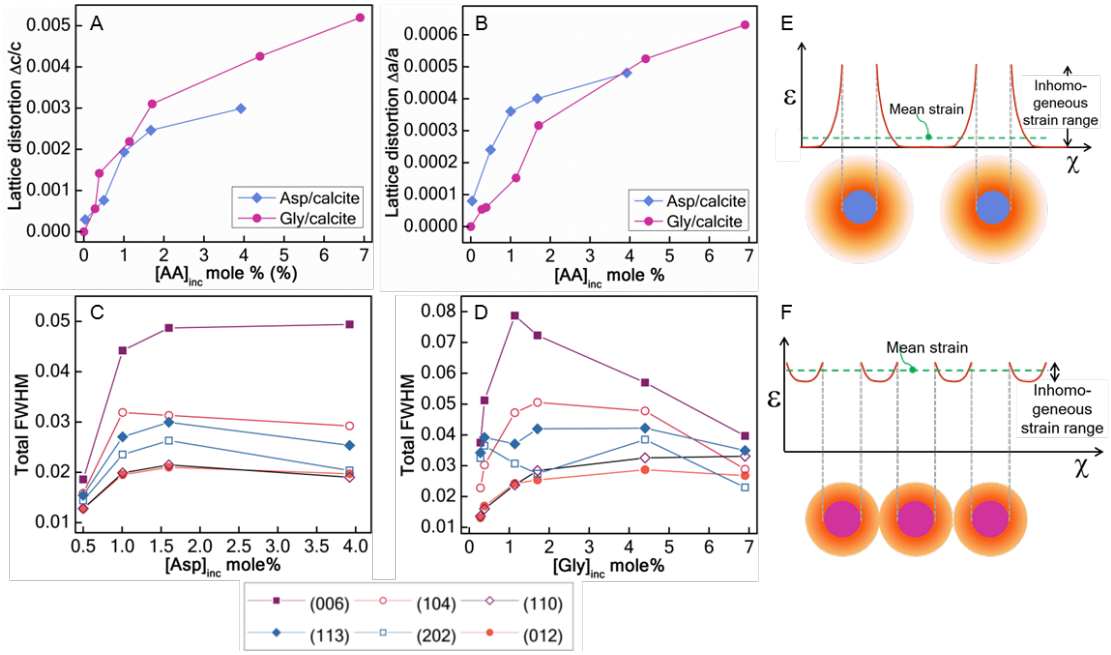

### ssNMR Analysis of Calcite Crystals Occluding Asp and Gly

ssNMR was employed to determine whether the amino acids are isolated, or clustered within the calcite lattice. Calcite crystals were precipitated in the presence of 25 mM of both 1,4-$^{13}C_2$ Asp and 3-$^{13}C$ Asp, and were analysed using proton driven spin diffusion (PDSD) (Figure 4). The figures show conventional contour plots from the 2D PDSD experiment (in blue), overlaid by a row (red) extracted from the dataset at the chemical shift of the Asp 3-carbon signal (Figure 4a) and the overlapped Asp 1- and Asp 4-carbon signals (Figure 4b). The extracted rows reveal whether there is any spin diffusion between the two isotopomeric amino acids, which would indicate proximities of ≈ 0.5 nm between the Asp 3-carbon and the Asp 1- and Asp 4-carbons. These would manifest as peak intensity in each of the extracted rows at the frequency corresponding to that of the "off diagonal" signal; the relevant frequencies are indicated by vertical red dashed lines in both figures. There is no intensity at either frequency, and thus no evidence of any intermolecular Asp-Asp association. Identical analyses was performed for calcite precipitated in the presence of 1-$^{13}C$ Gly and 2-$^{13}C$ Gly, and the data again suggested that Gly molecules are individually dispersed in the lattice (data not shown).

**Figure 4. Solid-state NMR Analysis.** Contour plots of a proton driven spin diffusion (PDSD) analysis of calcite precipitated in the presence of [1,4-$^{13}C_2$ Asp] = [3-$^{13}$C Asp] = 25 mM. The red traces are rows extracted from the 2D dataset at the frequency of the (a) 3-carbon signal and (b) the overlapped 1,4-carbon signals. Proximity between the 3- and the 1,4-labelled Asp would manifest as a peak (in the red trace) at the frequency of the (a) 1,4-carbon and (b) 3-carbon, as indicated by the dashed vertical red line.

a)

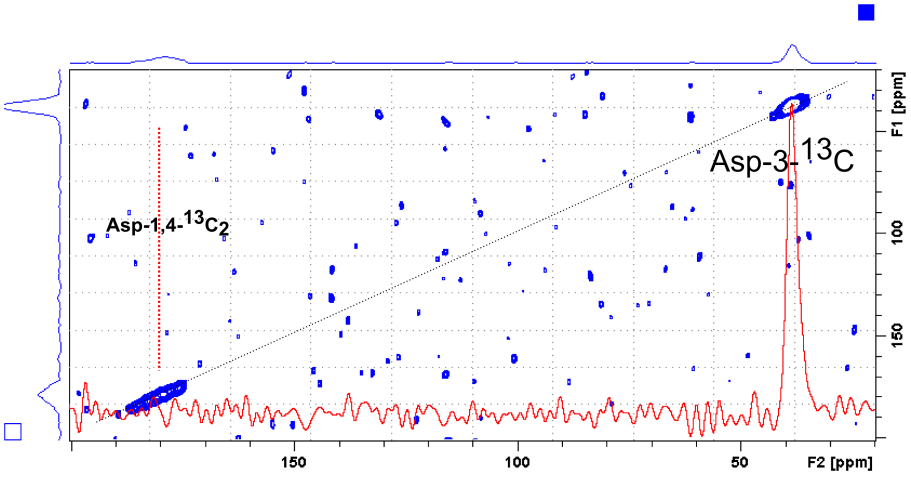


b)

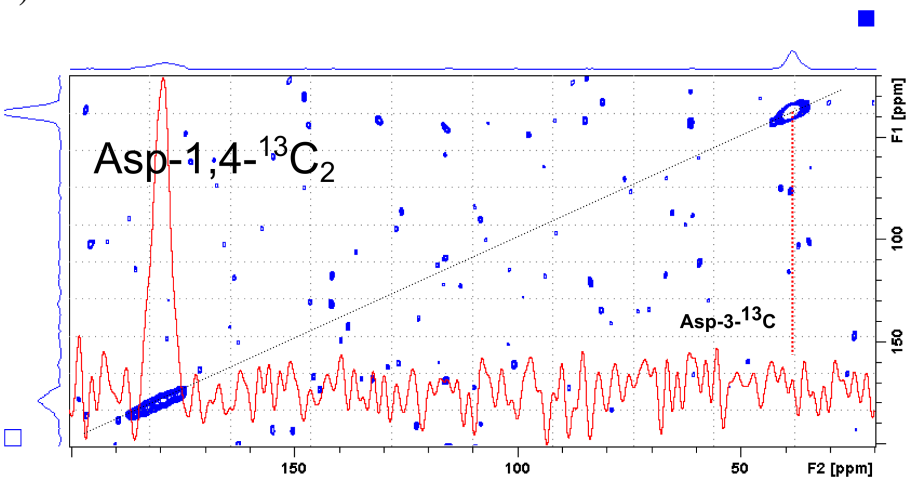

## Simulations of the Incorporation of Asp and Gly in Calcite

Molecular Dynamics simulations were performed to gain an understanding of the atomistic interactions between the mineral and amino acids. The calcite model consisted of a block of calcite (34 x 44 x 34 Å) with 864 $CaCO_3$ formula units and two charged states of each amino acid ($Asp^{2-}$, $Asp^{1-}$, $Gly^{1-}$ and $Gly^{0}$) were considered as the pKa values of the amino acids were close to experimental pH values (Figure S7). The amino acids were inserted by first removing $Ca^{2+}$ and $CO_3^{2-}$ ions, and then placing the amino acids within the resulting defect. Charge matching and minimum strains were achieved when each $Gly^{0}$ replaced one $CaCO_3$ formula unit, each $Asp^{2-}$ one $CaCO_3$ unit and a $CO_3^{2-}$ ion, two $Gly^{1-}$ replaced one $CaCO_3$ unit and a $CO_3^{2-}$ ion, and two $Asp^{1-}$ replaced two $CaCO_3$ units and a $CO_3^{2-}$ ion.

The configurations of the $Asp^{2-}$ and $Gly^{0}$ molecules in the calcite lattice are shown in Figure 5a. The Asp molecules are occluded such that the carboxylic acid groups on Asp replace $CO_3^{2-}$ groups on adjacent carbonate planes with a very good fit. A less favourable fit is obtained with Gly. This effect is also seen in the radial distribution data of the Ca-Ca distances in pure calcite and those for calcite occluding $Asp^{2-}$ and $Gly^{0}$, which show that $Gly^{0}$ is more disruptive of the calcite lattice than $Asp^{2-}$ (Figure 5b). These distortions may well account for the reduced efficiency of incorporation of Gly than Asp. Simulations were also performed to model the macrostrains arising from occlusion of amino acid molecules, where these data provide a bridge between our model of amino acid incorporation in the lattice and the experimental XRD data. This model was implemented by expanding the crystal axes independently. The calculated configurational energies rose much faster when the crystal was strained along the *a*-axis than the *c*-axis (Figure 5c), as is consistent with the elastic anisotropy of calcite.(29A) For crystals containing 2.3 mol% $Asp^{2-}$ and 2.8 mol% $Gly^{0}$ (to correspond to samples characterised by XRD) the minimum energies are found at

macrostrains that are in excellent agreement with the experimental values. The total inclusion energy also steadily increases with the amount of occluded amino acid (Figure 5d), as would be expected based on a certain misfit per molecule.

Interestingly, the total inclusion energies (reported per mole of $CaCO_3$) were similar for both $Asp^{2-}$ and $Gly^0$. Back-of the-envelope calculations of the misfits of $Gly^0$ and $Asp^{2-}$ in the calcite lattice give values of 8.1% for $Gly^0$ and 3.9% for $Asp^{2-}$ (see SI for calculation), where these misfits result in large tensile strains in the calcite lattice in the neighbourhood of each AA molecule that drop off rapidly with distance from the molecule. (*30*) Although each occluded Gly is associated with larger strains than Asp, Gly is also significantly smaller than Asp, such that each molecule affects a smaller volume of the calcite lattice. Our data suggest that these contrasting effects are of similar magnitude here, giving rise to the similar inclusion energies.

**Figure 5. (NEXT PAGE)**

**Molecular Dynamics Simulations.** (A) The total occlusion energy for $Asp^{2-}$ and $Gly^{0}$. (B) Radial distribution function of Ca-Ca distances in pure calcite and calcite with occluded $Asp^{2-}$ and $Gly^{0}$. (C) Configurational energies of calcite with occluded $Asp^{2-}$ and $Gly^{o}$, calculated on expansion of the calcite crystal along the *c*-axis and *a*-axis. The energy minima are found at $\Delta c/c$ values of 0.002 and 0.003 for the incorporation of 2.3 mol% $Asp^{2-}$ and 2.8 mol% $Gly^{0}$ respectively. 'x' denotes the energy minimum of pure calcite, where the arrow shows the distortion from the pure calcite sample to the experimental values found at and 'o'. (D) Schematics showing $Asp^{2-}$ and $Gly^{o}$ occluded in the calcite crystal.

**Figure 5. Molecular Dynamics Simulations.**

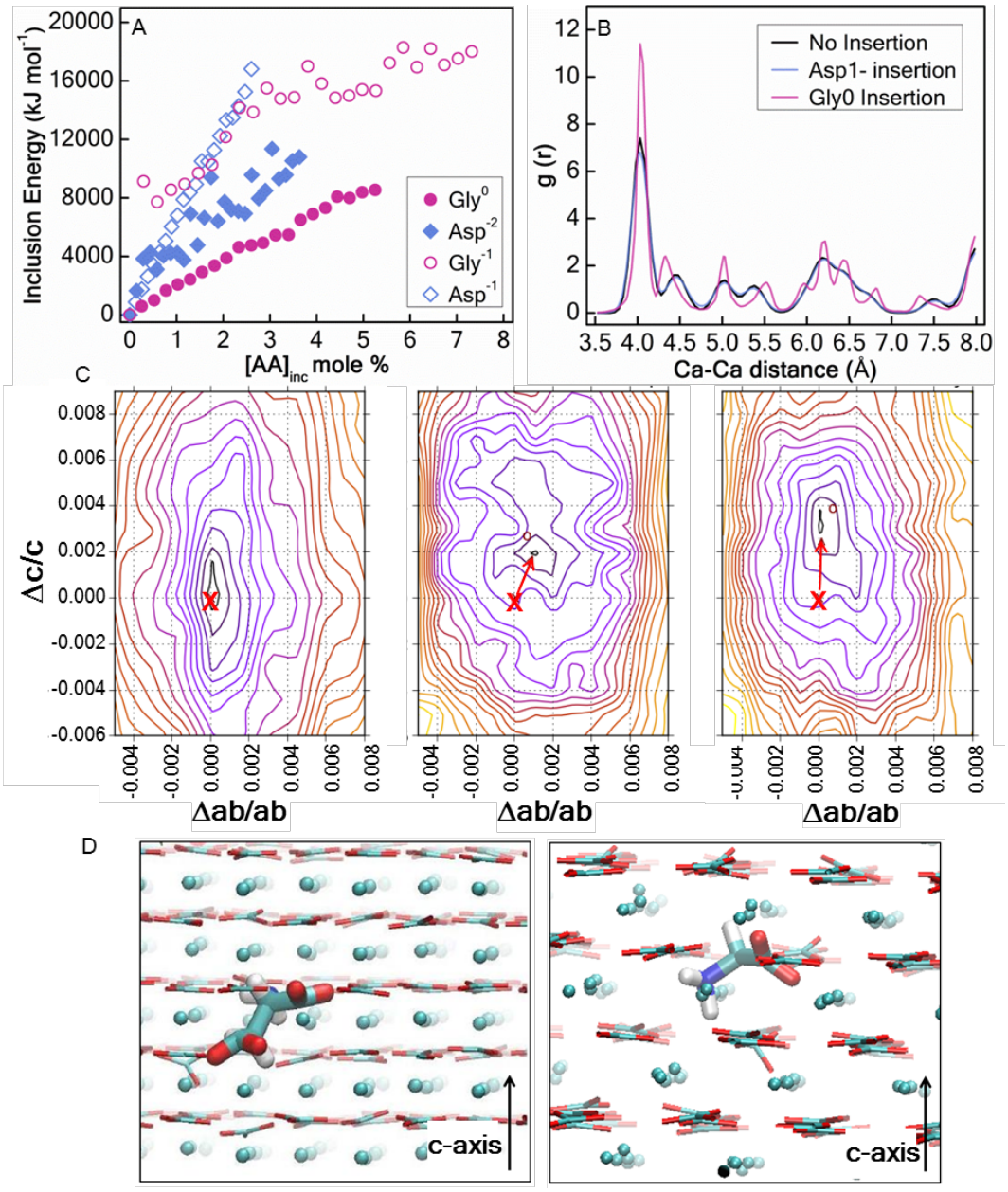

## Determination of the Mechanical Properties

Finally, the mechanical properties of the amino acid-containing calcite crystals were measured using nanoindentation. Indentations approximately 200 nm deep and 1.4 $\mu$m wide were made using a Berkovich (triangular pyramid) indenter, and the load-displacement data from each indentation were analysed to determine hardness, $H$, and indentation modulus, $E_{IT}$. (*31*). Loads applied were sufficiently small (10 mN) that cracking was suppressed and indentations were formed by plastic deformation (Figure 6a). The hardness of the calcite crystals significantly increased with occluded amino acid content, starting at 2.5 GPa—equivalent to Iceland spar, a pure and highly perfect geologic form of calcite (*9*)—and reaching values of 4.1 +/- 0.3 GPa for occlusion of 2.2 mol% Asp, and 4.1 +/- 0.3 GPa for occlusion of 6.9 mol% Gly (Figure 6a). Crystals with higher mol% of Asp inclusion were not tested because of the small and irregular sizes of these samples (data not shown). These values are comparable to biogenic calcite (values of 3.4–4.2 GPa have been reported on the {001} face of the mollusk *Atrina rigida*),(*9*) and exceed the hardnesses of other synthetic calcite systems with occluded species reported to date including calcite grown with occluded polymer micelles ($H_{max} \approx 3.0$ GPa),(*8*) and with Mg substitutions for Ca ($H_{max} \approx 3.4$ GPa).(*12*) In contrast, the indentation modulus was insensitive to $[AA]_{inc}$, as expected based on a rule of mixtures model for a material containing a small volume fraction of a different phase.

**Figure 6. (NEXT PAGE)**

**Mechanical Properties**. (A) Hardness vs. $[AA]_{inc}$ for calcite occluding Asp and Gly (inset: scanning force image of representative plastic indentation in calcite). Schematics of (B) dislocation bowing out between AA molecule pinning points, and (C) force balance between dislocation line tension $T$ and the resisting force $F$ provided by the molecule. The "cutting force" $F_c$ is the force needed for the dislocation to cut the molecule. Since $F_c << T$, the effective spacing $L'$ is greater than the actual spacing $L$. (D) Hardness vs. $L^{-1} = (C_{v,AA}*t)^{0.5}$, where the linear behaviour supports blocking by molecules as the strengthening mechanism. (E) $F_c$ calculated using measured hardness and estimated molecular spacings as compared with expected mechanical bond strengths.

**Figure 6. Mechanical Properties.**

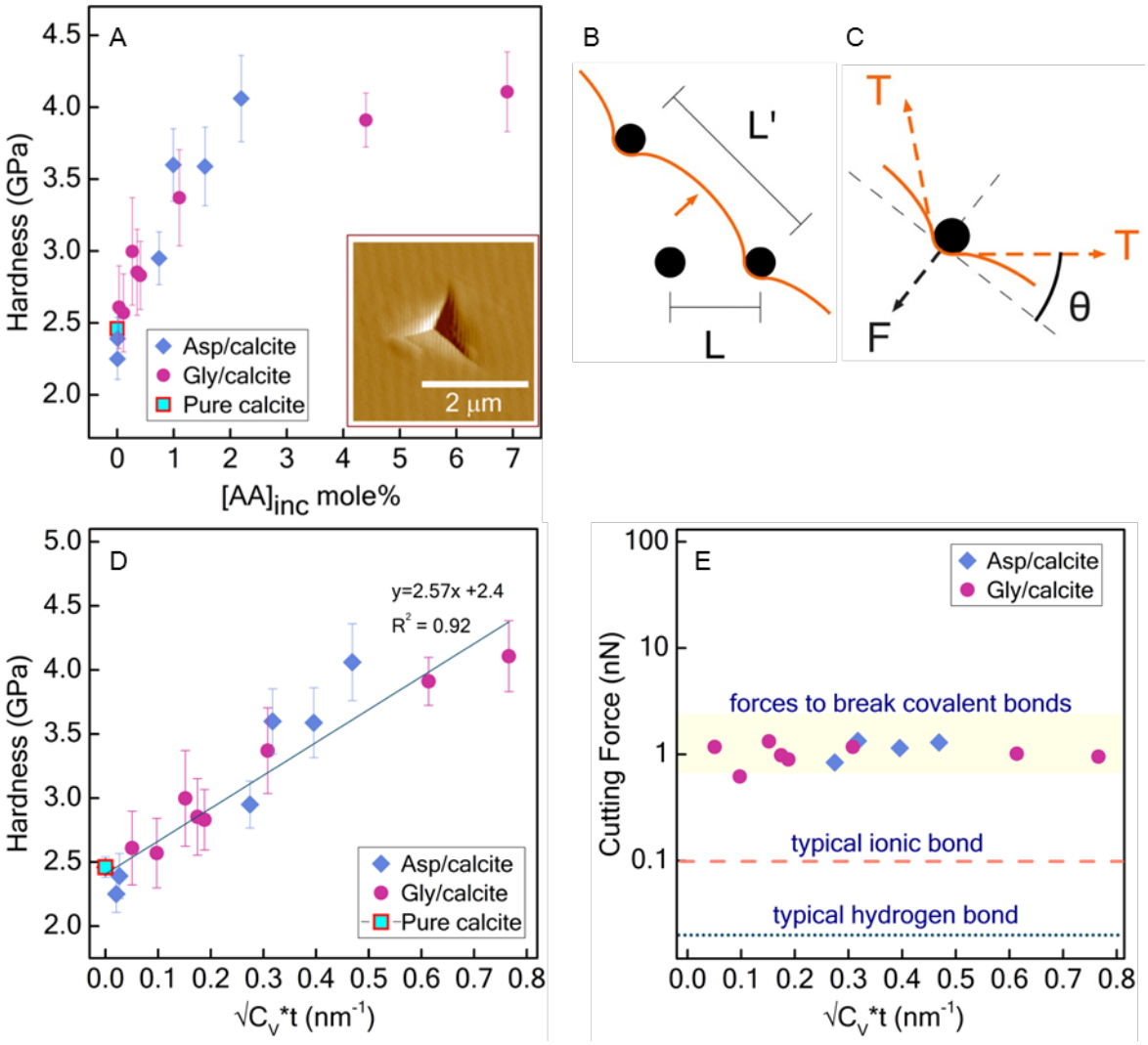

## Discussion

Precipitation of $CaCO_3$ in the presence of Asp and Gly provides a system in which we can precisely tune the amounts of these small molecules within calcite single crystals across a broad composition range, allowing us to study in detail the relationship between the quantities of molecules occluded, their effects on the lattice distortions, and ultimately on the hardness. Since the calcite deformed plastically without cracking in these small-scale experiments (Figure 6a), the origin of the hardening effect can be determined by analyzing the slip systems in the material and the stresses needed to activate them with respect to the amount of amino acid occluded (full derivation not shown here). As hardness provides a measure of the resistance to motion of dislocations on these slip planes, the increase in hardness with increasing AA content demonstrates that the AA molecules provide effective impediments to dislocation motion.

The AA molecules can impede dislocations when either the stress fields around the molecules interact with the stress fields of the dislocations (like solutes), and/or when dislocations are blocked by the molecules themselves (like second phase particles). However, while the peak width (inhomogeneous strains) level off or decrease above $[AA]_{inc} \approx 1$ mM, hardness continues to increase to $[AA]_{inc} \approx 2$ mM (compare Figures 3c and 3d with Figure 6a). Furthermore, the hardness is the same for both amino acids at the same $[AA]_{inc}$, despite the fact that the distortions are very different. These observations suggest that direct blocking by the molecules is the dominant hardening mechanism. To test this idea, we consider a dislocation interacting with a random array of AA molecules (Figure 6b). The molecules impede the dislocation's motion, causing it to bow out.(*32*) Since lattice diffusion is not observed in calcite at room temperature, the dislocation can continue to move only by shearing the molecules. At each molecule, the dislocation line tension $T$ is balanced by the resisting force of the

molecule (Figure 6c) and when a critical force is reached, known as the "cutting force," $F_c$, the dislocation cuts the molecule and moves on. Thus, if blocking by AA molecules dominates the increase in hardness, then $F_c$ corresponds to the force required to cut a molecule.

If we assume that $T > F_c$, and that the hardness of the crystal is just the sum of its intrinsic resistance to dislocation motion—*i.e.* the hardness of pure calcite—and the additional hardening due to AA molecules, we can write (derivation not shown here):

$$H = H_0 + 4.8(F_c / bL)\sqrt{F_c / 2T}\ , \qquad (1)$$

where $H_o$ is the hardness of pure calcite, $b$ the Burgers vector magnitude, and $L$ the spacing between molecules. Since we know $H_o$, can estimate $T$ and $b$, and have measured $H$ as a function of $[AA]_{inc}$, if we can determine $L$ from $[AA]_{inc}$, then we can determine the actual cutting force for the molecules. To estimate $L$, we consider the AA molecules to be uniformly distributed throughout the crystal, consistent with the SS-NMR data, and approximate the configuration of the molecules as a square array. This analysis gives $L = (C_{v,AA}t)^{-0.5}$ where $C_{v,AA}$ is the number of AA molecules/volume and $t$ is the thickness of a thin slice, which is set equal to the diameter of the AA molecule (derivation not shown here). We can now use Eq. 1 to find the cutting force, $F_c$, for each experimentally measured $H$, where we obtain values around 1 nN (Figure 6d). This value lies just below reported strengths of single covalent bonds (1.5 to 4 nN (*33-35*)) and well above a typical ionic bond strength of 0.1 nN.(*36*) Since the hardness represents an average of all of the events that inhibit dislocation motion, this result strongly suggests that the hardening effect of these occluded molecules comes from the force required to shear them.

Further support for this model comes from the functional form of the variation of hardness with $[AA]_{inc}$. For a constant obstacle strength ($F_c$ in this case), $H$ should vary

linearly with the inverse of the obstacle spacing, $L^{-1}$ (Eq. 1). Since $L = (C_{v,AA}t)^{-0.5}$, $H$ is expected to vary linearly with $(C_{v,AA}t)^{0.5}$. A power law fit to the $H$ *vs*. $C_{v,AA}t$ data returns an exponent of 0.52, so $H$ indeed varies linearly with $(C_{v,AA}t)^{0.5}$ (Figure 6e). Despite the different sizes of the molecules, when intermolecular spacings are taken into account, the hardness depends on the bond strengths in the individual molecules, which are essentially the same for Asp and Gly.

## Conclusions

This work provides new insights into the mechanical properties of inorganic/ organic nanocomposites. By creating a system that is at first sight very simple – the occlusion of amino acids within calcite single crystals – we are finally able to quantitatively correlate the composition of the resultant composite crystals, to the hardness. At the heart of our strategy is the ability to achieve extremely high levels of occlusion of up to 3.9 mol% Asp and 6.9 mol% Gly, while retaining calcite single crystals. Analysis of the changes in hardness and lattice distortions with respect to the composition shows that the hardening effect derives primarily from dislocations cutting the amino acids, as indicated by the fact that the estimated dislocation obstacle cutting force is in good agreement with the strength of the covalent bonds in the amino acid backbones. While the lattice distortions due to the occluded molecules are large, the trends in the hardness values were not well correlated with them. These results are of particular significance to the mechanical properties of single crystal biominerals, and open up the possibility of using this strategy to tailor the mechanical properties of a wide range of materials.

## Acknowledgments

This work was supported by an Engineering and Physical Sciences Research Council (EPSRC) Leadership Fellowship (FCM and YYK, EP/H005374/1), by an EPSRC Materials World Network grant (EP/J018589/1, FCM and YYK) and an EPSRC Programme Grant (grant EP/I001514/1) which funds the Materials Interface with Biology (MIB) consortium (FCM, JH and DS). We acknowledge Diamond Light Source for time on beamline I11 under commissioning time and proposal EE10137. LAE, JDC, MEK, and SPB were supported by the US National Science Foundation (NSF) via a Materials World Network grant (DMR 1210304). BP acknowledges support from the European Research Council under the European Union's Seventh Framework Program (FP/2007–2013)/ERC Grant Agreement n° [336077]. This work made use of the Cornell Center for Materials Research Shared Facilities, which are supported through the NSF MRSEC program (DMR-1120296).

## REFERENCES


1. U. G. K. Wegst *et al*., Bioinspired structural materials. *Nat. Mater.* **14**, 23-36 (2015).

2. P. Fratzl, R. Weinkamer, Nature's hierarchical materials. *Prog. Mater. Sci.* **52**, 1263-1334 (2007).

3. K. Gries *et al*., Investigations of voids in the aragonite platelets of nacre. *Acta Biomater.* **5**, 3038-3044 (2009).

4. H. Y. Li *et al*., Calcite prisms from mollusk shells (atrina rigida): swiss-cheese-like organic–inorganic single-crystal composites. *Adv. Funct. Mater.* **21**, 2028-2034 (2011).

5. K. J. Davis, P. M. Dove, J. J. De Yoreo, The role of Mg2+ as an impurity in calcite growth. *Science* **290**, 1134-1137 (2000).

6. A. E. Stephenson *et al*., Peptides enhance magnesium signature in calcite: insights into origins of vital effects. *Science* **322**, 724-727 (2008).

7. Y. Y. Kim *et al*., Bio-inspired synthesis and mechanical properties of calcite-polymer particle composites. *Adv. Mater.* **22**, 2082-2086 (2010).

8. Y. Y. Kim *et al*., An artificial biomineral formed by incorporation of copolymer micelles in calcite crystals. *Nat. Mater.* **10**, 890-896 (2011).

9. M. E. Kunitake *et al*., Evaluation of strengthening mechanisms in calcite single crystals from mollusk shells. *Acta Biomater.* **9**, 5353-5359 (2013).

10. L. Li, C. Ortiz, Pervasive nanoscale deformation twinning as a catalyst for efficient energy dissipation in a bioceramic armour. *Nat. Mater.* **13**, 501-507 (2014).

11. T.H. Courtney, Mechanical Properties of Materials—2nd Edition. Waveland Press Inc. Long Grove, IL p. 173-209 (2005).

12. M. E. Kunitake, S. P. Baker, L. A. Estroff, The effect of magnesium substitution on the hardness of synthetic and biogenic calcite. *MRS Commun.* **2**, 113-116 (2012).

13. S. Borukhin *et al*., Screening the incorporation of amino acids into an inorganic crystalline host: the case of calcite. *Adv. Funct. Mater.* **22**, 4216-4224 (2012).

14. G. Magnabosco *et al*., Calcite single crystals as hosts for atomic-scale entrapment and slow release of drugs. *Adv. Healthcare Mater.* **4**, 1510-1516 (2015).

15. R. A. Metzler, G. A. Tribello, M. Parrinello, P. Gilbert, Asprich peptides are occluded in calcite and permanently disorder biomineral crystals. *J. Am. Chem. Soc.* **132**, 11585-11591 (2010).

16. S. Albeck, J. Aizenberg, L. Addadi, S. Weiner, Interactions of various skeletal intracrystalline components with calcite crystals. *J. Am. Chem. Soc.* **115**, 11691-11697 (1993).

17. J. Aizenberg *et al.*, Control of macromolecule distribution within synthetic and biogenic single calcite crystals. *J. Am. Chem. Soc.* **119**, 881-886 (1997).

18. A. N. Kulak *et al.*, One-pot synthesis of an inorganic heterostructure: uniform occlusion of magnetite nanoparticles within calcite single crystals. *Chem. Sci.* **5**, 738-743 (2014).

19. A. N. Kulak *et al.*, Colouring crystals with inorganic nanoparticles. *Chem. Commun.* **50**, 67-69 (2014).

20. H. Li, H. L. Xin, D. A. Muller, L. A. Estroff, Visualizing the 3D internal structure of calcite single crystals grown in agarose hydrogels. *Science* **326**, 1244-1247 (2009).

21. H. Y. Li, L. A. Estroff, Calcite growth in hydrogels: assessing the mechanism of polymer-network incorporation into single crystals. *Adv. Mater.* **21**, 470-473 (2009).

22. J. Ihli *et al.*, Elucidating mechanisms of diffusion-based calcium carbonate synthesis leads to controlled mesocrystal formation. *Adv. Funct. Mater.* **23**, 1965-1973 (2013).

23. C. L. Chen *et al.*, Tuning calcite morphology and growth acceleration by a rational design of highly stable protein-mimetics. *Sci. Rep.* **4**, (2014).

24. B. Demarchi *et al.*, Intra-crystalline protein diagenesis (IcPD) in Patella vulgata. part I: isolation and testing of the closed system. *Quat Geochronol* **16**, 144-157 (2013).

25. P. J. Tomiak *et al.*, Testing the limitations of artificial protein degradation kinetics using known-age massive Porites coral skeletons. *Quat Geochronol* **16**, 87-109 (2013).

26. S. Elhadj, J. J. De Yoreo, J. R. Hoyer, P. M. Dove, Role of molecular charge and hydrophilicity in regulating the kinetics of crystal growth. *Proc. Natl. Acad. Sci. U. S. A.* **103**, 19237-19242 (2006).

27. T. P. Hopp, K. R. Woods, Prediction of protein antigenic determinants from amino acid sequences. *Proc. Natl. Acad. Sci. U. S. A.* **78**, 3824-3828 (1981).

28. J. J. De Yoreo, P. G. Vekilov, Eds., *Principles of crystal nucleation and growth*, (Mineralogical Society of America, Washington, 2003), vol. 54, pp. 57-93.

29. E. Weber, B. Pokroy, Intracrystalline inclusions within single crystalline hosts: from biomineralization to bio-inspired crystal growth. *Crystengcomm* **17**, 5873-5883 (2015).

29A. J. D. Bass, Elasticity of minerals, glasses, and melts, in: Mineral Physics and Crystallography, A Handbook of Physical Constants, T. J. Ahrens, ed., American Geophysical Union, Washington, D.C., p. 45-63 (1995).

30. J. D. Eshelby, The determination of the elastic field of an ellipsoidal inclusion, and related problems. *Proc. R. Soc. London, Ser. A* **241**, 376-396 (1957).

31. W. C. Oliver, G. M. Pharr, An improved technique for determining hardness and elastic-modulus using load and displacement sensing indentation experiments. *J. Mater. Res.* **7**, 1564-1583 (1992).

32. A. J. E. Foreman, M. J. Makin, Dislocation movement through random arrays of obstacles. *Philos. Mag.* **14**, 911-924 (1966).

33. S. Akbulatov, Y. C. Tian, R. Boulatov, Force-reactivity property of a single monomer is sufficient to predict the micromechanical behavior of its polymer. *J. Am. Chem. Soc.* **134**, 7620-7623 (2012).

34. C. E. Diesendruck *et al.*, Mechanically triggered heterolytic unzipping of a low-ceiling-temperature polymer. *Nat. Chem.* **6**, 624-629 (2014).

35. M. Grandbois *et al.*, How strong is a covalent bond? *Science* **283**, 1727-1730 (1999).

36. E. Spruijt, S. A. van den Berg, M. A. C. Stuart, J. van der Gucht, Direct measurement of the strength of single ionic bonds between hydrated charges. *ACS Nano* **6**, 5297-5303 (2012).

(from 37, supplementary information refs)

37. K. E. H. Penkman, D. S. Kaufman, D. Maddy, M. J. Collins, Closed-system behaviour of the intra-crystalline fraction of amino acids in mollusc shells. *Quat. Geochronol* **3**, 2-25 (2008).

38. D. S. Kaufman, W. F. Manley, A new procedure for determining DL amino acid ratios in fossils using reverse phase liquid chromatography. *Quat. Sci. Rev.* **17**, 987-1000 (1998).

39. N. M. Szeverenyi, M. J. Sullivan, G. E. Maciel, Observation of spin Exchange by two-dimensional fourier-transform C-13 cross polarization-magic-angle spinning. *J. Magn. Reson.* **47**, 462-475 (1982).

40. S. P. Thompson *et al.*, Beamline I11 at Diamond: a new instrument for high resolution powder diffraction. *Rev. Sci. Instrum.* **80**, 075107 (2009).

41. W. C. Oliver, G. M. Pharr, Measurement of hardness and elastic modulus by instrumented indentation: advances in understanding and refinements to methodology. *J. Mater. Res.* **19**, 3-20 (2004).

42. L. Martinez, R. Andrade, E. G. Birgin, J. M. Martinez, PACKMOL: A package for building initial configurations for molecular dynamics simulations. *J. Comput. Chem.* **30**, 2157-2164 (2009).

43. J. M. Wang, W. Wang, P. A. Kollman, D. A. Case, Automatic atom type and bond type perception in molecular mechanical calculations. *J. Mol. Graphics Modell.* **25**, 247-260 (2006).

44. A. Jakalian, D. B. Jack, C. I. Bayly, Fast, efficient generation of high-quality atomic charges. AM1-BCC model: II. parameterization and validation. *J. Comput. Chem.* **23**, 1623-1641 (2002).

45. P. Raiteri, J. D. Gale, D. Quigley, P. M. Rodger, Derivation of an accurate force-field for simulating the growth of calcium carbonate from aqueous solution: a new model for the calcite-water interface. *J. Phys. Chem. C* **114**, 5997-6010 (2010).

46. J. M. Wang *et al.*, Development and testing of a general amber force field. *J. Comput. Chem.* **25**, 1157-1174 (2004).

47. C. L. Freeman *et al.*, New forcefields for modeling biomineralization processes. *J. Phys. Chem. C* **111**, 11943-11951 (2007).

48. W. G. Hoover, Canonical dynamics - equilibrium phase-space distributions. *Phys. Rev. A* **31**, 1695-1697 (1985).

49. S. Melchionna, G. Ciccotti, B. L. Holian, Hoover npt dynamics for systems varying in shape and size. *Mol. Phys.* **78**, 533-544 (1993).